3-26-2015

Simulation of Locking Space Truss Deployments for a Large Deployable Sparse Aperture Reflector

Dylan M. Van Dyne

Simulation of Locking Space Truss Deployments for a Large Deployable Sparse Aperture Reflector

THESIS

Dylan Van Dyne
AFIT-ENY-MS-15-M-250

DEPARTMENT OF THE AIR FORCE
AIR UNIVERSITY

AIR FORCE INSTITUTE OF TECHNOLOGY

Wright-Patterson Air Force Base, Ohio

AFIT-ENY-MS-15-M-250

SIMULATION OF LOCKING SPACE TRUSS DEPLOYMENTS FOR A LARGE DEPLOYABLE SPARSE APERTURE REFLECTOR

THESIS

Presented to the Faculty

Department of Aeronautical and Astronautical Engineering

Graduate School of Engineering and Management

Air Force Institute of Technology

Air University

Air Education and Training Command

in Partial Fulfillment of the Requirements for the

Degree of Master of Science in Astronautical Engineering

Dylan Van Dyne, B.S.M.E.

March 2015

AFIT-ENY-MS-15-M-250

SIMULATION OF LOCKING SPACE TRUSS DEPLOYMENTS FOR A LARGE DEPLOYABLE SPARSE APERTURE REFLECTOR

THESIS

Dylan Van Dyne, B.S.M.E.

Committee Membership:

Dr. Alan Jennings, PhD
Chair

Dr. Jon Black, PhD
Member

Dr. Eric Swenson, PhD
Member

AFIT-ENY-MS-15-M-250

Abstract

Large deployable space structures require an significant amount of effort to fully design and test on Earth. The Large Deployable Space Aperture Reflector is one such structure that is intended to increase ground to orbit satellite communications abilities by an order of magnitude. To aid in the determination of the feasibility of the reflector, a method to simulate the structure's deployment was developed using the COMSOL simulation software suite. The simulation model is comprised of a locking hinge truss that constitutes the partial reflector structure. To meet computational and temporal restrictions, the structure is simplified to use beams with square cross sections and is meshed to a sufficient accuracy with second order elements. The geometry itself is modeled in the truss's stowed configuration, with the connecting hinges and applied forces created via constraint equations in COMSOL. These equations dictate the unique behavior of the truss's radial deployment. Many different simulations were run with varied design parameters to not only demonstrate the global motion of the deploying truss under differing conditions, but to also showcase the capabilities of COMSOL's implicit solver. It was found through all of the simulation variations that the success of the truss's deployment is largely dependent on the orientation of the lower truss members as well as the interaction between the spring-loaded hinges and tension cables. Although the results from these simulations are representative of the simplified truss model, they demonstrate how COMSOL can be used to aid in the advancement of the Large Deployable Space Aperture Reflector design.

AFIT-ENY-MS-15-M-250

To Dr. Robyn King, who first introduced me to AFIT and got me excited about a Masters degree. To Dr. Michael Caylor, who made the arrangements for me to attend AFIT at a time when it seemed impossible. To my mother, whose previous graduate school experience allowed her to truly empathize with the rigors of my Masters program. To my aunt, for being as excited about my graduate school experience as I was. To my girlfriend, for always being there for me and never allowing me to be anything less than my best. And to my friends, who have no idea what it is I was doing at AFIT, but still cheered me on anyway.

Acknowledgements

First and foremost, I would like to sincerely thank my advisor, Dr. Alan Jennings, for his unending patience with my struggles through this entire process. Without his expertise, guidance, and trust I would have never accomplished as much as I have in so little time. He has my eternal gratitude for showing me how a scientist is supposed to think and I hope to carry his lessons with me as I endeavor to begin my professional career.

I must also acknowledge Dr. Jonathan Black, whose initial guidance on my course trajectory here at AFIT proved to be invaluable for my thesis work. In the future, I hope to have even a little of the savvy he has with the scientific community.

I am also grateful to have worked for Dr. Eric Swenson, who first received me at AFIT all that time ago in the summer of 2013. I will always remember his passion for the space industry and his belief in the value of hard work.

Dylan Van Dyne

Table of Contents

Page

Page

List of Figures

Figure Page

Figure Page

Figure Page

Figure Page

Figure Page

Figure Page

List of Tables

List of Symbols

List of Abbreviations

SIMULATION OF LOCKING SPACE TRUSS DEPLOYMENTS
FOR A LARGE DEPLOYABLE SPARSE APERTURE REFLECTOR

I. Introduction

1.1 Problem Statement

High bandwidth satellite to ground communication requires large antennas to overcome the signal attenuation experienced over the enormous transmission distance [9]. Although satellites are limited in power by their solar cells, there exists the potential to increase the signal gain by using a larger antenna reflector aperture. However, the use of large reflectors, or any large space structure, is impeded by the constraints of current launch vehicle technology. The Large Deployable Sparse Aperture Reflector[1] design concept offers a large reflector area that can be stowed within modern payload fairings [10]. Unfortunately, a 150 meter diameter structure designed only for space operations would be exceedingly difficult to build and properly test on Earth [11]. It is instead proposed that computer simulations of the reflector's deployment using FEM (Finite Element Methods) can significantly contribute to the design and future feasibility of the reflector. Additionally, it is suggested that the methodology created to study the behavior of this reflector's deployment may also be extended to other large space structures and therefore make a contribution to this field of research.

[1]This deployable structure is detailed in Section 2.1

1.2 Research Objectives and Focus

The objective of this research is to simulate the deployment of the folding trusses that constitute the structure of the Large Deployable Sparse Aperture Reflector. The hinges of the folding trusses employ locking hinges with pre-deformed springs that must be modeled correctly in order to simulate deployments representative of the envisioned design. The simulation model will be strategically altered to test its resilience when faced with variances in component quality, operation, or structural integrity. In particular, controlled deployments, uncontrolled deployments, deployments with centripetal acceleration, and deployments with weak hinge pairs were simulated.

The research will focus on building a methodology that can be used to reliably simulate the deployment of the folding trusses. The methods used to build the model were designed to be modular so that in the future they can be easily scaled with additional truss segments. The research will use the COMSOL Multiphysics software suite[2] to model the deployments with FEM. The numerical methods used to solve for the dynamic FEA (Finite Element Analysis) in the simulations are used only as tools and some discussion is given on method selection and adjusting method parameters in Section 3.5. The analysis of the deployments will concentrate on the envelope in which the truss deploys as well as the global response of the truss' deployment to different types of manufacturing error.

1.3 Assumptions and Limitations

The geometry of the deploying truss is assumed to be perfect as the research intent is to characterize the system as a whole and not its individual components. From previous research, geometric deviation resulting from manufacturing error will be

[2]Although many other finite element software packages have the capability to do large displacement multibody dynamics simulations, COMSOL was chosen due to its sizable physics library and unique numerical solver methods. The choice of package will be discussed in Section 2.3.

expected to be on the order of 0.01% [12], making this a very reasonable assumption. In addition, all constraints placed on geometry (displacements, hinges, forces, etc.) are adhered to perfectly by the system and are not representative of a real world test. Real systems would likely have additional flexibility, but modeling the additional compliance is difficult and very much tied to the actual test setups. The calculations for the deployment envelope assume that the horizontal and vertical battens remain rigid throughout the simulation. It is also assumed that the numerical solvers being used are working as expected and are not introducing any considerable error into the simulations. Results are visually inspected to gauge divergence or "numeric chatter." Commercial software was used and assumed to be verified for proper function, which proved to be the case.

The COMSOL MultiBody Dynamics package used for the simulations will only accept solid body geometry. Therefore, only solid finite elements were used. The equivalent material properties used with the simplified geometry in the simulations does not correctly represent axially loading and may create spurious results. It is assumed that bending modes of vibration dominate the model's predicted response because truss deployment is largely a function of moments applied to the long, slender beams that comprise the longerons. It should also be noted that the computer hardware being used for the simulations can only be classified as personal computers, and therefore do not have the capabilities to run simulations with very fine geometric detail.

1.4 Methodology

Figure 1 illustrates the methodology of this work. The geometry of the trusses was constructed and then simplified in SolidWorks. The solid models were imported in COMSOL where the connecting bodies, joints, and boundary conditions were declared. The models were meshed using COMSOL's built-in functionality. The numerical solver settings in COMSOL were adjusted according to the needs of the simulation, and probes were placed at important locations on the model to monitor the simulation. Numerous simulations were run to test the model's compliance with various disturbances. The results of these simulations were analyzed to identify deployment behaviors and the truss's sensitivity to hinge variations. Additionally, conclusions about the methodology's effectiveness were made.

1.5 Overview

Chapter 2 presents background information crucial to the understanding of this work. Here, historical designs of large space structures are introduced, and the design of the Large Deployable Sparse Aperture Reflector is shown. The challenges of testing large deployable space structures on Earth are also discussed. Next, the basics of Finite Element Methods as well as some select element types are explained. The different methods for solving dynamic Finite Element Analysis problems and the numerical method that COMSOL uses are then shown. Finally, some concerns about the computational hardware being used are shared.

Chapter 3 presents the methodology used to create the simulation model that includes: FEA software selection, solid modeling, model simplification, creating equivalent material properties, explaining the nomenclature being used within the model, importing the geometry into COMSOL, meshing the geometry, establishing the physics that define the motion of the model, coding the cables used between the truss members, adding probes to monitor the model during the simulation, and configuring the solver in COMSOL. This chapter ends with a brief mesh study to justify the technique used to mesh the model, and a word on how the deployment envelope is calculated in MATLAB. Figure 1 gives a visual representation of this methodology.

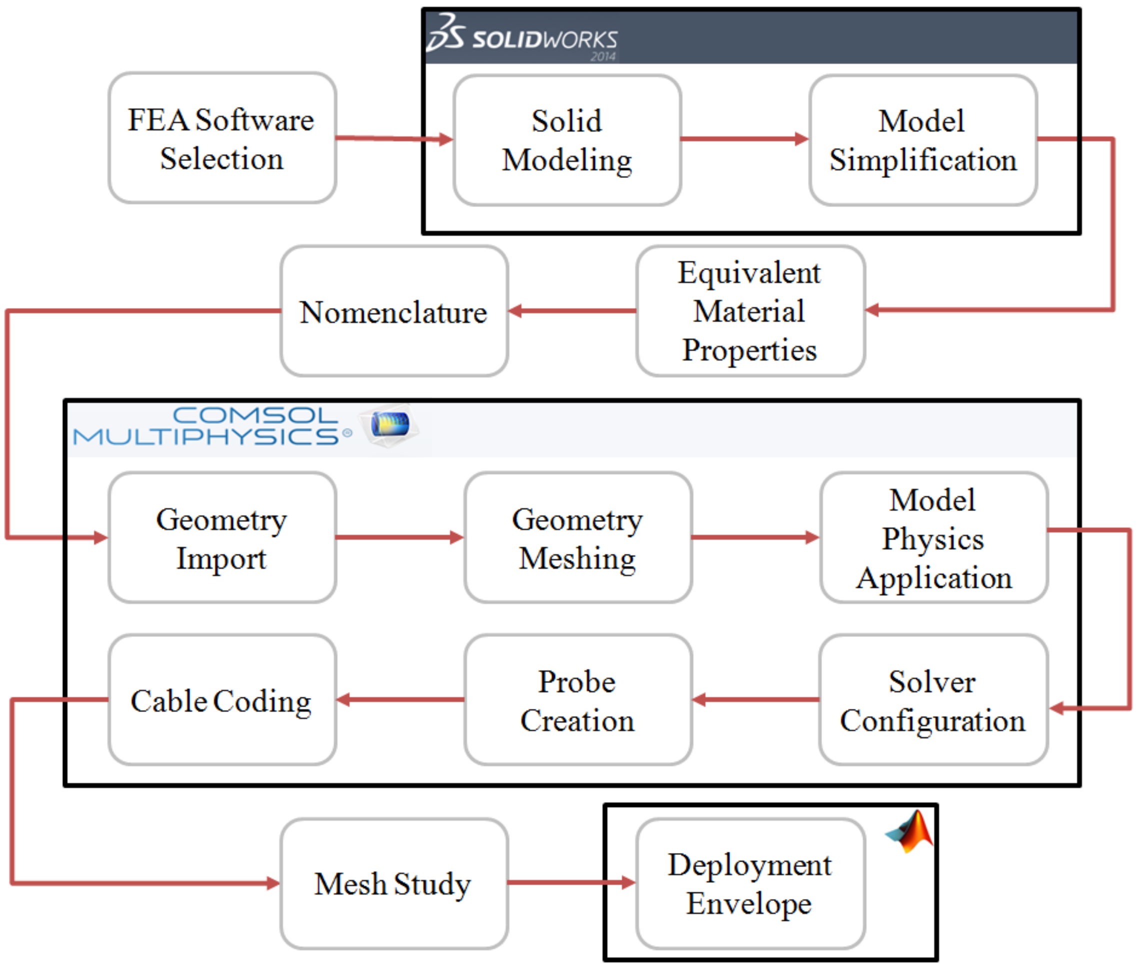

Figure 1. Flowchart illustrating the methodology presented in Chapter 3.

Chapter 4 analyzes the results of the different simulations beginning with the uncontrolled deployment methods, then deployments involving centripetal acceleration, deployments with weak upper or lower hinge pairs, and finally controlled deployments. Chapter 5 contains a summary, the conclusions from the analysis and recommendations for future work.

II. Background

Chapter 2 introduces the pertinent background information that is related to the important aspects of this work. First, Section 2.1 offers a brief overview of the historic space structures that inspired the Large Deployable Sparse Aperture Reflector. Then, the reflector itself and its deployment methods are described in order to familiarize the reader with its operation. The section wraps up with a quick word on the challenges of testing space structures in Earth's gravity. Section 2.2 introduces FEM to the reader so as to provide a basis of understanding of the mathematical concepts being used. The fundamentals of FEM are explained, expanded to higher dimensions, and the importance of proper element interpolation schemes are noted. Section 2.3 takes the general-purpose finite element methodology and applies it to structural dynamics. The theories behind the dynamics themselves are first submitted, and are then followed by two prominent methods of dynamic finite element computation. All of these concepts culminate in the last part of this section, showing how they are applied by COMSOL and used for the simulations in this work. Finally, Section 2.4 covers some computational considerations that play an important part in any computationally-intensive work such as this.

2.1 Large Deployable Space Structures Design

Filled Aperture Deployment Simulation.

Deployment analyses of filled aperture reflectors have been conducted many times in the past. The NTT Wireless Systems Laboratory not only simulated the deployment of an experimental 4.8 meter diameter filled aperture reflector, but also conducted validation experiments with a laboratory prototype [1]. The filled aperture was comprised of a mesh reflector held by a truss structure stiffened by a network of cables. The authors of the work stressed the importance of simulating the design with flexible bodies to more properly represent the actual prototype [13] and avoid losing the inertial forces due to superposition. Through flexible body computer simulations, the drive force required for successful deployment was found. The drive force was validated through experimental data as well, and it was concluded that "flexible multibody dynamics can provide a clear and concrete numerical solution and unveil problems that cannot be or is difficult to be detected by conventional rigid body simulations." [1] Figure 2 shows the size and packaging of the filled aperture. Note how the aperture's stowage height increases with the diameter of the reflector. Increasing the diameter of the reflector would require even more height that would have to be fit into launch vehicle payload fairings.

Martin Marietta Box Truss Development.

In 1978 the Martin Marietta Corporation began work on deployable box truss cubes to meet Shuttle-transportable large space system requirements [2]. The box truss cube was comprised of a deployable frame in which the horizontal members were split by midlink hinges that were folded for stowage. The final shape was controlled by the tension of diagonal tape running crossing through the square faces of the sides of the cube (Figure 3).

Some of the advantages of the box truss were its versatility to be used in different configurations, its efficient stowage of structural members, and its potentially low cost. The design of a 4.6 meter proof-of-concept cube (Figure 4) was completed in 1980, and a prototype was built and tested the following year. Test results show that the box truss cube was very efficient, having high stiffness and low weight. Even better, the box truss cube was accurate to 0.1 millimeters on all axes and endured through multiple deployments without any structural failures[2].

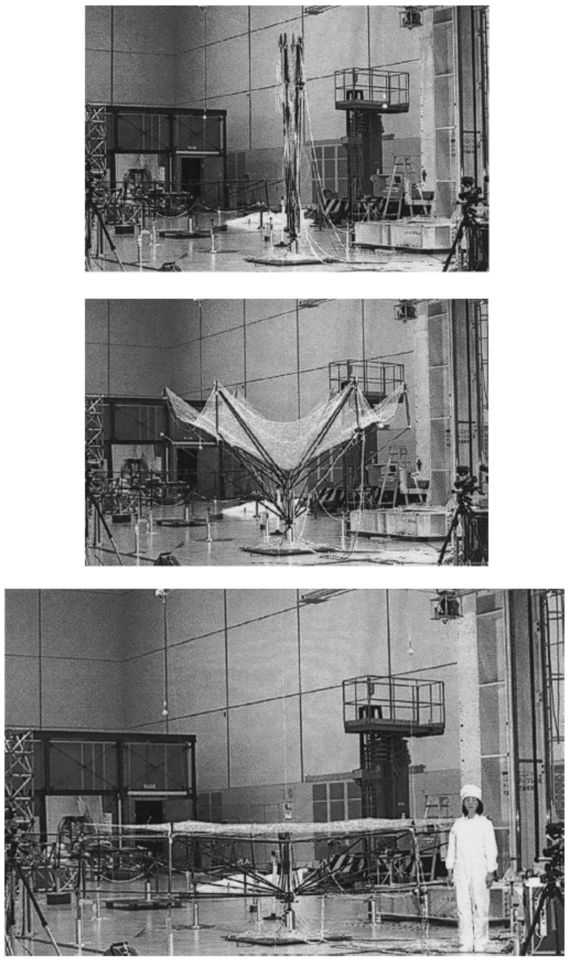

Figure 2. NTT Wireles Systems Laboratory 4.8 meter Filled Aperture Reflector Prototype. From top to bottom: Stowed, Deploying, Deployed. [1].

Further work was done by Martin Marietta to investigate the possibility of creating parabolic reflectors from multiple box trusses with differing top and bottom member lengths. Additional designs were envisioned that applied the deploying box truss idea to many different aspects of space structures. One FEA was performed on a stowed deployable antenna model in order to see whether or not its fundamental frequency was high enough to be considered launch capable. Due to the technology at the time (1982), however, the FEA was very low fidelity: just an eight node cube with lumped masses on the corners of the central box truss. Kinematic testing of the deployable box truss used the complete fabrication of prototypes to validate the

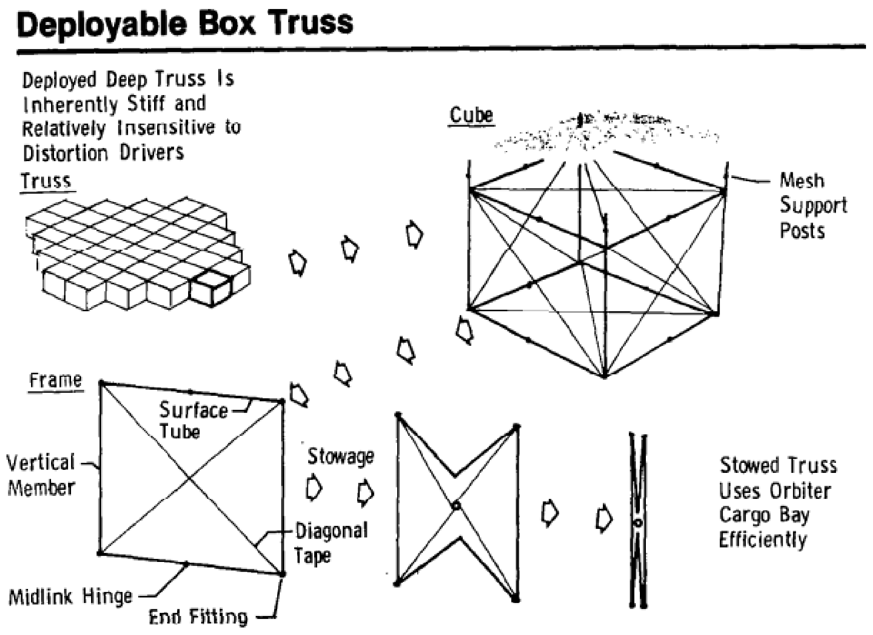
Deployable Box Truss
Deployed Deep Truss Is Inherently Stiff and Relatively Insensitive to Distortion Drivers
Truss
Cube
Mesh Support Posts
Frame
Surface Tube
Vertical Member
Stowage
Diagonal Tape
Midlink Hinge
End Fitting
Stowed Truss Uses Orbiter Cargo Bay Efficiently

Figure 3. Martin Marietta Deployable Box Truss Design [2].

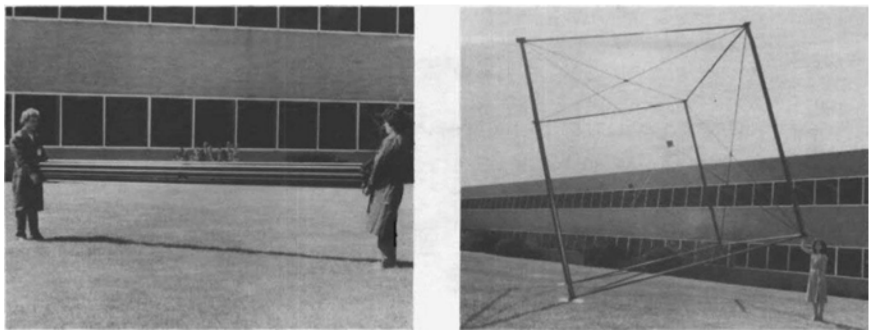

Figure 4. Martin Marietta Deployable Box Truss Prototype [2]. Left: Stowed box truss. Right: Deployed box truss.

expected performance. Such tests were conducted in the gravitational environment of Earth, and could only be correlated to on-orbit behavior.

Able Deployable Articulated Mast (ADAM).

The Shuttle Radar Topography Mission mapped the topography of nearly 80% of Earth's land surfaces in February of the year 2000 [3]. The mission required an outboard antenna to be placed on the end of a rigid boom extending 60 meters from the shuttle itself. The ADAM (Able Deployable Articulated Mast) was a truss structure consisting of 87 cube-shaped truss cells that not only held the outboard antenna at a precise location, but could also retract back into the shuttle after the mission.

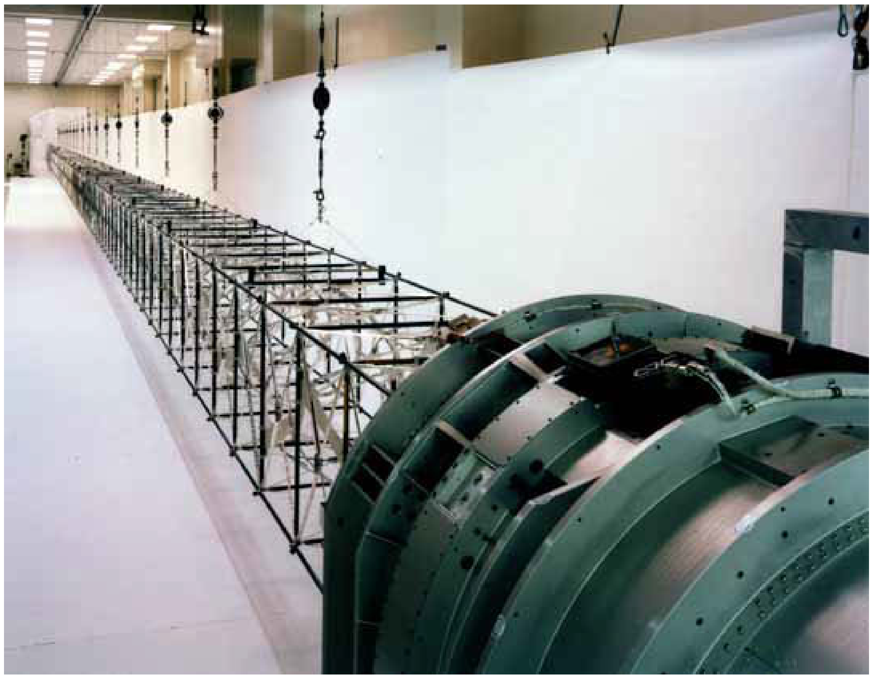

Figure 5. ADAM deployed from canister in laboratory environment with gravity offloading [3].

Today, the design and manufacture of this deployable mast is done by ATK Aerospace Structures [14]. Unlike the Martin Marietta design, the box truss members do not fold themselves. Rather, the members have ball joints on their ends to allow the specialized corner fittings to fold the members as the box truss is rotated in a deployment canister. Figure 6 shows a stowed 10 meter ADAM that was used most recently for the NuSTAR mission in 2012 performed by JPL (Jet Propulsion Laboratory) and the California Institute of Technology [4]. To date, ATK has flown 11 of these masts and has had a 100% success rate [14].

ATK lists some important advantages of using deployable truss systems for space operations: high deployment reliability and repeatability, extensive flight heritage,

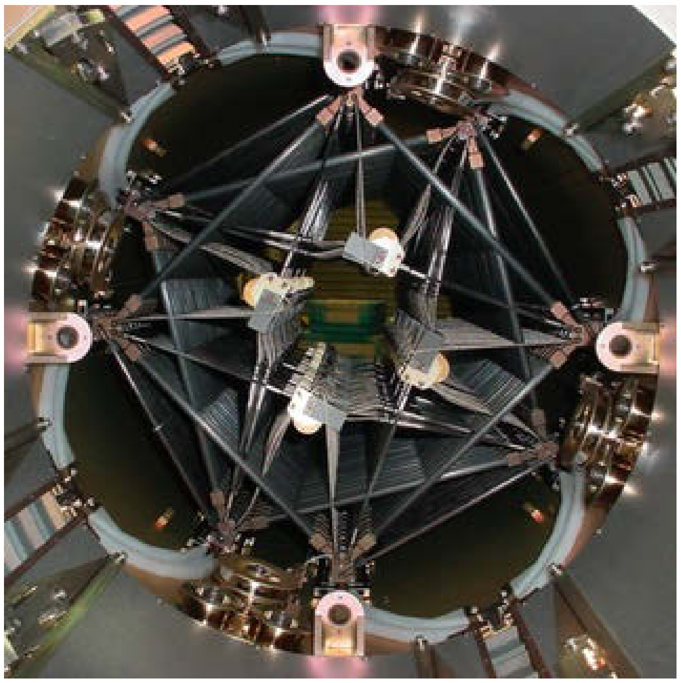

Figure 6. NuSTAR ADAM in stowed configuration [4].

validated on-orbit strength and stiffness performance, efficient stowage volume ($< 5\%$ of total length), and a modular design that allows the mast length to be tailored for specific mission requirements. However, this modularity only extends the length of the mast and does not allow for additional truss cells in any other direction, unlike the Martin Marietta concepts. Packaging efficiency is also not great, as Figure 6 shows a considerable amount of unused space in the deployment canister.

Large Deployable Sparse Aperture Reflector Structural Design.

The Martin Marietta box truss cube showed significant promise. It had great packaging efficiency, had multi-directional modularity, and was very strong. Unfortunately, further design iterations were hampered by limited resources and applications for the trusses. Very few prototypes were tested. The ADAM, on the other hand, is a multi-joint, deployable truss structure with great flight heritage that has been proven to be a viable solution for creating large structures in space. The thought then, is to combine the best aspects of each design into a new large deployable space structure. Enter the Large Deployable Sparse Aperture Reflector design that is currently being investigated by the Air Force Institute of Technology (AFIT).

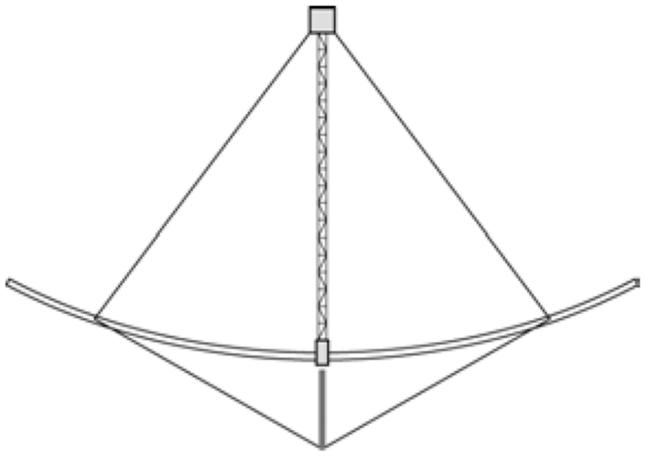

Figure 7. Conceptual side layout view of Large Deployable Sparse Aperture Reflector. Courtesy of Dr. Gyula Greschik [5].

The Large Deployable Sparse Aperture Reflector concept (Figure 7) was conceived as a means to recreate the area of a 50 meter diameter filled reflector aperture with a sparse design that could be stowed into existing payload fairings of approximately 5 meters in diameter. The reflector is intended to be used on a satellite in a geostationary orbit and receives L-Band signals of 1-2 GHz [15]. Much work as been done to down-select the design [10], increase packaging efficiency [10], calculate its electrical performance [15], and determine the required manufacturing accuracy requirements [12]. This work focuses on the deployment of the design chosen as a result of these previous works.

In essence, the sparse aperture reflector is comprised of four arms which deploy from a central hub (Figure 8). The arms are made from eight box trusses each, henceforth known as truss cells, that are shaped into a parabola. The parabola is created through the use of shaping tension cables on the sides of the cells as well as unequal length top and bottom members of the truss cells. Additional structural

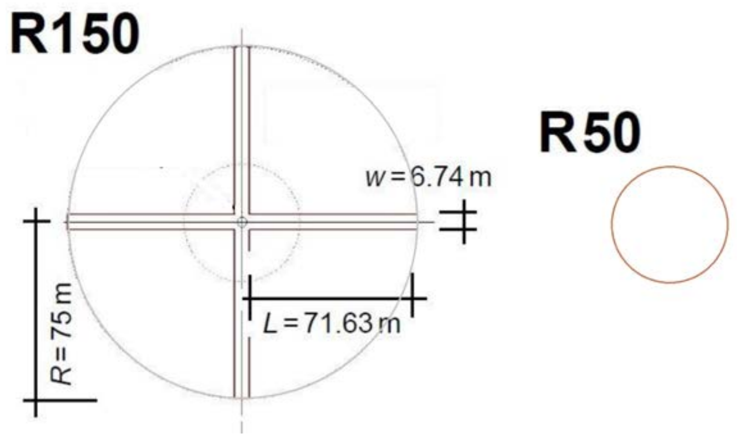

Figure 8. Top view of sparse aperture with 150 meter diameter compared to a filled aperture with 50 meter diameter. Courtesy of Dr. Gyula Greschik [5].

cables reside in the top and bottom faces of the cells as well, and serve to add more rigidity to the truss cell. The deployment occurs in two stages: a bounded horizontal opening of the truss cells via a motor in the hub (first stage), and an unbounded radial expansion along the lengths of the truss cells (second stage). These stages are shown in Figure 9 which is a more detailed representation of the geometry shown in Figure 8. The first stage of deployment unfolds the “horizontal battens” of the truss cell, and the second stage of deployment unfolds the “longerons,” or the members that run the radial length of the truss cell. Both the horizontal battens and the longerons are split by hinges that lock after 180 degrees of rotation, but only the longeron’s hinges contain a pre-deformed spring that motivates the radial deployment. The upright structural members of the truss are known as vertical battens, and are static in their length. Please refer to Figure 10 for an illustration of these structural members. Once fully deployed, the entire structure is held in tension by the multitude of cables within each cell as well as many other cables spanning different arms and the central mast.

The advantages of the Large Deployable Sparse Aperture Reflector concept are numerous. Through the use of truss cells with tension cables, the reflector will have a high stiffness to mass ratio similar to the Martin Marietta design. By collapsing

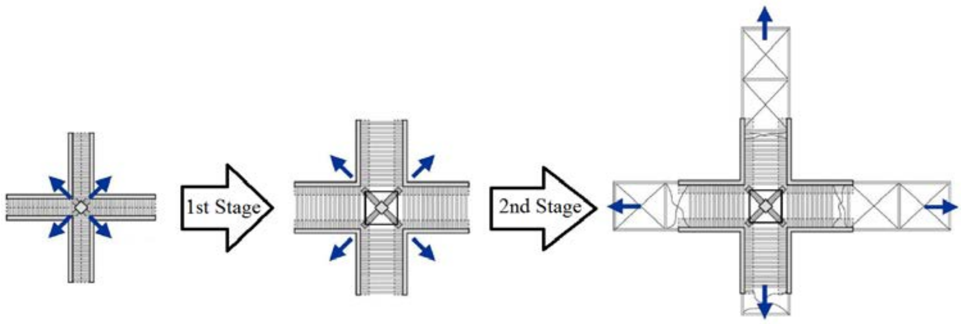

Figure 9. Top view of sparse aperture deployment stages. Courtesy of Dr. Gyula Greschik [5].

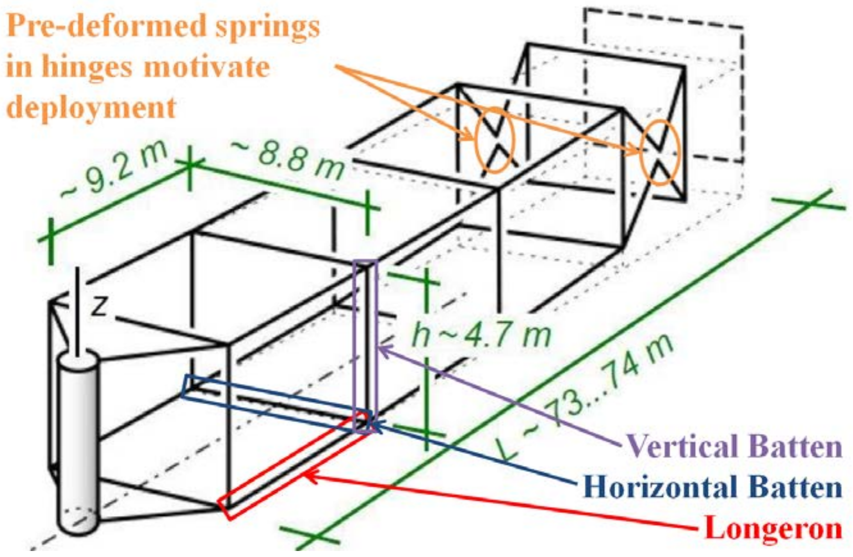

Figure 10. Nomenclature of truss cells shown during possible radial deployment with some nominal dimensions. Courtesy of Dr. Gyula Greschik [5].

the truss cells along their horizontal battens and longerons, an entire 150 meter diameter structure can be packaged into a 5 meter payload fairing. Although the truss structure is inherently complex, the ADAM's flight history has shown that deployable truss structures are a viable design for on orbit operations. Therefore, the next step in determining the feasibility of the sparse aperture reflector is to explore the deployment mechanisms at work. Logically, this would involve building scale models to test the proposed deployment methods.

High-Fidelity Gravity Offloading System.

The fabrication and test of proposed designs are critical to the development of new technologies. Space structures require special consideration because they are sometimes designed for a weightless environment. Measures need to be taken to "offload" the structures so that the tests done to them are representative of the space environment. Unfortunately, "ground tests to explore the *zero-g* performance of mechanical systems inevitably employ various compromised solutions" [11]. Such solutions usually involve hanging the structure so that it does not have to support its own weight (Figure 5), or free-fall drop tests in which the subject is virtually weightless for a short amount of time. For kinematic testing, more creative offloading schemes must be devised so that the motion of the structure remains unimpeded by both gravity and the offloading hardware itself [16]. Although many viable solutions for gravity offloading exist and have been proposed, the fact remains that fabricating and testing the hardware would be time-consuming and expensive. Most likely the design under review in this work would at first be scaled to test the structure's deployment validity. Eventually though, a full-scale test to certify the structure for flight would have to be conducted, which would require an enormous test facility. Fortunately, modern computers and certain mathematical methods can be employed to conduct analysis on large space mechanisms before they ever need to be fabricated. This allows the designers of such large structures to test and iterate their designs many times before the expensive full-scale fabrication and testing need to occur.

2.2 Static Finite Element Methods

Finite Element Analysis.

"FEA (Finite Element Analysis), also called the FEM (Finite Element Method), is a numerical method to finding the solution to field equations" [7]. The field equations spatially subdivide the whole domain of a problem into simpler, finite parts. Solving for the dependent variables present in the field equations in a piece-wise fashion for the whole domain yields an approximation of the exact solution. The exact solution itself would almost certainly be impossible to solve for save the simplest of problems. Such methods are extremely useful for solving complex problems and have applications in a myriad of scientific fields. In particular, this work explores how FEM can be used to simulate the deployments of space structures.

The foundation of finite elements lies in the discretization of geometry into "elements." These elements are connected at points known as "nodes" where the field equations are applied and the dependent variables solved for. When dealing with structural analysis, the nodal applications usually involve the material properties of the geometry being segmented as well as the individual node's local displacement. The local displacements are commonly labeled as follows: u (Local X-Displacement), v (Local Y-Displacement), and w (Local Z-Displacement). Interpolating these properties and displacements is done along the elements, and can be done with different polynomial orders. The combination of multiple nodes and elements to describe a geometry is known as a "mesh". Figure 11 shows a simple 2D beam mesh in which the three nodes are free to rotate and translate vertically, and are connected by two elements.

Mathematically, the static finite element problem is represented as a system of equations: $[K]\{D\} = \{R\}$. Here, the matrix $[K]$ is the assemblage of the elements' stiffnesses that are derived from the material properties of the geometry in question.

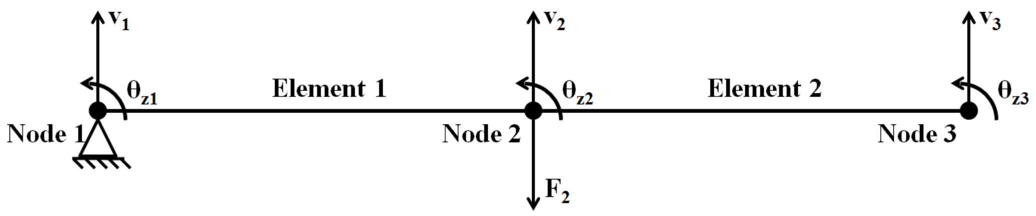

Figure 11. Simple 2D beam mesh comprised of two elements.

When two elements share a node, the overlapping sections of the $[K]$ matrices are merely added together. The vector $\{D\}$ represents the nodal displacements. The other vector $\{R\}$ contains the forces applied to the geometry (F (Force)). Shown in Equations 1 and 2, solving for the displacements that result from the applied forces is a matter of multiplying $\{R\}$ by the inverse of $[K]$. From there, the displacements of the nodes can be solved for using linear algebra. In order to constrain the problem, boundary conditions are applied throughout these systems of equations. When solving, the $[K]$ matrix is partitioned for the unconstrained parted and inverted to solve for the displacements. Equation 1 shows the initial systems of equations used for the beam shown in Figure 11.

$$\begin{Bmatrix} -F_1 \\ -M_1 \\ F_2 \\ 0 \\ 0 \\ 0 \end{Bmatrix} = \begin{bmatrix} \frac{12EI_z}{L^3} & \frac{6EI_z}{L^2} & \frac{-12EI_z}{L^3} & \frac{6EI_z}{L^2} & 0 & 0 \\ \frac{6EI_z}{L^2} & \frac{4EI_z}{L} & \frac{-6EI_z}{L^2} & \frac{2EI_z}{L} & 0 & 0 \\ \frac{-12EI_z}{L^3} & \frac{-6EI_z}{L^2} & \frac{12EI_z}{L^3} + \frac{12EI_z}{L^3} & \frac{-6EI_z}{L^2} + \frac{-6EI_z}{L^2} & \frac{-12EI_z}{L^3} & \frac{6EI_z}{L^2} \\ \frac{6EI_z}{L^2} & \frac{2EI_z}{L} & \frac{-6EI_z}{L^2} + \frac{-6EI_z}{L^2} & \frac{4EI_z}{L} + \frac{4EI_z}{L} & \frac{-6EI_z}{L^2} & \frac{2EI_z}{L} \\ 0 & 0 & \frac{-12EI_z}{L^3} & \frac{-6EI_z}{L^2} & \frac{12EI_z}{L^3} & \frac{-6EI_z}{L^2} \\ 0 & 0 & \frac{6EI_z}{L^2} & \frac{2EI_z}{L} & \frac{-6EI_z}{L^2} & \frac{4EI_z}{L} \end{bmatrix} \begin{Bmatrix} 0 \\ 0 \\ v_2 \\ \theta_{z2} \\ v_3 \\ \theta_{z3} \end{Bmatrix} \tag{1}$$

Here, E (Youngs's Modulus) is stiffness of the material in Newtons per square meter, I_z (Area Moment of Inertia) relates the cross-sectional geometry of the beam in quartic meters, and L (Length) is the elemental length in meters.

After applying the boundary conditions, the rows and columns of the DOF (Degrees of Freedom) that were constrained are removed. Then, the forces vector is multiplied by the inverse of the stiffness matrix to solve for the displacements and create a solution for the problem.

$$\begin{Bmatrix} v_2 \\ \theta_{z2} \\ v_3 \\ \theta_{z3} \end{Bmatrix} = \begin{bmatrix} \frac{12EI_z}{L^3} + \frac{12EI_z}{L^3} & \frac{-6EI_z}{L^2} + \frac{-6EI_z}{L^2} & \frac{-12EI_z}{L^3} & \frac{6EI_z}{L^2} \\ \frac{-6EI_z}{L^2} + \frac{-6EI_z}{L^2} & \frac{4EI_z}{L} + \frac{4EI_z}{L} & \frac{-6EI_z}{L^2} & \frac{2EI_z}{L} \\ \frac{-12EI_z}{L^3} & \frac{-6EI_z}{L^2} & \frac{12EI_z}{L^3} & \frac{-6EI_z}{L^2} \\ \frac{6EI_z}{L^2} & \frac{2EI_z}{L} & \frac{-6EI_z}{L^2} & \frac{4EI_z}{L} \end{bmatrix}^{-1} \begin{Bmatrix} F_2 \\ 0 \\ 0 \\ 0 \end{Bmatrix} \tag{2}$$

COMSOL 3D Elements.

The formulation of the beam elements used in Equation 1 is just one of a great many that can be used to describe a 1D beam geometry in 2D space. When moving to 2- or 3D geometries, elements become a sort of combination of beam elements that help describe the added dimensions. In this work, 3D elements are used in order to properly discretize the 3D geometry. The particular elements under review here are Lagrangian tetrahedral (4-sided polygon) and Lagrangian hexahedral (6-sided polygon) elements that are used in COMSOL [17].

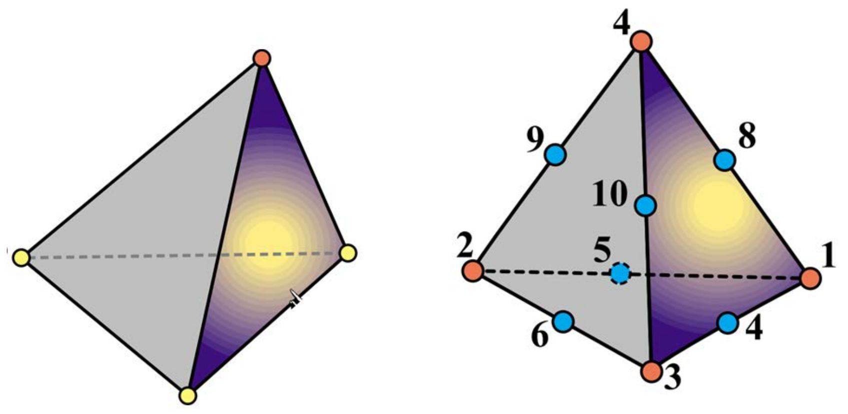

Figure 12. Left: Linear tetrahedral element. Right: Quadratic tetrahedral element. [6]

By default, COMSOL meshes geometries with tetrahedrons. Tetrahedrons are useful for meshing because almost any geometry can be approximated to arbitrary precision with a sufficiently dense tetrahedral mesh. COMSOL even features an ‘adaptive meshing” tool that will coarsen or refine a meshduring a simulation in response to certain convergence criteria at every time step. Figure 12 shows both a linear tetrahedral element as well as a quadratic tetrahedral element[1] The linear tetrahedral element has 4 nodes, and the quadratic tetrahedral element has 10 nodes. With 3 DOF per node, this gives the linear element 12 DOF and the quadratic element 30 DOF.

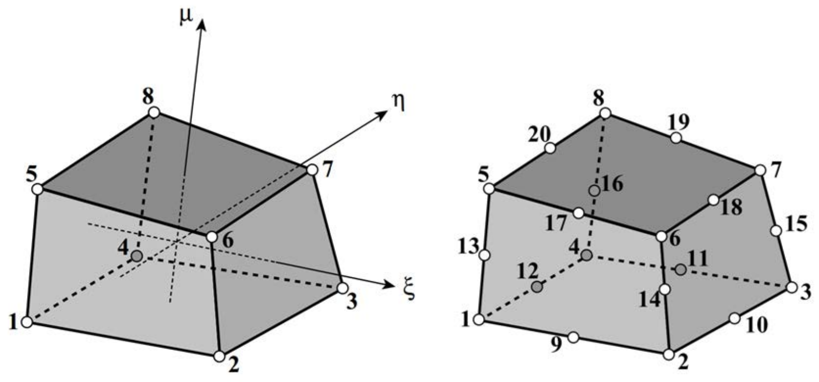

Figure 13. Left: Linear hexahedral element. Right: Quadratic hexahedral element. [6]

Although tetrahedrons can be used for many geometries, they are not always the most efficient method for meshing. For certain geometries, especially certain simplified 3D trusses, hexahedrons are more effective. In COMSOL, hexahedrons require extra effort from the engineer since they are not automatically meshed. Fortunately, the mesh process is quite swift. Figure 13 shows both a linear hexahedral element as well as a quadratic hexahedral element. The linear element has 8 nodes and 24 DOF (3 DOF per node). The quadratic element has 20 nodes and 60 DOF (3 DOF per node).

[1]The use of the terms ‘linear” and ‘quadratic” are elaborated in the following section.

Element Interpolation.

An important aspect of finite elements is the interpolation between the nodes of the mesh. The formulations for the interpolation methods are numerous, and stem from the "shape function" on which they are based. These shape functions are generally classified by the order of interpolation they can provide between the major nodes. For instance, a first order element can only interpolate linearly between two nodes. A second order element places a secondary node between two primary nodes, and thus allows for quadratic interpolation. In most cases, adding in these extra nodes allows the element to approximate the "true" solution even better. As a consequence, the total DOF of a mesh of quadratic elements will have a sizable increase. The system stiffness matrix $[K]$ will also be more densely populated. Both of these factors will greatly penalize the simulation times. However, the mesh resolution could also be lowered when using quadratic elements and reduce the size of the stiffness matrix and the simulation time. At the end of the day, it is up to engineer to decide how to balance the element order and mesh density when building a FEM model.

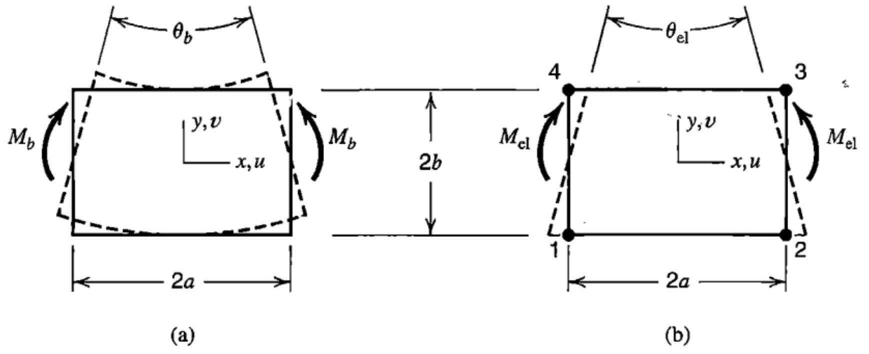

Figure 14. Left: Deformation mode of a rectangular block of material in pure bending. Right: Deformation mode of the Q4 element under bending load. [7]

Figure 14 is a simplified 2D case of when a higher order element is needed. The Q4 (Four-node Bilinear Rectangle Element) on the right cannot exhibit pure bending. "When bent, it displays shear strain as well as the expected bending strain.

This *parasitic shear* absorbs strain energy, so that if a given bending deformation is prescribed, the bending moment needed to produce it is larger than the correct value. In other words, the Q4 element exhibits *shear locking* behavior" [7]. In short, the use of linear elements such as the Q4 in a mesh under a bending load will cause the stiffness of the mesh to be egregiously high. This elemental defect can be overcome through the use of a higher order element. In this case, a Q8 (Eight-node Quadratic Rectangle Element) with mid-side nodes would enable the sides of the element to form a curve and correctly transfer the bending moment through the entire mesh. This logic can be applied to 3D elements and meshes, such as the elements described in the previous section.

2.3 Dynamic Finite Element Methods

Theory.

Many methods for structural dynamics were developed before the advent of FEM for use on structures and so the calculation methods are largely independent. Today, however, many methods have been tailored to fit the discretization of FEM models. These methods not only use the same stiffness matrix found in static FEM, but also require mass and damping matrices. Together, the matrices can be applied to the solve for Newton's second law as seen in Equation 3 [7].

$$f = ma \Rightarrow r - ku - c\dot{u} = m\ddot{u} \Rightarrow m\ddot{u} + c\dot{u} + ku = r \tag{3}$$

where m (Mass), r (Forcing Function), a (Acceleration), k (Stiffness Constant), c (Damping Constant), $\dot{u}$ (Velocity), and $\ddot{u}$ (Acceleration). Note that the resulting force of the spring ku may be called an internal force [7].

From this equation and some FE theory, the global form of Newton's second law for FEA can be written as Equation 4 or Equation 5 [7].

$$[M]\{\ddot{D}\} + [C]\{\dot{D}\} + \{R^{int}\} = \{R^{ext}\} \tag{4}$$

$$[M]\{\ddot{D}\} + [C]\{\dot{D}\} + [K]\{D\} = \{R^{ext}\} \tag{5}$$

where the capital letters indicate the matrix or vector form of their lower case counterparts to show that these are discretized sample locations. Also note that matrices are represented by brackets and vectors are represented by braces.

Explicit and Implicit Integration Methods.

There are two basic methods of integration used to solve these equations: explicit and implicit. Both have their own advantages and disadvantages, but the main goal of these methods is to solve for the displacement $\{D\}$ of the system for one time step.

Explicit direct integration is a conditionally stable form of numerical integration that requires both the knowledge of the past and present to compute the solution to the future. It is best suited towards "wave propagation" type problems. The stability of this method hinges upon the time step chosen, which is a function of the structure's mass and stiffness. Usually, the time step chosen must be very small to yield a stable result, meaning that the solutions found with this method are often very exact at the cost of a high amount of time steps needed. Thankfully these steps are usually cheap in terms of computation time because the matrices are diagonal. Shown here as an example is the "Half-Step Central Difference" method in Equation 6.

$$\frac{1}{\Delta t^2}[M]\{D\}_{n+1} = \left\{R^{ext}\right\}_n - \left\{R^{int}\right\}_n + \left[\frac{2}{\Delta t^2}M - \frac{1}{\Delta t}C\right]\{D\}_n - \left[\frac{1}{\Delta t^2}M - \frac{1}{\Delta t}C\right]\{D\}_{n-1} \tag{6}$$

The time step (Δt (Time Step)) is limited by the resonance of the highest frequency component, which generally corresponds to the smaller elements used for detailing the structure. For highly detailed structures, it becomes quite difficult to find a stable time step with explicit methods. It is therefore more advantageous to use implicit methods whose accuracy, not stability, depend on the time step used. Implicit methods only require knowledge of the present to compute the solution to the future. This allows most methods to be unconditionally stable and is more useful for structural dynamics. The biggest downside to this possible unconditional stability is the amount of computation it takes to solve for the non-diagonal matrices in the problem. For this particular example, the numerically stable Newmark Method is used and is shown in Equation 7.

$$\begin{aligned}[K^{eff}]\{D\}_{n+1} = \left\{R^{ext}\right\}_{n+1} + [M]\left\{\frac{1}{\beta\Delta t^2}\{D\}_n + \frac{1}{\beta\Delta t}\left\{\dot{D}\right\}_n + \left(\frac{1}{2\beta}-1\right)\left\{\ddot{D}\right\}_n\right\} \\ + [C]\left\{\frac{\gamma}{\beta\Delta t}\{D\}_n + \left(\frac{\gamma}{\beta}-1\right)\left\{\dot{D}\right\}_n + \left(\frac{\gamma}{2\beta}-1\right)\left\{\ddot{D}\right\}_n\right\} \quad (7)\end{aligned}$$

Where γ (Gamma) and β (Beta) are numerical factors that control characteristics of the Newmark Method such as accuracy, numerical stability, and algorithmic damping.

Previous work [8] with these methods show systems that can be precisely characterized are best represented with explicit methods. However, for systems that cannot be fully characterized, only the implicit methods yield converging[2] results easily.

As an example, take a cantilevered beam similar to that of the problem detailed in Figure 11 with an impulsive load is applied along its length at the free end. Figure 15 shows how the stress in the middle of the beam increases as a stress wave propagates

[2]Convergence here meaning that the algorithm is stable enough to find a solution within set tolerances.

through it[3]. The explicit results are more intuitively representative of the stress wave propagation while the implicit results are filled with noise. Yet, these explicit results are gained from a precisely calibrated time step. Figure 16 shows what happens if this time step is altered by just one nanosecond. The COMSOL results shown are different dimensional representations of the same beam that were run for the sake of comparison. Plainly, this kind of instability is not conducive for a system more complex than the simple cantilevered beam shown here. It is for this reason that the implicit solvers[4] within COMSOL were chosen to compute the solution to the deploying trusses in which the final solution is relatively unknown. Figure 17 shows that COMSOL's implicit solver fares very well in various dimensions against the aforementioned numerical methods and thus validates COMSOL's implicit solver for this scenario.

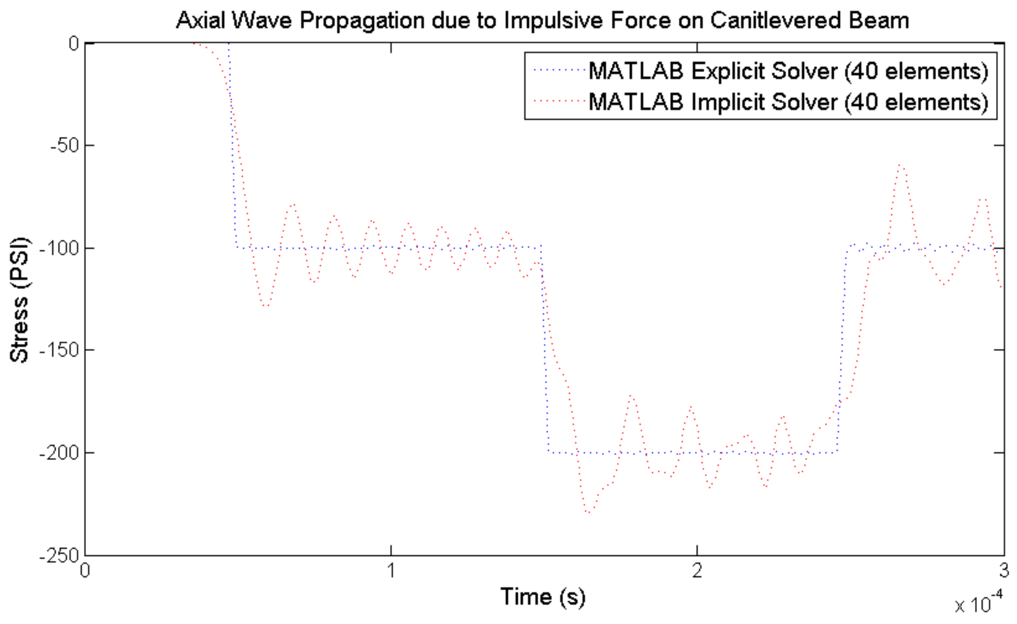

Figure 15. Axially-loaded cantilevered beam: explicit vs. implicit methods. [8]

[3]Note that the simulation time is only for 0.3 milliseconds in order to view the stress wave's propagation.

[4]The implicit solver used in COMSOL is described in detail in Section 2.3.

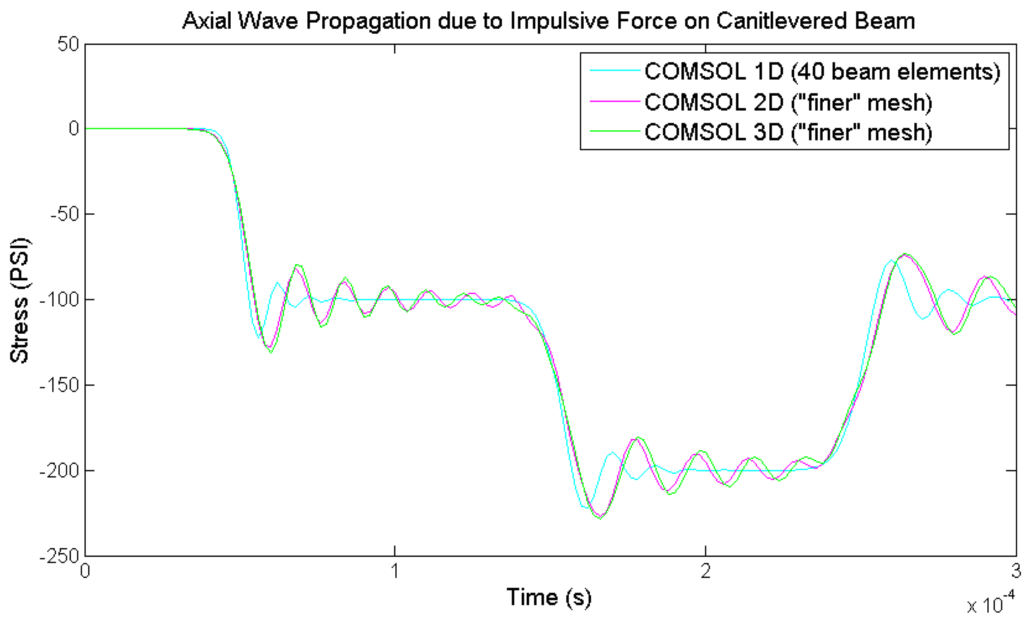

Figure 16. Axially-loaded cantilevered beam: explicit method deviation due to time step variance. [8]

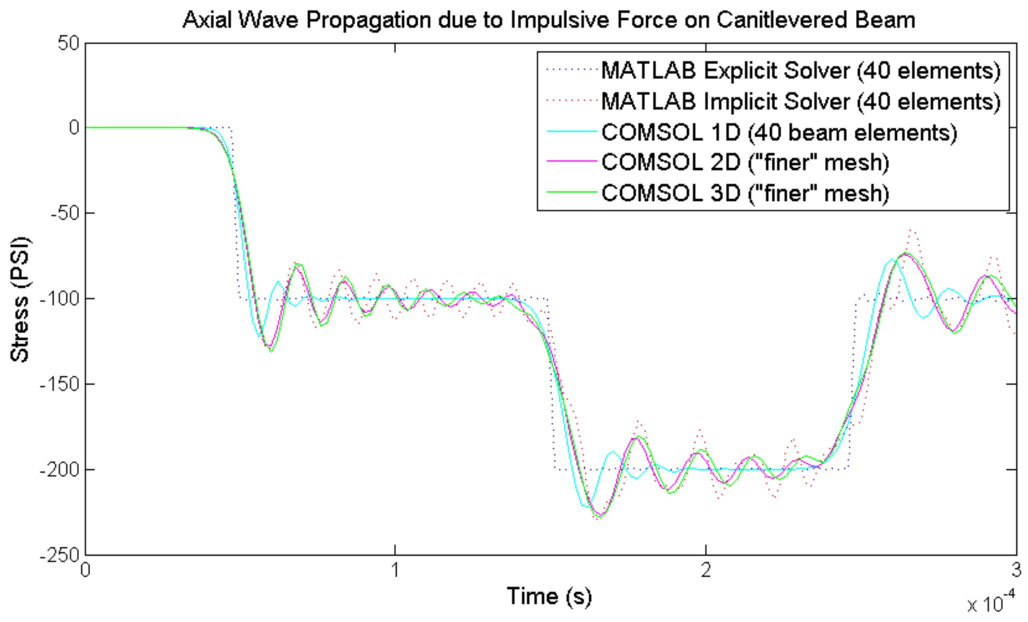

Figure 17. Axially-loaded cantilevered beam: COMSOL vs. explicit and implicit methods. [8]

Dynamic FEA Software Solvers.

COMSOL Backward Differentiation Formula Solver.

COMSOL contains an abundance of time dependent solvers that the user can choose from, both explicit and implicit in nature[18]. As mentioned in the previous section, it was decided to forgo the use of an explicit solver due to the instability when solving problems with large unknowns. Of all the implicit solver choices, the BDF (Backwards Differentiation Forumula) solver was chosen in COMSOL because it offers the most stability when solving these unconstrained simulations. The BDF solver in COMSOL uses the IDA package from SUNDIALS (SUite of Nonlinear and DIfferential/ALgebraic equation Solvers). IDA was developed by the Lawrence Livermore National Laboratory and is essentially a differential algebraic equation solver that uses variable-order, variable-step-size backward differentiation formulas[19]. In short, the IDA package allows the solver to adjust the time step of the simulation in response to the system gradient. This allows the user capture high frequency events without having to use a very high time frequency throughout the entirety of the simulation, which significantly reduces computational overhead. The proper understanding of how the solver achieves this requires a brief description of how it works.

First, the solver initializes all of the system matrices, recognizes all of the physics that were applied to the model, and determines the total number of system DOF. Once these matrices are assembled, "the solver breaks down the problem - linear or nonlinear - into one or several linear systems of equations by approximating the given problem with a linearized problem" [18]. From here, "a nonlinear solver is used to update the variables [in the matrices] at each time step" [18]. If the nonlinear solver's solution contains more error than what was specified in the settings, then the Jacobian[5] is updated and the variables are again updated at a smaller time

[5]The Jacobian matrix, or stiffness martix, is the coefficient matrix of the discretized linearized

step[6]. Error is usually a result of the system becoming more dynamic through high acceleration and usually correlates to high stress events. The iterations continue until the error is small enough to satisfy the settings, and then the step is written out for that time interval. The iterative method also works in reverse: if the nonlinear solver's solution has very small error, then the solver will strive to increase the time step to its maximum allowable amount in order to speed up the total computation time.

To illustrate this point, Figure 18 shows the longeron stresses at the top and time step reciprocal at the bottom from an early two cell truss deployment simulation. Note that both plots are matched up despite their different X axes. Following the annotations present in the figure: Event 1 marks the start of the deployment when the spring-hinges applied their moment to the longerons. Although the stress is not high here, a lot of rapid acceleration occurs as the applied moments begin to move the truss cells. After the mechanism "settles" to a steady state, the time steps return to the default level of 0.01 seconds. Event 2 marks the locking hinges for the first truss cell to fully deploy. The first peak is the upper longerons and the second peak is the lower longerons. Note that the spikes in time steps cover a period of time before and after the locking occurs. Smaller time steps are needed here because the system is rapidly changing as the longerons accelerate towards their peak velocity. After the locking event, the time steps remain small for a time while the stress is dissipated. Event 3 marks the locking event in the second trusses lower longerons. The upper longerons failed to deploy before the simulation ended. Again, the time steps needed to capture the stress event are small, yet they are allowed to become larger once the system reaches a steadier state and the stress waves dissipate below the tolerances set.

problem. Although it does not necessarily have to be updated for every iteration, the problem is quicker to converge if it is.

[6]COMSOL is also wont to try a higher order approximation here to gain more accurate results, however this occurs much more infrequently.

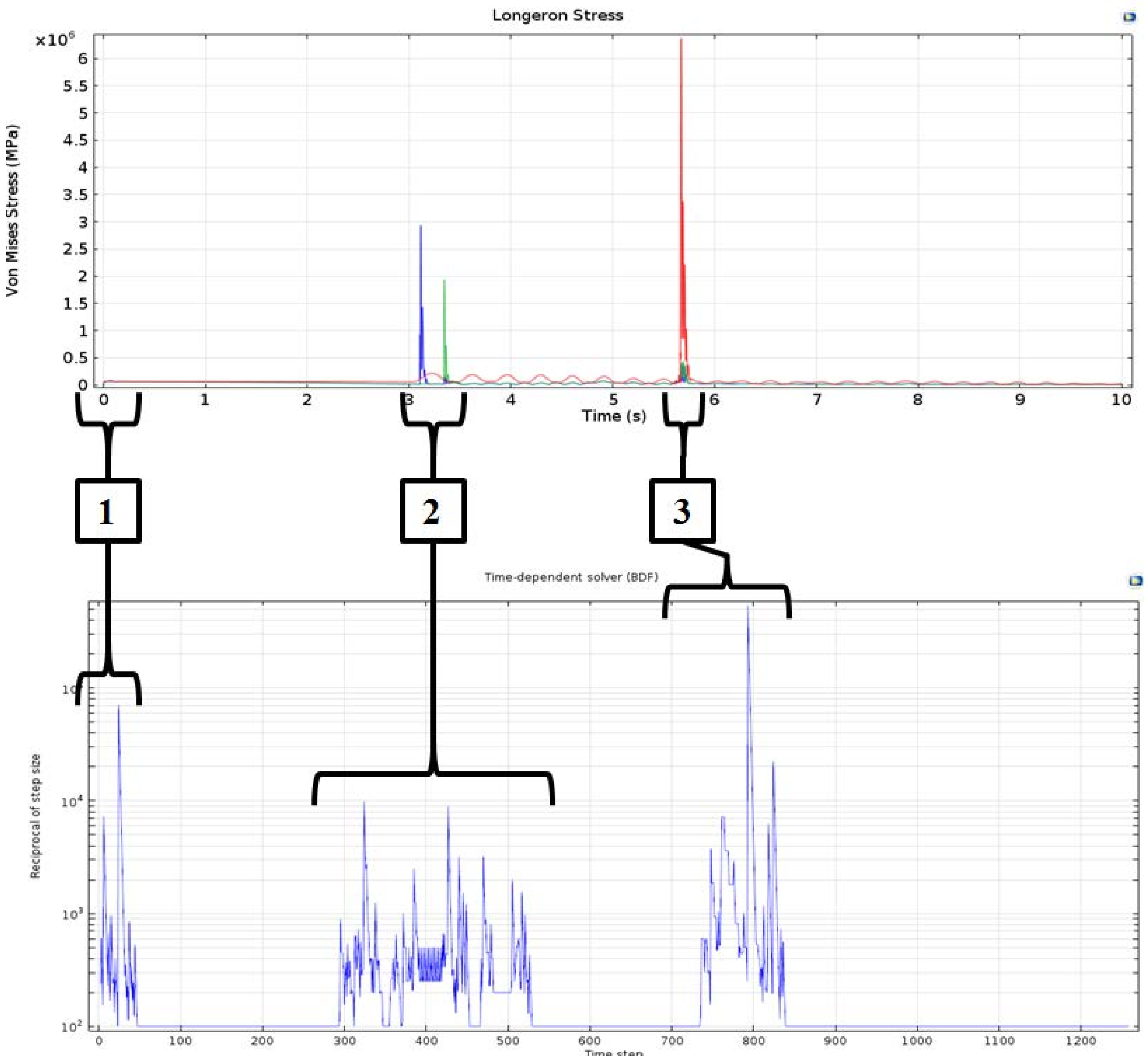

Figure 18. Top: Longeron stresses during two truss deployment simulation with respect to time. Bottom: Reciprocal of the time steps used during the simulation with respect to time steps.

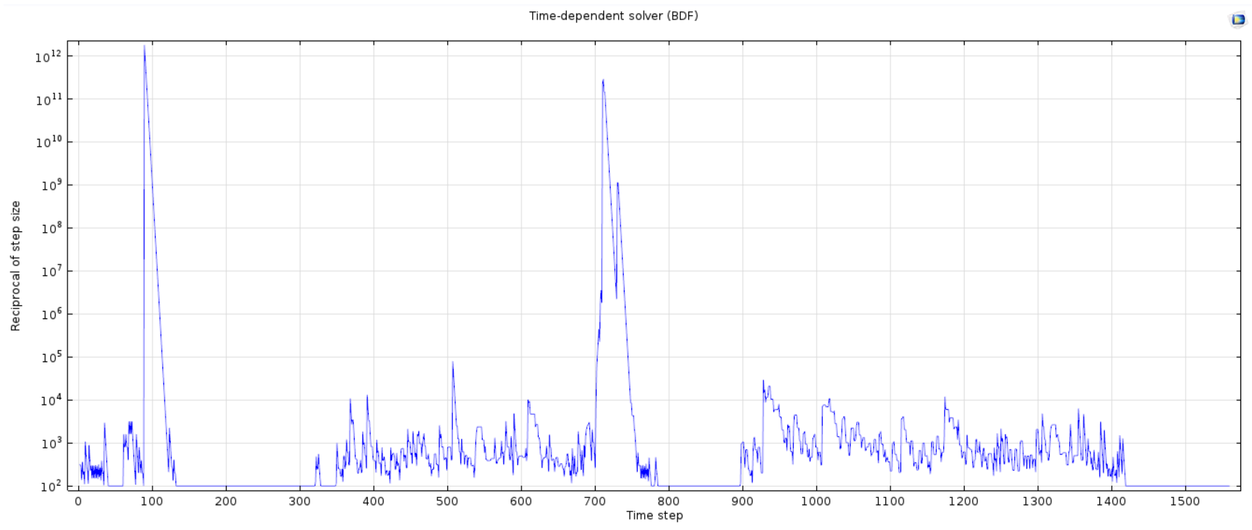

Figure 19. Example of the reciprocal time steps during a simulation for a poorly made model.

On a final note, it should be mentioned that the reciprocal time step plot is also very useful in determining the health of an ongoing simulation. All too often a model will not be set up correctly or is meshed poorly and the time steps needed for a converged solution become quite microscopic. Figure 19 is an example of a model that is not stable during certain movements of its deployment. By reviewing the results from this simulation during the instances where a time step of 1 picosecond was needed, one can attempt to "debug" the model. Many times spikes such as these are indicative of an error in the modeling, but some times the model may need to be adjusted by adding damping or loosening some of its constraints.

2.4 Computational Hardware Concerns

Throughout the course of developing this work - configuring models, creating meshes, testing solver settings, etc - it became apparent that the computer hardware being used would significantly affect the pace of the work being done for this thesis. As the models became larger with added complexity, not only would a more powerful computer enable the simulations to finish sooner, but the user would be able to iterate upon the design at a faster pace if multiple instances of COMSOL could be used simultaneously. It then became a secondary objective to explore some different hardware options to potentially improve this work's throughput. COMSOL itself has many suggestions to improve simulation performance with hardware [20], chief among them is the memory bandwidth. As most of COMSOL's solver algorithms are multi-threaded and can be spread around to available processor cores, the amount and speed of the memory channels feeding into the cores is of utmost importance. In this way the computer can assemble the system matrices in memory, shuttle the information to the processor for computation, and then read the computed information back into memory, as fast as possible. In addition to COMSOL's suggestions, there exists a plethora of anecdotal information of other user's experiences online. Many users found that increased processor clock speed as well as server-grade hardware (multiple processors) considerably reduced simulation time. Table 1 offers some anecdotal information encountered during the development of this work.

Table 1. Computer Simulation Benchmark

Computer	**Desktop**	**Laptop**
Processor	Quad Core 4.2 Ghz	Quad Core 2.3 Ghz
Memory	16 GB @ 2133 MHz	8 GB @ 1600 MHz
Memory Channels	4	2
Peak Processor Temperature	47°C	86°C
Simulation Time (1 Cell)	21m 41s	28m 48s
Simulation Time (4 Cells)	4hr 17m 28s	5hr 49m 30s

The first computer that was used in the early stages of this work's development was the laptop. For a laptop, it is very powerful and features a quad core processor and workstation graphics card. However, the memory provided little overhead for bigger simulations and its cooling system did not cope well with the processor's thermal load. The simulation time for a single cell truss deployment was respectable, but for a four cell truss the laptop would have to push itself for almost six straight hours.

For the sake of comparison, the same simulations were run on a desktop computer. The desktop has a newer quad core processor that is overclocked and has twice the available memory channels as the laptop. More importantly, the desktop's memory is 25% faster than that of the laptop, enabling the both simulations to run approximately 25% faster. Although this direct correlation is dubious, it cannot be denied that running a four cell truss simulation in 4 hours, 17 minutes is much better than 5 hours and 49 minutes. For larger simulations, the time differences will most likely scale so that a simulation that might take four days could be instead accomplished in three. Not to mention the additional memory overhead of the desktop allows the user to run multiple instances of COMSOL simultaneously and at much safer processor temperatures.

A 25% increase is a good gain from moving from the laptop to the desktop, but one could posit that the increased speeds gained from the desktop should be even greater. After all, the desktop has twice the number of memory channels and almost twice the processor clock speed. There are two specific factors that refute this conjecture. First, while the simulations still take a considerable amount of time, they are still considered small with "only" 20,000 DOF. The benefits of more memory bandwidth and higher clock speed may not be apparent until the model's matrices are big enough to take advantage of it. Second, the specific solver being used here may not be completely optimized for parallelization. Amdahl's Law states that the expected improvement of a parallel computing system is a function of the percentage of parallelized threads [21]. Meaning that if a portion of an algorithm is serialized, then the minimum execution time of the algorithm cannot be less than that of the serial process. Therefore, COMSOL's partially parallelized algorithms will not be sped up as a function of cores added and is instead at the mercy of the slowest serial process.

2.5 Summary

Section 2.1 started by showing an overview of the work done on the Martin Marietta deployable space truss and ATK's ADAM. These subsections show that while the deployable space truss was ingenious, the lack of available applications at the time prevented it from being iterated further. ATK's ADAM proved that large deployable space trusses with a multitude of joints can indeed be successful in space, but that perhaps more efficient packaging could enable even larger space structures. The next subsection explained how the Large Deployable Sparse Aperture Reflector borrowed some of the best ideas from the aforementioned historical works, and put them to use to design a new breed of antenna reflector. The final subsection here then briefly talked about the challenges of testing space structures on Earth, and how testing the designs computationally is a viable, cost-effective alternative to the classic design-fabricate-test-review cycle. Section 2.2 first covered the basics of the Finite Element Method through the use of a simple example. These basics were then pushed further to show how FEM can be used to solve for different 3D geometries with different types of elements. It then stressed the importance of higher order elements and how the can more accurately describe the behavior of structures under bending loads. Section 2.3 showed how explicit and implicit methods can be applied to solve dynamic FEA problems. It was stated that although explicit methods are the most accurate, they require a system characterization that could not be properly made from the relatively unknown deployment of the locking space trusses. The section finished by describing the techniques being used by COMSOL to solve its simulations implicitly. COMSOL's method of varying the solver's time step in response to system gradients was also outlined with an accompanying example simulation. Finally, some computation considerations were voiced to show how different hardware affects the simulation time. It was found that for these simulations, the main contributor to reduce simulation time was most likely the computer's memory speed. A note was also made to state that computer hardware scaling is not trivial, and is extremely reliant on the parallelization of the software code.

III. Methodology

Chapter 3 explains the methodology used to simulate the truss deployment of the Large Deployable Sparse Aperture Reflector concept described in the previous chapter. It begins in Section 3.1 which details why COMSOL was the FEA software of choice for this work. Next, Section 3.2 illustrates the 3D modeling of the trusses in Solidworks to show how the trusses are stowed and deployed. This geometry is simplified in the following section so that the simulations can focus more on the deployment behavior and less on the individual components that constitute the structure. Due to the simplification, the as-designed material properties are adjusted in Section 3.3. Section 3.4 then introduces the nomenclature that was created as a shorthand and is used to called out the different aspects of the model throughout this work. After this preparation, the model is imported into COMSOL in Section 3.5. Here the entire process of composing the simulation in COMSOL is detailed from importing the geometry to entering the correct solver settings. Subsection 3.5 is of particular interest and describes the method in which the cable "elements" were created. Section 3.6 explains how a meshing study was done in COMSOL to determine the most efficient meshing strategy for the simulations. The study aims to create a mesh that is both accurate and computationally inexpensive. Section 3.7 is the final section in Chapter 3 and describes how the deployment envelope of the simulation can be calculated from the results of COMSOL in MATLAB.

3.1 FEA Software Selection

One of the first steps in this work was to select the FEA software package that would run the truss deployment simulations. Five different commercial packages were vetted in order to determine their capabilities, specifically their ability to model multibody dynamics. It was also important that these packages be able to use flexible bodies, handle large amounts of data, and have in-depth documentation. The following subsections briefly discuss the different packages that were explored, and why they were not chosen over COMSOL.

FEMAP.

FEMAP (Finite Element Modeling And Postprocessing) is a FEA program that excels at static FEA problems. It is extremely configurable, and allows the user to change almost every aspect of the model. Unfortunately, FEMAP is not built for *multibody* dynamics, and is generally used only to create the meshes for multibody dynamic simulations. To run these simulations, the meshes would have to be imported into a partnered program such as MSC ADAMS.

MSC ADAMS.

ADAMS (Automated Dynamic Analysis of Mechanical Systems) is a software package that excels at multibody dynamics simulations. In general, ADAMS is an industry standard package that can provide high fidelity simulations of mechanical mechanisms. It accepts many different types of meshes and can even use beam elements in place of solid bodies, unlike COMSOL. However, the types of motions that would be expected for the deploying truss did not align very well with the ADAMS' toolkit. Through testing done with an educational version of ADAMS, it was found that the motion constraints of a simulation are largely predicated on the geometry being used. For a locking hinge truss, it appeared as though the geometry would have to be built to physically stop and lock the hinges. This was not optimal for simulations that were being run to explore the global deployment of a large structure. Additionally, ADAMS did not seem to have much control over the meshes, and would rely on a secondary software package. This would not be ideal if the mesh needed to be iterated quickly. Therefore it was decided that although ADAMS would most likely be a fit for this work, it might take a large amount of effort to properly model the locking truss.

Abaqus.

Abaqus was the software of choice used in the second Finite Elements course at AFIT. Throughout this course it was shown that Abaqus allows the user a great amount of control over the model, and that accurate results could be had with the large library of elements available. In fact, Abaqus is very popular with major auto manufacturers, who use it to simulate crash tests. However, during conversations with faculty at AFIT who were extremely familiar with Abaqus, it was decided that Abaqus would not be a good fit for simulating the deploying truss. It was advised that a large amount of work would needed in a supporting program such as MATLAB in order to properly model relative motion inside of Abaqus. It was suggested that it would be wiser to seek another FEA program for the deployment simulations.

Recurdyn.

Recrdyn is a relatively new FEA program that offers a promising multibody dynamics package. It is currently being used extensively by Asian automotive manufacturers and even includes special tool kits for automotive simulations. It is also listed as a complementary software to ANSYS [22], which is a FEA program with great heritage. A full version of the software was obtained and tested. The user interface for Recurdyn was simply laid out and easy to understand. It allowed the user to easily build rigid 3D models, declare joints between bodies, and plot results very quickly. However, the software still had some of the same issues as ADAMS. It was geared towards finalized geometries, had very little control over the meshes, and custom functions would have to be built to create the appropriate mechanisms for locking the trusses. Despite these issues, Recurdyn was used to create an extended abstract on locking hinge truss deployments for the 2015 AIAA SciTech conference. This extended abstract precedes the conference paper, which in turn precedes this very thesis. Through this process it was discovered that although Recurdyn models simplified rigid bodies very well, custom locking parameters had to be created to in order to stop the bodies without geometry. Before continuing the work for the conference paper, it was decided to explore another FEA program.

COMSOL.

COMSOL multiphysics is a FEA program that is built for simulations that involve multiple physical interactions, such as a beam under bending and heating. At first, one of the main attractions to COMSOL was its multibody dynamics package that includes a large library of physics to create mechanisms. Importantly, spring, dampers and locking attributes could be added to hinges which is not a convenient task in ADAMS or Recurdyn. It was found that these hinges could be created quite easily between faces of simplified geometries as well and did not require fully-realized designs. Once COMSOL's variable step solver was investigated and shown to save valuable computation time, the decision to use COMSOL was almost certain. Unfortunately, COMSOL's multibody dynamics package used to simulate relative motions demands the use of solid bodies to declare relationships between geometries. This meant that the simulation sizes would be much larger than a FEA package that could solve dynamics with simple beam elements. However, this drawback was accepted because of all the choices, COMSOL appeared to offer the path of least resistance to creating a locking truss simulation.

3.2 Geometry Modeling

3D Geometry Modeling.

The 3D geometry was created from 2D drawings from the work previously done to design the truss [10]. The dimensions listed in the work were followed as closely as possible. However, some dimensions have yet to be determined for the truss cells and had to be estimated in order to create a reasonable representation of the geometry. All modeling was done in Solidworks, which was chosen because of its availability and familiarity to the author. Figure 20 illustrates how the 2D drawings were interpreted to create the 3D geometry.

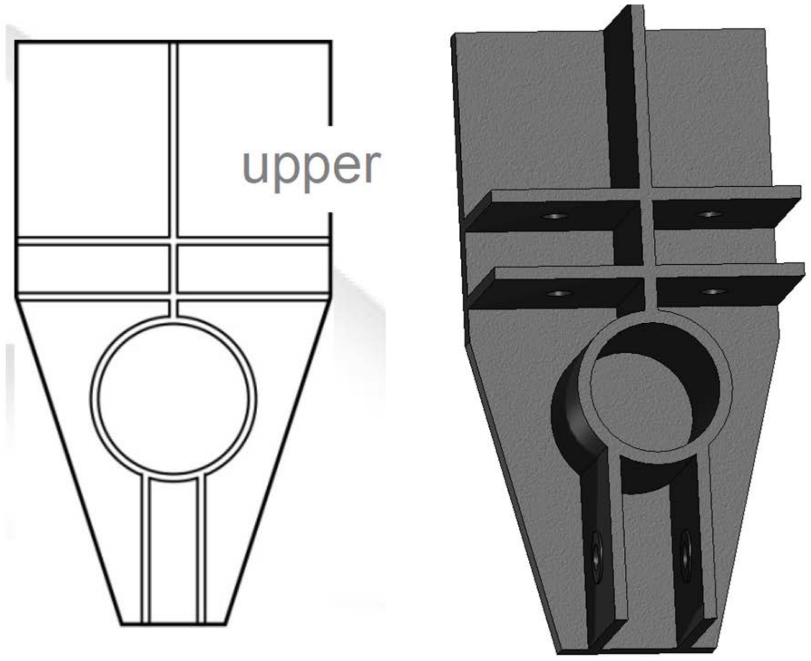

Figure 20. Left: 2D upper end fitting drawing (Courtesy of Dr. Gyula Greschik). Right: 3D upper end fitting model (angled view).

The ends of the longerons and battens were also modeled using the 2D drawings. The hinges that split the longerons and horizontal battens have not yet been designed, and are therefore omitted from the 3D models. Instead the longerons and horizontal battens are spaced in order to allow for future design additions, and these spaces along with the lengths of the members adhere to the nominal dimensions of the truss cell. Figure 21 shows the stowed configuration of the truss cell and Figure 22 shows the deployed configuration of the truss cell. Note that the view shown is of a nominal "straight" cell, whereas the cells comprising the reflector are trapezoidal to create a parabolic shape.

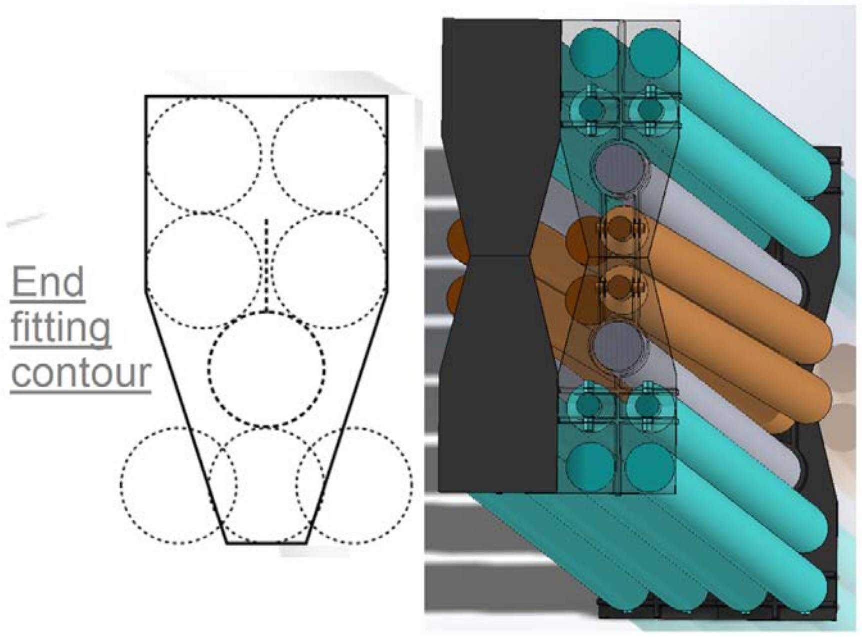

Figure 21. Left: Top view of 2D stowed configuration (Courtesy of Dr. Gyula Greschik). Right: Angled top view of 3D stowed configuration with some transparency.

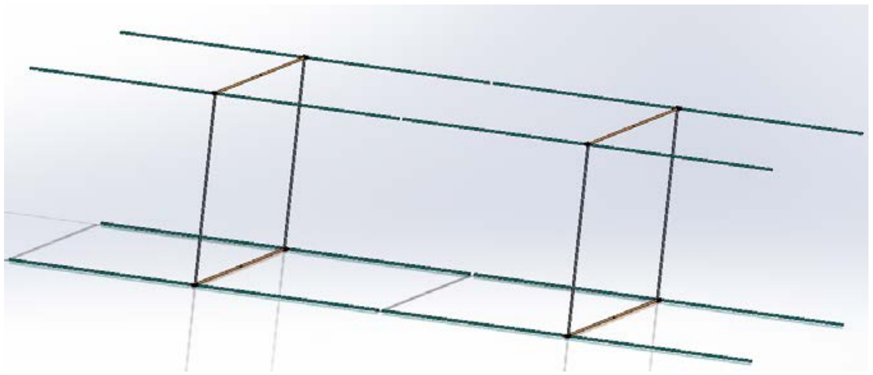

Figure 22. Angled view of 3D deployed truss cell.

The nominal material properties of the as-designed geometry are shown in Table 2. Note that only one truss cell was modeled in this manner, and that additional

Table 2. Truss Member Material Properties

Young's Modulus	70 GPa
Coefficient of Thermal Expansion	7.4 mm/(m×K)
Density	1600 kg/m^3
Truss Diameter	51 mm
Truss Wall Thickness	0.635 mm
Cable Diameter	3 mm
Cable Tension	10 N

truss cells would be added serially along the longeron direction. Each truss cell would also be made from longerons of differing lengths top and bottom, varying cell to cell, in order to create the final parabolic shape of the reflector.

3D Model Simplification.

As previously mentioned, the nominal geometries shown in the previous section have not yet been finalized, and so it was decided that the geometry be simplified. This not only allows for the simulations to focus more on the global deployment of the trusses, but also considerably reduces the computational burden by requiring less elements in the model to properly describe the geometry. Shown in Figure 23, the 3D model was simplified into hexahedrons, which enables the geometry to be discretized by either hexahedral or tetrahedral elements. The simplified geometry was only modeled in the stowed configuration with the horizontal battens represented as a solid member. This not only simplifies the model further, but also helps focus the simulation on the second radial deployment.

Care was taken during the simplification process to make the simplified model very easy to work with in COMSOL. The end fittings of the simplified geometry are shrunk into blocks that allow for accessible hinge declarations on their edges. Consequently, this also increases the visibility of the partially hidden lower longerons. Attached to the back of each end fitting is a solid "bumper" that allows for contact to be

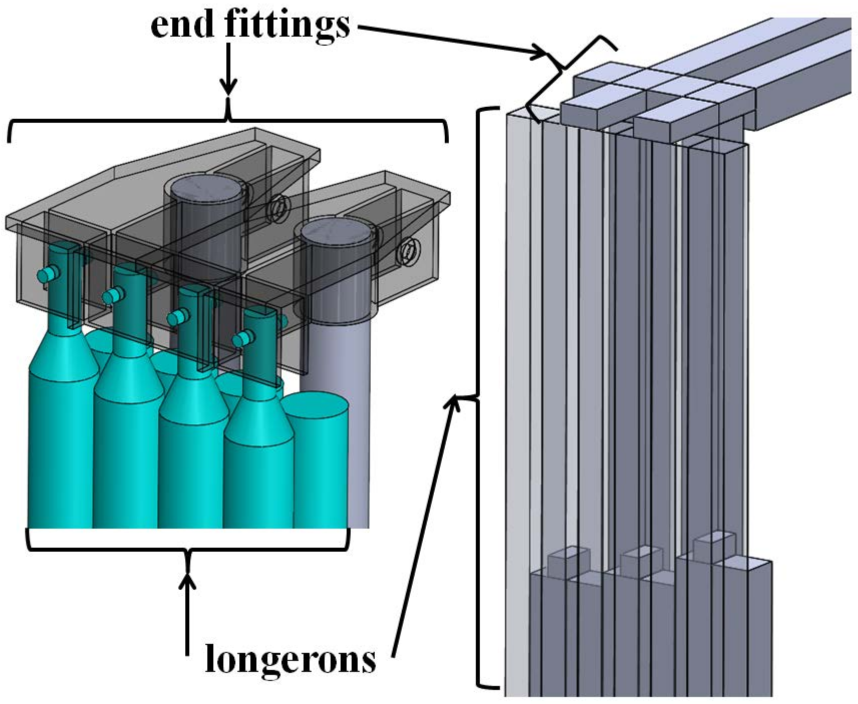

Figure 23. Left: As-designed geometry. Right: Simplified geometry with some transparency.

made between adjacent end fittings so that the geometry does not intersect during the simulation[1]. The as-designed outer diameter of the longerons and battens is 51 millimeters and is designed so that there is very little gap between the longerons of adjacent truss cells. The simplified geometry has a square cross section with an edge length of 50 millimeters, to allow for more separation of the hexahedral boundaries as well as reducing the chance of geometry intersection. Every truss cell was created in its own SolidWorks assembly with an offset of its location in space relative to the other truss cells when stowed. To create the reflector arm, these assemblies are merely added together in a master Solidworks assembly. This modular approach allows the simulations to be scaled by number of truss cells, and proves to be a boon when

[1]During the development of this methodology it was found that multiple cell simulations would cause the end fittings to intersect as one would be "kicked back" into another. Contact pairs adds a force between the selected faces when they reach a predetermined spacing and were created on the bumpers to keep the end fittings and battens from intersecting.

investigating these deployment simulations in COMSOL. The entire simplified truss is shown in Figure 24.

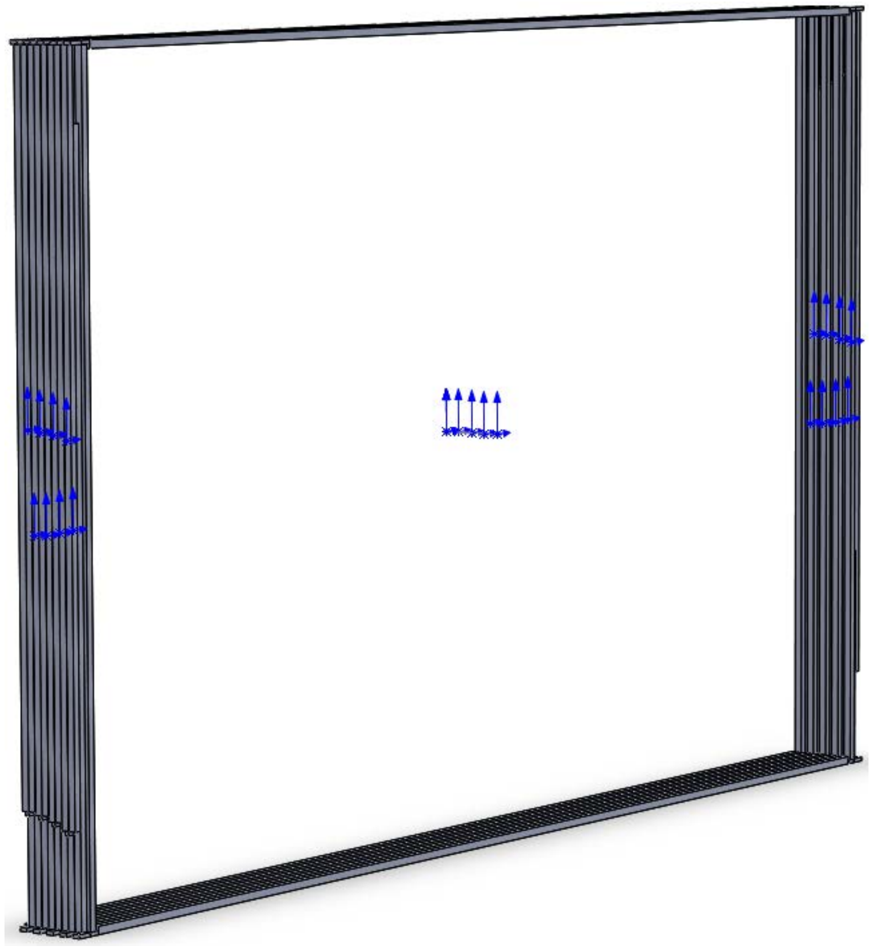

Figure 24. Simplified geometry of stowed four cell truss.

3.3 Equivalent Material Properties

Due to the simplification of the geometry, the material properties of the solid hexahedrons were adjusted so that they behaved as the as-designed carbon fiber tubes. This was simply done by using the geometric properties of the hexahedrons and carbon fiber tubes in Equations 8 and 9 to create an equivalent Young's Modulus (E) and density (ρ).

$$E_{adjusted} = \frac{E_{carbonfiber} I_{tube}}{I_{block}} \tag{8}$$

$$\rho_{adjusted} = \frac{\rho_{carbonfiber} V_{tube}}{V_{block}} \tag{9}$$

Where E (Young's Modulus), I (Second moment of area), ρ (Density), and V (Volume).

These new values were then validated using Equations 10 and 11 [23][24]. The validation equations were used with the parameters of a slender, simply supported beam (Figure 25) that is analogous to a fully extended longeron.

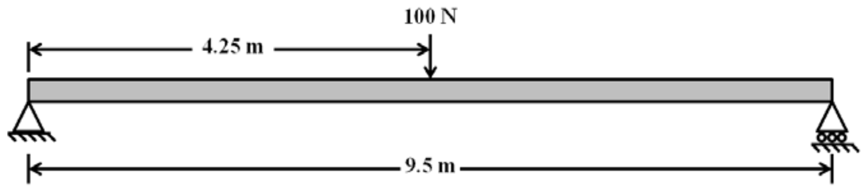

Figure 25. Simply supported beam validation problem setup.

$$\delta_{max} = \frac{Pl^3}{48EI} \tag{10}$$

$$\omega_n = \frac{1}{2\pi}\left(\frac{n\pi}{l}\right)^2\sqrt{\frac{EI}{\rho A}} \tag{11}$$

Where P (Applied load), l (Length of beam), n (Natural frequency integer), and A (Cross-sectional area).

Table 3 shows that the material properties of the carbon fiber tubes are carried over exactly to those of the solid hexahedrons. However, it should be noted that this conversion only works for bending modes of the longerons and is not valid for axial loads. It will be shown later in this work that the members making up the truss cell experience almost all bending loads during deployment, and that this equivalency is

Table 3. Adjusted material values: Constants and dependent values

	Carbon Fiber Tube	**Adjusted Solid Block**
Second Moment Area of Inertia (I)	2.5973×10^{-7} m	5.2083×10^{-7} m
Young's Modulus (E)	70 GPa	34.892 GPa
Density (ρ)	1600 kg/m^3	32.3543 kg/m^3
Max Displacement (δ_{max})	0.0982 m	0.0982 m
1^{st} Natural Frequency (ω_1)	8.2517 Hz	8.2517 Hz

acceptable.

3.4 Modeling Nomenclature

A naming convention scheme was created in order to keep track of the various hinges and forces within the COMSOL model as a shorthand code. Although this system reduces clutter within the model, it does require some explanation. First of all, it should be understood that the model is centered in space with the origin in the center of square made from the end fittings, horizontal battens, and vertical battens (Figure 26). In particular the vertical battens lie along Y direction while the horizontal battens lie along X direction. The shorthand for the corners of the truss cells is to merely state the positive or negative X and Y locations of the corner. For example, "pxpy" indicates the positive X, positive Y corner of the truss cell. As the longerons deploy outwards from the base square at Z = 0, they travel in the positive Z-direction. This base square is known as the zeroth cell, represents the base of the truss arm, and is a stationary reference frame. Moving in the positive Z-direction from here, the truss cells are numbered 1, 2, 3, and 4, with the 4th truss cell being the furthest out.

The joints within the cells are labeled according to their connections and spatial position in the deployed truss state. Moving in the positive Z-direction, the joints connecting the longerons to the frame square (and their shorthand) are: frame-to-longeron (frlg), longeron-to-longeron (lglg), longeron-frame (lgfr). Therefore, a callout

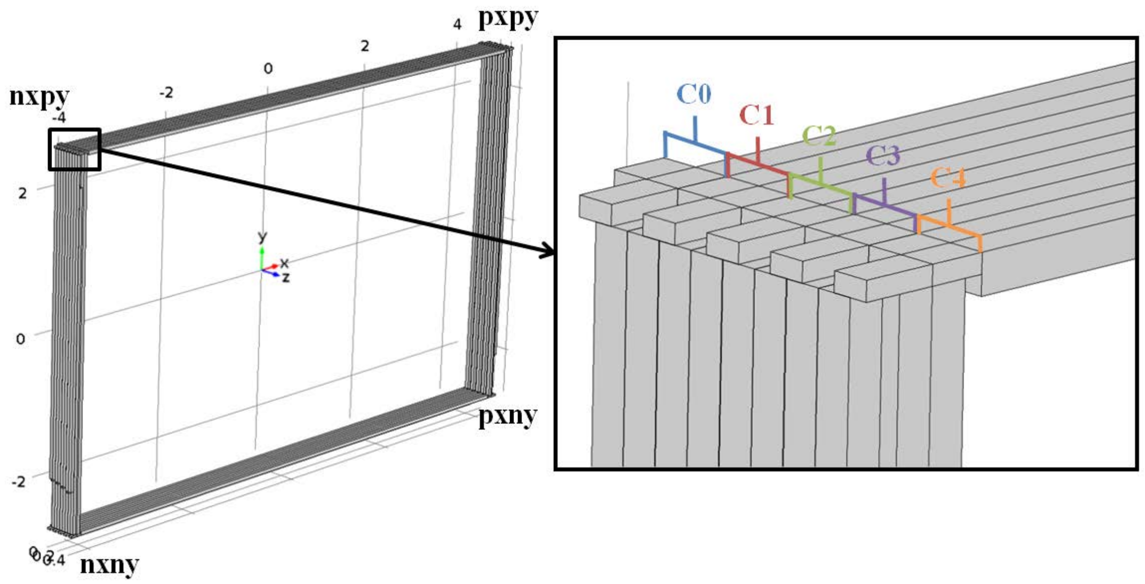

Figure 26. Left: Spatial positioning of four cell truss. Right: Order of truss cell squares.

in the results for "c3.nxpy.lgfr" indicates the joint connecting the longeron member to the square frame in truss cell 3 on the corner of negative X and positive Y. The variable being viewed appends all of the nomenclature in the results section of this paper. Meaning that "c2.pxny.lglg.Ms" is the $M_{applied}$ (Applied Spring-Moment) of the longeron-to-longeron joint located in the positive X, negative Y corner. As a special case, the cables follow these basic principles, and can be located in the model by noticing last capitalized characters: "c1.NXnypy" signifies the cable that lies on the negative X face that travels from (in the positive Z direction) the negative Y corner to positive Y corner of the truss cell. Figure 27 shows a visual example of the nomenclature applied to a truss cell and Figure 28 can be used as a reference guide when viewing the results.

3.5 COMSOL Simulation Setup

The section presented here outlines a "best practice" work flow for setting up simulations in COMSOL. It is intended to show the advantages and disadvantages of

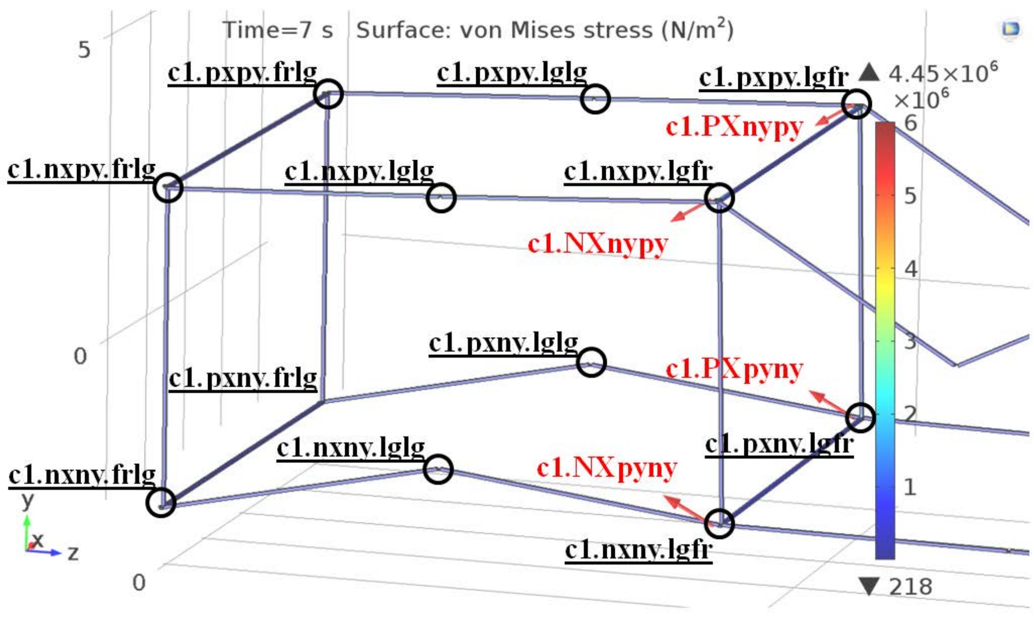

Figure 27. Truss cell 1 deployment at 7 seconds with hinge and cable callouts.

using COMSOL for multibody dynamic simulations. The methodology begins with geometry import and conditioning, then moves through meshing, material properties application, physics setup, cable modeling, probe creation, and finally solver configuration. All of these steps result in a model that can be varied and possibly run systematically for parameter sweeps.

Geometry Import and Conditioning.

Importing geometry into COMSOL is a simple affair, requiring the user to select which kind of files they are importing (COMSOL accepts a wide variety of CAD files), and choosing which bodies or faces to import. The next step is to declare graphically which imported bodies, or domains as they are called in COMSOL, are solidly connected to one another. This is done with a "Union" boolean function. In Figure 29, the square comprising the horizontal battens, end fittings and vertical battens were declared to be one domain, and the hinge attachment to the longerons was also declared to be one domain with its adjacent longeron.

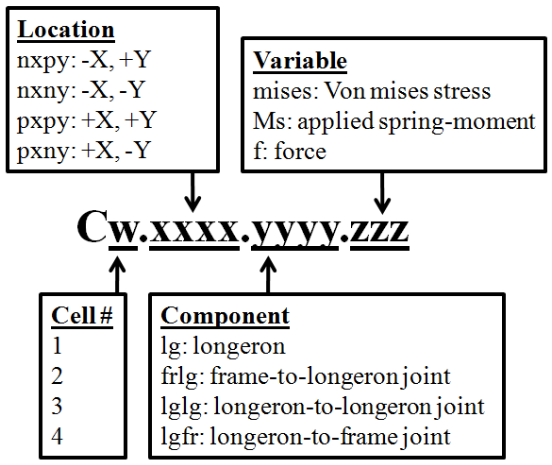

Figure 28. Legend for naming convention reference.

Meshing.

It is important to mesh the domains of the model that have been imported into COMSOL before anything else to ensure that the 3D modeling and geometry conditioning functioned as expected. An oversight in the settings of Soliworks can affect how the mesh is applied to the domains where the various components meet. By default, COMSOL automatically meshes the domains with tetrahedrons [18]. For many applications a tetrahedral mesh may work well, but as will be seen in Section 3.6, it does not work for the slender components in use here. A hexahedral mesh can be applied quite simply in COMSOL by selecting a face to map a quadratic grid upon, and then “sweeping” this grid through the 3D domain. The number of edge elements can be controlled by attaching a “distribution” sub-node and altering the values. The truss cell was meshed in this manner with a different distribution setting for the longerons, battens, and end fittings. Interestingly, the setting for the order of the elements in COMSOL does not reside within the meshing node and is hidden by default. It is instead found in the main physics node and can be adjusted from 1st (linear) order up to 4th (quartic) order. Figure 30 shows the meshed model, please note that the lines perpendicular to the members are indicative of elemental

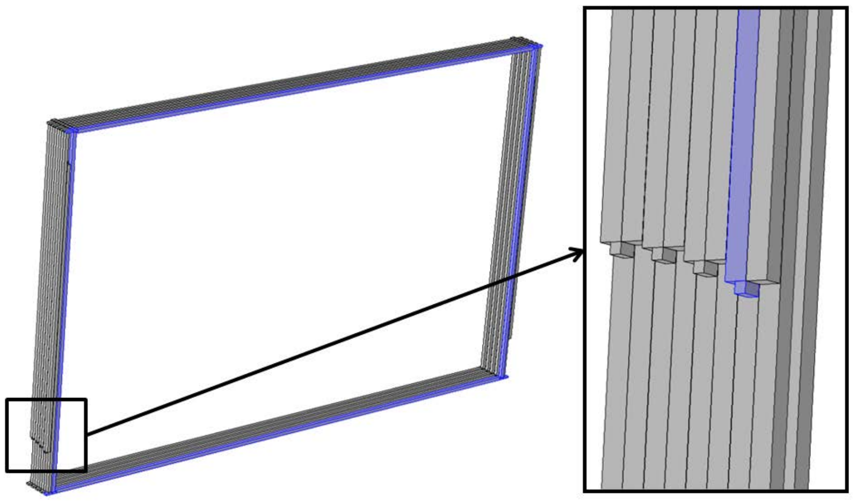

Figure 29. Left: Battens and end fittings declared as one domain. Right: Longeron and hinge attachment declared as one domain.

Table 4. Applied Material Properties

	Longerons and Battens	**End Fittings**
Young's Modulus (E)	34.892 GPa	70 GPa
Density (ρ)	32.3543 kg/m^3	1600 kg/m^3
Poisson's Ratio (ν)	0	0

boundaries. Section 3.6 will provide reasoning for the particular discretization shown.

Material Properties Application.

The material properties of the cell trusses are applied graphically to the geometric bodies. The properties themselves are declared as simple materials: only applying a Young's Modulus, Poisson's ratio, and density. All of the longerons and battens are given the material properties from Section 3.3. The end fittings are given basic properties of carbon fiber[25] because nominally they would be made from molded composite material[10].

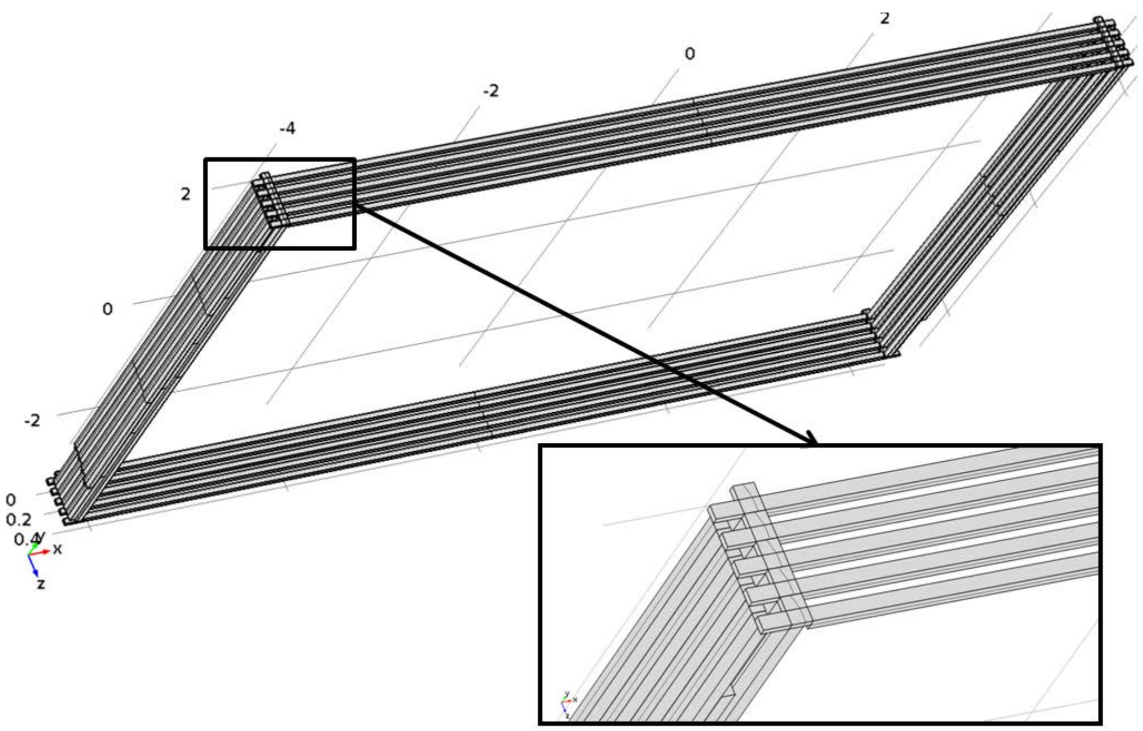

Figure 30. Rotated view of meshed model with end fittings closeup.

Physics Setup.

"Physics" nodes in COMSOL are sets of equations that are applied to selected geometries within the model [18]. These equations determine the behavior of the geometry throughout the simulation. During the time spent creating the methodology for the truss deployment simulations, it was found that COMSOL is usually more agreeable to having lesser constrained models. Adding in possibly redundant constraints not only causes the solver to run slower because of the additional equations, but also restricts the model to very few modes of movement and reduces the chance of a converged solution.

At their most basic level, a physics node such as "Fixed Constraint" acts as a boundary condition that locks a geometry face in a static position in space ($u = v = w = 0$). The Fixed Constraint was applied to the bumper blocks of Cell 0, and is the only constraint holding the deployment in place. The next step was to declare the hinge joints of the mechanism. This was done by choosing two geometric faces as attachments for the joint; one as the source and another as the destination. A hinge joint was then created that uses both of these attachments with an axis declared on a viable geometric edge. Figure 31 illustrates the main idea behind joint creation. Within the hinge joint node are many options to give the joint extra properties. For the hinges created between longerons (lglg), “Spring and Damper” as well as “Locking” attributes are added. The hinges that join the back of the longeron to the square frames (frlg), also have a constraint attribute that prevents the longerons from rotating backwards. Next, forces were attached to the same hinge attachments mentioned earlier to translate the cable force to the structure. Each cable exerts a force on both of the attachments it is connected to, creating a tension force that “squeezes” the truss cell. Finally, distinct contact boundaries were defined between the front of each truss cell corner and the back of the “bumpers” on the next truss cell. The contacts are set to use a “penalty” force between the two faces if a minimum contact threshold is breached.

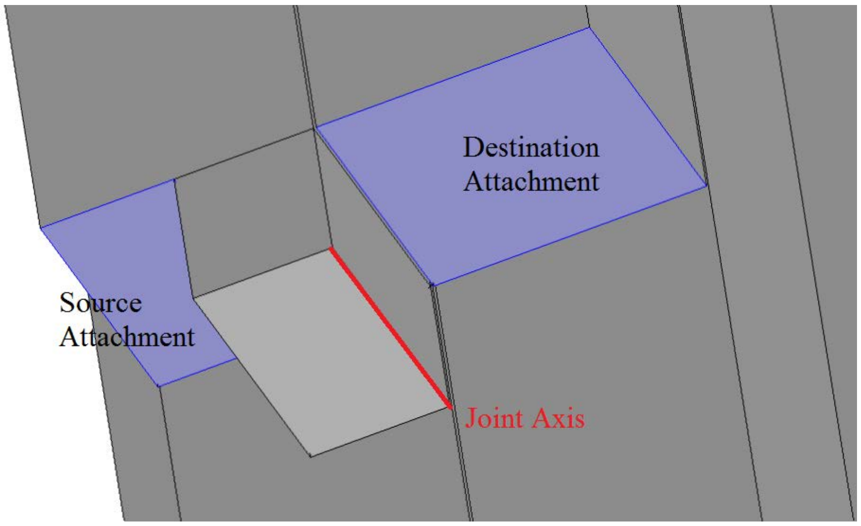

Figure 31. Example of joint being created between stowed longerons.

The order of the joint creation in this model was very important as it enhances the overall modularity of the model. As mentioned earlier, the Solidworks model is a modular design in which additional cells can be added one at a time. In COMSOL, the same pattern was followed to declare each of the hinges in the cell before moving on the the next. This makes calling out the same corner hinge from each cell very easy, as they are all multiples of each other. The next section benefits tremendously from this, as the files that determine the cable forces need only be adjusted slightly to work with the next cell.

Cable Modeling.

Modeling cables in FEA programs is usually quite difficult due to their physical behavior. Cables do not compress, and are referred to as “zero compression” elements [26]. This behavior challenges a lot of FEA solvers because they must continually check the direction of the cable force to determine whether that force is in tension or compression. COMSOL does not have any cable physics nodes, but has a large library of other types of joints with equations available for viewing. By studying the equations that model different kinds of joints, a “cable-joint” was created. This new pseudo-joint is a combination of a contact and distance joint. At its most basic level, the distance between the two attachment faces is monitored until it reaches a certain threshold. Once past, a force is applied between the attachments, just as a cable would. If for some reason the distance between the attachments becomes less than the unstretched length, then the force goes back to zero. Figure 32 shows the equations of just one of the cables in the simulation, with explanations appearing in the following paragraph.[2]

Note that these are text files that are imported into COMSOL, and do not have numbers on the left column. The numbers are used for illustration purposes only. When COMSOL does read in the file, however, the spaces between the strings of

[2] c1.NXnypy indicates the cable in Cell 1 that spans from the negative Y to positive Y corners (moving in the positive Z direction) on the negative X face of the cell.

```
1   mbd.dsj1.xsx mbd.att6.xcx          % mbd = MultiBody Dynamics
2   mbd.dsj1.xsy mbd.att6.xcy          % dsj1 = Distance Joint 1
3   mbd.dsj1.xsz mbd.att6.xcz          % xsx = X-axis center of rotation of Source attachment
4   mbd.dsj1.xdx mbd.att7.xcx          % att = Attachment
5   mbd.dsj1.xdy mbd.att7.xcy          % xcx = X center of rotation
6   mbd.dsj1.xdz mbd.att7.xcz          % xdy = Y-axis center of rotation of Destination attachment
7   mbd.dsj1.uc.src mbd.att6.u         % u,v,w = Local displacements
8   mbd.dsj1.vc.src mbd.att6.v         % uc.src = Center of Source attachment for u-displacement
9   mbd.dsj1.wc.src mbd.att6.w
10  mbd.dsj1.uc.dest mbd.att7.u
11  mbd.dsj1.vc.dest mbd.att7.v
12  mbd.dsj1.wc.dest mbd.att7.w
13  c1.NXnypy.dist sqrt((mbd.dsj1.xsx+mbd.dsj1.uc.src-mbd.dsj1.xdx-
mbd.dsj1.uc.dest)^2+(mbd.dsj1.xsy+mbd.dsj1.vc.src-mbd.dsj1.xdy-
mbd.dsj1.vc.dest)^2+(mbd.dsj1.xsz+mbd.dsj1.wc.src-mbd.dsj1.xdz-mbd.dsj1.wc.dest)^2+eps)
14  c1.NXnypy.distx (mbd.dsj1.xsx+mbd.dsj1.uc.src-mbd.dsj1.xdx-mbd.dsj1.uc.dest)/c1.NXnypy.dist
15  c1.NXnypy.disty (mbd.dsj1.xsy+mbd.dsj1.vc.src-mbd.dsj1.xdy-mbd.dsj1.vc.dest)/c1.NXnypy.dist
16  c1.NXnypy.distz (mbd.dsj1.xsz+mbd.dsj1.wc.src-mbd.dsj1.xdz-mbd.dsj1.wc.dest)/c1.NXnypy.dist
17  c1.NXnypy.damp d(c1.NXnypy.dist,TIME)
18  c1.NXnypy.sw c1.NXnypy.dist>l.c1.nypy
19  c1.NXnypy.f (k*(l.c1.nypy-c1.NXnypy.dist)-c*(c1.NXnypy.damp>0)*c1.NXnypy.damp)*c1.NXnypy.sw
20  c1.NXnypy.Ws c1.NXnypy.sw*.5*k*(l.c1.nypy-c1.NXnypy.dist)^2
21  c1.NXnypy.fx c1.NXnypy.f*c1.NXnypy.distx
22  c1.NXnypy.fy c1.NXnypy.f*c1.NXnypy.disty
23  c1.NXnypy.fz c1.NXnypy.f*c1.NXnypy.distz
```

Figure 32. Cable c1.NXnypy equation. Comments and line numbers added for clarification.

characters are separators to place the strings in adjacent columns. Therefore, the left column states a variable, and the right column defines it. The first 12 lines of the equation file declare the names of the pseudo joint. In line 1, "mbd.dsj1.xsx" denotes the rotational center in the global X direction for the distance pseudo-joint. In the adjacent column, "mbd.att6.xcx" indicates that this center should reside within the center of attachment 6. This was declared internally in COMSOL during the attachment and hinge joint creation step in the physics setup. This declaration continues for the displacement and rotation of both the source and destination attachments. Line 13 calculates the distance between the two attachments. Note that "eps" is the variable name for the smallest float used in COMSOL, and is included to ensure solver stability. The next three lines, 14, 15, and 16, break the distance between the attachments into its constituent X, Y, and Z vectors by dividing the respective coordinate direction distance by the total distance. Line 17 calculates the velocity between the two attachments by taking the derivative of the distance with respect to global time. Line 18 is the switch which indicates whether or not the predefined cable length has been reached by the pseudo-joint.[3] If this main switch is true then the cable force equation comes to life. Equation 12 clarifies the equation used for the magnitude of the cable force in Line 19.

$$F_{cable} = k \cdot (l_0 - l) - c \cdot \frac{d}{dt}(l) \tag{12}$$

The terms in Equation 12 are as follows: k (Stiffness Constant), l_0 (Cable unstretched length), l (Distance), c (Damping Constant), and $\frac{d}{dt}(l)$ (Speed of elongation). An extra switch is included for the damping of the cable in order to minimize the risk of it exerting a compression force on the attachments. Early iterations of this equation did not include this secondary switch, and compression force was exhibited where it should not have. The lengths of the cables were found using the geometry of the truss cells and the MATLAB code containing the calculations are included in Appendix 6.1. Lines 21, 22, and 23 then split up this force into components that are applied at the attachments. Lastly, line 20 calculates W_s (Strain Energy) of the cable (Equation 13).

$$W_s = \frac{1}{2}k(l_0 - l) \tag{13}$$

These series of equations are repeated for each of the 8 cables in all four cells of the deploying truss system. By utilizing the modular build technique outlined in the previous sections, each equation set must only be modified in cell and attachment designator that requires only a shift in index number. Figure 33 comes from a double truss simulation that was done early on to verify that the equations worked correctly. The forces shown are from the second cell, with the first cell being the at the root

[3]In COMSOL, this function returns a 0 if the condition is not met, and a 1 if the condition is met.

of the mechanism. From the start of the simulation to the location of Annotation 1, the applied cable forces are zero. Here is where the truss is deploying, and the cables have not yet been stretched. Moving to the lower image that gives a close-up view of the upper image, Annotation 2 marks the point at which the upper cables activate when the negative tension force is applied. The first activation is of the shaping cables on either side of the truss cell that run from the negative Y to the positive Y. "c2.PXnypy.f" is on the positive X face of the truss cell, and "c2.NXnypy.f" crosses the negative X face of the truss cell. Soon after the shaping cables activate, the structural cables on the positive Y face of truss cell also activate. "c2.pxnxPY.f" crosses from positive to negative X, and "c2.nxpxPY" crosses from negative to positive X. Some small time after this, the complimentary shaping and structural cables activate at Annotation 3. Interestingly, the structural cables activate before the shaping cables, which shows that the furthest end of the truss cell must have been skewed upwards. Proceeding towards the upper image once again, Annotation 4 illustrates how the truss cell begins to settle towards the target cable tension of 10 Newtons. Here is where the damping present in the cable force equations helps. However, Annotation 5 marks the point at which the first root cell locks its hinges, and causes the shape of the second truss cell to fluctuate. It is important to note here that the structural cables remain at negative 10 Newtons, as they should. The tension forces also never rise above 0 Newtons, indicating that the cables never exert a compression force on the truss cell. Lastly, Annotation 6 identifies a damping trend in which the truss cell again starts to settle into its steady-state. Although most cable systems do not have marked damping characteristics, adding them to these simulations helps the system to converge in a reasonable amount of time. Finally, it should be said that predefined constants mentioned earlier are loaded into COMSOL via a separate text file. It contains all of the cable lengths, spring and damping constants required by the physics nodes in the simulation. This file, along with an example cable can be found in Appendix 6.2.

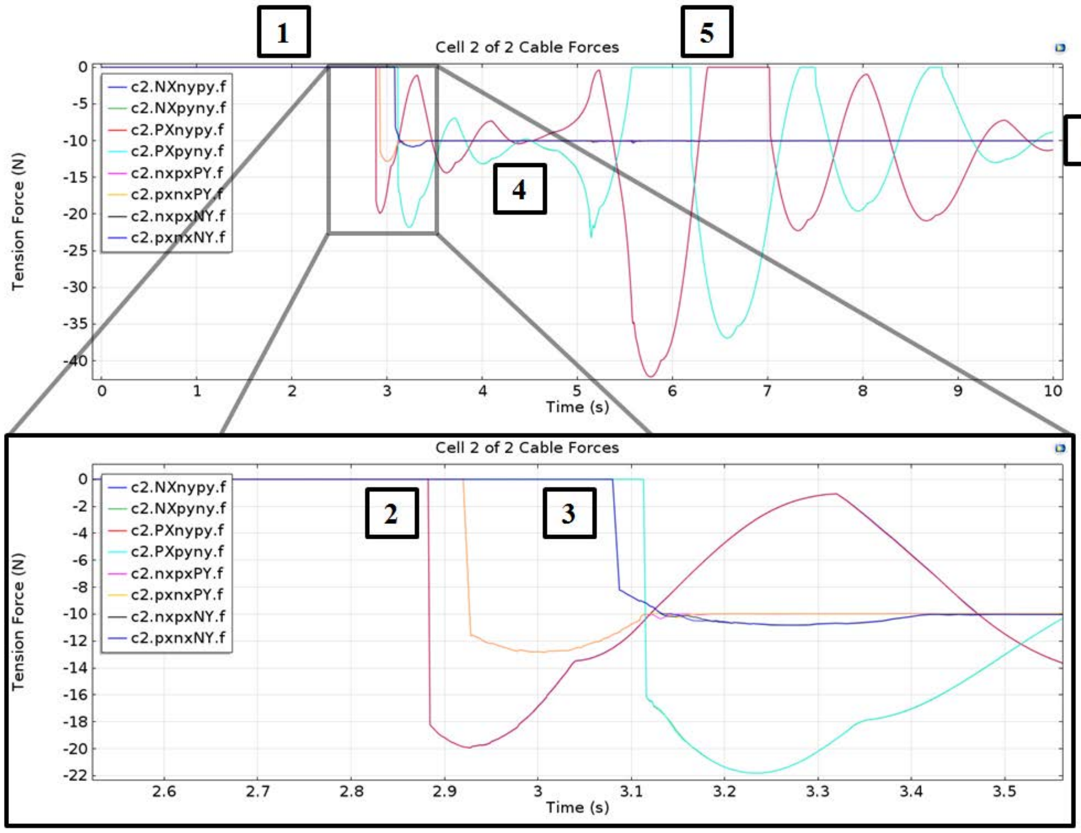

Figure 33. Top: Cable forces from second truss cell in two truss cell simulation. Bottom: Focus from top plot of cable activation events.

Probe Creation.

Probing variables is COMSOL's method of choosing the results to display to the user and prepare for export. Almost any variable can be viewed, and more variables can be made thanks to an extensive library of functions and operators. For these simulations, each truss cell is monitored with three different types of probes: longeron von mises stress, applied spring-moment, and cable force. For each longeron that is split in each cell, a probe was placed throughout both distinct domains to monitor the Von mises stress, and is averaged. Monitoring the average stresses in the longerons enables a view of the stress in each cell as they lockout as well as showing if this event causes stress in any of the other cells. The applied spring-moment is monitored in order to view the progress of each cell's deployment since the applied moment is a function of the joint's rotation. Equation 14 is used by COMSOL to compute the applied moment, which is the the product of k_s (Spring Constant) and the difference between θ (Relative Angle) and θ_0 (Pre-deformed Angle).

$$M_{applied} = -k_\theta(\theta - \theta_0) \tag{14}$$

The cable forces, which were discussed in the previous section, give a sense of the general shape of the deployed truss. For instance, if one set of shaping cables has a higher force than the other, then the upper longeron will be at a positive or negative angle with respect to the lower longerons. If all the cable forces are holding at the target tension of negative 10 Newtons, then the truss cell has reached its final shape. Also monitoring the system are three more probes that calculate the total energy of the system. The first measures the total kinetic energy of the system, which is declared as a simple global variable within COMSOL. The second measures the total strain energy of the system, which is also a global variable in COMSOL but has strain energy from the cables added as well. The third sums up the kinetic and potential energies. In total, 67 probes feed into 13 plots that describe the deployment of the truss cell mechanism and can be exported for further analysis in a variety of file formats.

Solver Configuration.

Throughout the process of running deployment simulations in COMSOL, many different values were tried in the solver settings in an attempt to optimize the simulation time. Although Section 2.3 details COMSOL's time dependent solver, this section aims to show how the solver was configured and to justify the values that were chosen. Many settings within the solver were left at their default value because they either made no discernible difference or increased the simulation's chance of divergence. The values shown here were all adjusted from their defaults in three main, descending hierarchical nodes: the "Time Dependent" solver configuration node, the "Time-Dependent Solver" operation node, and the "Fully Coupled" attribute node.

The "Time Dependent" control node has two noteworthy settings that have major impacts on the simulation. The first of which is the time range. Here, the begin and end times are set as well as the steps between them. Being set to "0:0.01:20" indicates that the simulation runs from 0 to 20 seconds with a nominal step of one hundredth of a second. As will be explained later, this nominal time step is really just a target for the BDF solver to aim for, and does not necessarily mean the solver will abide by it. The second noteworthy setting is the "Relative Tolerance" of the solver, and is set to a relatively high value of 0.1 or 10%. Adjusting this value from the suggested 0.01 allows the solver to be less responsive to perturbations when adjusting time steps in the simulation [18]. It was found through numerous trials that asking the solver to keep to a tighter tolerance caused the simulation to diverge more often. This divergence, shown in Figure 34, usually takes the form of uncontrolled vibrations in the lateral members of the cells. The thought is that the benefit of faster, more consistent simulation convergence outweighs the loss of precision.

The operation node "Time-Dependent Solver" makes finer adjustments to the simulation behavior. Importantly, the tolerance of all the simulation variables and the settings for the time stepping methods are set here [18]. Known as the "Absolute Tolerance", this setting is adjusted to control the absolute error of the variables to just 1%. Higher values for less precision and the possibility of faster simulation times were attempted, however the error within some nodes of the mesh becomes great enough

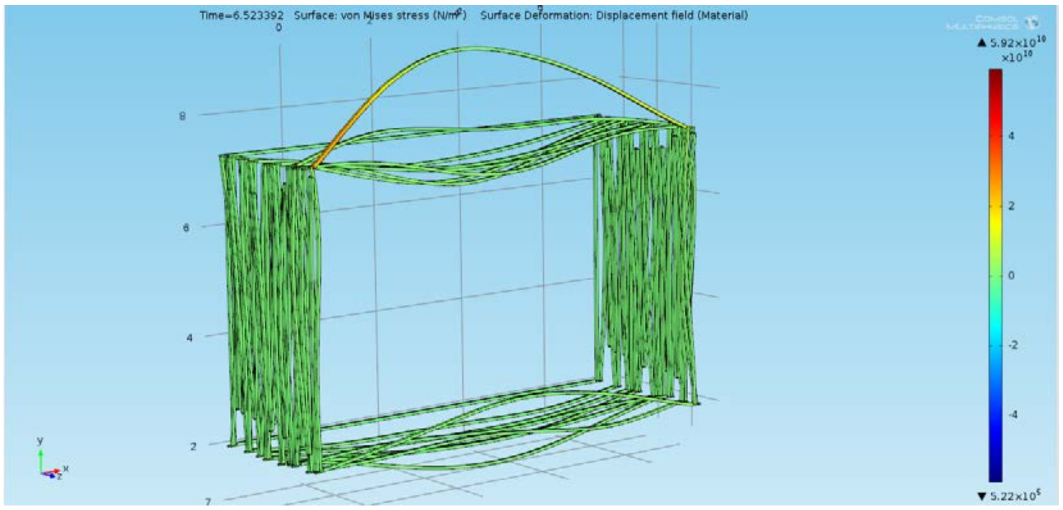
Time=6.523392 Surface: von Mises stress (N/m²) Surface Deformation: Displacement field (Material)
▲ 5.92×10¹⁰
×10¹⁰
4
2
0
-2
-4
▼ 5.22×10⁵
8
6
4
2
y
x
z

Figure 34. Example of solver divergence through uncontrolled vibrations propagating through the horizontal members of the cells.

to halt convergence during the simulation. Therefore it is recommended to keep this value below the point where it does not impede convergence and above the point that would require very high time steps to converge. The time stepping methods section in this sub-node are also very important. After the Backwards Differentiation Formula scheme is selected, it is important to set the solver to keep a "strict" adherence to the aforementioned 0.01 second time interval. This setting drives the solver to return to the set time interval after it is decreased during large gradient of the system during the simulation. Allowing the solver to opt for "intermediate" or "free" solver steps results in very long simulation times as the solver may stay at a very small time step throughout the simulation. Although this may be more precise, it is not conducive towards iterating the simulation's parameters in a timely fashion. The last important setting that should be mentioned is the "Maximum step". If this is not specified as the nominal time interval, the solver may find a chance to use even bigger time steps, which may result not only in divergence but in the loss of data from the simulation.

Last but not least, the "Fully Coupled" attribute node uses damped Newton-Raphson methods to converge upon a solution [18]. "Fully Coupled" here meaning that COMSOL solves for all physics in the simulation simultaneously. Through extensive testing, it was found that the "Constant nonlinear" method of solving works best for these simulations. The "Damping factor" is always set to one, and the Jacobian matrix is told to update on every Newton-Raphson iteration. Updating the Jacobian matrix, which can also be known as the stiffness matrix, allows for quicker convergence, at the computational expense of updating the matrix for every iteration. The number of iterations is controlled by either the maximum number of iterations or a tolerance factor. For these simulations, COMSOL is given 50 iterations to reach a tolerance of 10%[4] or else the overall time step is decreased. These settings were chosen for their influence on the solver behavior; a solver which is responsive to large gradients in the system that require smaller time steps, yet forgiving enough to use a larger time step when at all possible. There are many more settings that can be adjusted for the solver, however these numbers were found to optimize the solver and are a balance of computation time, precision, and solver convergence likelihood.

3.6 Mesh Study

Mesh Precision.

The geometry being used in these simulations allows for the meshing of either tetrahedral or hexahedral elements. Before choosing one over the other, it was important to study the effects of each element type on the geometry being used here. The goal was to balance the computation time of the simulation with its precision. Generally, lower computation time is had by lowering the DOF (Degrees of Freedom) of the system. However, a higher precision in finite elements is (usually) found through higher numbers of DOF. Therefore, it was necessary to perform a study of

[4]The real tolerance factor is actually the number specified here, which is one, multiplied by the relative tolerance that was set to 10% earlier.

both types of elements as well as their order, which significantly increases the elements' DOF and precision. The study uses the same test setup as seen earlier in Figure 25. Using this test setup, the center deflection (Equation 10) and the various natural frequencies (Equation 11) were calculated as the true values to be compared against a static FEA performed in COMSOL.

It was found that the deflection was 0.0983 meters, the first natural frequency was 8.249 Hz, and the second natural frequency was 32.999 Hz. These analytical or "true" numbers were then compared against the two different element types, each with three different orders of formulation: linear, quadratic, and cubic. Within each of these formulations, several different discretizations were tested. All of these variations were tested with COMSOL in 3D space, using a stationary study for the deflection, and an eigenfrequency study for the natural frequencies. Table 5 gives a breakdown of the mesh variations tested while Figures 35 and 36 show a selection of results from COMSOL.

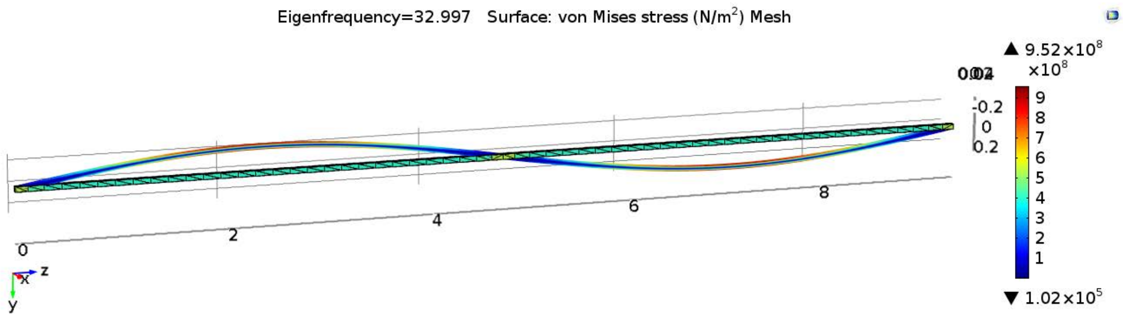

Figure 35. Second natural frequency of quadratic tetrahedral mesh.

The goal of this study was to find the most "efficient" type of mesh possible for this geometry. Here efficient means the most accurate mesh with the least amount of DOF. This is quite the balancing act, as Table 5 shows that the more accurate quadratic and cubic elements have a big increase in DOF that will ultimately put more strain on the solver for the dynamic simulations. All of the results from the COMSOL analysis were imported into MATLAB, where they were plotted to graphically show which

Table 5. Mesh Study Variations

Mesh Type and Order	COMSOL Sizing	Number of Elements	DOF
Cubic Tetrahedral	Extremely Coarse	125	2754
	Extra Coarse	164	3663
	Coarser	202	4551
	Coarse	228	5220
	Normal	348	8400
Cubic Hexahedral	Extremely Coarse	2	336
	Extra Coarse	4	624
	Coarser	6	912
	Coarse	8	1200
	Normal	10	1488
Quadratic Tetrahedral	Extremely Coarse	125	1014
	Extra Coarse	164	1353
	Coarser	202	1683
	Coarse	228	2079
	Normal	348	3159
Quadratic Hexahedral	Extremely Coarse	2	135
	Extra Coarse	4	135
	Coarser	6	243
	Coarse	8	459
	Normal	10	567
	Fine	14	783
	Finer	20	1107
Linear Tetrahedral	Normal	348	708
	Fine	600	1212
	Finer	826	1632
	Extra Fine	3595	4242
	Extremely Fine	4104	4914
Linear Hexahedral	Normal	10	132
	Fine	14	180
	Finer	20	252
	Extra Fine	30	372
	Extremely Fine	50	612

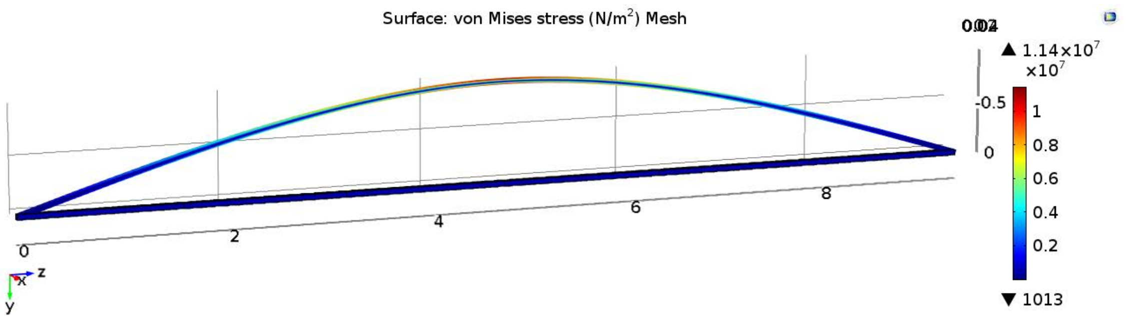

Figure 36. Deflection of cubic hexahedral mesh. Deflection Scaled 10x.

mesh is the most efficient. The code which also contains the raw results can be found in Appendix 6.1. The MATLAB results plot the percent error from the exact answers against the number of degrees of freedom. Figure 37 shows the solution efficiency of the meshes for center beam deflections, first natural frequency, and second natural frequency. When viewing the plots, take note that the best candidates or most efficient meshes are to be found in the bottom left-hand corner. Here is where the lowest number of degrees of freedom coincide with the smallest error.

When viewing Figure 37, any result below 10^1 is considered good as it represents a result that is within 10% of the true value. The quadratic hexahedral mesh is almost completely below this line, while the rest of the quadratic and cubic meshes are even further down, albeit with more degrees of freedom. The linear meshes, by comparison, are barely visible, as they have at least 100% error or more. Moving down to the first natural frequency plot, the linear order meshes are completely off the true answer. This behavior is most likely due to the “locking” behavior that is usually exhibited by linear order elements, as explained in Section 2.2. The quadratic and cubic meshes meanwhile have a great amount of precision. The tetrahedral meshes at higher order and the cubic hexahedral mesh are extremely precise, but do not have a lot of value because their DOF are much greater than that of the quadratic hexahedral mesh. Such a trend is continued in second natural frequency, which is very similar to the previous figure. At this point, the best value mesh appears to be a

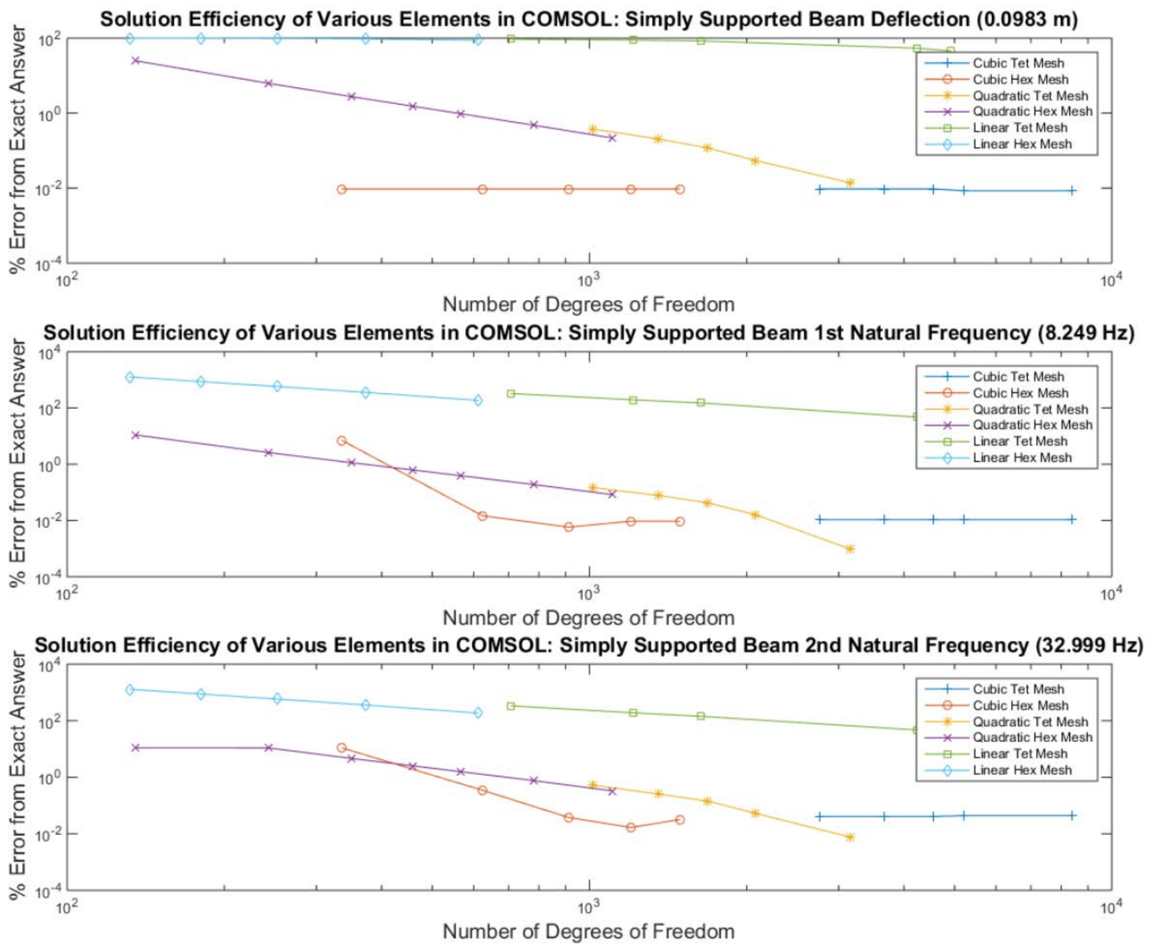

Figure 37. Solution efficiency of various element types in COMSOL. From top to bottom: center beam deflection, first natural frequency, second natural frequency.

lower fidelity quadratic hexahedral mesh, which is consistently below 10% error and has the lowest amount of DOF. However, it would not be wise to choose this mesh type until it is vetted at even higher natural frequencies in case they are experienced by the deploying truss model. Figure 38 compares the meshes at the simply supported beam's third, fourth, and fifth natural frequencies. These higher natural frequencies were calculated to be 74.249 Hz for the third, 131.998 Hz for the fourth, and 206.247 for the fifth.

These figures show that the first choice of the quadratic hexahedral elements do not fare so well at these higher frequencies. Note, however, that these frequencies

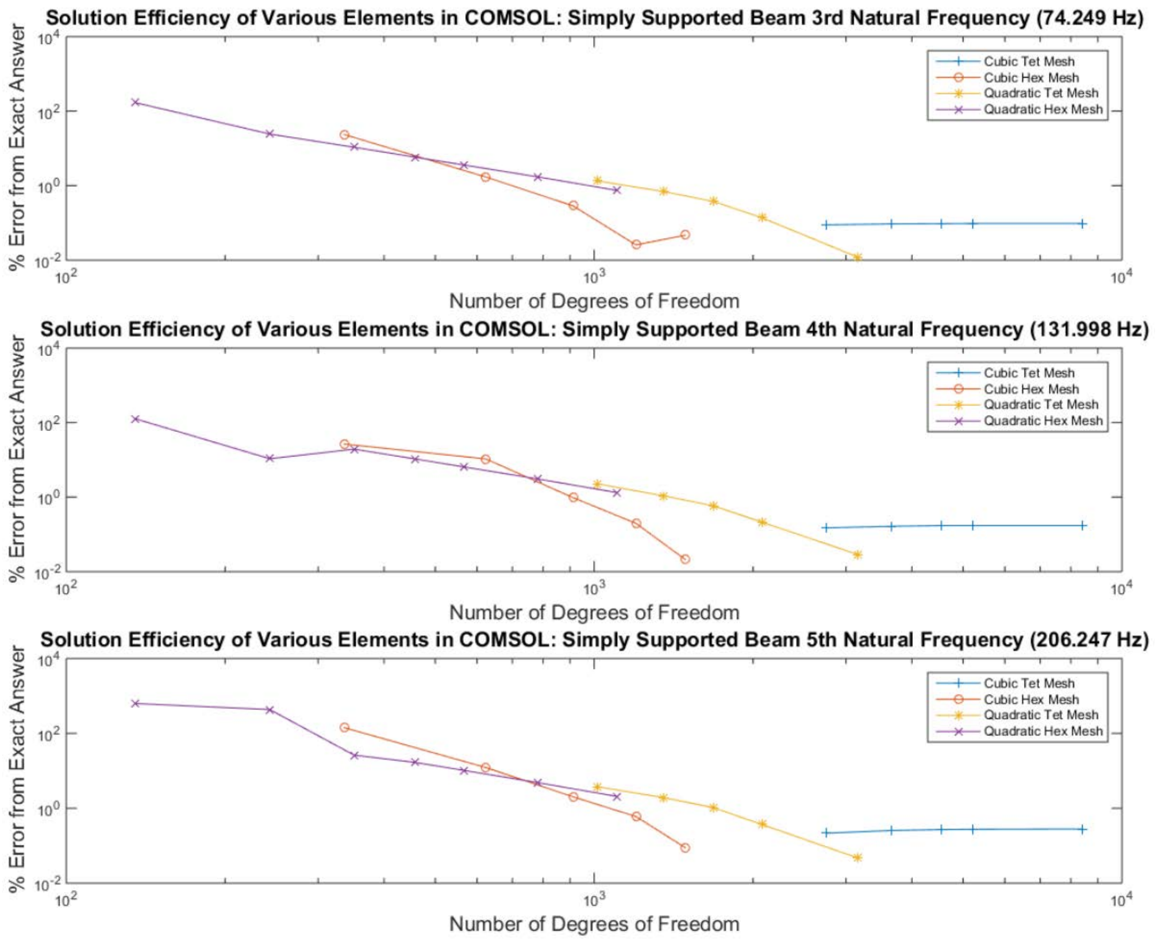

Figure 38. Solution efficiency of various element types in COMSOL. From top to bottom: third natural frequency, fourth natural frequency, fifth natural frequency.

are quite high: 74 Hz for the third natural frequency, 131 Hz for the fourth, and 205 Hz for the fifth. Compared to the first natural frequency of 8.25 Hz, such high frequencies may not even be sustainable for the brittle carbon fiber material that is envisioned to be used. Additionally, the mesh types that do fare better at these high frequencies require much more DOF. Since the test here models just one longeron, scaling the DOF to the entire system multiplies the DOF seen here by about 36 times. (4 battens + 4 longerons for each of the 4 cells, plus the 4 base battens.) Therefore, the quadratic hexahedral mesh was still chosen and the risk of the mesh not performing at higher frequencies was accepted.

Mesh Computation Time Considerations.

At first glance it would seem that the use of higher order elements to both increase model accuracy and decrease the system DOF is a win-win. However, there is a very important caveat that should be mentioned: increase simulation time. Higher order elements require more complex formulations that carry over into the system stiffness matrix. Although the system matrix is smaller due to the reduced amount of DOF, the matrix itself is much more dense. Figure 39 visualizes the stiffness matrices of two different meshes applied to the simply supported beam used in the previous section. The plot on the left shows the nonzero values in the stiffness matrix for a linear tetrahedral mesh. The mesh has 708 DOF, and the matrix is comprised of 10,918 nonzero values, meaning that the matrix is approximately 2% filled. By comparison, the plot on the right shows the nonzero values in the stiffness matrix for the same geometry discretized by a quadratic hexahedral mesh. This mesh has 351 DOF, but has 29,123 nonzero values. The matrix is approximately 24% filled. Therefore, even though the DOF of the simulation is halved by using quadratic hexahedrons, the total number of values that the solver must deal with is tripled. Anecdotally, the simulation time for the four cell truss increased from approximately 2.5 hours to 4 hours when switching from a linear tetrahedral mesh to a quadratic hexahedral mesh of similar discretizations shown here. This poses a significant increase to the simulation time, however it is accepted here as the accuracy gains of the quadratic mesh are more than worth it.

3.7 Deployment Envelope

An important measure of the health of the truss deployments is the envelope in which the deployment occurs. If the deployment is too wild and has a large envelope, then it may intersect with other geometries on the finished aperture structure while

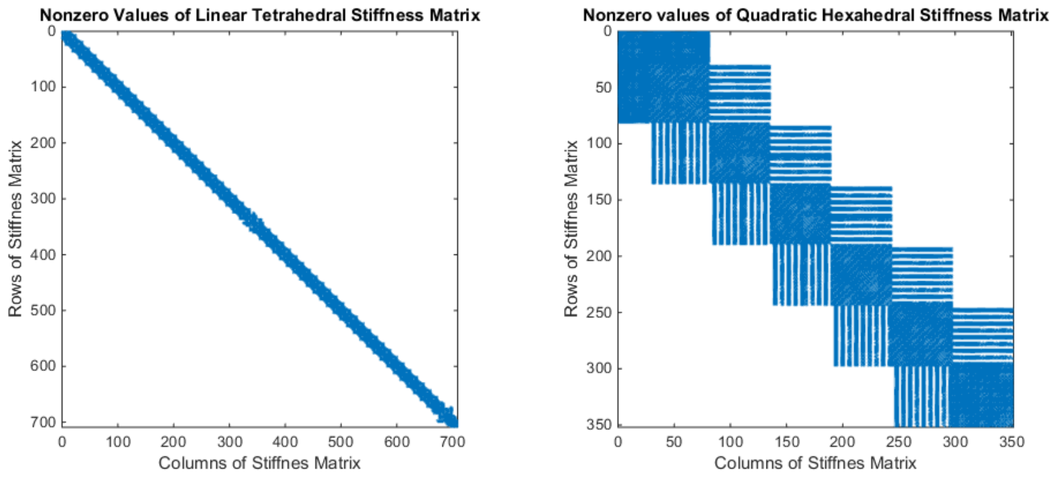

Figure 39. Left: Nonzero values of linear tetrahedral mesh stiffness matrix. Right: Nonzero values of quadratic hexahedral mesh stiffness matrix.

it deploys. Therefore a scheme was created to track the displacements of the end fittings to quantify the deployment envelope.

In COMSOL, the displacements and rotations of two end fittings that are situated diagonally from each other on each cell are entered into an export data table. (Diagonally situated here, for example, means the positive Y fitting on the positive X face, as well as the negative Y fitting on the negative X face.) The data table contains the displacements of the end fittings at each time step during the simulation. It is then exported into MATLAB, where it is trimmed of any extraneous data and saved as a binary MATLAB file (.mat). Next the file is imported into a MATLAB script (Appendix 6.1), and assuming that the batten square connecting the end fittings is rigid, the locations of the other two corners are extrapolated via simple geometry. Finally, the script determines the maximum and minimum displacements achieved during the simulation for the corners of all four truss cells. The output of this script file are the maximum and minimum displacements for each axis, from which a bounding box of the simulation can be made.

3.8 Summary

Section 3.2 showed how the as-designed geometry works and how it can be simplified for simulation purposes. The simplification not only decreases the computational overhead of the simulation significantly, but also places an emphasis on the deployment of the structure itself and not the performance of the structure's individual components. Section 3.3 calculated new material properties for the simplified geometry which enables it to behave similarly to the as-designed components. Section 3.4 gave examples of the modeling nomenclature on the simulation model to show how the different components are called out in this work. Section 3.5 walks through the process of setting up the simulation in COMSOL. It exemplifies several aspects of the setup and gives an in-depth explanation on how the cables are created. Section 3.6 lends credence to the decision of using a quadratic hexahedral mesh on the geometry because it represented the best combination of accuracy and economy for these simulations. Finally, Section 3.7 explained how the deployment envelope of the simulation will be calculated using MATLAB.

IV. Analysis

4.1 Introduction

The purpose of this chapter is to show and analyze the results of the truss deployment simulations. Although one of the main goals of this work was to create a simulation of the truss in COMSOL, it was also thought that additional simulations with differing parameters would be useful. Such simulations not only show how flexible COMSOL can be when adjusting parameters, but can also help determine potential susceptibilities of the structure to certain adjustments. Please refer to Chapter 3 when viewing the results, as the nomenclature established there will be used extensively in this chapter. Section 4.2 will analyze the uncontrolled deployment of the truss structure and show the manner in which it deploys. This includes graphical view of the structure with the surfaces displaying the von Mises stress, plots of the applied hinge moments in the longeron-longeron hinges that motivate the deployment, plots of the cable forces that occur when the truss cells reach their deployed state, and plots of the von Mises stress within the longerons with an emphasis placed on their behavior during the hinge-locking "lockout" events. Next, Section 4.3 will show two different simulations in which the truss structure was placed into a rotating frame. In one simulation the rotating frame is set to rotate at 5 degrees per minute, and the other simulation is set to rotate at 60 degrees per minute. Both rotations are about the Z-axis and are meant to show how the deployment reacts to centripetal forces acting on the arms. The rates of rotation are built to taper as the structure deploys and the moment of inertia increases. Section 4.4 explores what happens when one weak hinge is introduced into the structure. In this case, a "weak hinge" is a hinge that only applies 80% of its moment to the longeron-longeron hinge joint. Here, the susceptibility of the deployment to manufacturing flaws is shown. In total eight simulations were run, each with one weak hinge on the top or bottom of each cell. Finally, Section 4.5 shows how the truss deploys in a "controlled" manner. Controlled here meaning that the deployment order of the individual truss cells is delayed so that a truss cell will be fully open before its adjacent neighbor is deployed. Two simulations were run, one with the deployment order from root-to-end, and the other from end-to-root, as the truss was designed.

The main model parameters chosen for all of the simulations remain the same throughout this analysis unless otherwise specified. They are shown in Table 6 and reflect the values that were not necessarily as-designed, but allowed the first uncontrolled deployment simulation to successfully deploy with a reasonable simulation time. In a real world deployment scenario, such a large structure would not be designed to deploy in under eight seconds.

Parameter	Value
Longeron-Longeron Hinge Spring Constant	10 Newton-meters/radian
Longeron-Longeron Hinge Pre-Deformation Angle	3.14 radian
Longeron-Longeron Hinge Damping Coefficient	1 Newton-meter-seconds/radian
Cable Spring Constant	25 Newton-meters
Cable Damping Coefficient	5 Newton-meter-seconds
Cable Target Tension	10 Newtons

Table 6. Static Model Parameters

4.2 Uncontrolled Deployment

The uncontrolled deployment of the four cell truss simulation was the first to be successfully completed. It was the testbed from which all of the best settings were found for a successful deployments, as outlined in the previous chapter. This model is notable for having the least amount of constraints placed on it, which is the most likely explanation for its early success. To reiterate, the base zeroth cell is fully constrained in space and the hinge moments are applied instantaneously at the beginning of the simulation. From there, the structure deploys as a function of the hinge moments and the geometry through which the moments are transmitted.

Initial Displacement.

This subsection graphically shows the deployment of the truss system at select time intervals. Care will be taken to highlight some of the important aspects of the deployment during certain simulation times. Due to the limitations of the paper media, this is the only section that will show a full play-by-play simulation of the truss. All other section serve merely to show the differences from this particular simulation. The time steps at which the simulation is shown are chosen to showcase the more important movements of the deploying truss.

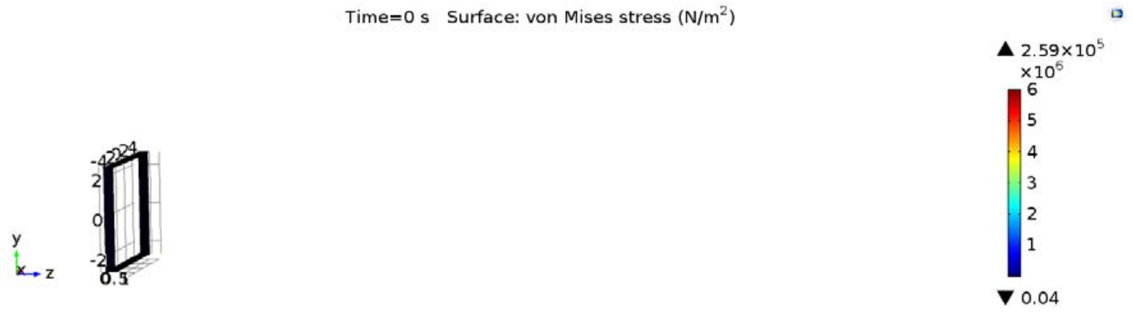

Figure 40. Uncontrolled deployment simulation displacement at 0 seconds.

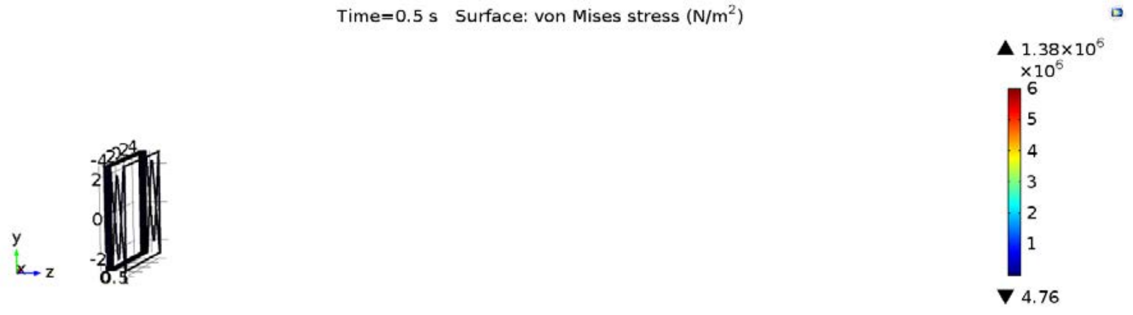

Figure 41. Uncontrolled deployment simulation displacement at 0.5 seconds.

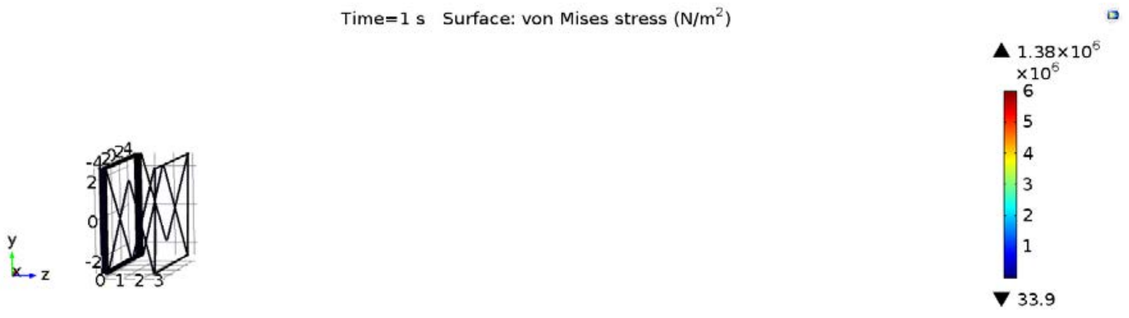

Figure 42. Uncontrolled deployment simulation displacement at 1 second.

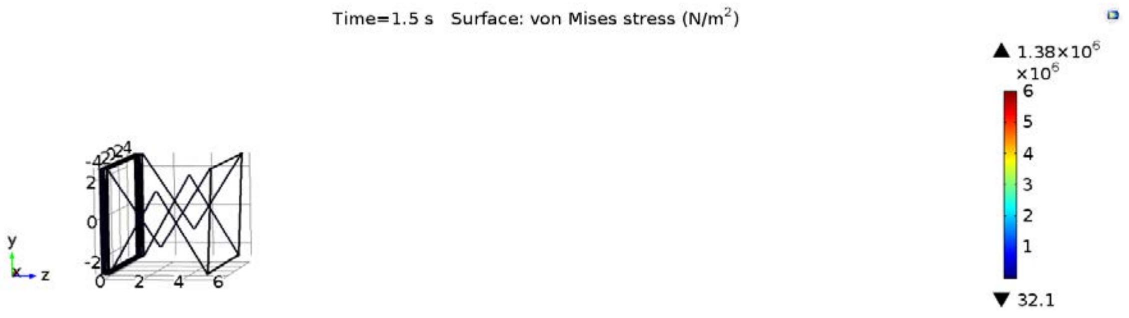

Figure 43. Uncontrolled deployment simulation displacement at 1.5 seconds.

First Cell Lockout Event.

Figures 40 through 43 show the displacement of the truss during the first 1.5 seconds. In Figure 41, only Cell 4 is deploying even though all of the hinge moments are applied in the structure. This shows that the "pushback" force from Cell 4 as it expands outwards is enough keep the rest of the cells in their stowed positions. Figures 42 and 43 show that this continues during most of Cell 4's deployment.

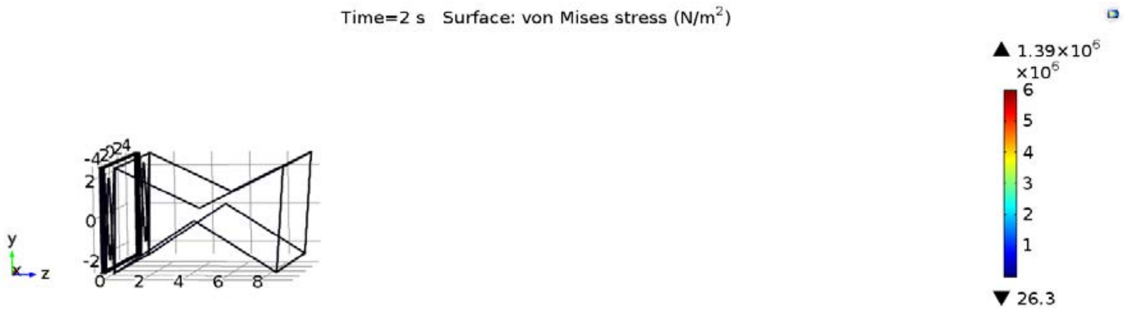

Figure 44. Uncontrolled deployment simulation displacement at 2 seconds.

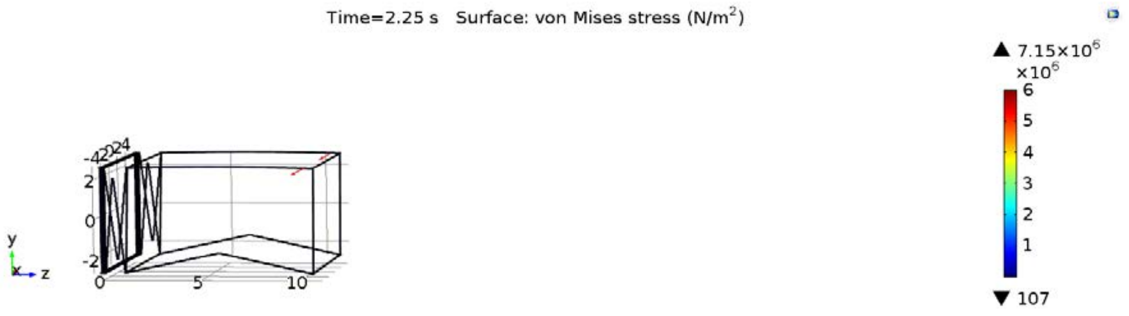

Figure 45. Uncontrolled deployment simulation displacement at 2.25 seconds.

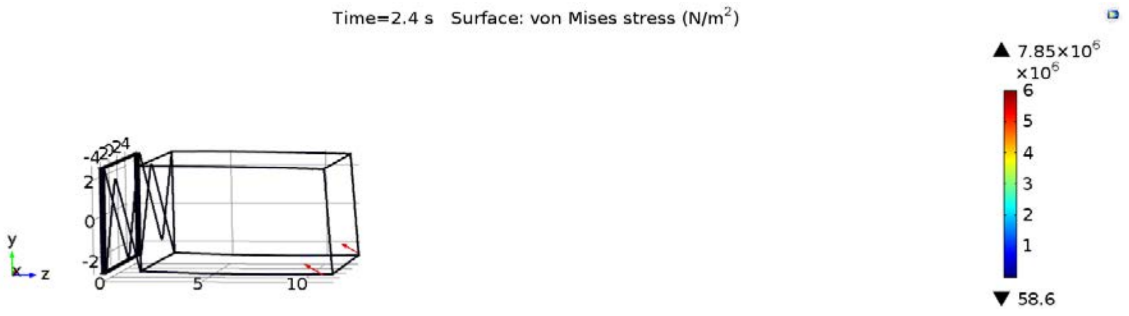

Figure 46. Uncontrolled deployment simulation displacement at 2.4 second.

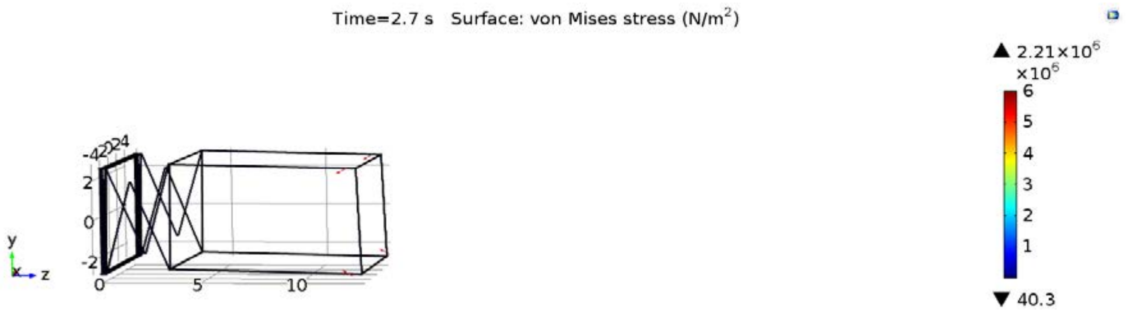

Figure 47. Uncontrolled deployment simulation displacement at 2.7 seconds.

Here Figure 45 shows that as Cell 4 reaches its hinge lockout angles, Cell 3 begins to deploy. At this point in the simulation, the applied moments from Cell 4's longerons are closing in on zero, allowing the next truss cell to start moving. Figure 45 shows the lockout of the top longerons in Cell 4. The top longerons lock first because they are shorter than the bottom longerons yet have the same applied moment. The red arrows have now appeared as well, indicating that the shaping cable forces are now active[1]. Although the bottom longerons must combat these cable forces from the top lockout event, the applied moment is still great enough for the bottom longerons to lockout in Figure 46. Figure 47 completes Cell 4's deployment by showing both cable forces being activated and pulling on the truss to form the desired shape.

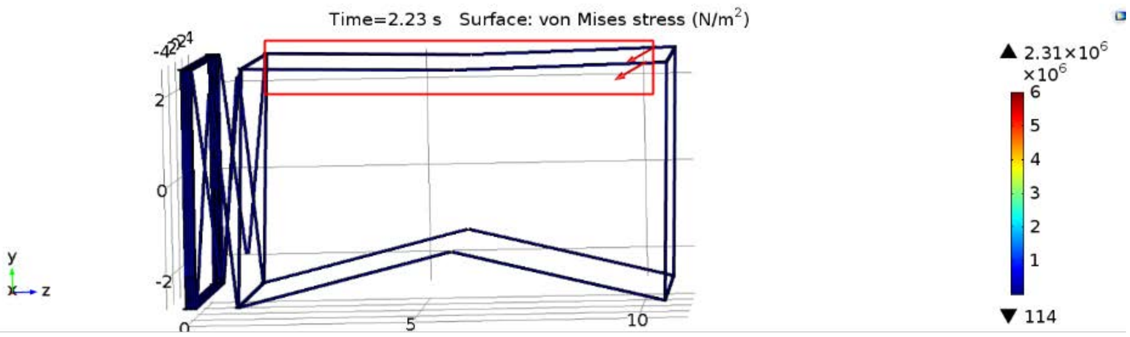

Figure 48. Uncontrolled deployment simulation displacement at 2.23 seconds.

The following figures show the lockout event of the top longerons in detail. The snapshots are taken at the peak and middle amplitudes of the oscillatory motion caused by the lockout event for one cycle. During the motion, the time steps are greatly reduced in order to properly model the motion, and so the time steps are only a selection for the tight cluster found in the simulation. Figure 48 highlights the local area that will be focused on for these figures.

Although the size of the time steps vary throughout the lockout event, they average

[1]The top structural cables are active at this point as well, but are not shown in these simulation results. Please note that the direction of the arrows is the same as the direction of the force being applied, and that the size of the arrows is based on the magnitude of the force. Therefore, a large arrow indicates a large force being applied, and a small arrow indicates a small force being applied.

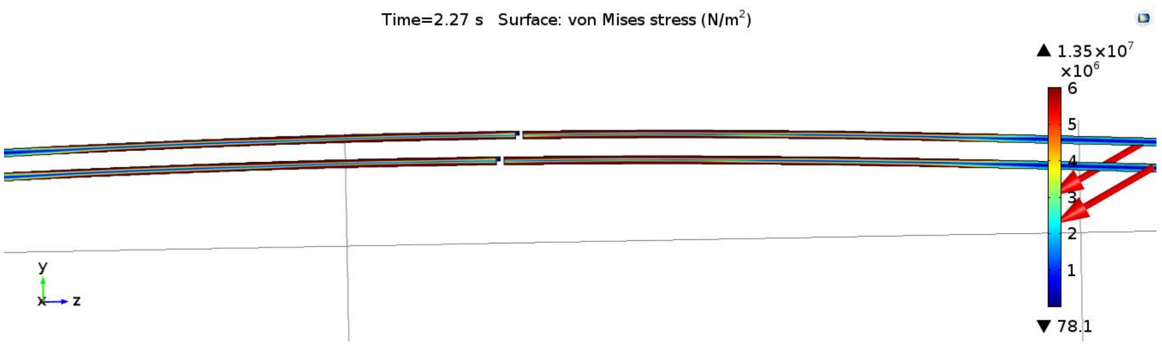

Figure 49. Uncontrolled deployment simulation stress at 2.27 seconds. (Cropped)

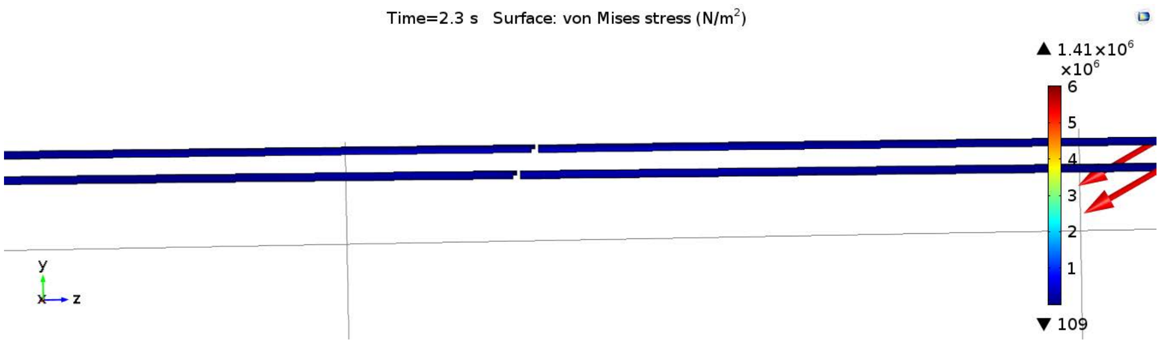

Figure 50. Uncontrolled deployment simulation stress at 2.30 seconds. (Cropped)

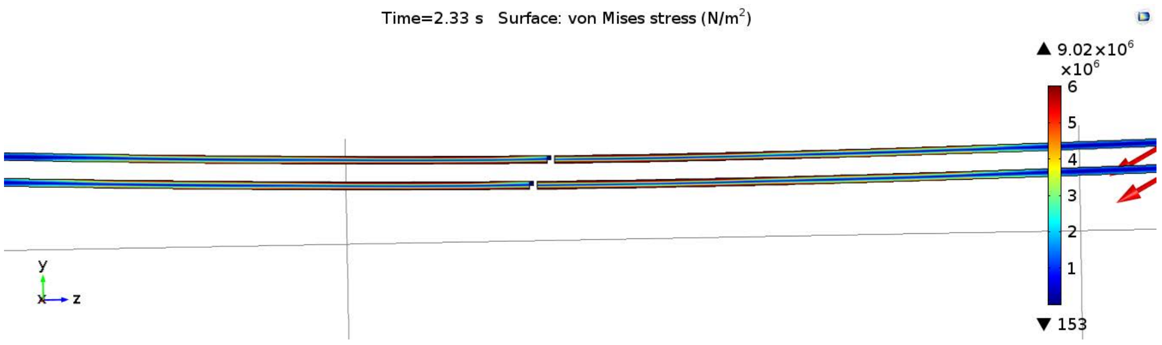

Figure 51. Uncontrolled deployment simulation stress at 2.33 seconds. (Cropped)

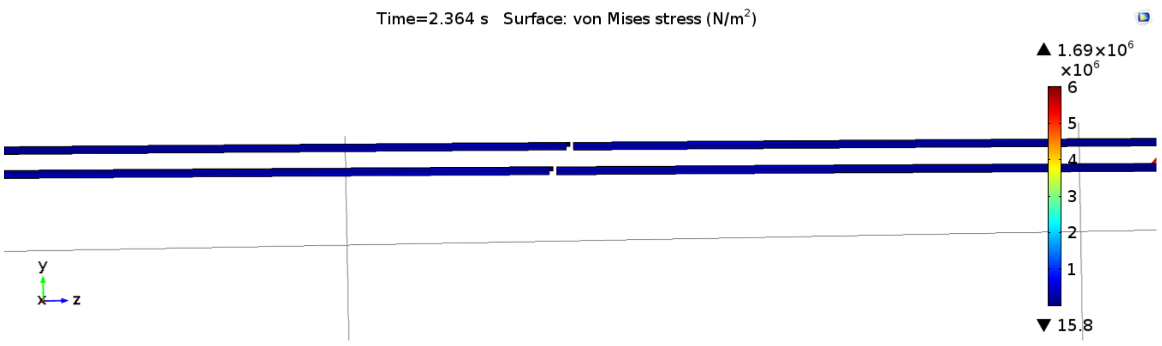

Figure 52. Uncontrolled deployment simulation stress at 2.364 seconds. (Cropped)

approximately 5 milliseconds, or half of the 10 millisecond target time step. Figures 49 through 52 visually represent half of an "oscillatory cycle" forced as a result of the lockout event, and in reality this motion is comprised of approximately 20 time steps. As the longerons bend through this cycle, the von Mises stress in the longerons increases as a function of the bending magnitude. The values of the stress are not very important here, as they are merely representative of deploying truss. Instead, the stress is really indicating the amount of bending in the members during the simulation and proves that COMSOL can capture this motion after lockout.

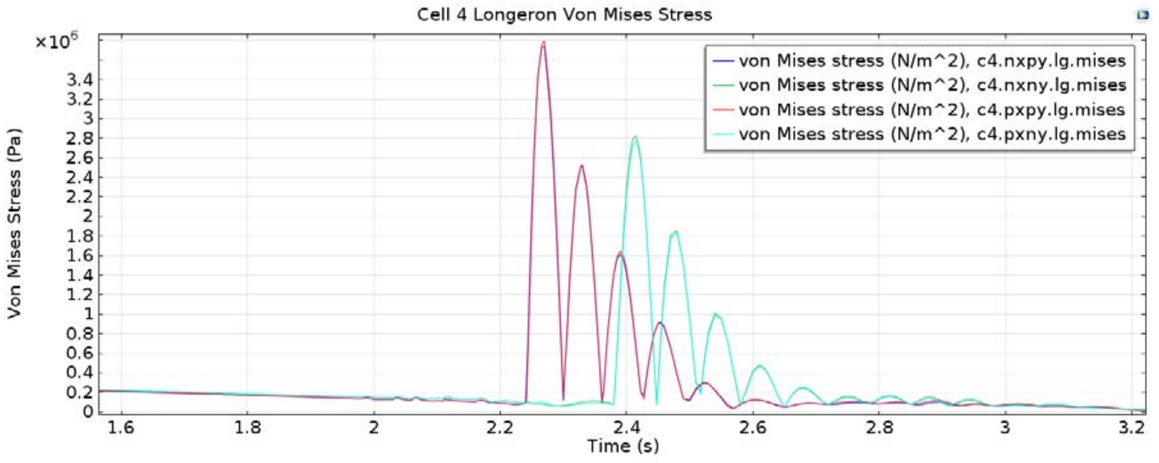

Figure 53. Von Mises stress of Cell 4's longeron lockout events during uncontrolled deployment simulation (Cropped).

Figure 53 contains the plot of the von Mises stress probes attached to the domains of the longerons[2]. The figure more clearly represents the oscillatory motion spoken of in the previous paragraph. The frequency of the oscillations is important here, as it is approximately 7 cycles per second. This is quite close to the first natural bending frequency of 8.54 Hz that was found in Section 3.6, and indicates that the longerons do not experience the higher frequencies in which the chosen quadratic hexahedral mesh performed poorly. The oscillations of the longerons can also be seen to damp out in approximately a half second. Although the only damping present in

[2]The blue and red lines represent the top longerons and the cyan and green lines represent the bottom longerons.

the structure lies in the longeron-longeron hinges, the damping effect in the stress is most likely a result of the numerical solver used for the simulation. It should also be noted that there are some small perturbations in the stress before the lockout event from 2 to 2.2 seconds. Such behavior may be attributed to Cell 3, which at this time is beginning to open as the applied moments from Cell 4 drop to zero upon lockout. As Cell 3 opens, the base from which Cell 4 is propelled becomes less stiff, resulting in the extraneous motion seen here.

Cell 3 Lockout Attempt and Miss.

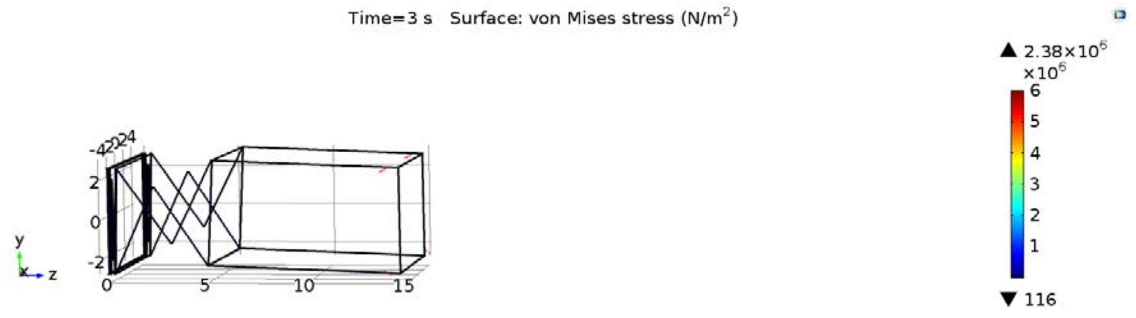

Figure 54. Uncontrolled deployment simulation displacement at 3 seconds.

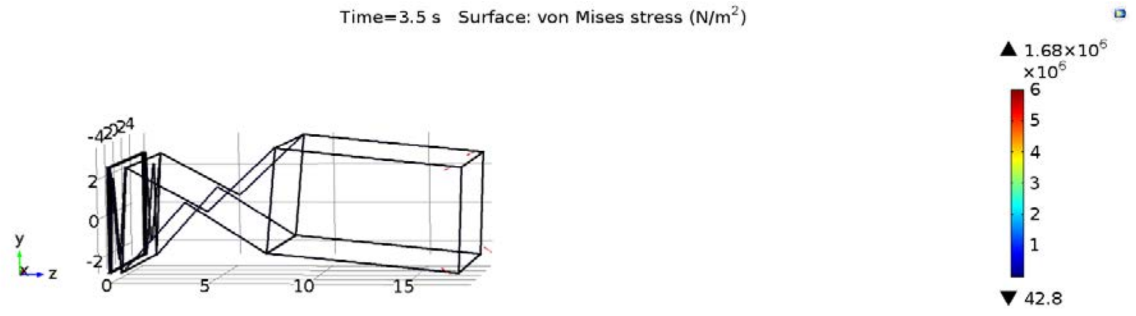

Figure 55. Uncontrolled deployment simulation displacement at 3.5 seconds.

Figures 54 through 60 show the deployment of Cell 3. This deployment is not so successful as the bottom longerons regress in their deployment motion. The bottom longerons are longer, and causes some vertical motion of Cell 4 which resides on the more positive Z face of Cell 3. The vertical motion means that when the shorter top

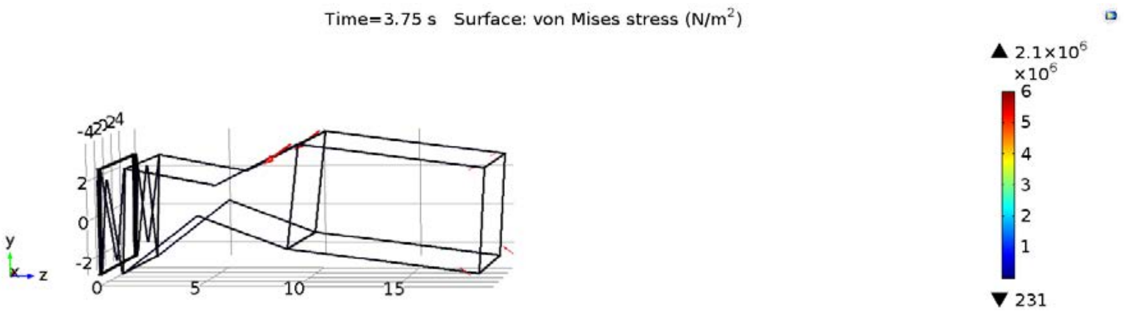

Figure 56. Uncontrolled deployment simulation displacement at 3.75 seconds.

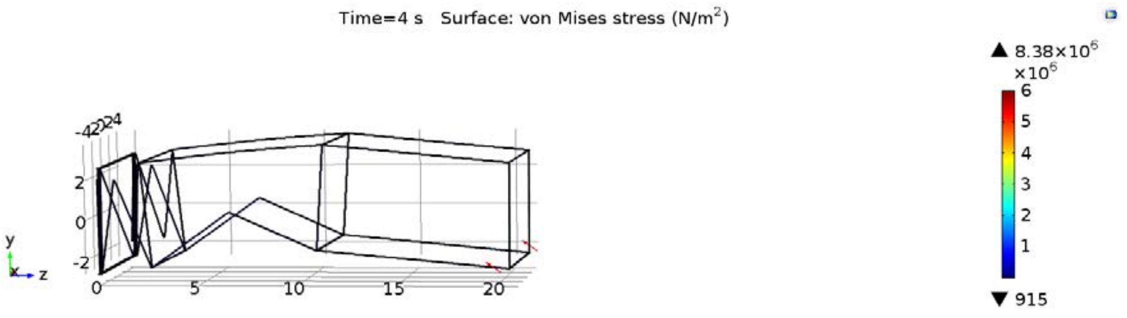

Figure 57. Uncontrolled deployment simulation displacement at 4 seconds.

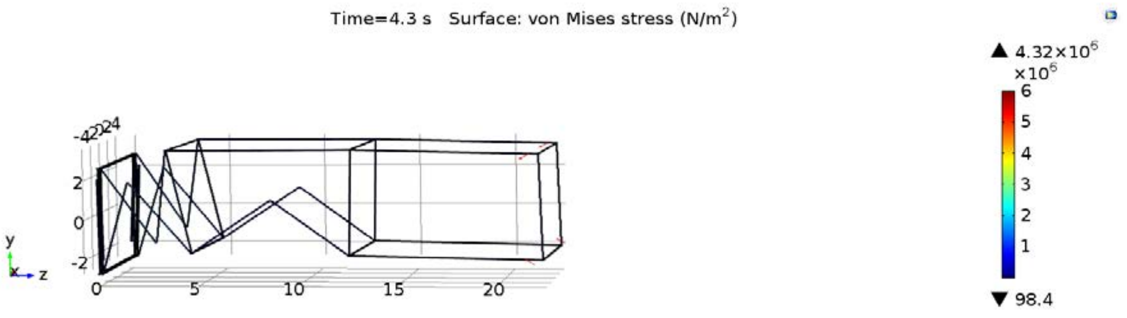

Figure 58. Uncontrolled deployment simulation displacement at 4.3 seconds.

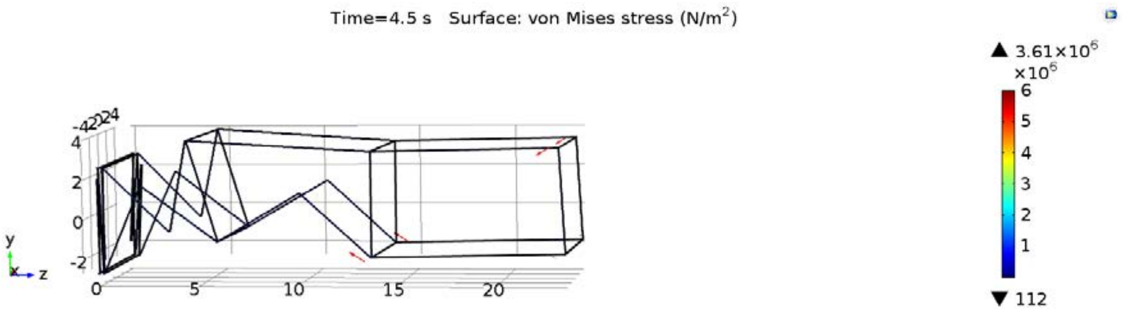

Figure 59. Uncontrolled deployment simulation displacement at 4.5 seconds.

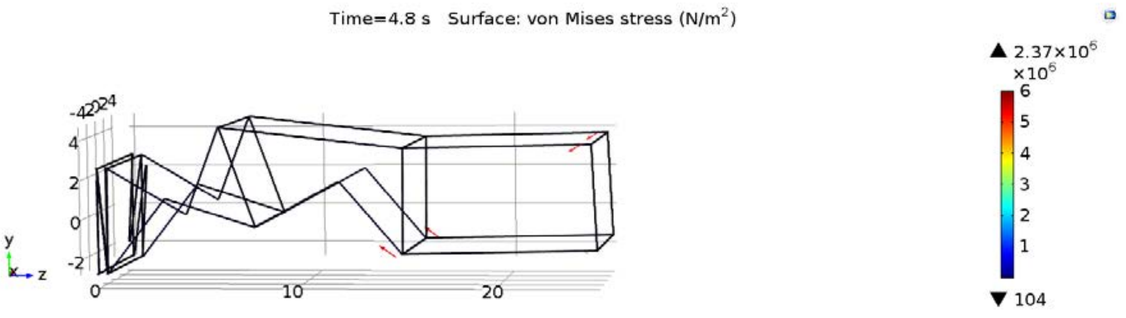

Figure 60. Uncontrolled deployment simulation displacement at 4.8 seconds.

longerons lockout first, there are sharper angles in the negative Y frame-to-longeron hinges and the positive Y longeron-to-frame hinges. As a result the distance that the cables must stretch is larger, and the force exerted by the cables overpowers the applied hinge moment of the bottom longerons.

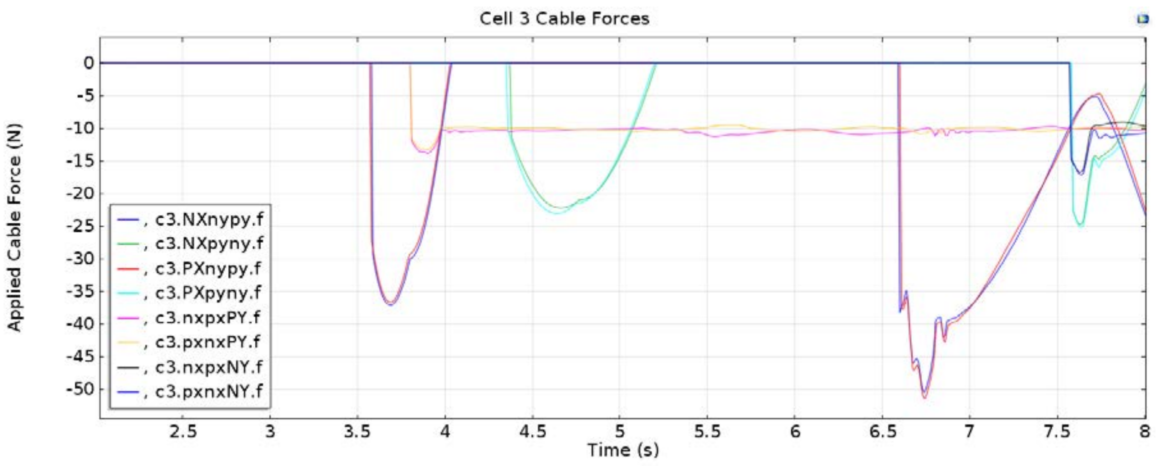

Figure 61. Cable forces of Cell 3 during uncontrolled deployment simulation (Cropped).

Figure 61 shows the applied cable forces in Cell 3 and Figure 62 shows the applied moment in Cell 3's longerons. The blue and red lines on both graphs represent the negative Y to positive Y shaping cables in the cell and the top longeron hinges. At approximately 4 seconds, the applied hinge moments of the top longerons reaches zero where the lockout angle of the longerons reside. At this point in time, there is a spike in the cable forces for the aforementioned shaping cables that form a truss triangle. Here the applied spring moment of the lower longerons, shown in cyan and

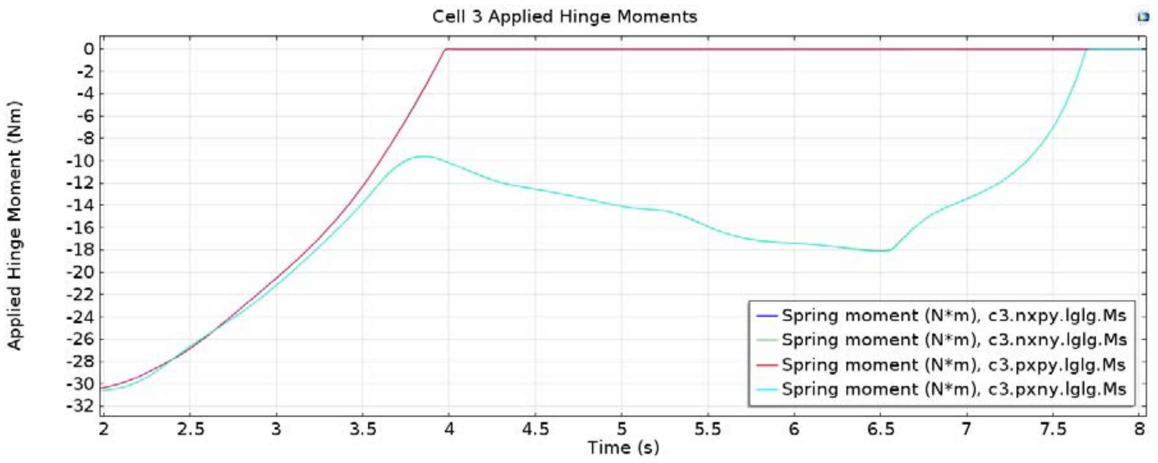

Figure 62. Applied hinge moment of Cell 3's longerons during uncontrolled deployment simulation (Cropped).

green in Figure 62, is only 10 Newton-meters. For the geometry of the truss cell at this point, it is not enough to overcome the applied cable forces of approximately 37 Newtons. Thus, the lower longerons are forced to reverse their direction and build more moment after this event. Later in the simulation, however, the geometry is such that the applied hinge moment of 18 Newton-meters combats the 50 Newtons of cable forces and is able to lockout at approximately 7.7 seconds. Although there appears to be a simple relation between the cable force and applied moment here that dictates a successful lockout, it is in fact more complicated. As the following Figures show, the entire kinetic motion of the structure during deployment is a major factor in cell deployment success.

Simulation Energies.

Figures 63 through 71 show the full deployments of Cells 1, 2, and 3. All of these deployments were in some way aided by the momentum of the structure moving outwards which "pulled" the cells open. This energy that is used to successfully deploy these Cells is critical to the deployment success of the truss arm. The next figures of this section show the raw data of the simulation, where the cable forces

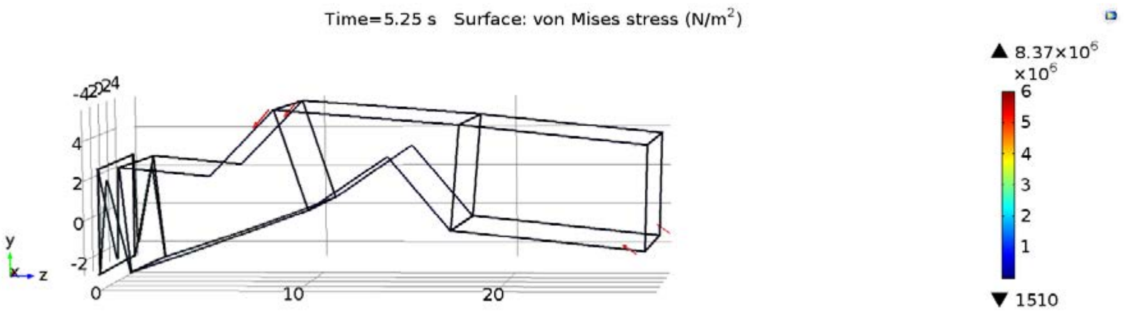

Figure 63. Uncontrolled deployment simulation displacement at 5.25 seconds.

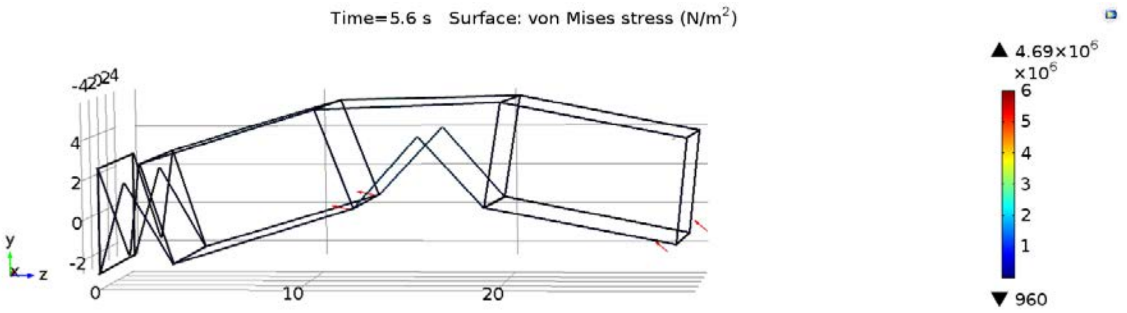

Figure 64. Uncontrolled deployment simulation displacement at 5.6 seconds.

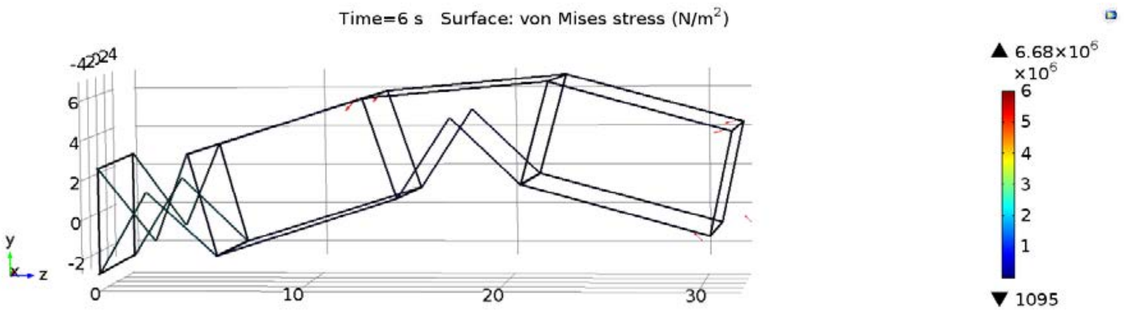

Figure 65. Uncontrolled deployment simulation displacement at 6 seconds.

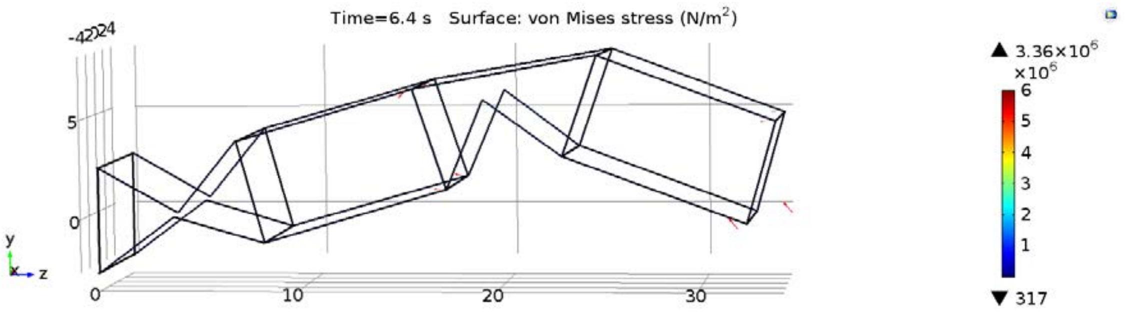

Figure 66. Uncontrolled deployment simulation displacement at 6.4 seconds.

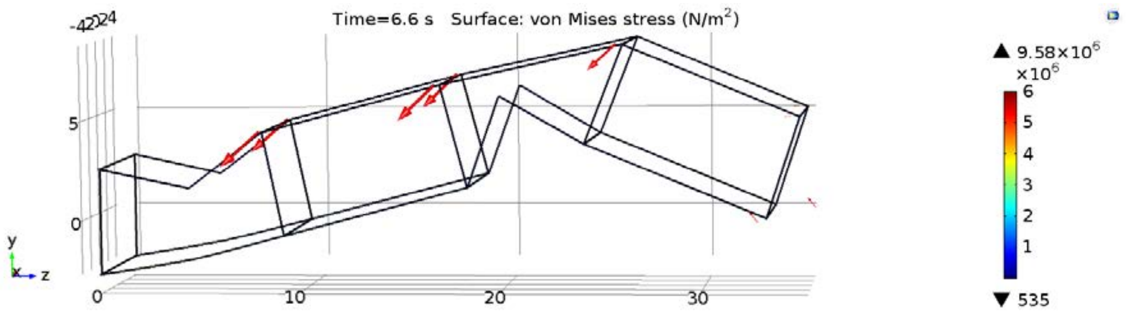

Figure 67. Uncontrolled deployment simulation displacement at 6.6 seconds.

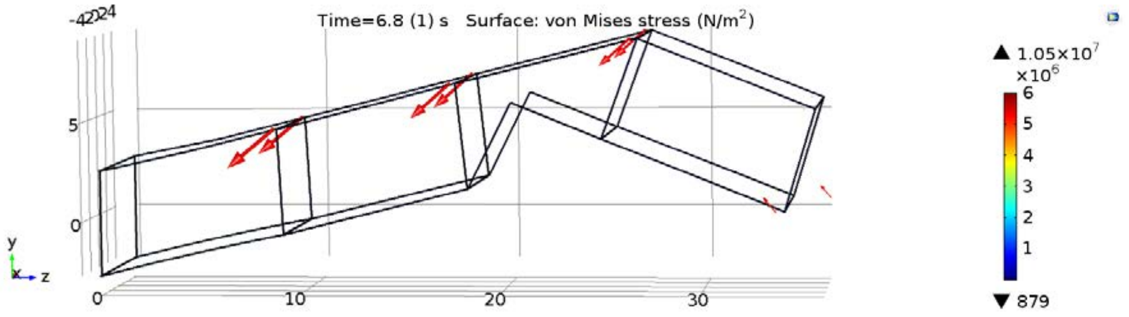

Figure 68. Uncontrolled deployment simulation displacement at 6.8 seconds.

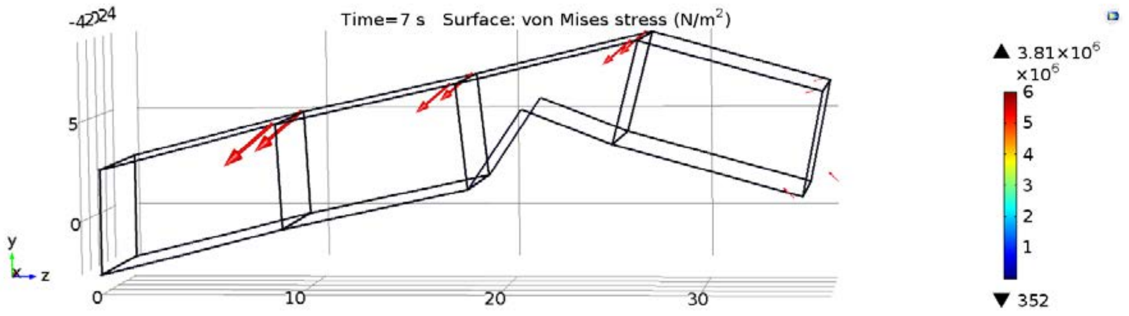

Figure 69. Uncontrolled deployment simulation displacement at 7 seconds.

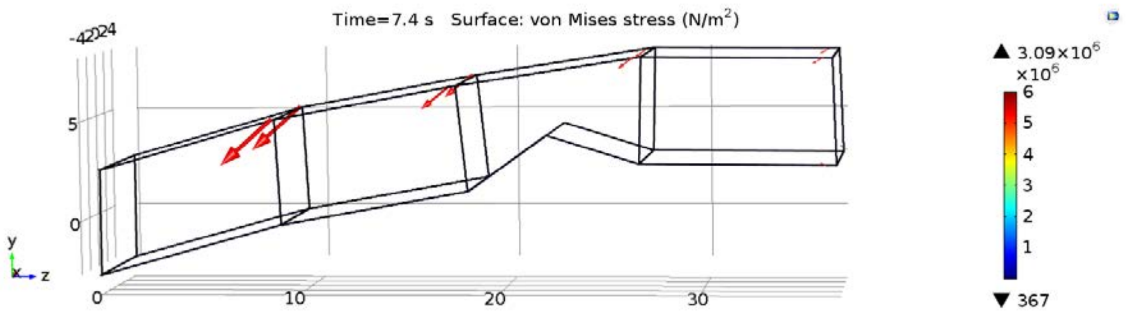

Figure 70. Uncontrolled deployment simulation displacement at 7.4 seconds.

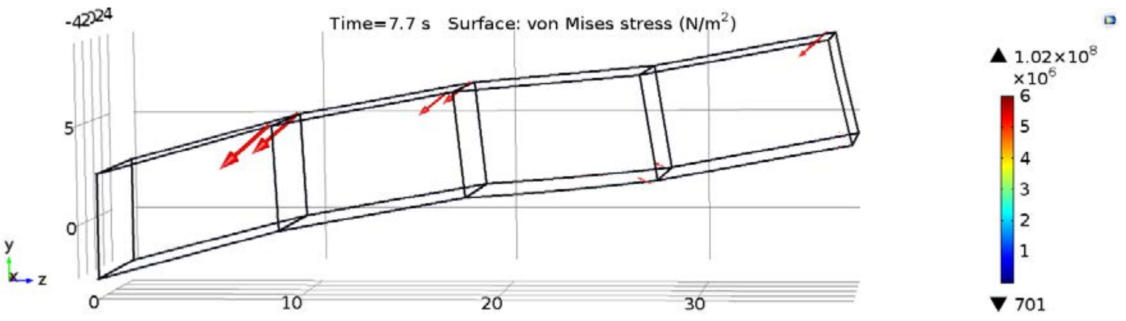

Figure 71. Uncontrolled deployment simulation displacement at 7.7 seconds.

applied to the Cells can be directly compared to the applied hinge moment. In these figures it is possible to see that for the cells closer to the base, the cable to hinge moment relationships are far greater than that of Cell 3's lower longerons which failed to properly deploy. To further support this claim, Figure 72 shows the total kinetic, strain, and summed energies of the entire structure. Keep in mind that the kinetic strain energy is calculated from the mesh of the domains in the structure, but that strain energy also includes the cables and hinges. The summed energy is merely an addition of the kinetic and strain energies.

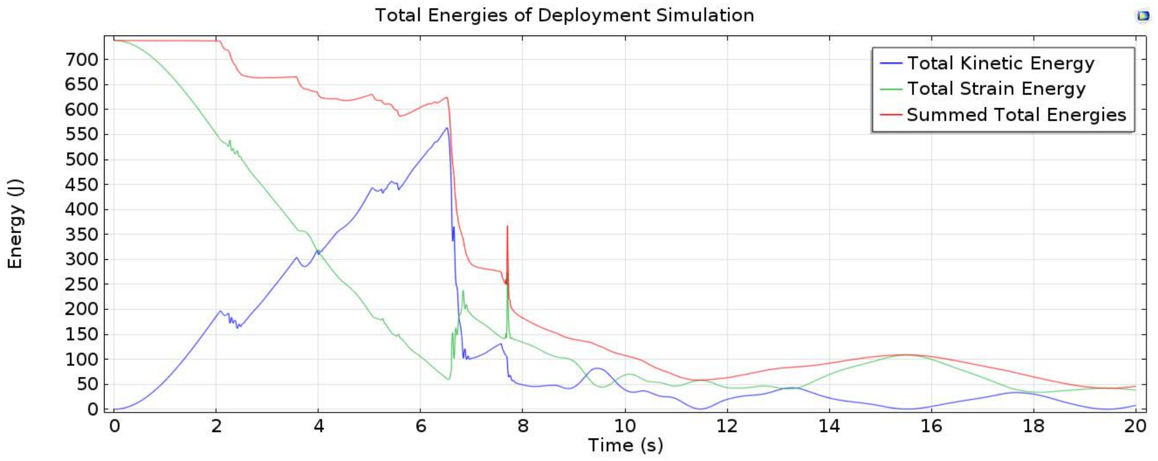

Figure 72. Uncontrolled deployment simulation kinetic and strain energies.

At the beginning of the simulation, the strain energy is at its highest and the kinetic energy is at its lowest, as one would guess. As each truss deploys, however, the kinetic energy keeps building even though the longerons lockout at certain times because the cells farther out are pushed by the cells nearer the base. Interestingly, both energies show the same disruptions caused by the lockout events. At approximately 6.4 seconds, the kinetic energy suddenly drops off as the base Cell 1 fully deploys and stops the truss from moving outwards. Conversely, the strain energy spikes quite suddenly, as all of the cables strain to hold and create their Cell's intended shape. Once Cell 3 finally locks around 8 seconds, the kinetic and strain energies form a loose inverse relationship as the deployed truss structure moves vertically in a periodic fashion. Last but not least, the summed energies of the deployment, shown in red, and helps to explain how the structure dissipates its energy. The kinetic energy of the truss members is mainly absorbed by themselves during the lockout events and damped by the numerical solver. Again, the summed energies slowly decline at first, but decay very rapidly after Cell 1 fully deploys. The notable exception being the sharp spike in strain energy caused by the cables of Cell 3 fighting the lower longerons finally deploying. By the end of the simulation, it is clear that the total energy is beginning to reach its equilibrium point where only the strain energies of the cables and truss elements are active. On its way to equilibrium, however, the sum of the energies increases briefly from 11 to 15.5 seconds, and should not be physically possible. Although the exact cause for the increase is not certain, it is thought that strain energies are not being taken into account correctly.

Post Deployment Transient Motion.

Figures 73 through 88 show the remaining 12 of the total 20 seconds of the simulation. Note that the structure does not uniformly move vertically and moves in more of a "wave" fashion. Such motion can be attributed not only to the unequal length longerons throughout the truss structure, but also the differing times of deployments. Most of the motion seen throughout this time period is a result of the shaping cables

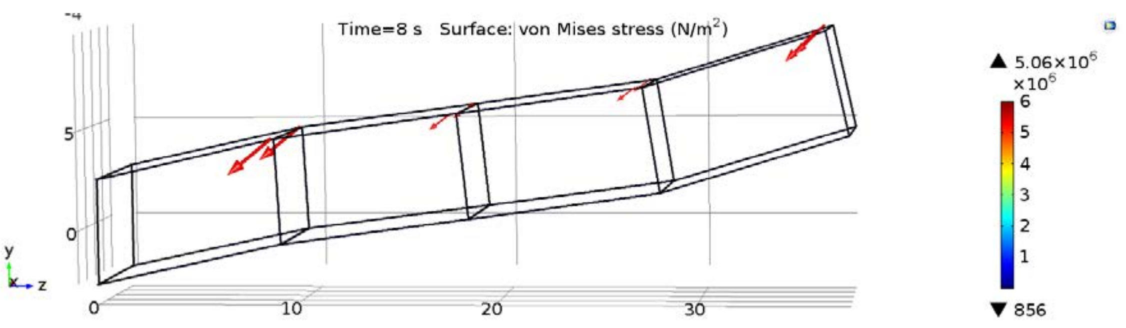

Figure 73. Uncontrolled deployment simulation displacement at 8 seconds.

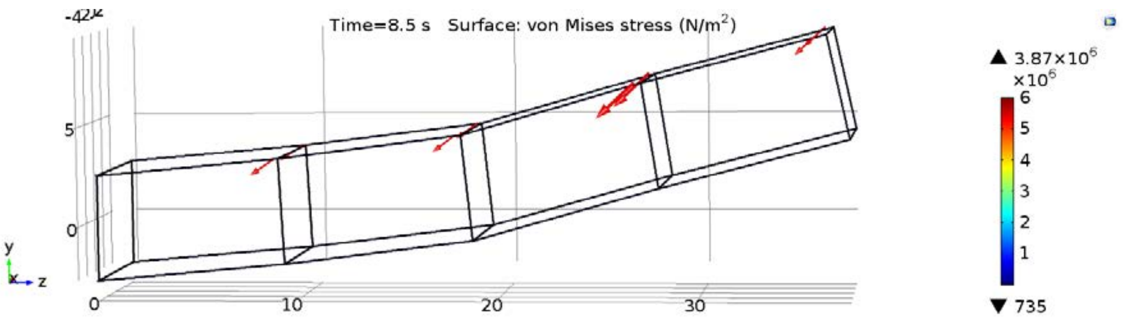

Figure 74. Uncontrolled deployment simulation displacement at 8.5 seconds.

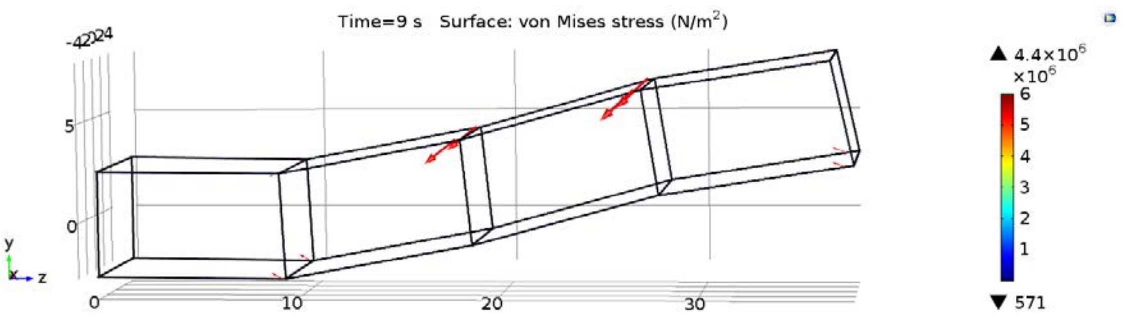

Figure 75. Uncontrolled deployment simulation displacement at 9 seconds.

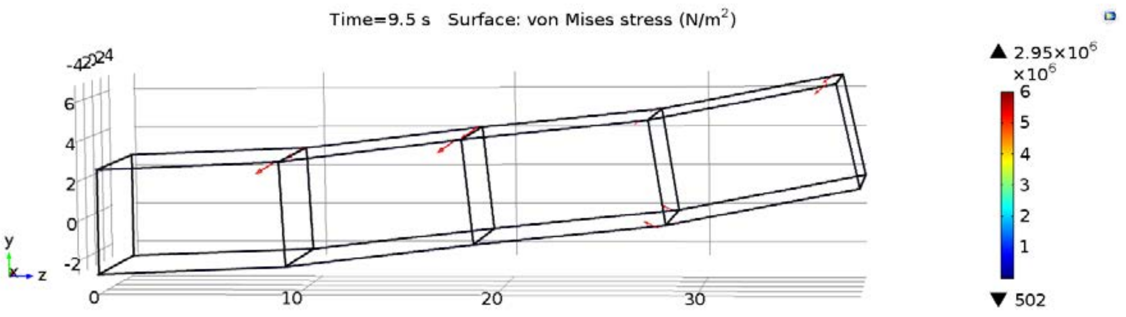

Figure 76. Uncontrolled deployment simulation displacement at 9.5 seconds.

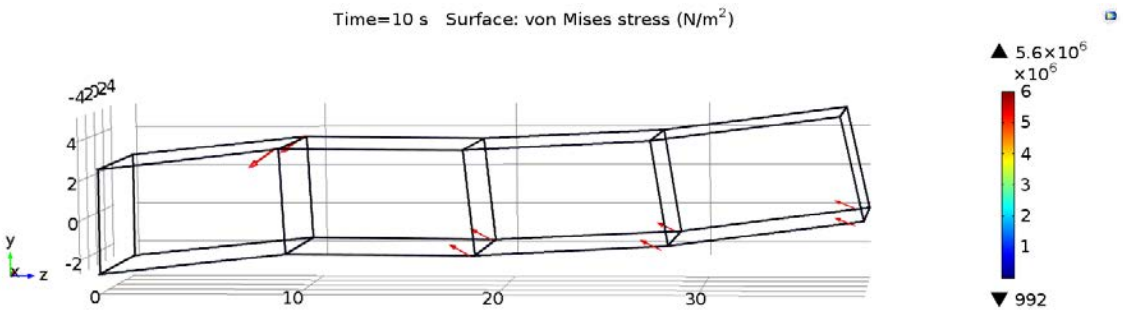

Figure 77. Uncontrolled deployment simulation displacement at 10 seconds.

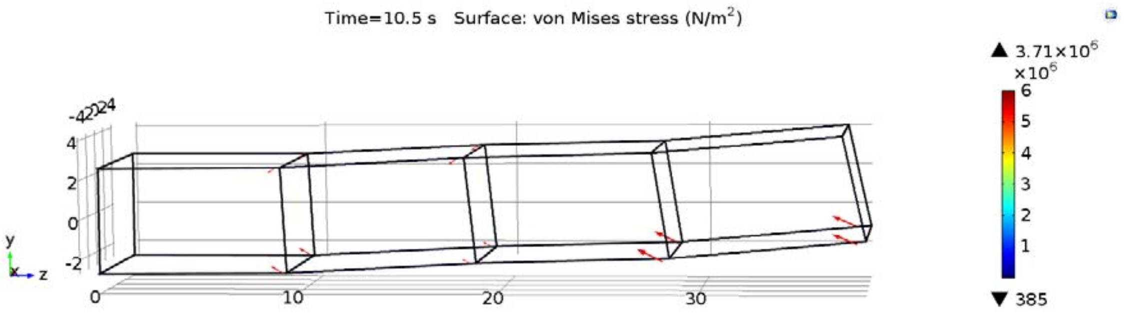

Figure 78. Uncontrolled deployment simulation displacement at 10.5 seconds.

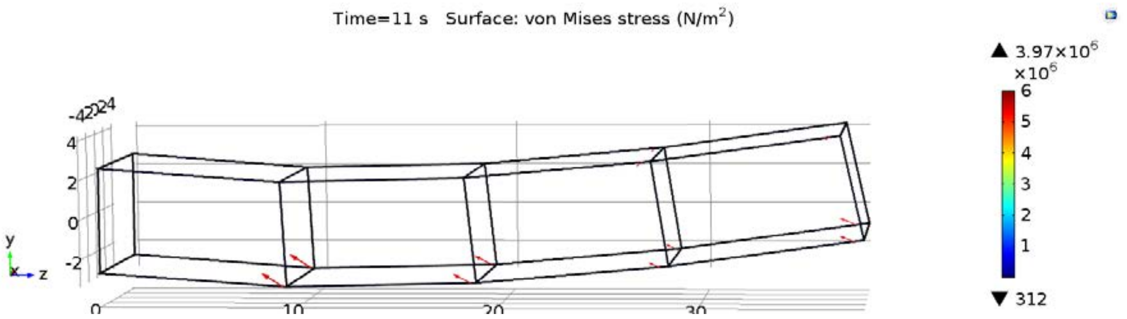

Figure 79. Uncontrolled deployment simulation displacement at 11 seconds.

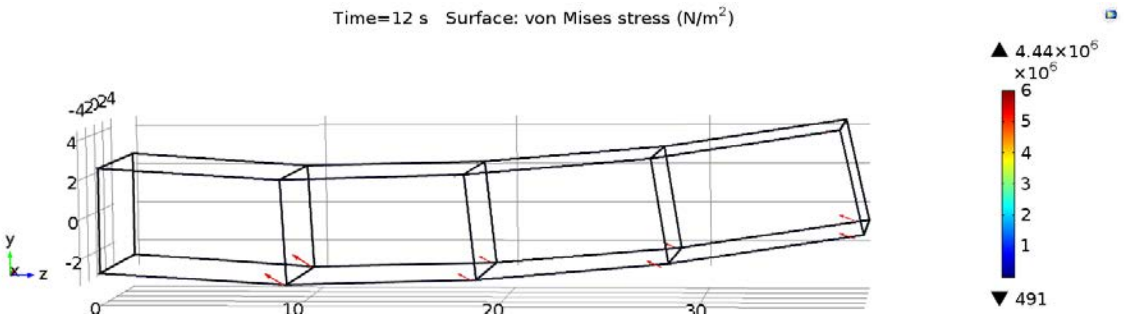

Figure 80. Uncontrolled deployment simulation displacement at 12 seconds.

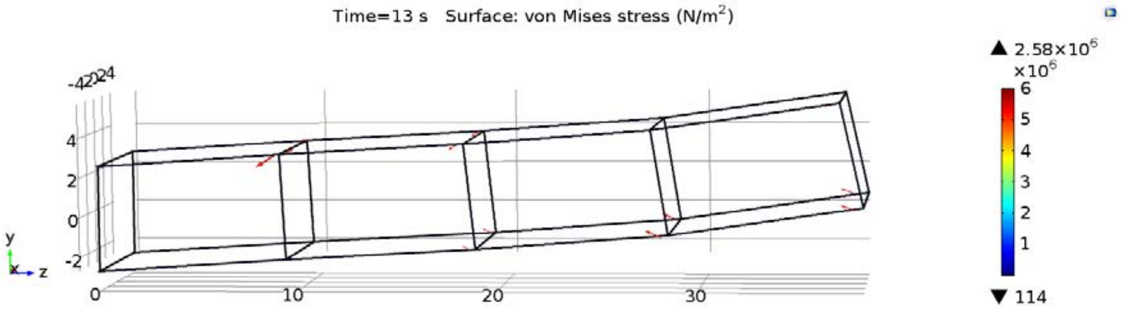

Figure 81. Uncontrolled deployment simulation displacement at 13 seconds.

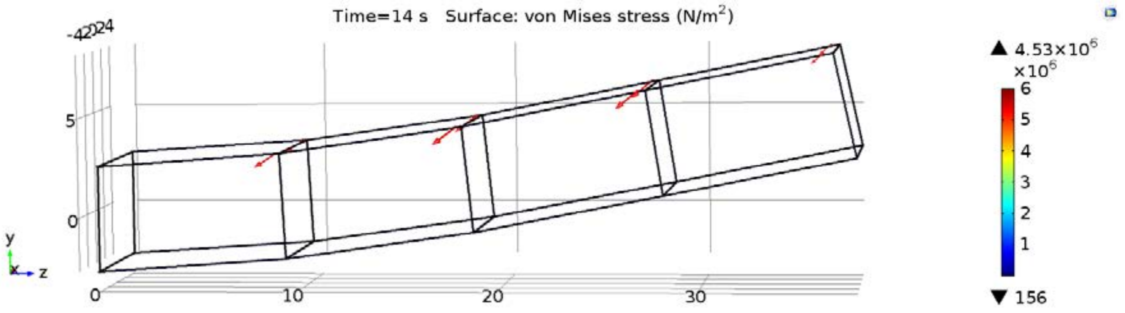

Figure 82. Uncontrolled deployment simulation displacement at 14 seconds.

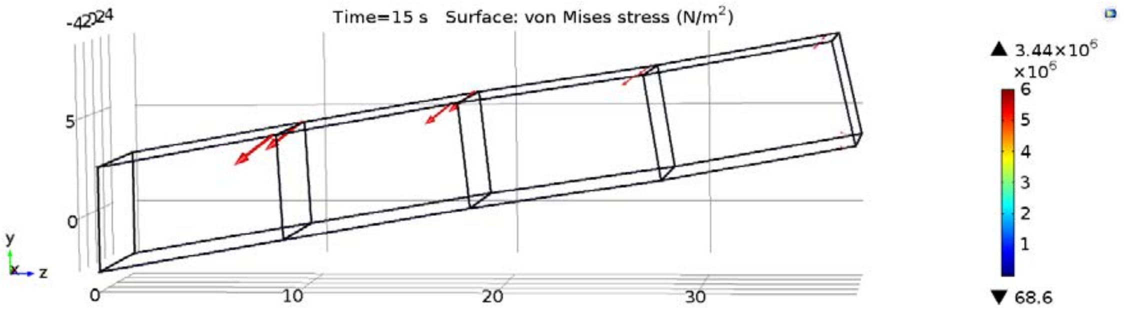

Figure 83. Uncontrolled deployment simulation displacement at 15 seconds.

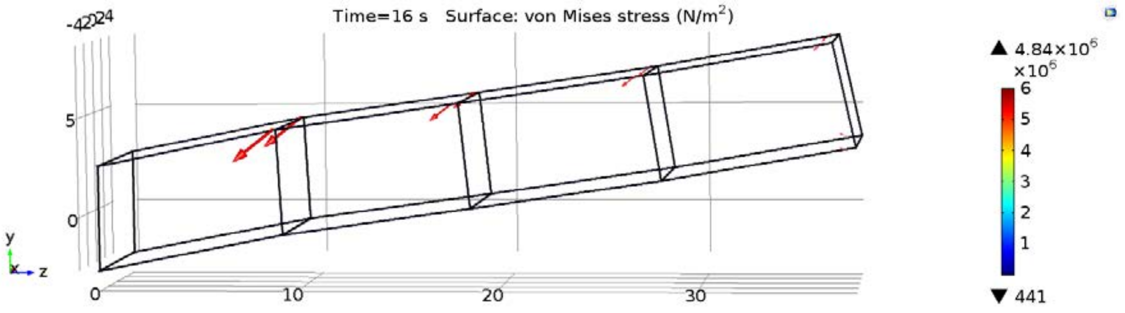

Figure 84. Uncontrolled deployment simulation displacement at 16 seconds.

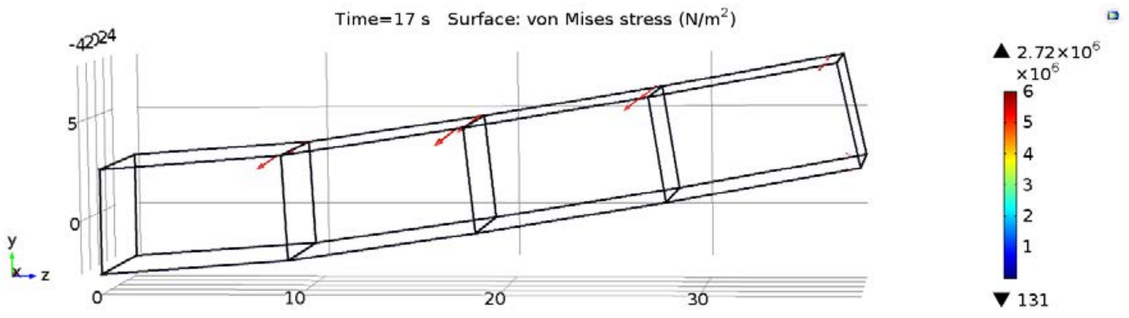

Figure 85. Uncontrolled deployment simulation displacement at 17 seconds.

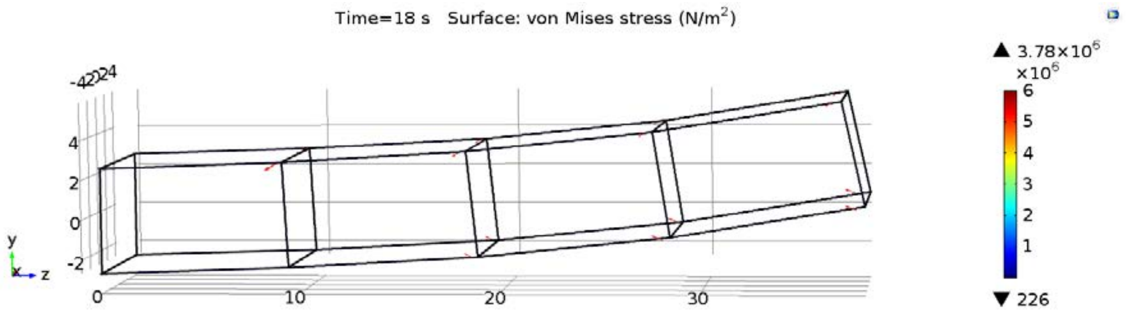

Figure 86. Uncontrolled deployment simulation displacement at 18 seconds.

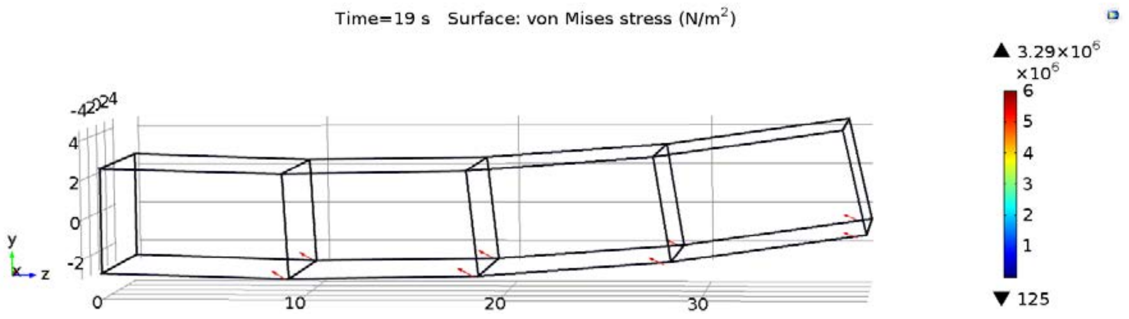

Figure 87. Uncontrolled deployment simulation displacement at 19 seconds.

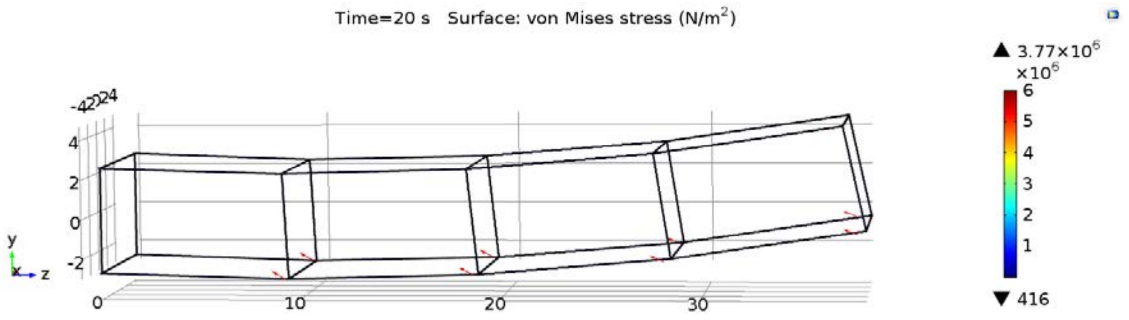

Figure 88. Uncontrolled deployment simulation displacement at 20 seconds.

trying to form the final parabolic shape of the reflector. Remember that the size of the arrows indicate the force being applied. The serialized cells moving with each other, fighting to find their own equilibrium often upsets that of its neighboring cell.

Simulation Data.

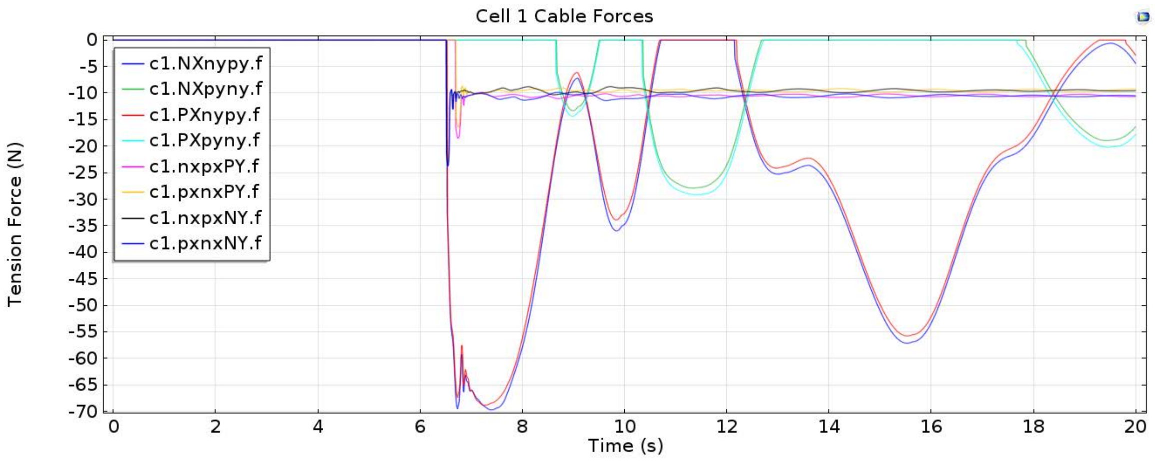

Figure 89. Uncontrolled deployment simulation cables forces of Cell 1.

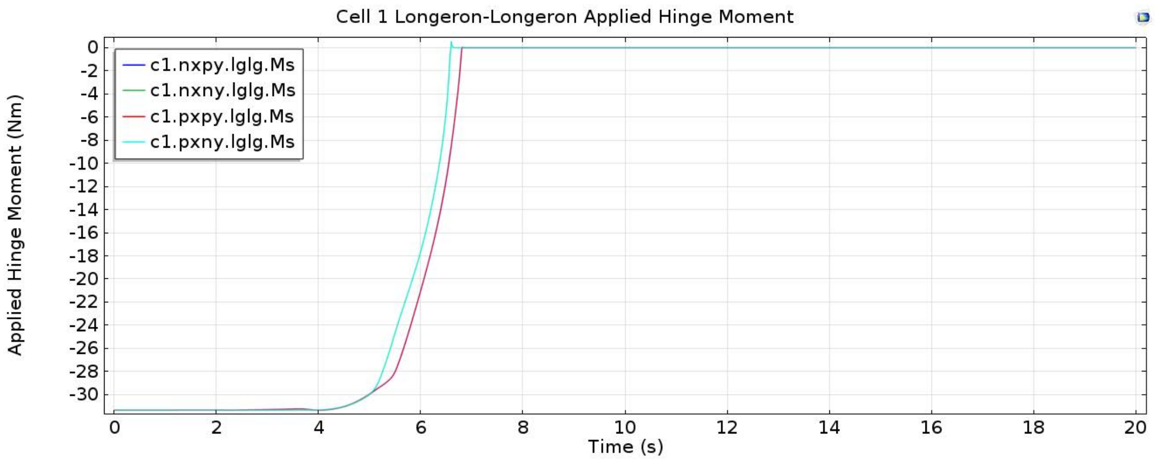

Figure 90. Uncontrolled deployment simulation applied hinge moments of Cell 1.

Figures 89 through 96 show the relationships between the cable forces and hinge moments for each cell. It is interesting to note here that although the top longerons are shorter and deploy first in Cells 3 and 4, it is the bottom longerons that deploy

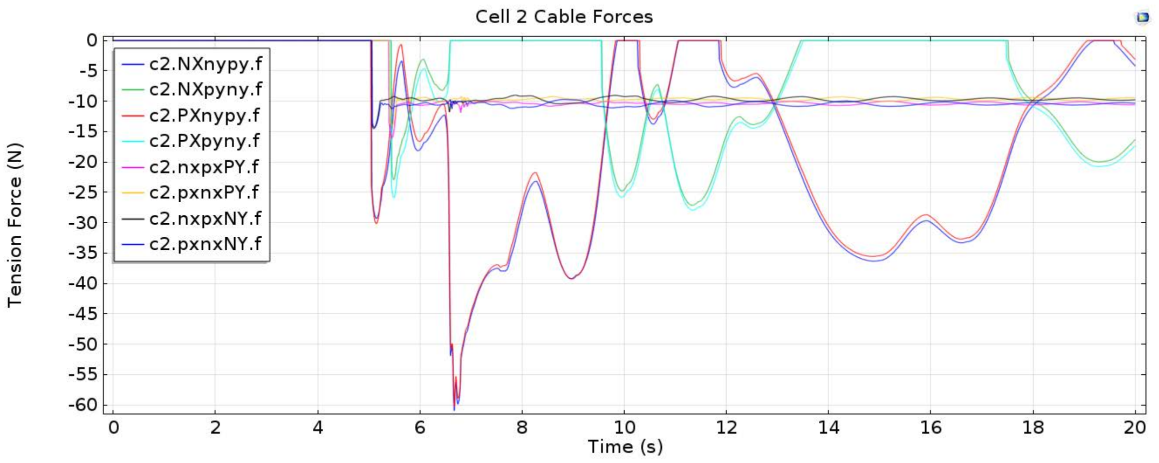

Figure 91. Uncontrolled deployment simulation cables forces of Cell 2.

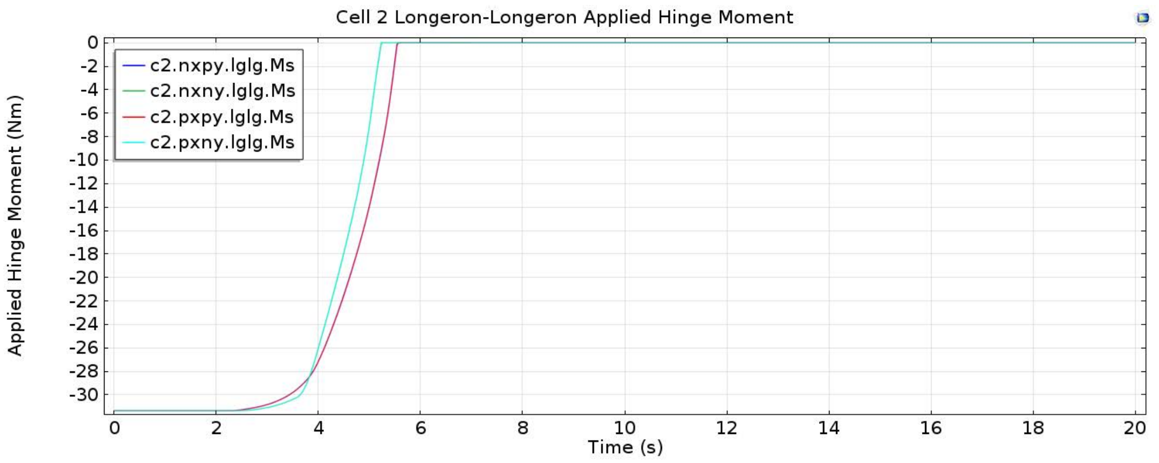

Figure 92. Uncontrolled deployment simulation applied hinge moments of Cell 2.

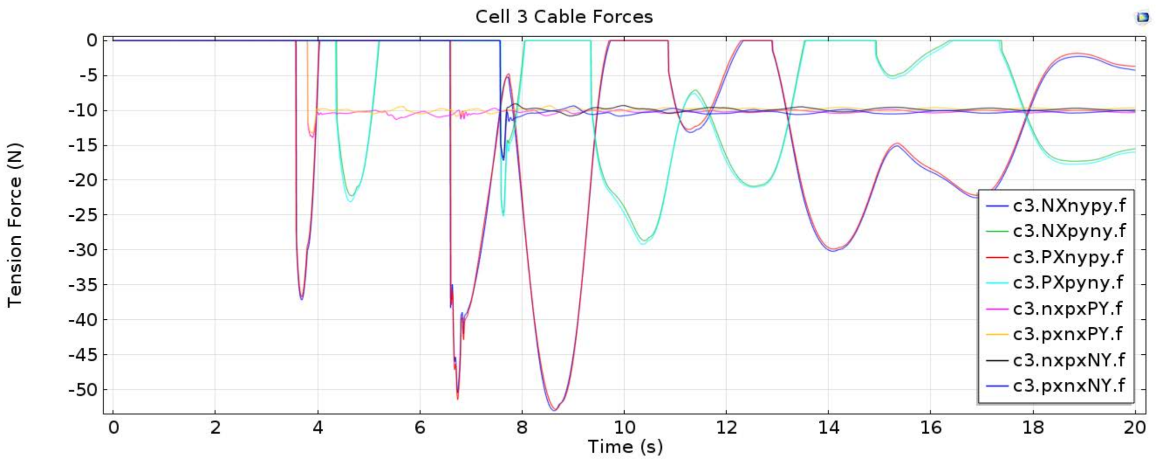

Figure 93. Uncontrolled deployment simulation cables forces of Cell 3.

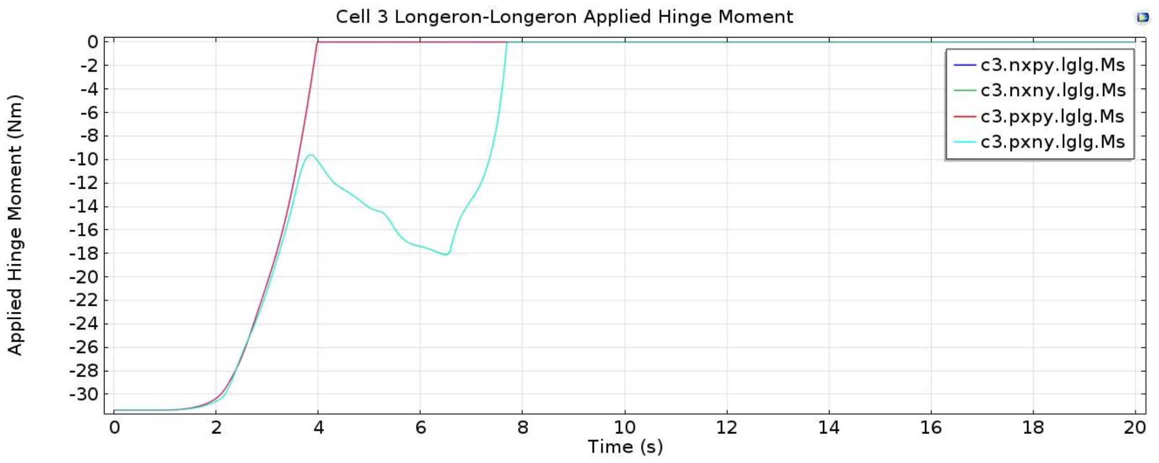

Figure 94. Uncontrolled deployment simulation applied hinge moments of Cell 3.

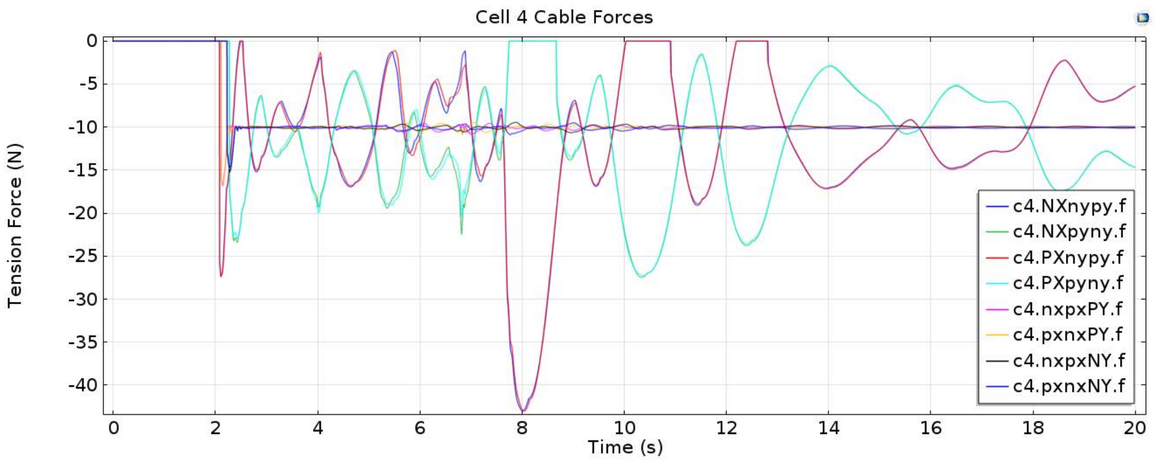

Figure 95. Uncontrolled deployment simulation cables forces of Cell 4.

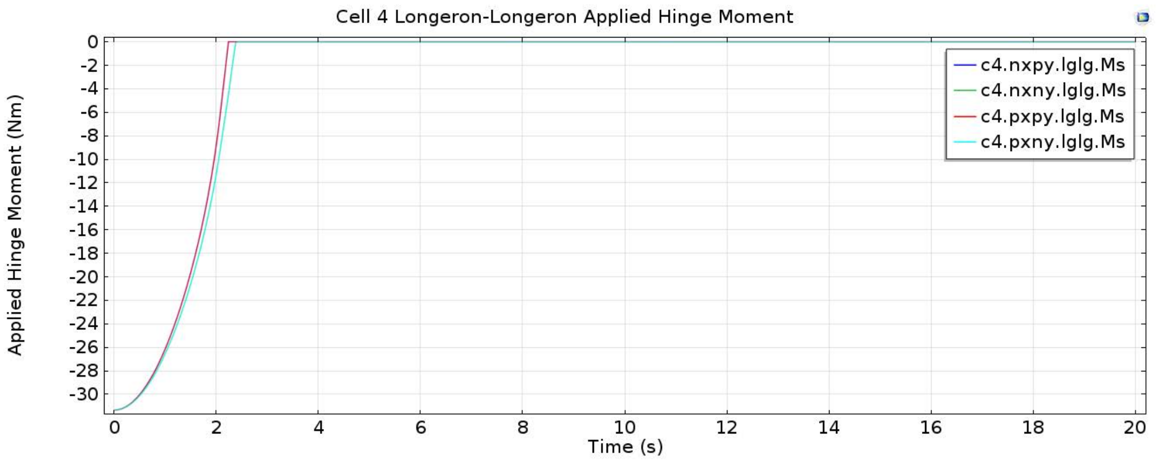

Figure 96. Uncontrolled deployment simulation applied hinge moments of Cell 4.

first in Cells 1 and 2. This phenomena is most likely a result of the geometry configuration at the later stages of the deployment. Figures 97 through 100 show the longeron stresses of each Cell during deployment. The first thing to notice on the stress plots is the initial stress of each cell at the start of the simulation. This represents the bending of the beams as the hinge moments from the hinges are applied to the folded longerons to begin the deployment. More importantly, however, the figures show that the stress waves from one cell's lockout event can be seen throughout the other cell's. For example, Cell 4 is the first Cell to fully deploy at approximately 2.5 seconds. The deployments of Cell 4's longerons are timed very closely together. After this deployment, a small positive variation in Cell 3's stress is seen at approximately 2.75 seconds as the lockout event stress travels to Cell 3. Some time later at approximately 4.5 seconds, Cell 2 experiences a similar positive stress variation. Although not conclusive, the results suggest that Cell 4's lockout event stress wave and Cell 3's top longeron lockout event stress wave cause Cell 2's small positive variation. Through the rest of time of the simulation similar stress wave sharing can be seen, especially between adjacent cells. It should be kept in mind though that some of the stresses seen in the latter parts of the simulation may also be from the slight bending of the cells by the shaping cables. It should also be said that the magnitude of these stresses really just indicate some displacement by the bending longerons. The main point, however, is that these simulations show that COMSOL does translate the events from each member in the system through the declared hinges (which are not meshed with flexible elements) to other members in a significant fashion.

The deployment envelope is one of the most important analyses done to these simulations. Table 7 shows the results from the MATLAB code written to determine the maximum displacements achieved by the truss in 3D space. Keep in mind that the truss itself is centered upon the origin of the XY Plane. Therefore, the upper and lower

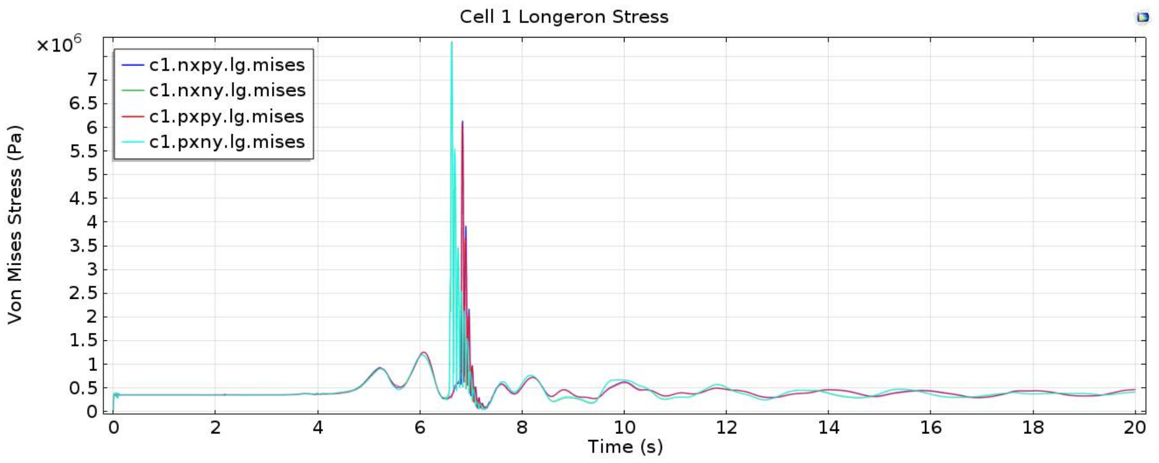

Figure 97. Uncontrolled deployment simulation longeron stress of Cell 1.

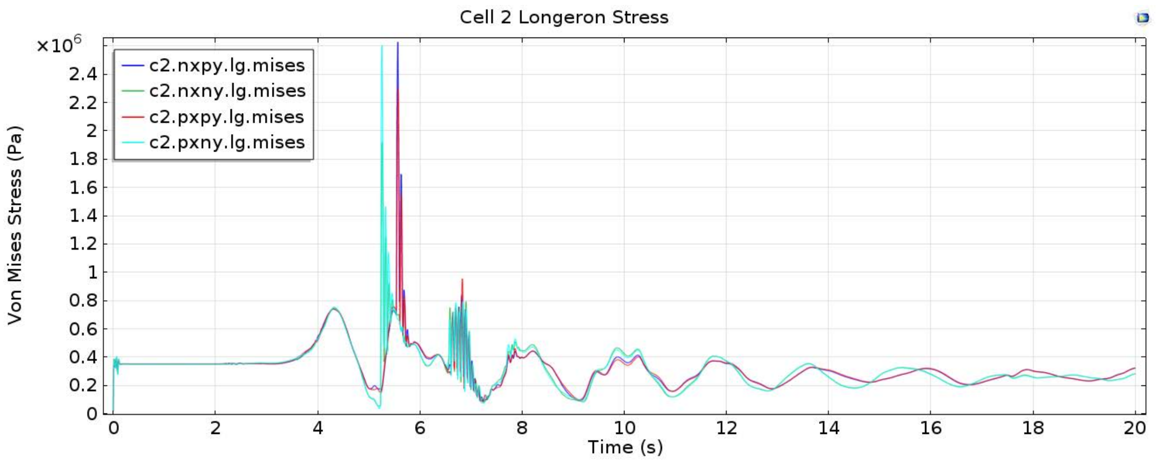

Figure 98. Uncontrolled deployment simulation longeron stress of Cell 2.

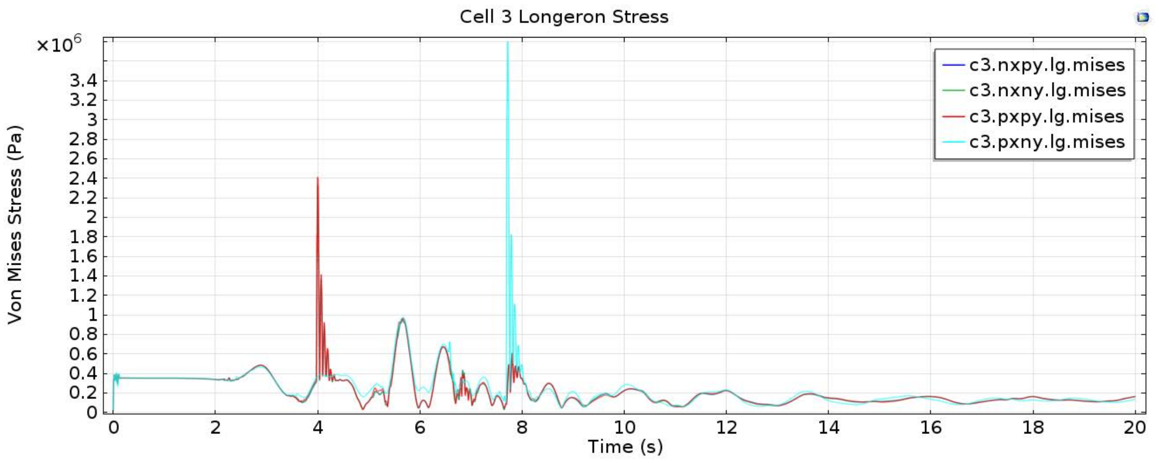

Figure 99. Uncontrolled deployment simulation longeron stress of Cell 3.

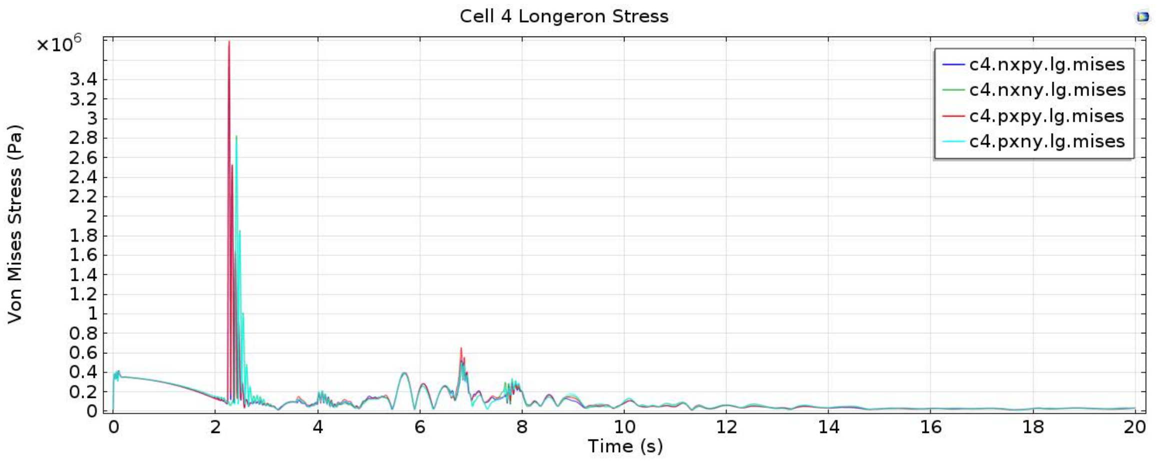

Figure 100. Uncontrolled deployment simulation longeron stress of Cell 4.

bounds for X-axis merely denote the width of the truss with some added horizontal displacement of approximately 4-5 centimeters[3]. It is interesting that the trusses' deployment shows any horizontal movement at all since the applied forces almost exclusively reside in the YZ-Plane. However, the horizontal forces of the structural cables may cause this motion as they will not always be perfectly symmetric due to a relatively high 1% tolerance factor imposed on the dependent variables of the simulation. The lower bound of the Y-displacement is almost a meter lower than the height of the cells (5.31 meters) centered at the origin. The upper bound of Y, shows an even more significant peak of almost 10 meters. Both of these may be of some concern in future work when the rest of the reflector aperture is constructed around this deployment. The upper Z bound validates that the solid modeling of the truss done in the early stages of this work was done correctly. The as-designed diameter of the complete sparse aperture is supposed to be approximately 150 meters, and one half of one truss arm extends roughly one quarter of this diameter. Lastly, the negative Z bound is zero, as one would expect with the model fully constrained on the XY Plane.

[3]The nominal width of the truss cells is 8.74 meters and the nominal height of the truss cells is 5.31 meters.

Completed Deployment	**X**	**Y**	**Z**
Upper Bound (m)	4.4710	6.0679	37.9799
Lower Bound (m)	-4.4710	-2.6422	0
Uncontrolled Deployment	**X**	**Y**	**Z**
Upper Bound (m)	4.4430	9.7763	37.8630
Lower Bound (m)	-4.5435	-3.6698	0

Table 7. Uncontrolled Deployment Simulation Deployment Envelope

4.3 Uncontrolled Deployments with Centripetal Acceleration

The practice of exploiting centripetal acceleration of orbiting bodies is nothing new. It was thought that by adding a rotating frame to the simulation that perhaps a better deployment behavior could be achieved. In this instance, two simulations were run: one with an initial rotation of 5 degrees per minute, and another with an initial rotation of 60 degrees per minute. Please note that a angular velocity of 60 degrees per minute is very excessive for a structure of this size in space, and is only used here to exemplify COMSOL's capabilities. Both of these rotations speeds are initial, since the deployment of the truss arm creates a larger moment of inertia to slow the rotation down. Both simulations place a rotating frame about the Z-axis, the center of which would be the hub of the four arms for the complete sparse aperture.

A simple function was created in COMSOL to control the angular velocity of the rotating frame as a function of the varying moment of inertia of the truss arm. An initial angular momentum was assumed for the stowed truss that was calculated as a simple centroid mass. The initial angular momentum is them divided by the same mass multiplied by the square of the increasing radius. The radius is determined by the Z displacement of Cell 2's frame connectors. This is the simplest formulation for moment of inertia and is used only to get some form of diminishing rotation in the simulation. All of these terms are used to solve for an angular velocity, which is applied to the rotating frame physics node built into the simulation model. Figure 101 shows this created function against the time steps of the simulation, and Equation 15 shows the basic kinetics used to determine the angular velocity of the rotating frame.

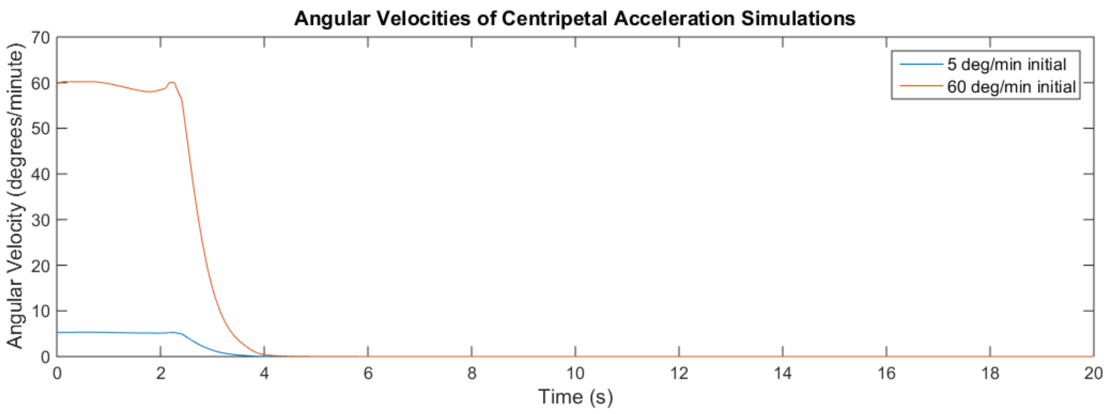

Figure 101. Uncontrolled deployment simulations in rotating frames.

$$H = mr^2\omega \rightarrow \omega = \frac{H_{initial}}{mr^2_{centroid}} \tag{15}$$

Where H (Angular Momentum), m (Mass), $r_{centroid}$ (Mass Centroid Radius), and ω (Angular Velocity).

This figure illustrates how quickly the moment of inertia changes for the truss. At approximately 4 seconds, the rotating frame has all but stopped acting on the structure. One would hope that the rotation would halt closer to the truss's fully deployed state, however that is not the case using this methodology. This methodology being used may have been grossly oversimplified, however the results gleaned from these simulations are still valuable and show how the model reacts to the applied centripetal acceleration, albeit only for the cells that are the first to deploy. The following subsections show how the deployment speeds of the simulations differ from the first uncontrolled simulation already detailed and will then show how the deployment speeds affected the lockout stress events. Both subsections will focus on Cells 3 and 4, as they were most affected by the centripetal acceleration.

Cell Deployment Speed.

As the frame rotates with the deploying truss in it, it would be reasonable to expect that the added centripetal force would pull the trusses out from their stowed position faster than if it had not been there. Upon analysis of the simulations, however, this is not really the case. Figure 102 shows only two distinct lines even though there are six sets a data present: the applied hinge moment for one of the top longerons of Cells 3 and 4 for the uncontrolled deployment, the deployment with an intial 5 degree per minute of rotation, and the deployment with an initial 60 degrees per minute of rotation. The presence of only two distinct lines means there was no difference between any of these simulations. This is most likely a result of the low density of the truss members, which are not affected too much by the applied centripetal acceleration. It should also be restated that the hinges contain a small amount of damping, which would keep the longerons from accelerating too quickly.

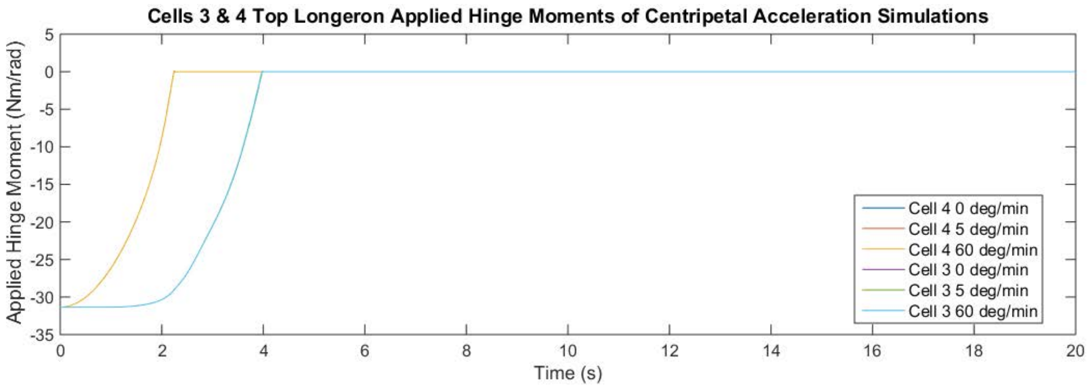

Figure 102. Select top longeron applied hinge moments in uncontrolled deployment simulations in rotating frames.

However, upon zooming into the graphs at the lockout event locations, some disparities in the data appear. Figure 103 is a cropped image of Figure 102 and shows the overshoot exhibited by the hinges in the rotating frame simulations. Although minimal, this kind of behavior at least validates that the rotating frame was indeed applied to the structure. If one were to look to Cell 3's results in this manner, the results are the same, albeit not as pronounced. These plots mean that although the hinges did not lock any faster, they did lock harder which means that more displacement in the locked longerons can be expected.

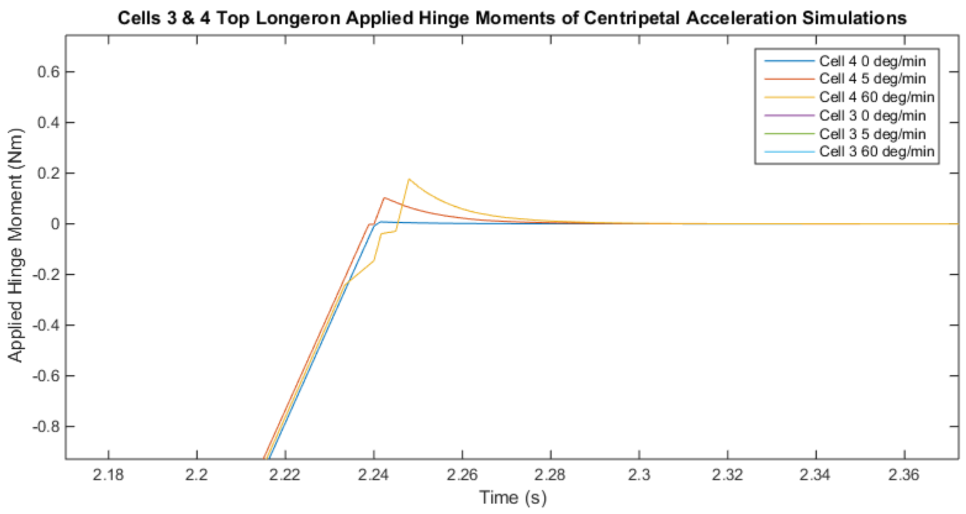

Figure 103. Select top longeron applied hinge moments in uncontrolled deployment simulations in rotating frames. (Cropped)

Cell Lockout Stress.

Increased displacement in the longeron-longeron hinges during the lockout event means increased displacement and stress in the members. Indeed, Figure 104 shows that the added centripetal acceleration from the rotating frame increases the stress sustained by the longerons during lockout. The highest stress is seen in the longerons from the faster rotating frame simulation. Not only is this stress higher, but even after the lockout event, the longerons exhibit some harmonic motion that was not present in the original non-rotating simulation. It seems as though the added force of the rotating frame is adding some kind of axial load to the extended longerons and is causing this extra motion. Although it should be said that such motion may be more indicative of the simplified geometry or the numerical solver tolerances, the fact remains that rotating the structure during deployment may result in some added motions.

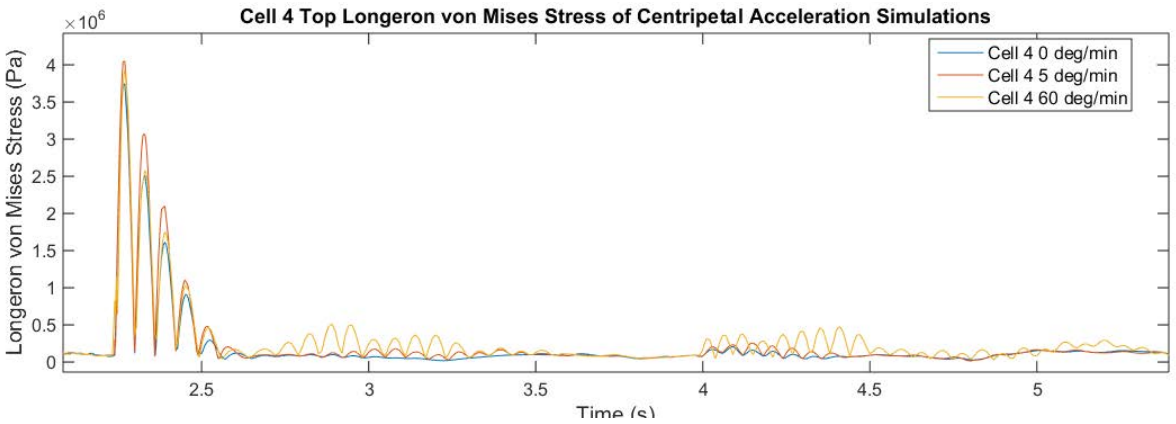

Figure 104. Cell 4 top longeron von Mises stress in different rotating frames. (Cropped)

Cell 3 exhibits the same harmonic disturbances as Cell 4, as seen in Figure 105, but the peak stress of the faster rotating frame simulation is more interesting. It appears as though the additional force applied to the completely deployed Cell 4 has pulled on Cell 3. This has created a much large peak stress than the other two simulations. This higher peak stress is even accompanied by a higher frequency response, which is generally not desirable in a structure such as this. Therefore, these results suggest that rotating the structure during the deployment does not seem to positively influence it at all.

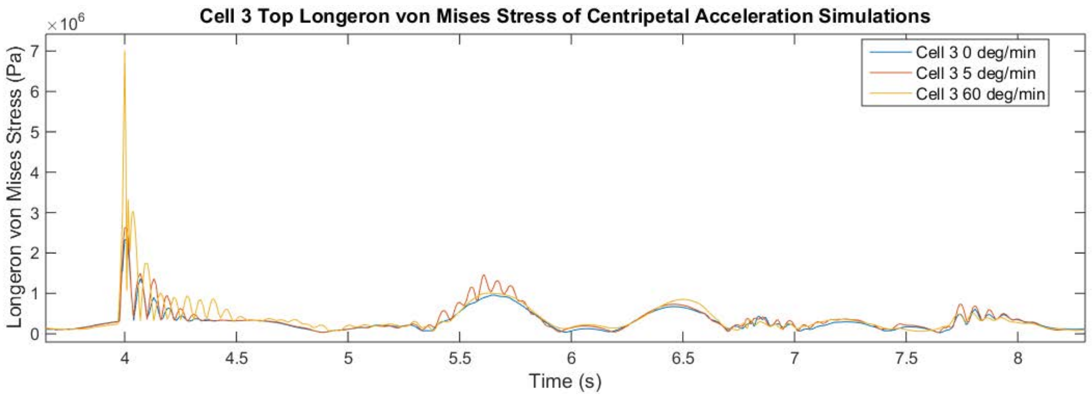

Figure 105. Cell 3 top longeron von Mises stress in different rotating frames. (Cropped)

From a larger perspective, the last two truss Cells 1 and 2 do not exhibit such notable increases seen in Cells 3 and 4. Most likely the damped hinges contained within Cells 1 and 2 were able to control the deployment so that the momentum from the first two deployments did not damage the structure. It should also be mentioned that the same Cell 3 bottom longeron initial miss occured as well, and that the remainder of the simulations emulated the non-rotating frame of the first. More importantly, comparison of the stress results in both cells reveals how the numerical solver may be sensitive enough to model the entirety of the stress behaviors in the longerons. Take Figure 105 for example. From 7.5 to 8 seconds, all three plots overlay onto each other. From 5.5 to 6 seconds, only the slower rotating frame exhibits any harmonic motion. These differences in results can most likely be directly attributed to the 10% tolerance factor imposed on the time steps in the solver settings. This setting allows the simulation to be run in a in a few hours on relatively low power computers and captures the global motion of the simulations quite well. Table 8 shows the deployment envelopes of these simulations.

Completed Deployment	**X**	**Y**	**Z**
Upper Bound (m)	4.4710	6.0679	37.9799
Lower Bound (m)	-4.4710	-2.6422	0
Uncontrolled Deployment	**X**	**Y**	**Z**
Upper Bound (m)	4.4430	9.7763	37.8630
Lower Bound (m)	-4.5435	-3.6698	0
5 Degrees per Minute Initial Rotation	**X**	**Y**	**Z**
Upper Bound (m)	4.4283	9.8037	37.8550
Lower Bound (m)	-4.5370	-3.6490	0
60 Degrees per Minute Initial Rotation	**X**	**Y**	**Z**
Upper Bound (m)	4.4850	9.9063	37.8430
Lower Bound (m)	-4.4801	-3.6472	0

Table 8. Various Deployment Simulation Deployment Envelope

4.4 Weakened Hinges

Manufacturing defects are a fact of life when it comes to fabricating engineering designs. The space industry spends a great deal of money on flight-ready hardware to reduce the chances of any individual part failing. As has happened many times in the past, however, if something can fail, it will fail. Therefore the purpose of this section is to explore the deploying truss structures susceptibility to manufacturing defects. In total, eight simulations were run. Each simulation places a "weak hinge" in the top or bottom of each cell. Here, "weak" means a longeron-longeron hinge that only applies 80% of its intended torque[4]. It was thought that since these hinges are what motivates the structure to deploy, that if one were to be outside manufacturing specifications, that they may compromise the deployment of the structure. From anecdotal evidence gleaned from creating these simulations, if one of these hinges applies no moment whatsoever, then that cell will fail to deploy all together. All other hinges in the structure are much simpler than these longeron-longeron hinges, and will reach steady state via the shaping cables that dictate the truss arm's final shape. Instead of showing the results from each individual simulation, this section will only discuss how the simulation with the particular defect differed from the nominal deployment shown in Section 4.2. Concluding this section will be some general remarks on the observed behavior of the structure in response to these manufacturing defects. A table of the deployment envelopes for each simulation will also be included at the end.

Weak Hinge in an Upper Longeron of Cell 1.

With a weak hinge present on the negative X positive Y longeron of the base Cell 1, the truss was able to fully deploy. However, the structure had some trouble coping

[4]80% was chosen somewhat arbitrarily and represents a value at which a single truss simulation would just barely achieve its lockout state in multiple observed attempts.

with the hinge moment deficit. Figure IV.106(a) shows the weak hinge in place in Cell 1. Figures IV.106(a) through IV.106(d) show that the bottom longerons of Cells 2-4 failed to deploy on their first attempt. Meanwhile, all of the top longerons in the entire structure were able to deploy quite easily. It is also interesting that the bottom longerons of Cell 4 were the last to deploy in the simulation. The exact cause for this behavior is not very well known, and may only reveal itself through further analysis of the following simulations. Although not included in this work, the stresses and cable forces of the deploying structure remain largely the same for this deployment simulation.

Weak Hinge in a Lower Longeron of Cell 1.

The weak c1.nxny.lglg hinge impeded the structure from fully deploying in this scenario. Again, it is only the lower longerons that have issues when a weak hinge is introduced in Cell 1. It is slightly counter-intuitive to think that a weaker lower hinge in Cell 1 would keep Cell 4's lower hinges to deploy. The weak hinge should allow for less push back on Cell 4's lower longerons, enabling them to deploy easier. However, the weak hinge may be affecting the geometry throughout the simulation and may be less conducive to a lower longeron lockout event. Indeed, Table 9[5] shows that the deployment envelopes for both Cell 1 weak hinge deployments causes more vertical, positive Y motion than the original uncontrolled deployment. Figure 108 shows the truss at the end of the simulation. Note that these weak hinge simulations were run up to 25 seconds to capture more of the post-deployment, transient motions of the structure. The stress and cable forces were once again on par with that of the uncontrolled simulation, and did not show any significant increase.

[5]This table is shown in the final subsection of this section.

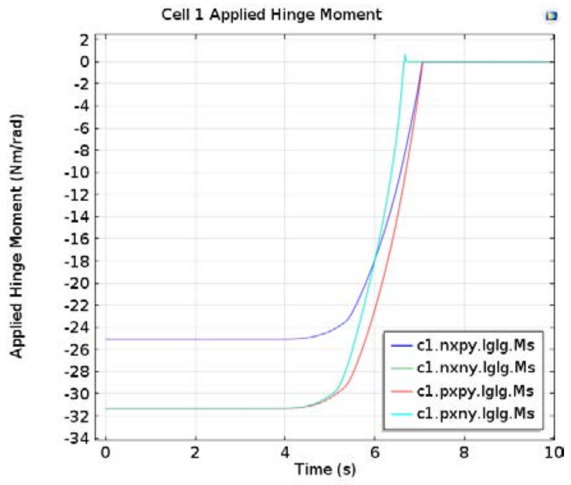

(a) Cell 1 applied hinge moment. (Cropped)

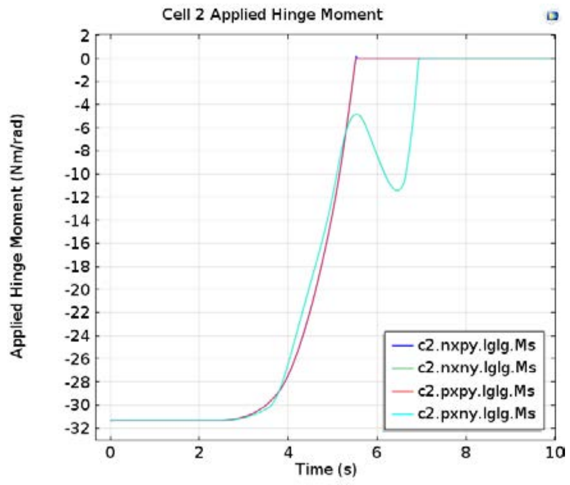

(b) Cell 2 applied hinge moment. (Cropped)

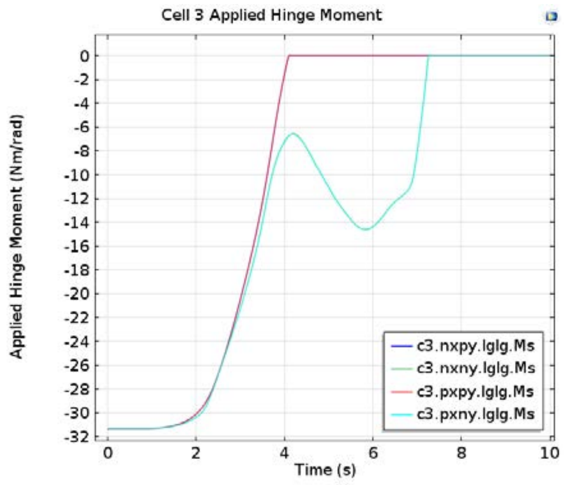

(c) Cell 3 applied hinge moment. (Cropped)

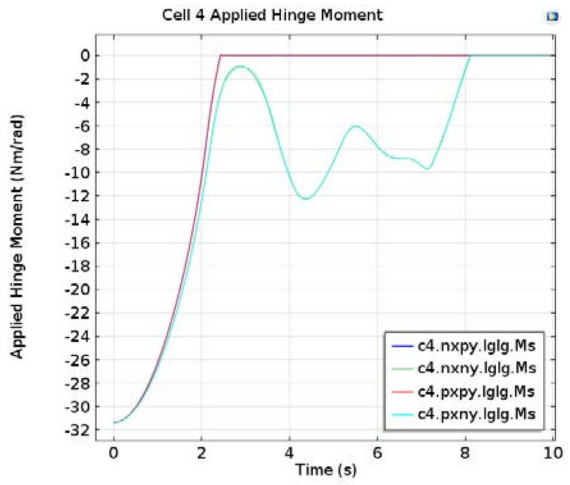

(d) Cell 4 applied hinge moment. (Cropped)

Figure 106. Applied hinge moments of uncontrolled deployment with hinge c1.nxpy.lglg set to 80%.

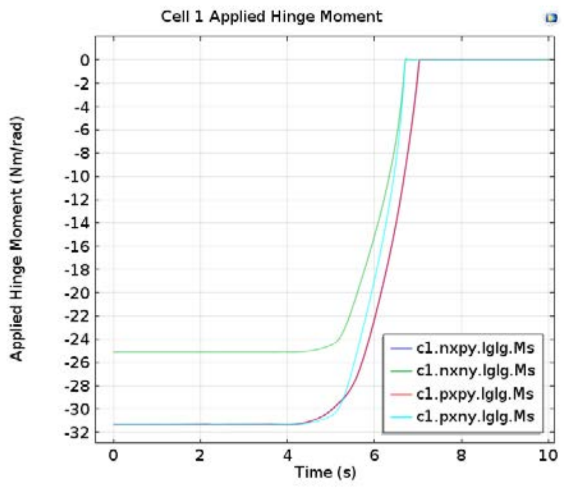

(a) Cell 1 applied hinge moment. (Cropped)

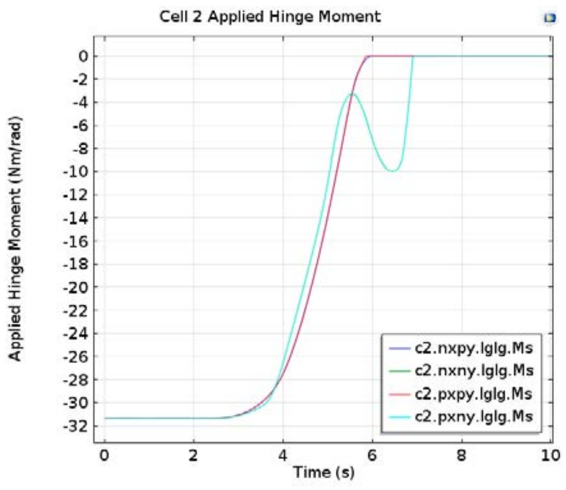

(b) Cell 2 applied hinge moment. (Cropped)

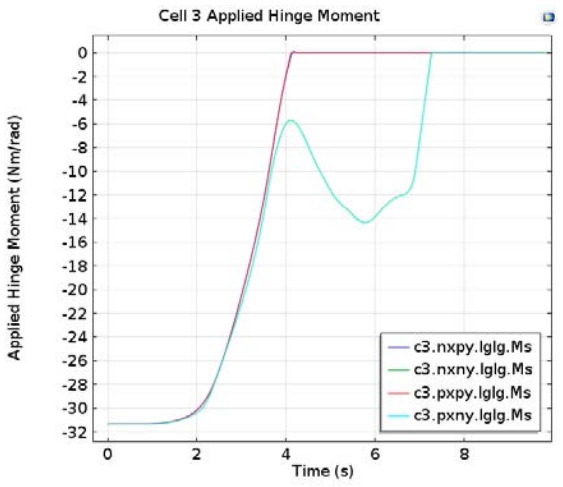

(c) Cell 3 applied hinge moment. (Cropped)

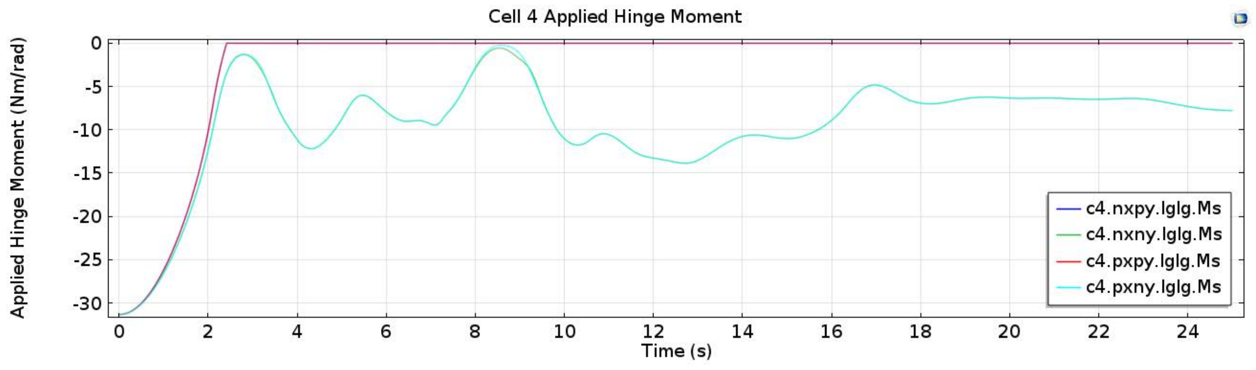

(d) Cell 4 applied hinge moment.

Figure 107. Applied hinge moments of uncontrolled deployment with hinge c1.nxny.lglg set to 80%.

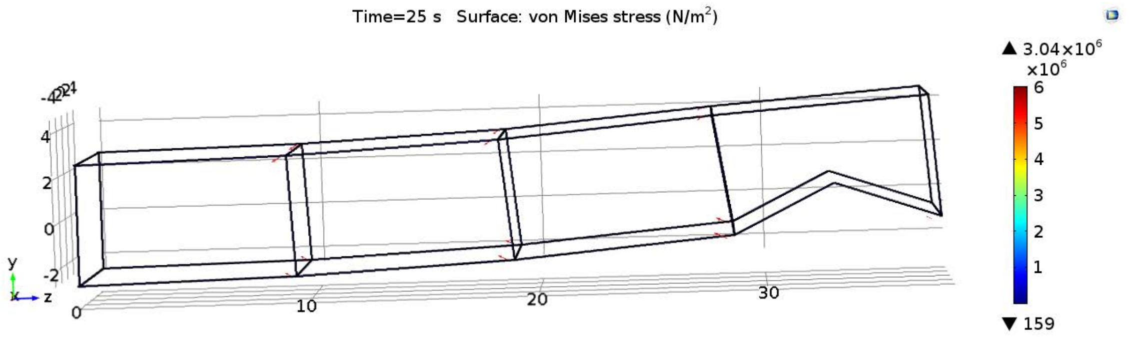

Figure 108. Incomplete truss deployment at final simulation time with weak lower longeron-longeron hinge in Cell 1 (c1.nxny.lglg).

Weak Hinge in an Upper Longeron of Cell 2.

The weak top hinge (c2.nxpy.lglg) kept the truss structure from fully deploying. Figure 109(a) shows the hinge moments for Cell 1, which progress similarly to the original uncontrolled deployment simulation. Figure 109(b) shows that Cell 2 does not have a failed attempt at deploying, but rather is delayed thanks to the weaker hinge. Although one weak hinge makes the cells asymmetric in their initial behavior, they eventually converge back to symmetry as the cell finalizes its deployment. Cell 3 again has some trouble deploying, but is not as bad as Cell 4, which failed to deploy throughout the simulation. It looks as though Cell 4 will not ever fully extend in this deployment mode as applied hinge moments are trending towards a horizontal line. Perhaps Cell 4 would eventually lockout if the structure was given enough time to stop moving altogether. Again, the likely culprit in this incomplete deployment is the more vertical motion caused by the weak hinge, as shown in Table 9. The stress and cable forces showed no significant changes that would affect the deployment.

Weak Hinge in a Lower Longeron of Cell 2.

Creating a weak hinge in c2.nxny.lglg affected the deployment of the truss arm quite dramatically. Figure 111 illustrates how poorly this deployment went. First off, the top longerons never fully extended. The shape of the geometry around 7

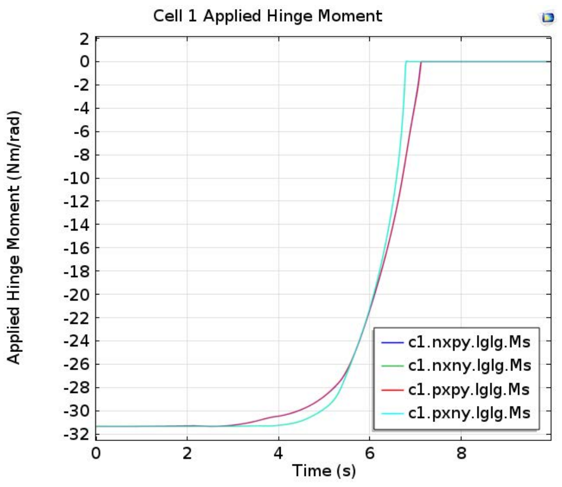

(a) Cell 1 applied hinge moment. (Cropped)

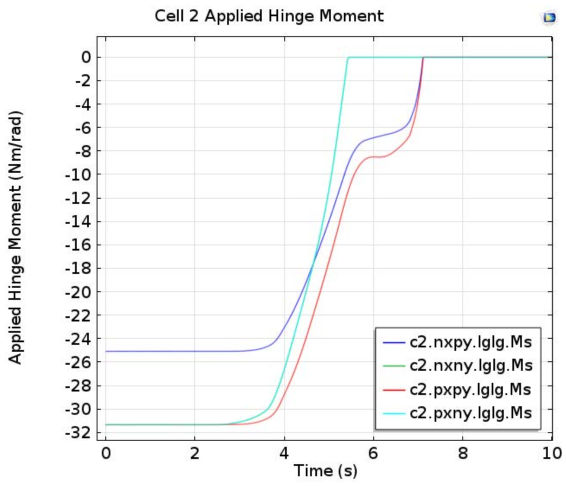

(b) Cell 2 applied hinge moment. (Cropped)

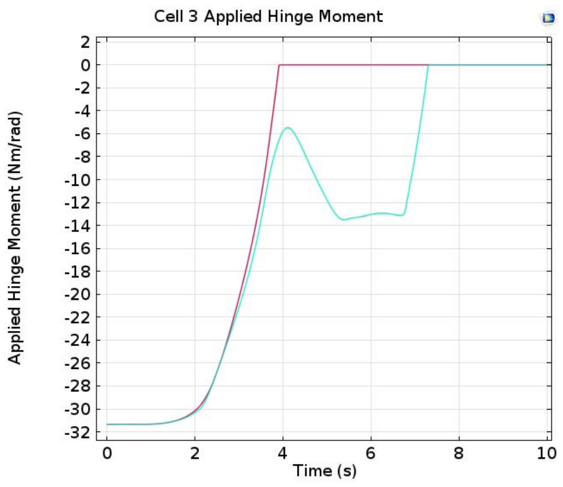

(c) Cell 3 applied hinge moment. (Cropped)

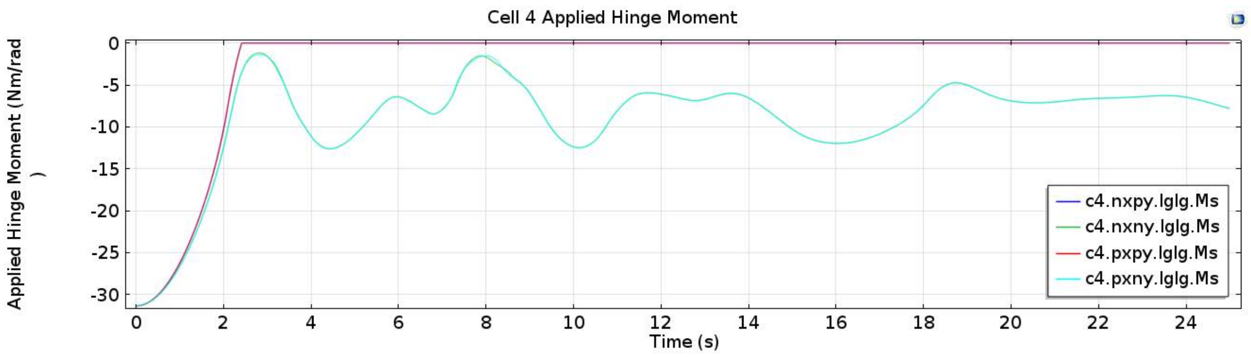

(d) Cell 4 applied hinge moment.

Figure 109. Applied hinge moments of uncontrolled deployment with hinge c2.nxpy.lglg set to 80%.

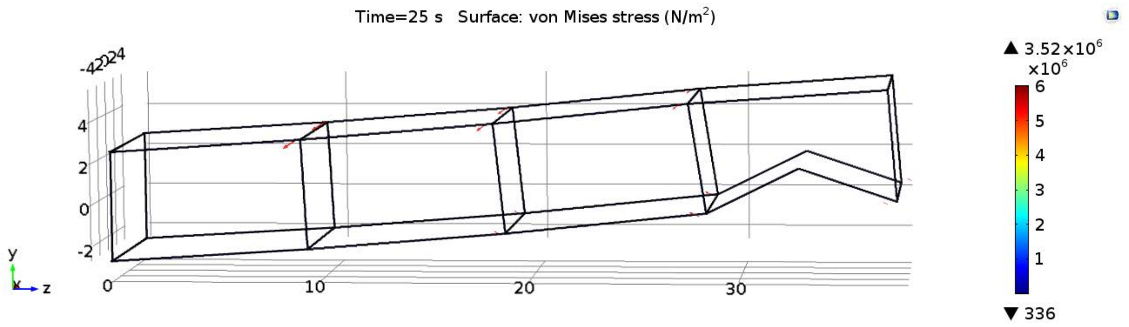

Figure 110. Incomplete truss deployment at final simulation time with weak c2.nxpy.lglg hinge.

seconds caused a large spike in the shaping cable forces (Figure 112) that oppose the top longerons in Cell 1 (Figure 113). This spike in addition to the upward momentum of the deploying truss causes the entire structure to swing upwards. The upward momentum was most likely caused by the incomplete deployment of all of the cells occuring almost simultaneously approximately one second before Cell 1's top longerons deployment failure. It is also interesting to note that the weak bottom hinge on the negative X face of the trusses translates to Cell 4, whose "nxny" never deployed throughout the simulation. This phenomena is quite strange as Figure 114 shows that this hinge did indeed reach its lockout rotation. Perhaps the default locking hinge settings within COMSOL were not strict enough to keep the hinge closed, or the solver tolerances were not close enough to catch the lockout. Once again, the stresses experienced by the structure were within normal ranges. Table 9 shows just how much vertical travel the truss underwent during this simulation.

Weak Hinge in an Upper Longeron of Cell 3.

In contrast to the previous two simulations, creating a weak hinge in the top of Cell 3 had very little effect on the deployment. Figures 115(a) through 115(d) show that there was little change in the deployment of the truss compared to the uncontrolled dpeloyment. Notably, the bottom longerons of Cell 4 were once again delayed in its

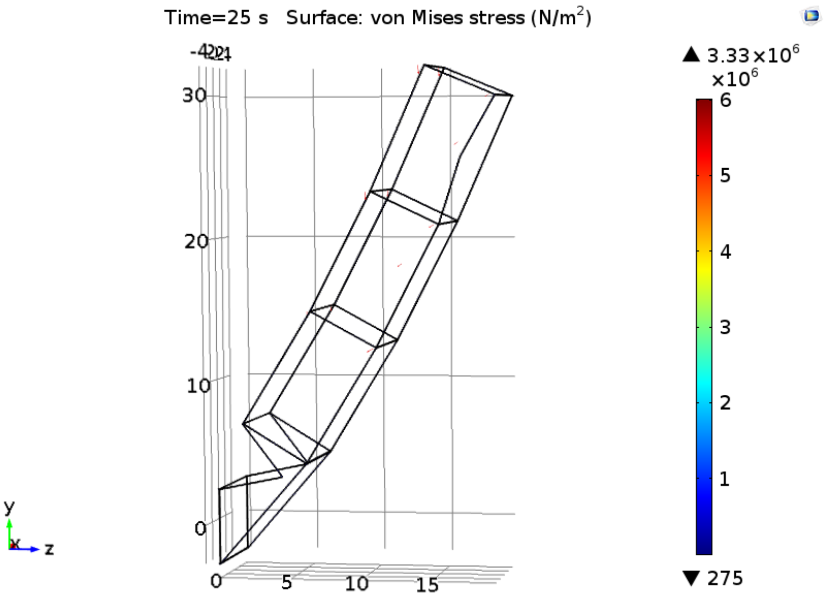

Figure 111. Incomplete truss deployment at final simulation time with weak c2.nxny.lglg hinge.

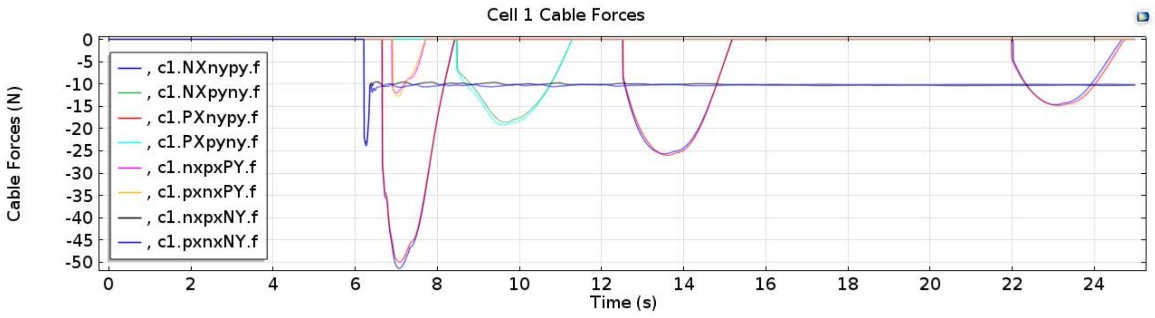

Figure 112. Cable forces of Cell 1 in c2.nxny.lglg weak hinge simulation.

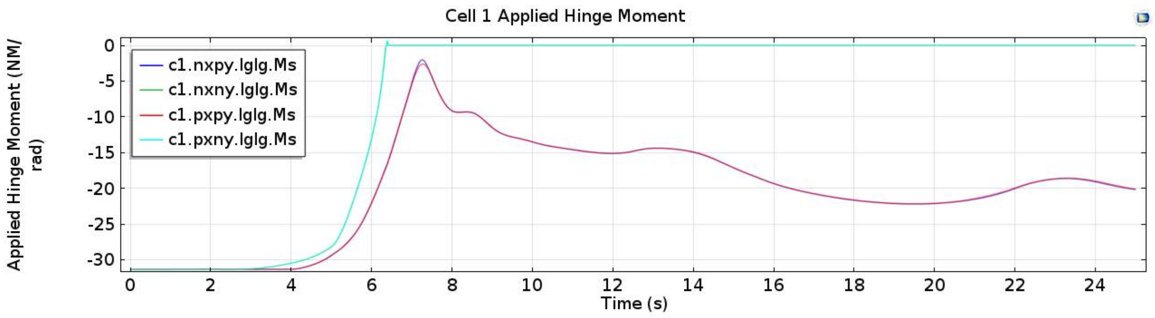

Figure 113. Applied hinge moments of Cell 1 in c2.nxny.lglg weak hinge simulation.

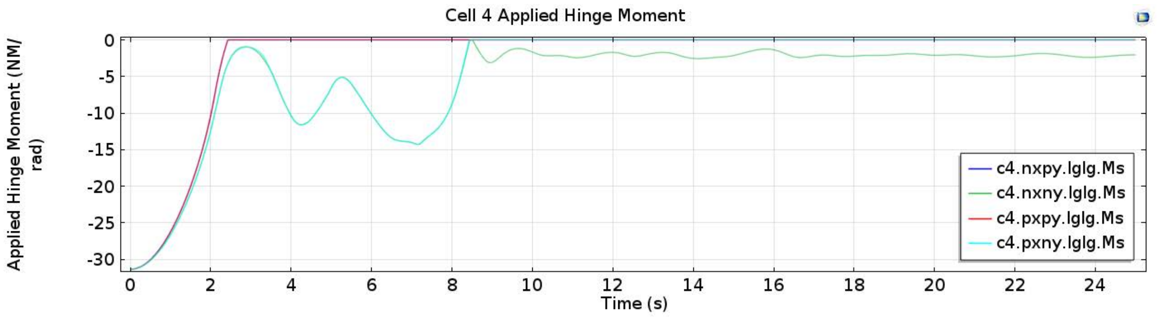

Figure 114. Applied hinge moments of Cell 4 in c2.nxny.lglg weak hinge simulation.

deployment, but were able to lockout around 9 seconds into the simulation. Figure 115(c) shows that the stronger of the two hinges will cause the weaker hinge lockout at the same time as the stronger. There is some delay in Figure 115(b) for Cell 2 to deploy, however it eventually does. The most interesting aspect of this simulation is that the weaker hinge in Cell 3 allows it to deploy on its first attempt, which does not happen with the stock settings in the uncontrolled deployment. This comes at a cost of Cell 4 being delayed to deploy, but may lead to some thoughts on varying the spring stiffnesses throughout the truss to create smoother deployments in the future. There were not any notable changes in the stresses or cable forces of this simulation.

Weak Hinge in a Lower Longeron of Cell 3.

The weak c3.nxny.lglg hinge did not have a great effect on the truss deployment. If anything, the weaker hinge pronounced Cell 3's problems with its lower longerons seen in the uncontrolled deployment, as seen in Figure 116(c). Other than this, there was nothing remarkable about this simulation. The stresses, cable forces, and deployment envelope showed no signs of any significant behavior.

Weak Hinge in an Upper Longeron of Cell 4.

A weaker hinge in an upper longeron of Cell 4 does not affect the deployment of the structure significantly. The lower longerons of Cells 2 and 3 were both delayed

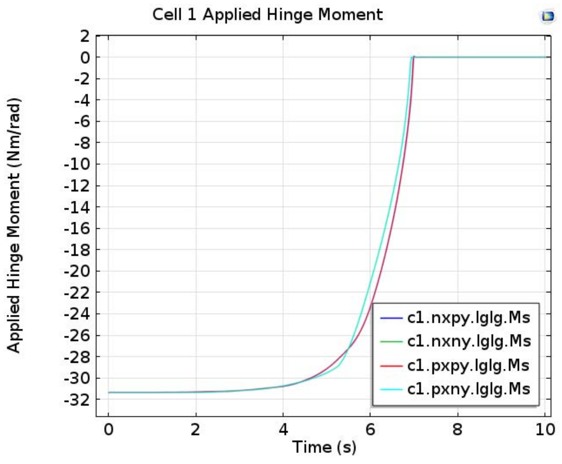

(a) Cell 1 applied hinge moment. (Cropped)

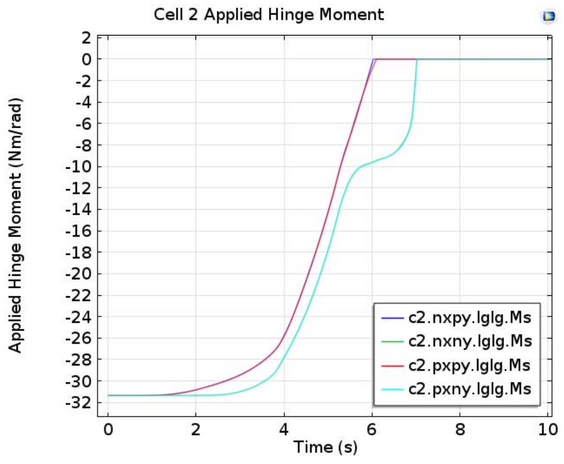

(b) Cell 2 applied hinge moment. (Cropped)

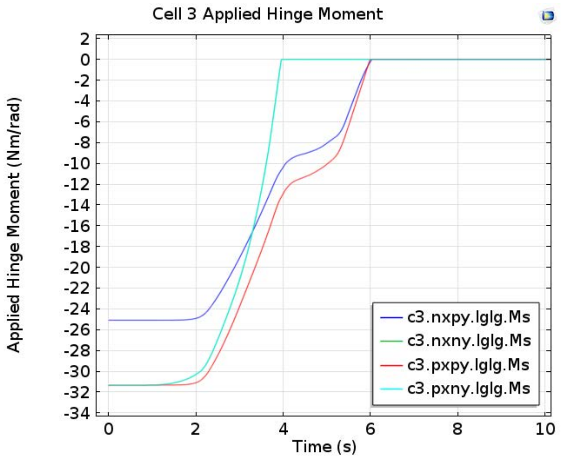

(c) Cell 3 applied hinge moment. (Cropped)

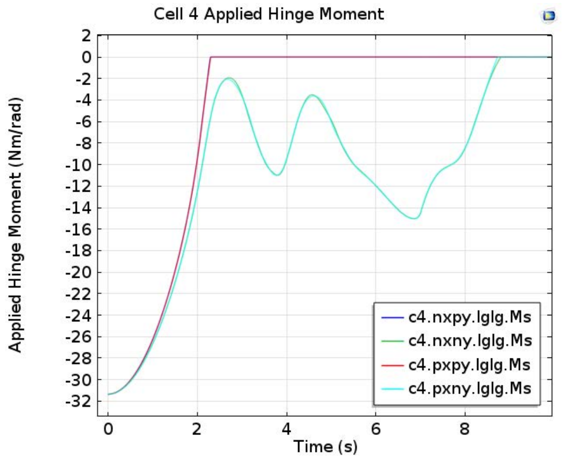

(d) Cell 4 applied hinge moment. (Cropped)

Figure 115. Applied hinge moments of uncontrolled deployment with hinge c3.nxpy.lglg set to 80%.

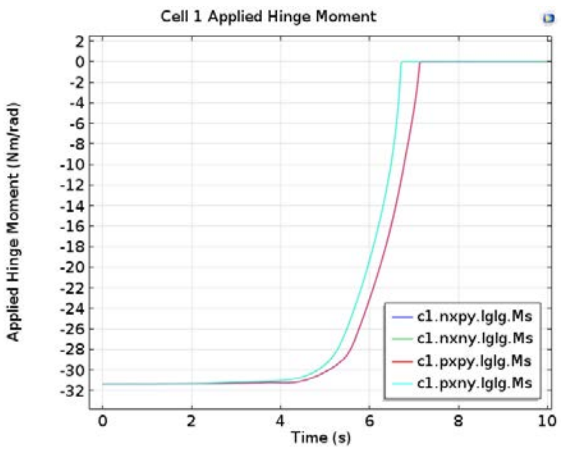

(a) Cell 1 applied hinge moment. (Cropped)

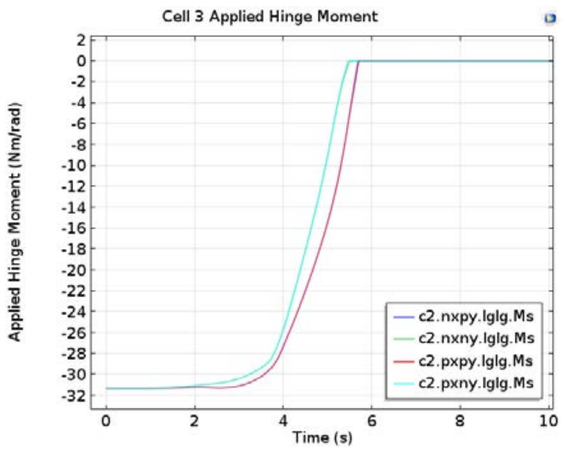

(b) Cell 2 applied hinge moment. (Cropped)

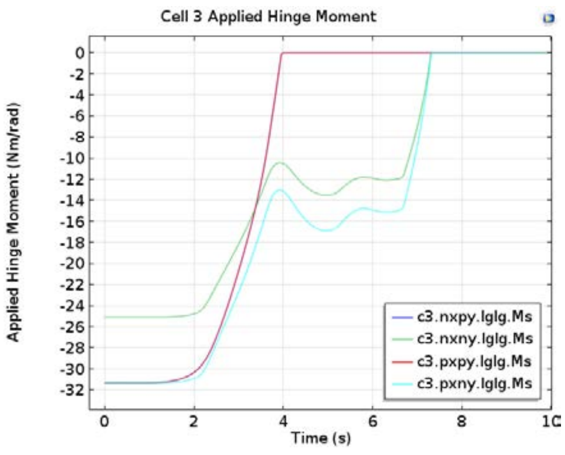

(c) Cell 3 applied hinge moment. (Cropped)

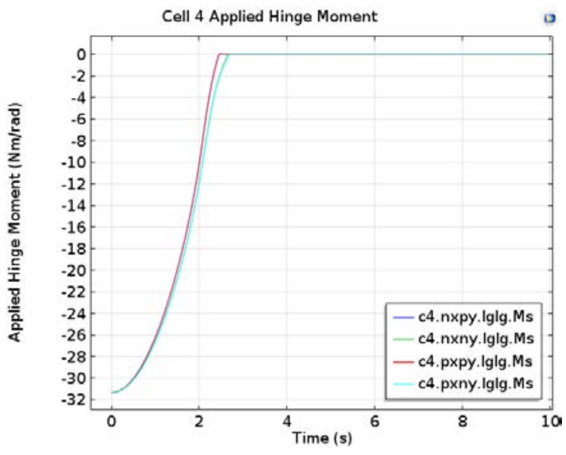

(d) Cell 4 applied hinge moment. (Cropped)

Figure 116. Applied hinge moments of uncontrolled deployment with hinge c3.nxny.lglg set to 80%.

in their deployment. Although Cell 3 is usually always delayed, as seen in the first uncontrolled deployment, Cell 2 is delayed by the geometry created by Cell 4. In Cell 4, the top longerons take approximately 5.5 seconds to fully extend due to the weaker hinge. It appears as though the stronger hinge takes some time to match the rotation of the weaker in order to fully deploy. Cell 1, as usual, is unaffected by a change so far away from itself. The stress and cable forces show very little difference compared to the uncontrolled simulation and the deployment envelope is unremarkable.

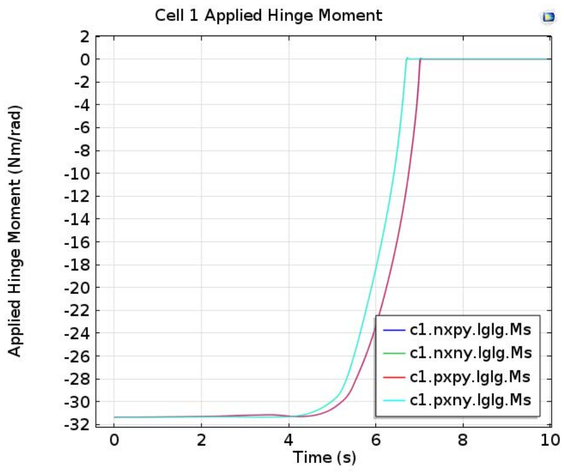

(a) Cell 1 applied hinge moment. (Cropped)

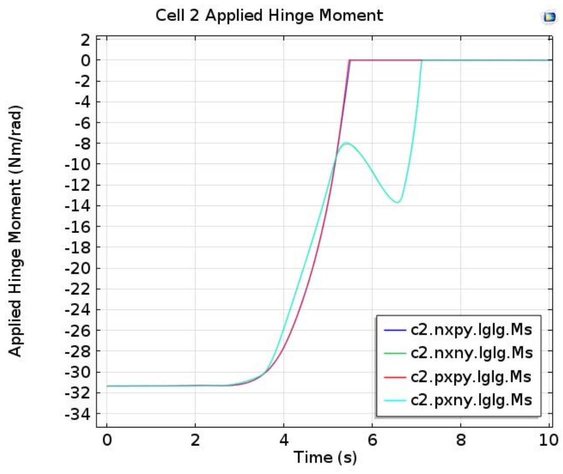

(b) Cell 2 applied hinge moment. (Cropped)

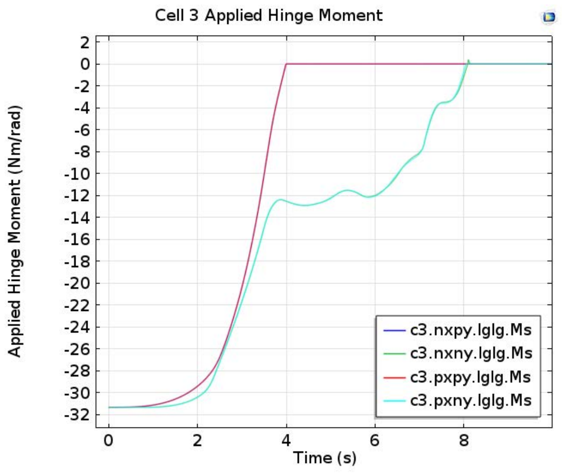

(c) Cell 3 applied hinge moment. (Cropped)

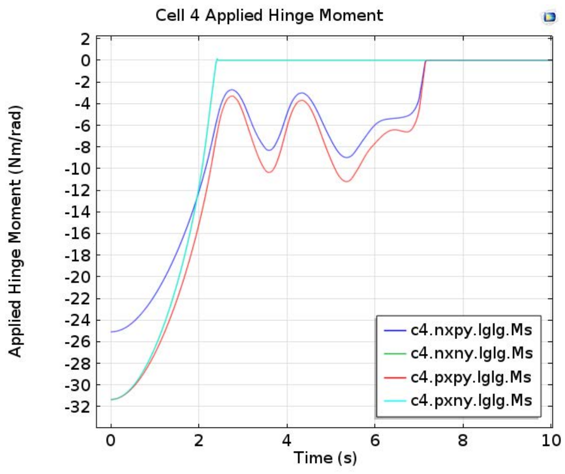

(d) Cell 4 applied hinge moment. (Cropped)

Figure 117. Applied hinge moments of uncontrolled deployment with hinge c4.nxpy.lglg set to 80%.

Weak Hinge in a Lower Longeron of Cell 4.

Once again a weak hinge in a lower longeron causes the truss arm to fail to deploy. Unlike the previous examples, however, the bottom longerons of Cell 4 fail to deploy thanks to the weaker hinge in one of the longerons. Other than this failure, the rest of the truss structure behaves as expected. Cells 1 and 2 deploy without any hesitation, and Cell 3 fails its first attempt. It appears as though the added mass of Cell 4 itself on the end of the truss arm does very little to affect the rest of the truss's deployment. The stresses and cable forces were once again wholly unremarkable.

Observations and Remarks.

Figure 120 shows a side view of the truss arm in its deployed state for each of the weak hinge deployment simulations. The weak hinges are shown as dashed lines, and the deployment time for each longeron pair is represented through the thickness of the line. The longer the time to deploy, the thicker the line. For example, if the longeron-longeron hinge regresses, then the time it takes to recover and fully extend is four seconds, then the line thickness is scaled by four times. If a longeron is not present in the Figure, then the longeron failed to deploy within the simulation time. For further clarification, the failed deployments are in red and the successful deployments are shown in blue. Table 9 complements Figure 120 and displays the deployment envelopes for all of the simulations discussed in this section.

The results are far from conclusive, but it might be said that the successful deployment of the truss is more dependent on the lower longerons. The lower longerons do not deploy as well as the upper longerons because they are longer yet have the same spring-hinge moment applied to them. This decreases the lower longerons' relative mechanical advantage and increases their deployment time. The increased lower longeron deployment time is further reduced by the shaping cables which activate

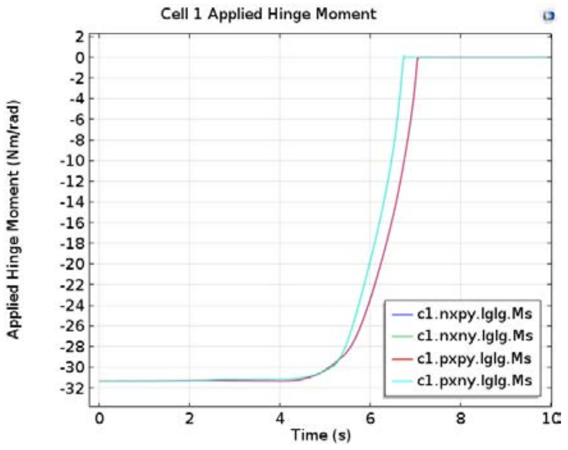

(a) Cell 1 applied hinge moment. (Cropped)

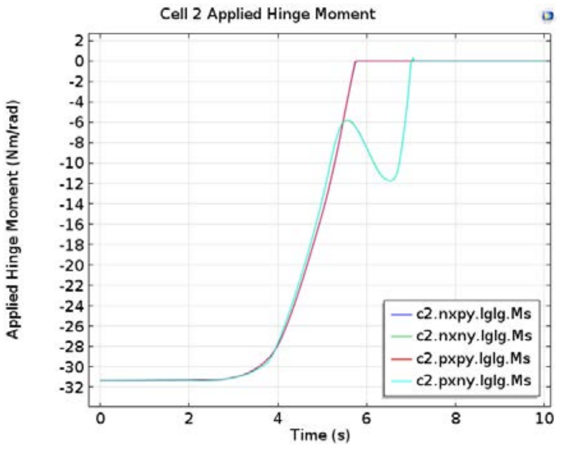

(b) Cell 2 applied hinge moment. (Cropped)

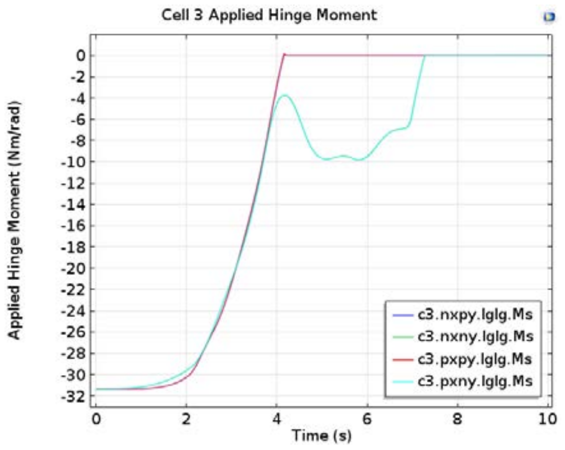

(c) Cell 3 applied hinge moment. (Cropped)

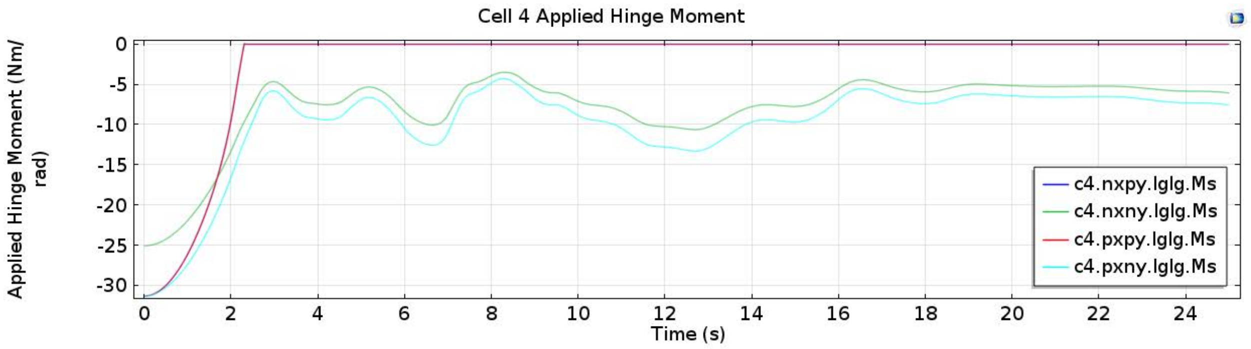

(d) Cell 4 applied hinge moment.

Figure 118. Applied hinge moments of uncontrolled deployment with hinge c4.nxny.lglg set to 80%.

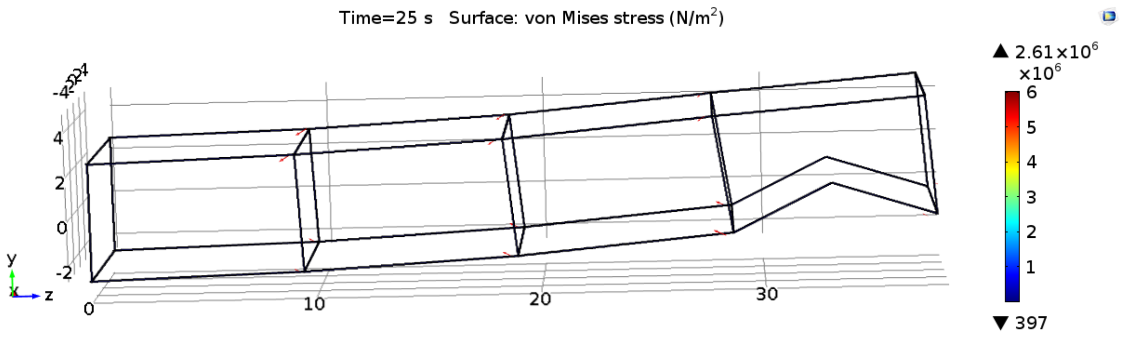

Figure 119. Incomplete truss deployment at final simulation time with weak c4.nxny.lglg hinge.

once the upper longerons deploy. They also create a vertically-moving geometry that impedes their own deployment as they move. Overall, the lower longerons may require an adjustment in parameters to increase their chance of successful lockout.

Weak hinges in Cell 2 proved to be fatal for the deployment of the truss arm, especially when a lower longeron contained the weak hinge. Most times, the failed deployment was caused by the lower longerons of Cell 4. Cell 4 does not have any added momentum from other cells connected to its positive Z face to pull it open. Additionally, the residual swaying of the truss arms triggers the shaping cables in Cell 4 and further impedes its lower longerons from locking out.

Many more conjectures can be made from this Section, but the main takeaway should be that COMSOL successfully solved all of these asymmetric simulations. It should be mentioned that setting up the different scenarios is very easy, requiring only the weak hinge's moment to be multiplied by 80%. Furthermore, the solver does not need to be adjusted in these instances. The only caveat, as mentioned in Section 4.3, is that the simulations here only represent the larger global motion of the deploying truss. This is not a problem for the work here, which seeks to merely model the truss's deployment, but deeper analysis into the truss's sensitivity to perturbations would require a more strict time stepping protocol.

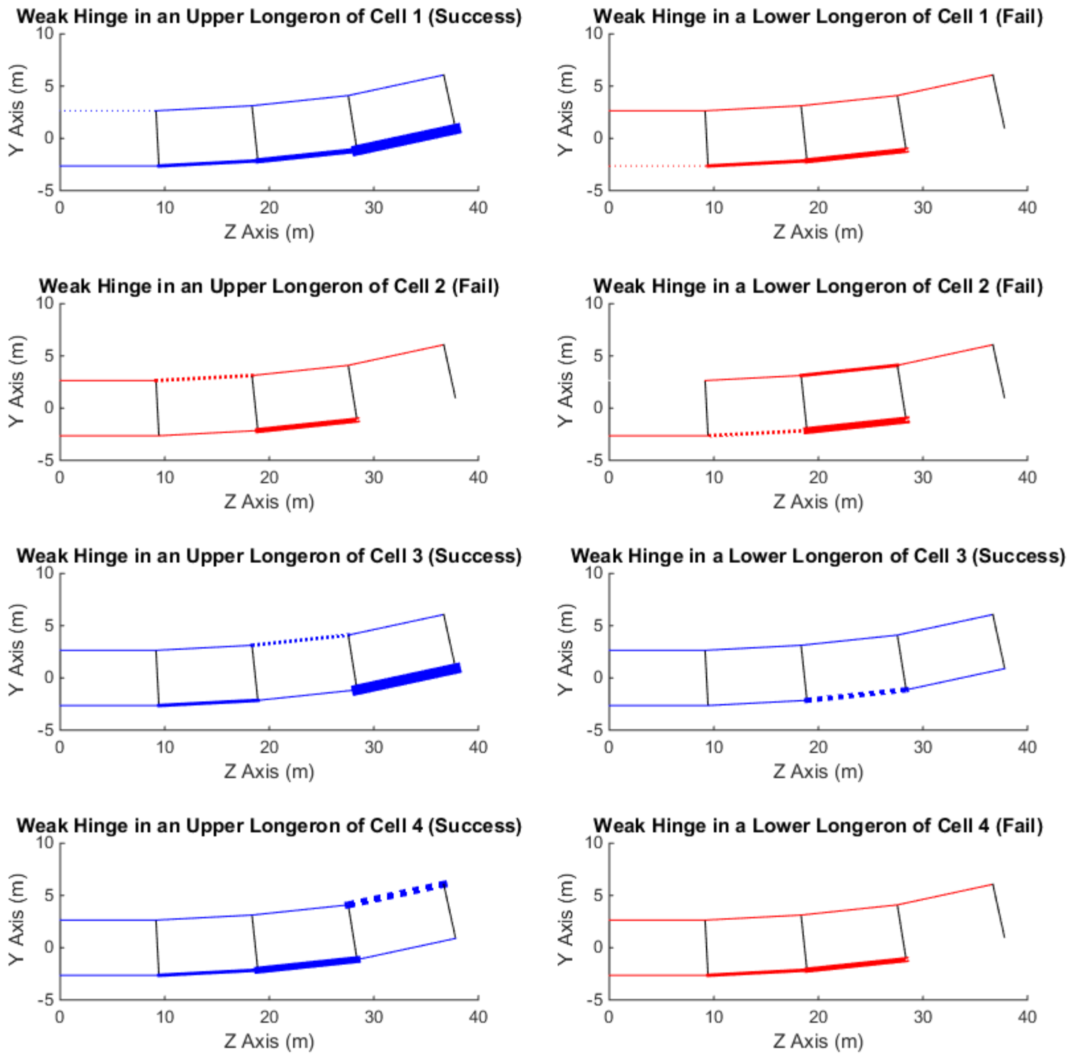

Figure 120. Weakened hinges study summary.

Completed Deployment	**X**	**Y**	**Z**	**Uncontrolled Deployment**	**X**	**Y**	**Z**
Upper Bound (m)	4.4710	6.0679	37.9799	Upper Bound (m)	4.4430	9.7763	37.8630
Lower Bound (m)	-4.4710	-2.6422	0	Lower Bound (m)	-4.5435	-3.6698	0
Weak c1.nxpy.lglg Hinge	**X**	**Y**	**Z**	**Weak c1.nxny.lglg Hinge**	**X**	**Y**	**Z**
Upper Bound (m)	4.4221	11.4660	37.8360	Upper Bound (m)	4.4088	11.5768	37.3200
Lower Bound (m)	-4.5671	-2.8143	0	Lower Bound (m)	-4.5898	-2.8442	0
Weak c2.nxpy.lglg Hinge	**X**	**Y**	**Z**	**Weak c2.nxny.lglg Hinge**	**X**	**Y**	**Z**
Upper Bound (m)	4.4157	10.0887	37.3610	Upper Bound (m)	4.4850	32.5646	36.5340
Lower Bound (m)	-4.5447	-2.7412	0	Lower Bound (m)	-4.5216	-3.3617	0
Weak c3.nxpy.lglg Hinge	**X**	**Y**	**Z**	**Weak c3.nxny.lglg Hinge**	**X**	**Y**	**Z**
Upper Bound (m)	4.4225	9.4141	37.7630	Upper Bound (m)	4.553	11.6904	37.8410
Lower Bound (m)	-4.5197	-3.6866	0	Lower Bound (m)	-4.5239	-4.5239	0
Weak c4.nxpy.lglg Hinge	**X**	**Y**	**Z**	**Weak c4.nxny.lglg Hinge**	**X**	**Y**	**Z**
Upper Bound (m)	4.4554	8.9432	37.7080	Upper Bound (m)	4.4306	11.1625	37.3080
Lower Bound (m)	-4.4677	-2.8025	0	Lower Bound (m)	-4.5682	-2.7809	0

Table 9. Uncontrolled and weak hinge deployment simulation deployment envelopes

4.5 Controlled Deployments

Controlled deployments, in this context, describes a deployment in which the motivating longeron-longeron spring hinges apply their moment only when the previous cell is fully deployed. Therefore, instead of the entire truss arm attempting to move radially all at once, each cell takes its turn to deploy. It is thought that by timing the release of each cell, the displacements sustained by the structural members and the deployment envelope would both be reduced. Two different models were created to test the controlled deployments. One model was set to deploy Cell 4 first, then move to Cells 3, 2 and then 1. This is how the as-designed truss is supposed to open. Another model was set to deploy Cell 1 first at the root of the arm, then deploy Cells 2, 3, and then 4. Modeling these controlled deployments turned out to be more difficult than first anticipated. Initially, it was thought to merely turn on the spring-hinges from an "off" position at different times throughout the model. Unfortunately, early attempts showed that completely disabling the spring-hinges near the base of the truss arm caused some unintended consequences. In the case of the end-to-root deployment, the bumper blocks between the batten squares would contact each other quite a lot. This caused the solver to seek very small time steps for extended periods of time to solve for the forces applied to the blocks. Additionally, the constant back and forth motion sustained by the longerons meant that they would begin to rotate in different directions due to the way in which the geometry was modeled. Figure IV.121(a) shows how the longerons would begin to rotate, and Figure IV.121(b) shows how the geometry shifts when the longerons move in this manner. Attempts to constrain the motions of the "frlg" and "lgfr" hinges did not alleviate this behavior. When the simulation was allowed to keep running with this awkward longeron placement, the deployment would fail rather spectacularly (Figures IV.122(a) and IV.122(b)).

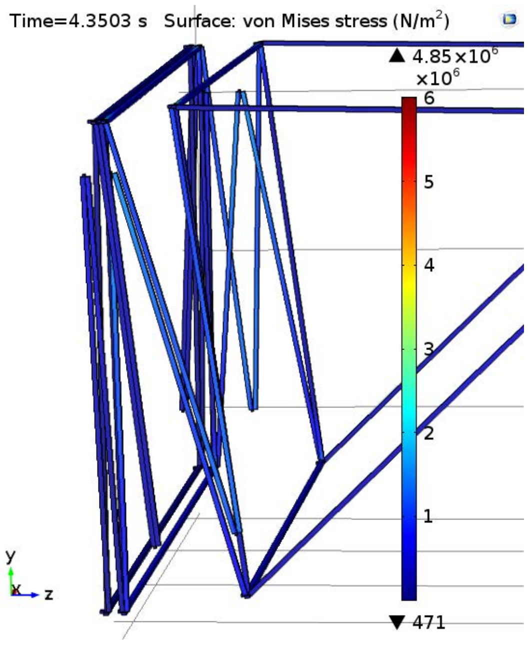

(a) Cell 1 longerons rotating at their connections to the batten frames.

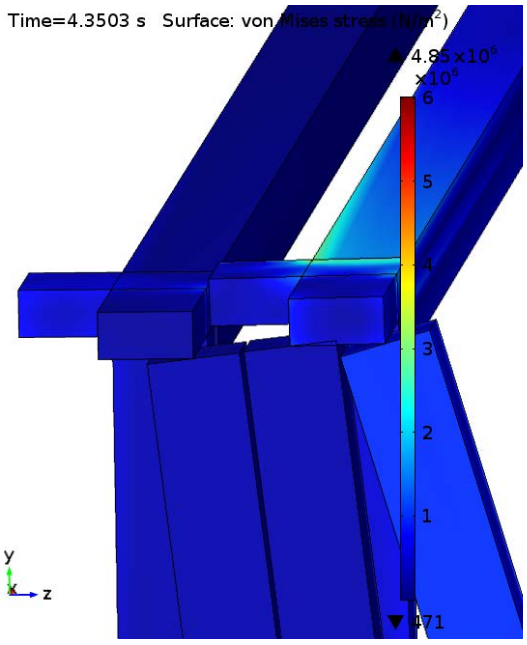

(b) Close up of Cell 0 and Cell 1 bumper blocks misaligning.

Figure 121. Examples of unwanted motion when longeron-longeron hinges are disabled.

To rectify this behavior, the hinges spring constants are halved, and then allowed their full spring stiffness when it is their turn to deploy. The deployment of each individual cell is triggered by a time delay function, which also integrates a smoothing function to apply the moment gradually. Figure 123 show how the hinge moments are applied throughout the simulation. For the end-to-root deployment at time zero, the "Initial Hinge Moment Curve" is applied to all of the Cells. Also at this time,

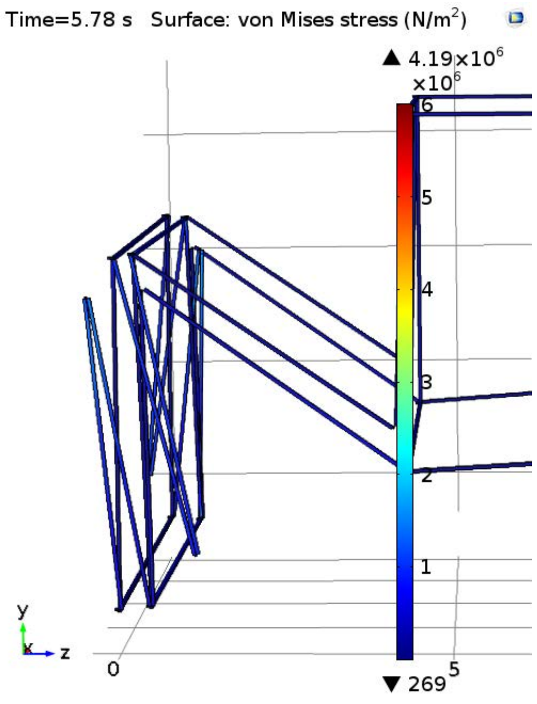

(a) Cell 1 longerons rotating at awkward angles.

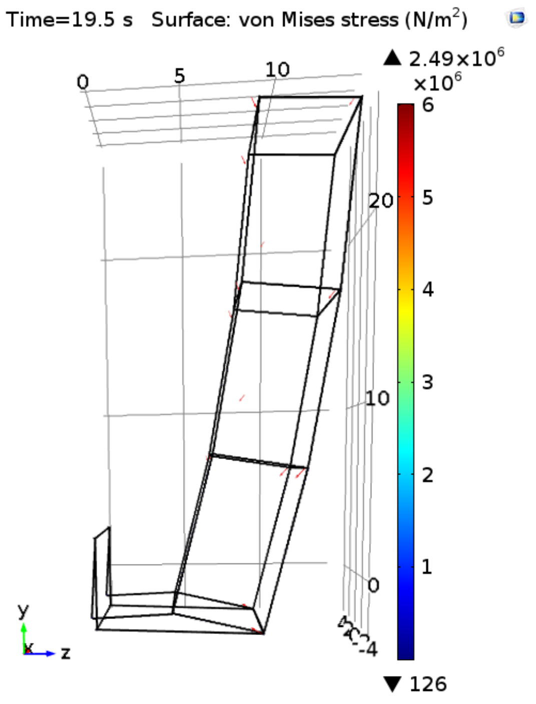

(b) Deployment status near the end of the simulation.

Figure 122. Unwanted motion propagating through simulation.

Cell 4's moment curve is applied. Then throughout the simulation at different times, the extra 50% of the spring stiffness constant is added to each cell. At four seconds, Cell 3's moment curve is added to the initial 50% from the beginning. For Cells 2 and then 1, this addition occurs at 8.5 seconds and 15 seconds respectively. Conversely, the root-to-end deployment applies the additional curves in the opposite order. It is important to note that these simulations have a higher base spring constants for the longeron-longeron hinges. It was found that when the original spring constant of 10 Newton-meters/radian was used with this scheme, that half was not sufficient to keep the longerons from rotating about their frame connection points. Also note the smoothing applied to the moment curves. The smoothing was built-in to prevent any shock loading on the structure during its deployment, which may have resulted in undesirable behavior. Everything else in these simulations is setup identically to the preceding simulations. The following subsections will describe the deployment characteristics of each controlled simulation, and will then compare the results to the uncontrolled simulation presented first in this chapter.

End-to-Root.

Figure 124 shows Cell 1 before it deploys, and Figure 125 shows Cell 1 directly after both upper and lower longerons complete their lockouts. It is early in this deployment, but so far the truss looks almost to identical to the uncontrolled deployment 46. The sameness even extends to Cell 3, which is beginning to deploy at this point. It seems as though the halved hinge moments are enough to move Cell 3 outwards.

Figure 126 shows Cell 3 as it is about to lockout. Notice here that some red arrows are visible already in Cell 3, and indicates that Cell 3 will have the same deployment issues as in the uncontrolled simulation. Figure 127 all but confirms this indication. The uneven upper and lower longerons again create a geometry that moves vertically

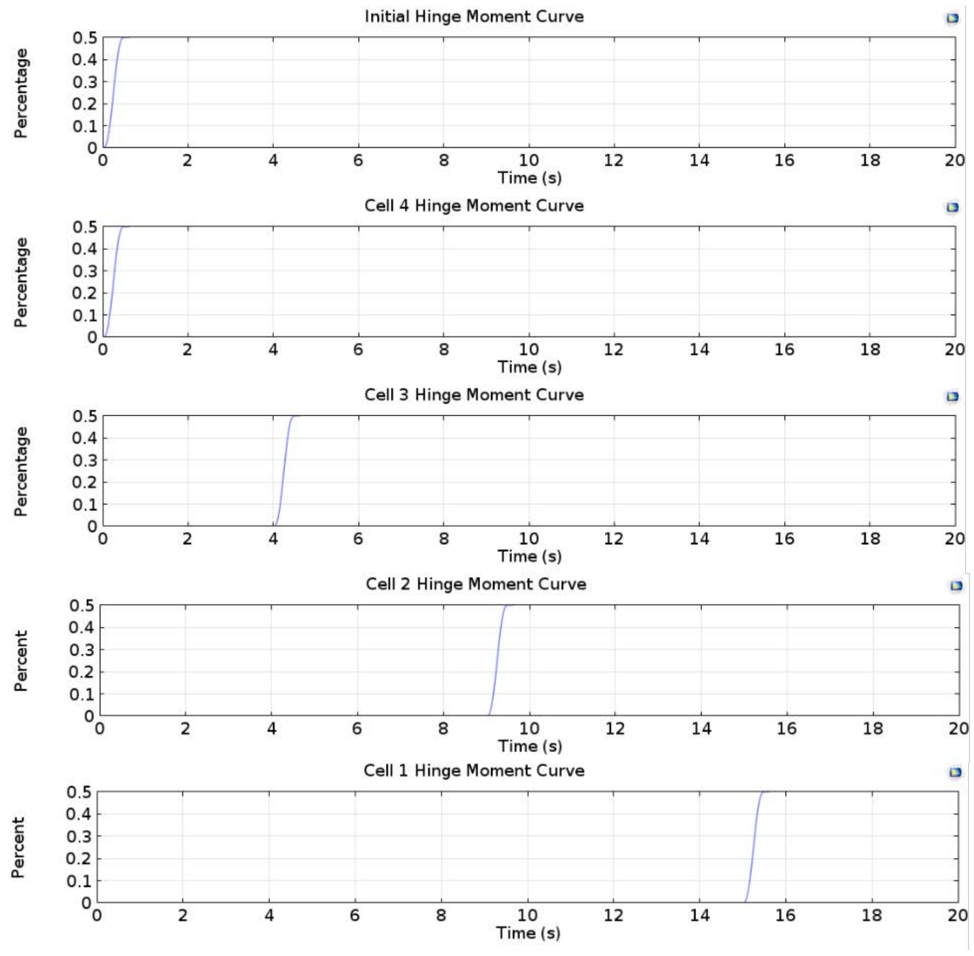

Figure 123. Applied hinge moment curves for controlled deployment simulations.

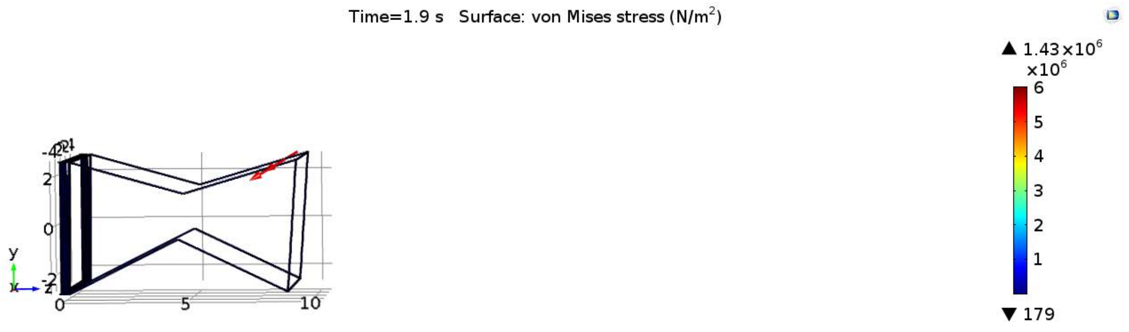

Figure 124. End-to-root controlled deployment simulation at T = 1.9 seconds.

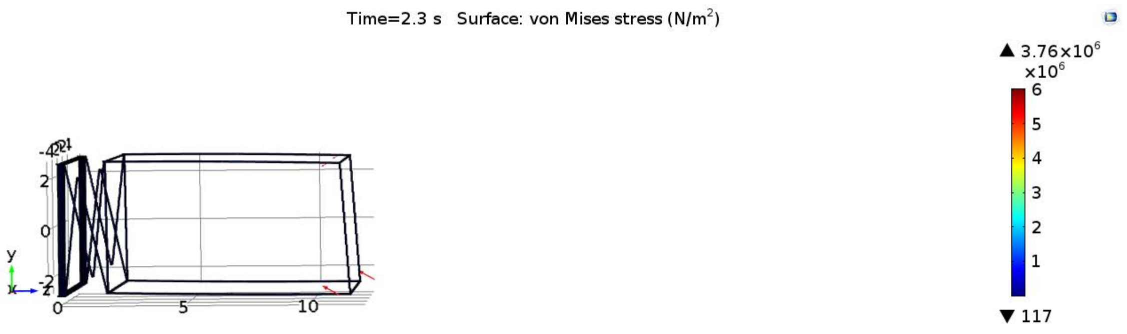

Figure 125. End-to-root controlled deployment simulation at T = 2.3 seconds.

as well as radially. This motion not only creates a larger deployment envelope, but impedes some of the cells in their lockout motions. Again the halved spring moments in the other cells proves sufficient to motivate the entire structure radially, albeit at a slower pace than in the uncontrolled simulation.

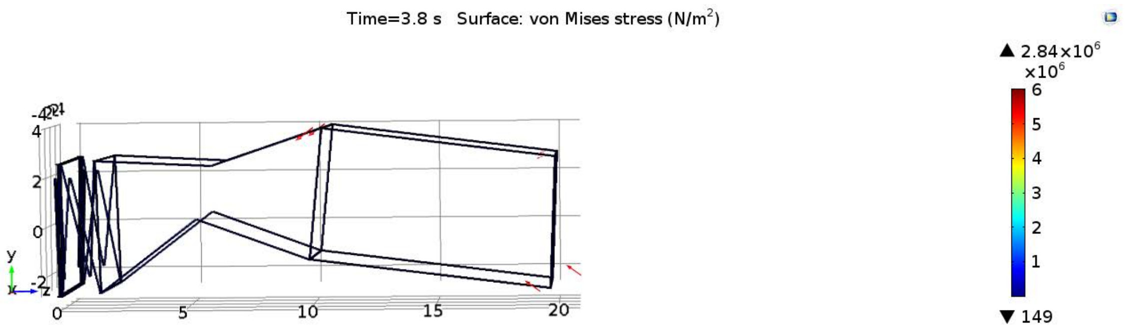

Figure 126. End-to-root controlled deployment simulation at T = 3.8 seconds.

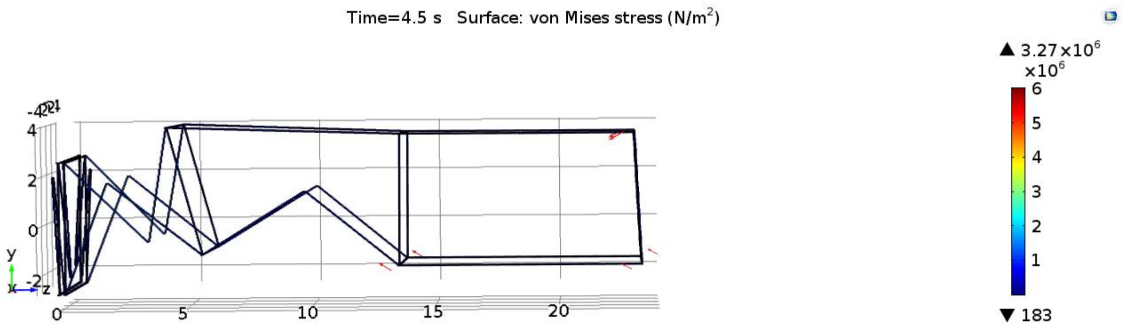

Figure 127. End-to-root controlled deployment simulation at T = 4.5 seconds.

Figure 128 shows the point in time in the simulation where Cell 2 is about to lock its upper longerons. Notice that the lower longerons in Cell 2 are also having trouble deploying completely, and Cell 1 is beginning to move as well. Figure 129 shows how the deployment of Cell 1 exacerbates the deployment of the lower longerons of Cells 2 and 3 in that they do not have enough moment to overcome the radial motion of the entire structure. It should also be noted here that the deployment is moving vertically in a significant fashion.

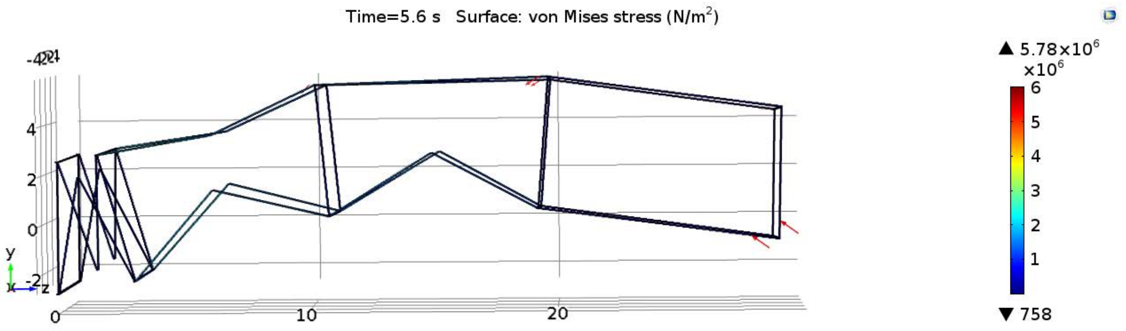

Figure 128. End-to-root controlled deployment simulation at T = 5.6 seconds.

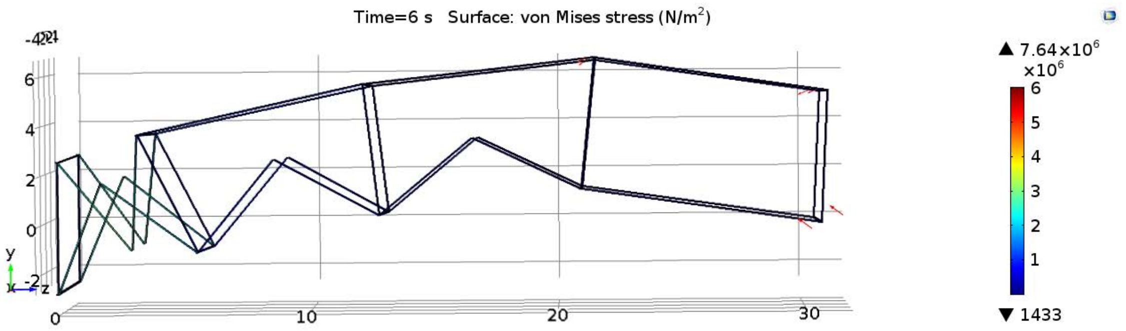

Figure 129. End-to-root controlled deployment simulation at T = 6 seconds.

Figure 130 shows how the lower longerons deploy before the upper longerons in Cell 1, which does not occur in any other Cell. This is most likely a result of the vertical and radial movement being exhibited by the structure at this point. The momentum of the structure is such that it pulls Cell 1 open. Figure 131 shows that even with a large cable force being applied by the two red arrows in the upper-right corner of Cell 1, the upper longerons are able to deploy thanks to the overall kinetic energy of the system. The lower longerons of Cell 2 are also about lockout at this point as well, also due to the system's kinetic energy.

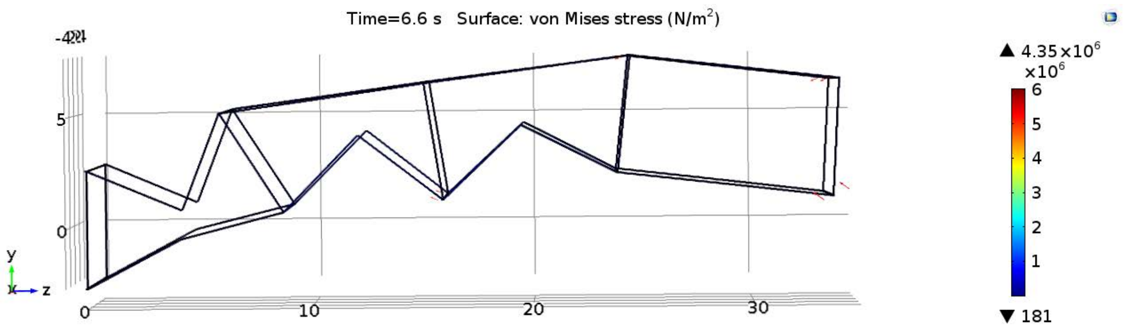

Figure 130. End-to-root controlled deployment simulation at T = 6.6 seconds.

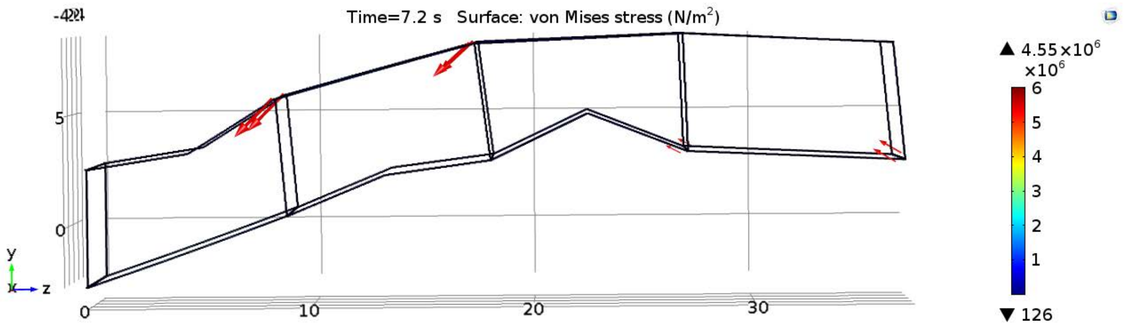

Figure 131. End-to-root controlled deployment simulation at T = 7.2 seconds.

Figure 132 fully realizes the radial momentum that the structure has built throughout the simulation as almost all of the longerons lock into place. Figure 133 completes the deployment of the longerons as everything is now locked out. The remainder of the simulation, which runs to 25 seconds, involves the same vertical swaying motion seen previously in the uncontrolled deployment.

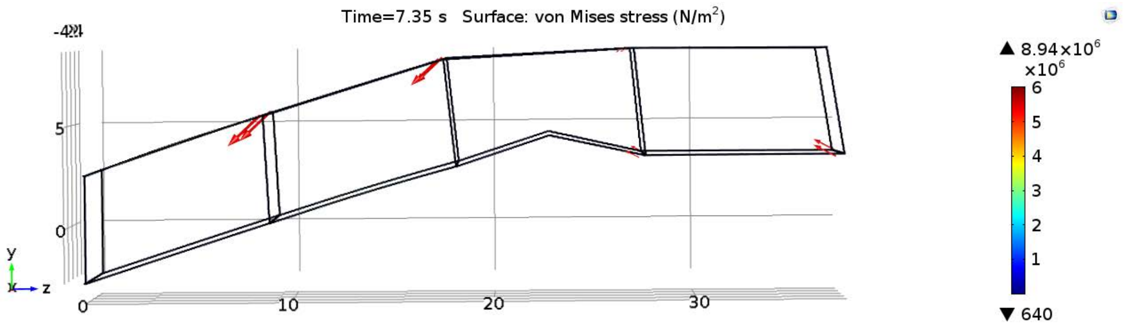

Figure 132. End-to-root controlled deployment simulation at T = 7.35 seconds.

Before expanding on the analytics of this deployment, it should be stated that

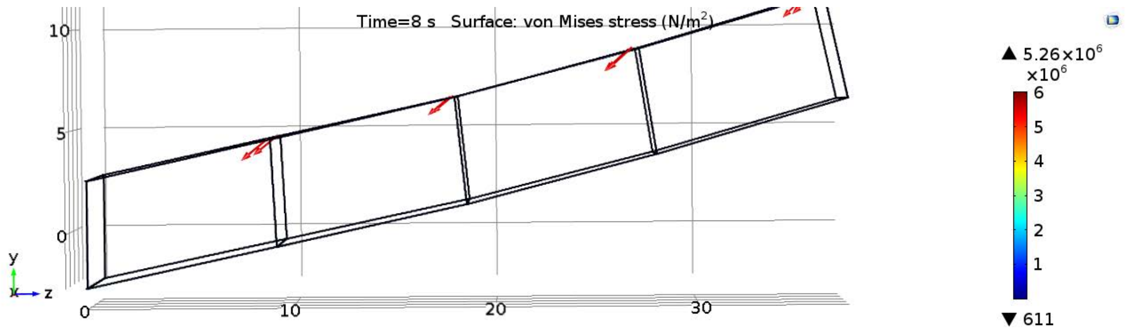

Figure 133. End-to-root controlled deployment simulation at T = 8 seconds.

the control scheme did not work as intended. Even though Cell 1 was not set to have its full moment applied until 15 seconds into the simulation, the entire structure was deployed at 8 seconds. Instead, this analysis is looking at a deployment with differing spring constants. When compared to the uncontrolled simulation, this simulation has three cells with 75% of the applied moment of the uncontrolled, and one cell with 150% of the applied moment. Therefore, the numbers cannot be directly compared between the two, but some general trends can be analyzed.

The controlled deployment offers a different energy distribution from the uncontrolled deployment (Figure 72). Figure 134 shows that instead of an almost directly proportional energy distribution between kinetic and strain energies, the controlled deployment has less kinetic energy. This may lead to a decrease in kinetic energy and lead to a deployment that suffers less stress in its components during lockout events. Figure 134 also seems to suggest that the increase in total energy seen in the latter parts of the simulation may be due to the increase in total strain enery. Perhaps the methodology for modeling the strain energy of the cables is incorrectly inflating the values seen here. Also of note is that even with the reduced spring-hinge moments, Cells 1-3 deploy pretty much the same. However, these Cells may have been helped by the extra momentum afforded to them from Cell 4's deployment.

Although this "controlled" deployment did not really control that well, it still shows how COMSOL can be used to alter the parameters of the simulation quite easily. Equally as important, the simulation is stable despite the parameter changes, which can prove challenging to many other FEA packages. Table 10 shows that the deployment envelope of this "controlled" deployment is significantly worse than the uncontrolled deployment in the positive Y direction.

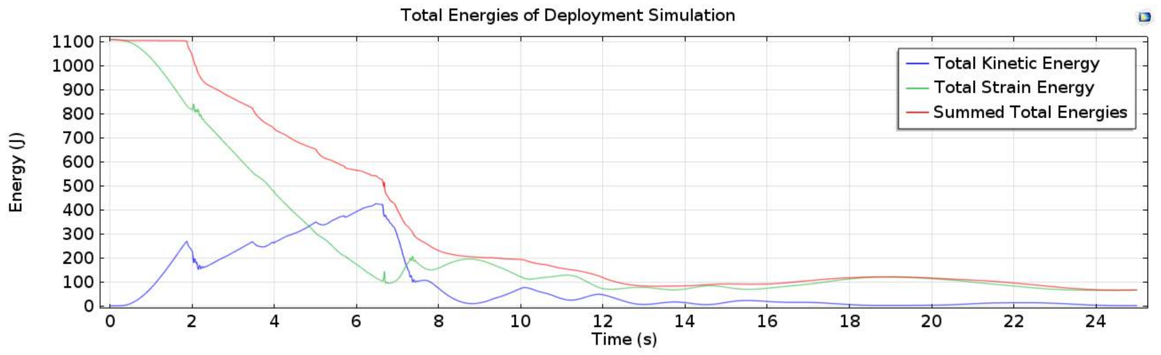

Figure 134. End-to-root controlled deployment simulation energy.

Completed Deployment	**X**	**Y**	**Z**
Upper Bound (m)	4.4710	6.0679	37.9799
Lower Bound (m)	-4.4710	-2.6422	0
Uncontrolled Deployment	**X**	**Y**	**Z**
Upper Bound (m)	4.4430	9.7763	37.8630
Lower Bound (m)	-4.5435	-3.6698	0
End-to-Root Controlled Deployment	**X**	**Y**	**Z**
Upper Bound (m)	4.4620	12.4622	37.8560
Lower Bound (m)	-4.5485	-3.3783	0

Table 10. Uncontrolled and end-to-root deployment simulation deployment envelopes

Root-to-End.

The purpose of this subsection is to show how a backwards deployment would function for this truss arm. To reiterate, the same methods are applied as the previous section, except the order in which the Cells are activated is reversed. Therefore, the goal of this simulation is to deploy Cell 1, then Cell 2, Cell 3, and finally Cell 4. Figure

135 shows the simulation after just two seconds of running time. It once again shows that although the halved spring-hinge moments keep the bumpers from touching each other too much, they do little to control the deployment of the Cells. As Cell 1 begins to open, Cell 4 still has enough applied moment to move itself radially faster than Cell 1 can push the entire structure. In Figure 136, Cell 4 is about to lock itself out as Cell 1 propels the entire structure outwards.

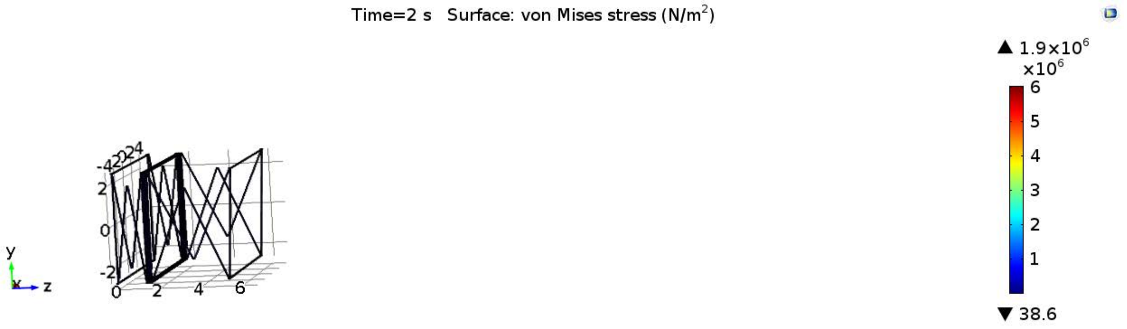

Figure 135. Root-to-end controlled deployment simulation at T = 2 seconds.

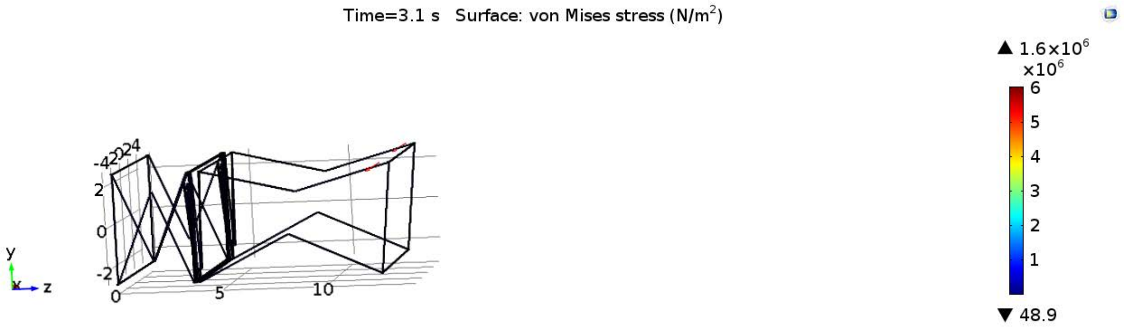

Figure 136. Root-to-end controlled deployment simulation at T = 3.1 seconds.

Figure 137 shows the point in the simulation where it appears as though Cell 4 is on the cusp of locking out. However, Figure 138 shows the simulation half a second later, where the doubled hinge moment of Cell 1 starts to overrun Cell 4. As Cell 4 is beginning to regress in its deployment here, Cell 3 which supports it is beginning to bend backwards quite a lot. So much in fact that the geometry here is intersecting and is therefore unrealistic.

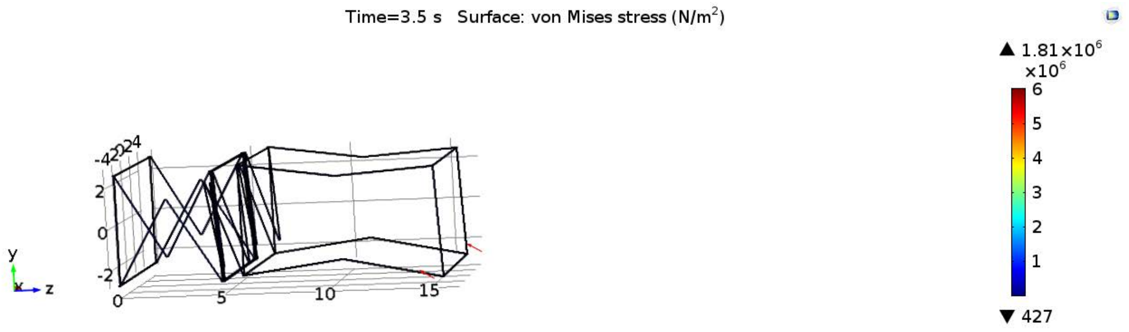

Figure 137. Root-to-end controlled deployment simulation at T = 3.5 seconds.

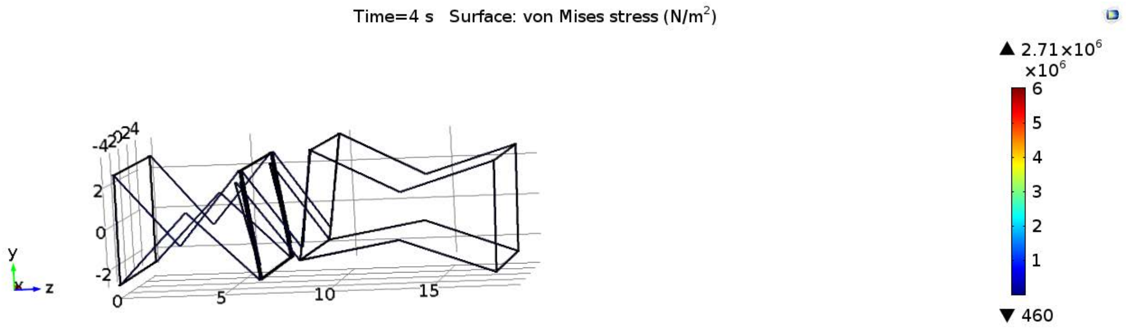

Figure 138. Root-to-end controlled deployment simulation at T = 4 seconds.

At 4.9 seconds into the simulation, Cell 1 is about to fully deploy, as shown in Figure 139. At this point, Cell 4 has regressed even further towards its stowed state, and Cell 3 has recovered in a way as to be realistic again. Figure 140 shows the simulation right after Cell 1 completely locks out. Cell 3 is in an extreme configuration at this point, and its prognosis for full deployment does not look good. Cell 2 exacerbates Cell 3's precarious outlook as it is triggered by the timing function in COMSOL and gains a higher hinge moment. Figure 141 shows how the activation of Cell 2 adds to the applied moment it had from the start of the simulation. Note, however, that the hinge never reaches its full potential, as it has enough moment to begin to deploy at approximately 5.5 seconds.

Figure 142 shows the point at which Cell 2 is about to lockout. This is where Cell 2 dominates the other remaining cells thanks to its double spring-hinge moment. Interestingly, the top longerons of Cell 3 have locked out due to the rotation of Cell

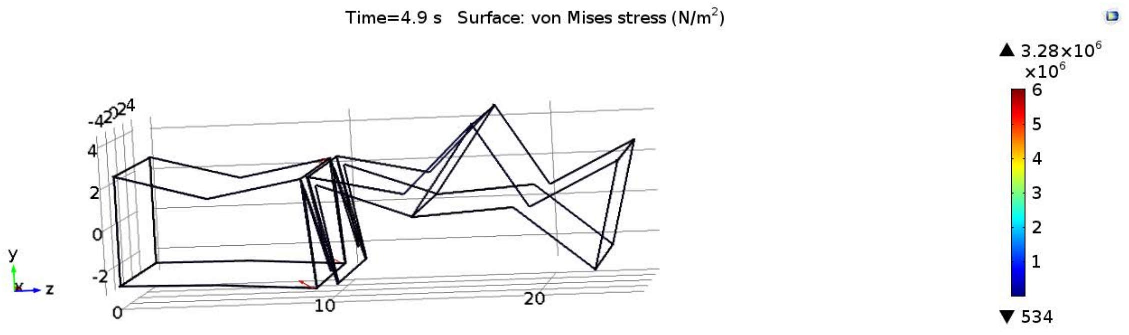

Figure 139. Root-to-end controlled deployment simulation at T = 4.9 seconds.

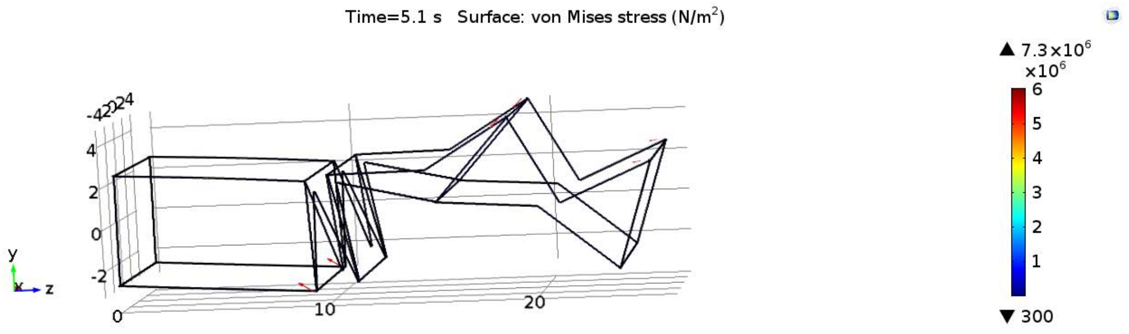

Figure 140. Root-to-end controlled deployment simulation at T = 5.1 seconds.

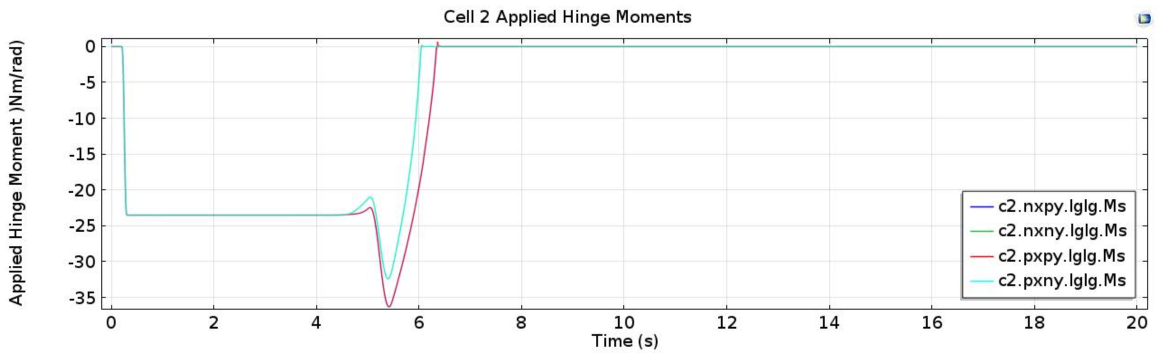

Figure 141. Root-to-end controlled deployment simulation Cell 2 applied hinge moment.

4 during the deployment. Figure 143 shows Cell 2's fully deployed state. It is also about the time where Cells 3 and 4 an begin moving on their own, instead of being driven into bad geometry conditions by the root cells. In addition, Figure 143 shows that three shaping cables are active and pointing downwards. This indicates that the entire truss arm is about to move downwards as the two root cells attempt to find their equilibrium.

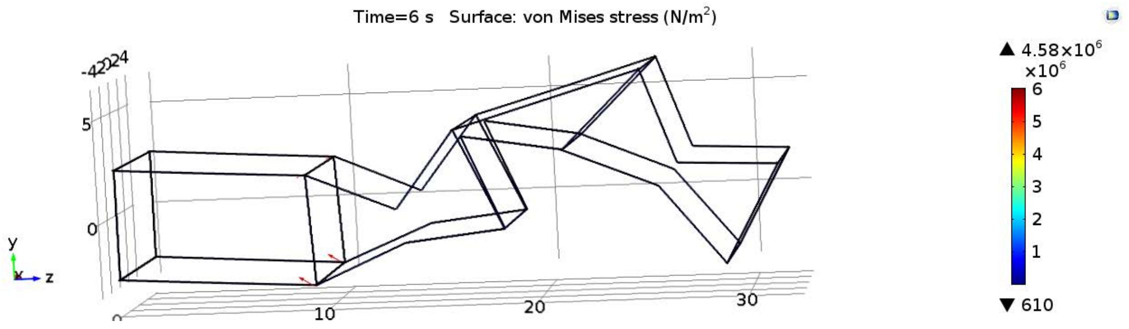

Figure 142. Root-to-end controlled deployment simulation at T = 6.0 seconds.

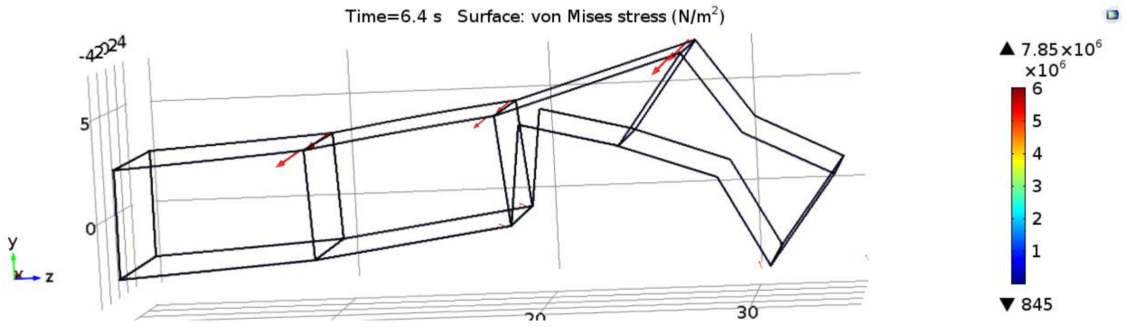

Figure 143. Root-to-end controlled deployment simulation at T = 6.4 seconds.

Figures 144 through 147 show the before and after instants in which the lower longerons of Cells 3 and 4 finally locked out. One will observe that these events take a considerable amount of simulation time. At the relatively small angular displacement these longerons must travel, the applied hinge moment is at its weakest, and is not conducive to seeking its final lockout position. Furthermore, Cells 1 and 2 are moving very quickly throughout these time steps. The end cells are subject to whatever motion they are connected to, and in this case the root cells' motion impedes the end cells' deployment. As mentioned in the previous subsection, the remaining residual motion does not exceed the boundaries seen here, and will not be discussed further.

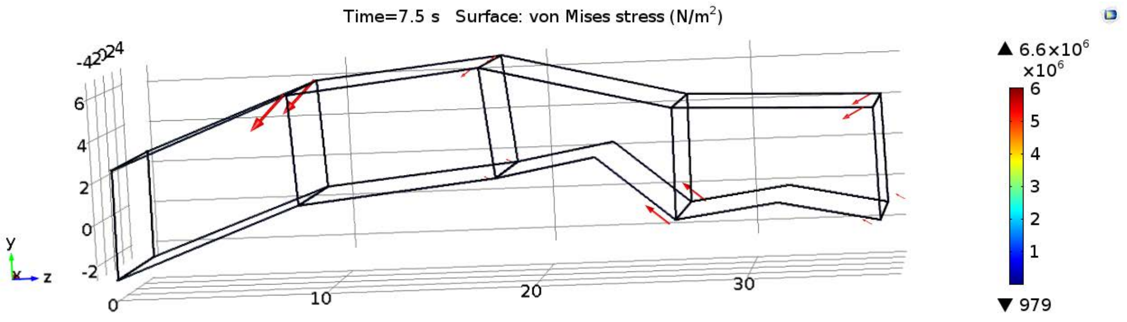

Figure 144. Root-to-end controlled deployment simulation at T = 7.5 seconds.

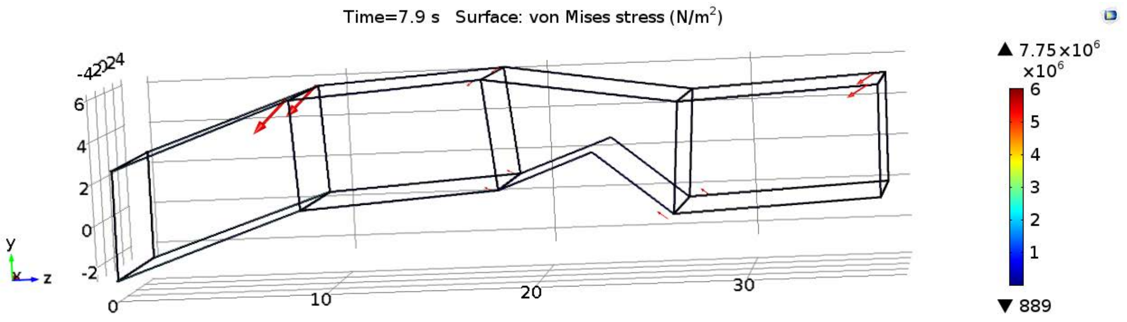

Figure 145. Root-to-end controlled deployment simulation at T = 7.9 seconds.

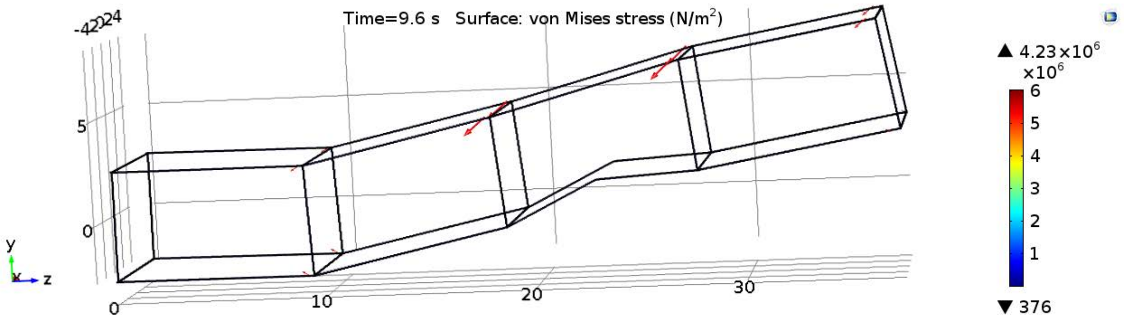

Figure 146. Root-to-end controlled deployment simulation at T = 9.6 seconds.

Figure 148 shows the energy calculations from this simulation. The disparity between the kinetic and strain energies is not as notable as the end-to-root deployment because the root cells moved the entire structure radially throughout the simulation like the uncontrolled deployment. Interestingly, the deployment envelope (Table 11)

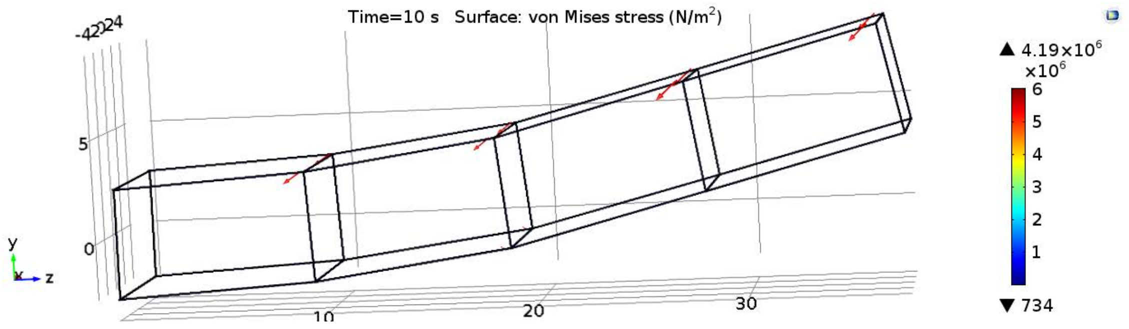

Figure 147. Root-to-end controlled deployment simulation at T = 10 seconds.

of this simulation is the smallest seen in this work. No doubt as a result of obtuse angles obtained by some of the cells in the simulation. It is plain from these simulation results, that a root-to-end deployment is not optimal. The root Cells that drive the structure outwards controls the outermost Cells in a way that is simply harmful to the structural members. Although it is possible to model more contacts in COMSOL to avoid the geometry intersections seen here, the added computation time would not be trivial. Furthermore, such a deployment scheme may not be worth the computational cost to pursue. At the end of the day, perhaps a different control scheme needs to be developed for this application in COMSOL. There are a variety of possibilities that could be considered and made with the tools that COMSOL has to offer. Else, the model would need to be geometrically modifed to avoid the bumping that would occur between the batten frames if the spring-hinge moments were completely turned off. The current model could be more strictly constrained to meed the demands of a controlled model. However this would result in a cumbersome model that would take significantly longer to solve.

4.6 Summary

There are many key ideas to take away from this Chapter. Section 4.2 showed how an uncontrolled truss might deploy and gave an in-depth analysis on what happened

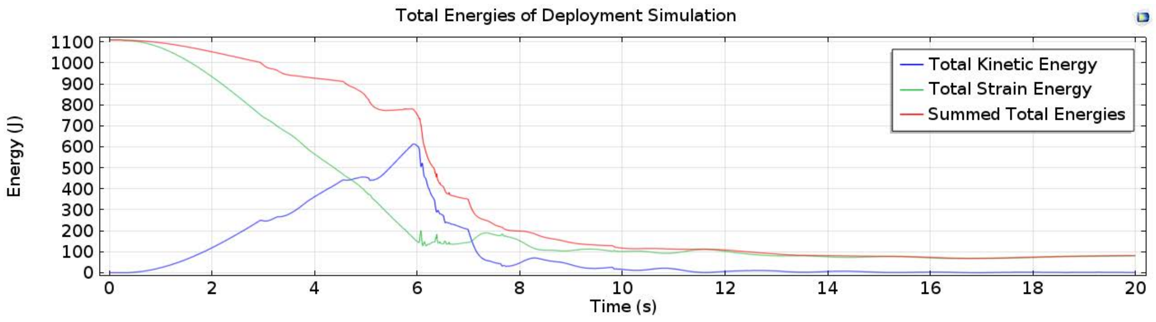

Figure 148. End-to-root controlled deployment simulation energy.

Completed Deployment	X	Y	Z
Upper Bound (m)	4.4710	6.0679	37.9799
Lower Bound (m)	-4.4710	-2.6422	0
Uncontrolled Deployment	**X**	**Y**	**Z**
Upper Bound (m)	4.4430	9.7763	37.8630
Lower Bound (m)	-4.5435	-3.6698	0
Root-to-end Controlled Deployment	**X**	**Y**	**Z**
Upper Bound (m)	4.4770	8.9678	37.7390
Lower Bound (m)	-4.6206	-3.4089	0

Table 11. Uncontrolled and root-to-end deployment simulation deployment envelopes

throughout this deployment. The model that was created using the methods in Chapter 3 performed as it should and showed that the geometry and cables were modeled correctly. Remember that none of the motion paths were preordained, and that the stowed model was created and simply released. Throughout the analysis it was shown that COMSOL is able to detect high frequency events and adjust the time steps in response to them. Different idiosyncrasies of the truss deployment were found as well. It was explained that the deployment success of each Cell was highly dependent on the geometry and motion of the rest of the structure. The summed total energies of the simulation acted as one would expect throughout most of the simulation. Towards the end, however, it was shown that the summed energy actually increases. This is not representative of a closed system, and may be caused by an overly general approximation of the strain energies in the system. Perhaps as a result of this added energy, the transient motion of the deployed truss remained for the duration of the simulation. The end of this Section showed more of the output data from the simulation in order to show how different aspects of the deploying truss are related to each other. It was shown that COMSOL's joints do indeed transfer displacements throughout the model. Section 4.3 shows what happens when the uncontrolled truss is placed in a rotating frame. Although the frame only rotated for a small fraction of the simulation, it did have an effect on the longeron lockout events. It was also pointed out here that due to the loose tolerance factors imposed on the time-dependent solver, that only global motion was really being captured. Section 4.4 ran a quick study on the effects of weak hinges on the deployment of the truss arm. Through a lot of simulation data, it was found that if a weak hinge exists in a bottom longeron, then the simulation will most likely fail. Cell 2 also proved to be vital for the truss arm's deployment success. Finally, Section 4.5 explores how a truss arm deployment might be controlled and what effects the control would have on the deployment. Unfortunately, the scheme created to control the truss did not work as intended, and the truss's deployment ran away from the time triggers. The results from these simulations still proved valuable, however, as they once again showed how simulations in COMSOL could be easily modified. Table 12 shows the deployment envelopes for all of the simulations. Furthermore it was shown that even a partially controlled simulation aided in curbing the kinetic energy of the system. The second half of this Section showed why a root-to-end deployment sequence needs to be carefully implemented. It was concluded that either a new methodology for controlling the deployment should be developed, or that the current model should be more strictly constrained. Either way, it was established that there exist a multitude of possibilities inside COMSOL to approach this problem.

Completed Deployment	**X**	**Y**	**Z**
Upper Bound (m)	4.4710	6.0679	37.9799
Lower Bound (m)	-4.4710	-2.6422	0
Uncontrolled Deployment	**X**	**Y**	**Z**
Upper Bound (m)	4.4430	9.7763	37.8630
Lower Bound (m)	-4.5435	-3.6698	0
5 Degrees per Minute Initial Rotation	**X**	**Y**	**Z**
Upper Bound (m)	4.4283	9.8037	37.8550
Lower Bound (m)	-4.5370	-3.6490	0
60 Degrees per Minute Initial Rotation	**X**	**Y**	**Z**
Upper Bound (m)	4.4850	9.9063	37.8430
Lower Bound (m)	-4.4801	-3.6472	0
Weak c1.nxpy.lglg Hinge	**X**	**Y**	**Z**
Upper Bound (m)	4.4221	11.4660	37.8360
Lower Bound (m)	-4.5671	-2.8143	0
Weak c1.nxny.lglg Hinge	**X**	**Y**	**Z**
Upper Bound (m)	4.4088	11.5768	37.3200
Lower Bound (m)	-4.5898	-2.8442	0
Weak c2.nxpy.lglg Hinge	**X**	**Y**	**Z**
Upper Bound (m)	4.4157	10.0887	37.3610
Lower Bound (m)	-4.5447	-2.7412	0
Weak c2.nxny.lglg Hinge	**X**	**Y**	**Z**
Upper Bound (m)	4.4850	32.5646	36.5340
Lower Bound (m)	-4.5216	-3.3617	0
Weak c3.nxpy.lglg Hinge	**X**	**Y**	**Z**
Upper Bound (m)	4.4225	9.4141	37.7630
Lower Bound (m)	-4.5197	-3.6866	0
Weak c3.nxny.lglg Hinge	**X**	**Y**	**Z**
Upper Bound (m)	4.553	11.6904	37.8410
Lower Bound (m)	-4.5239	-4.5239	0
Weak c4.nxpy.lglg Hinge	**X**	**Y**	**Z**
Upper Bound (m)	4.4554	8.9432	37.7080
Lower Bound (m)	-4.4677	-2.8025	0
Weak c4.nxny.lglg Hinge	**X**	**Y**	**Z**
Upper Bound (m)	4.4306	11.1625	37.3080
Lower Bound (m)	-4.5682	-2.7809	0
End-to-Root Controlled Deployment	**X**	**Y**	**Z**
Upper Bound (m)	4.4620	12.4622	37.8560
Lower Bound (m)	-4.5485	-3.3783	0
Root-to-End Controlled Deployment	**X**	**Y**	**Z**
Upper Bound (m)	4.4770	8.9678	37.7390
Lower Bound (m)	-4.6206	-3.4089	0

Table 12. Deployment envelopes for all simulations.

V. Conclusions

5.1 Summary of Work

In summary, this work has simulated the deployment of a locking hinge truss using FEM in COMSOL. The simulated truss comprises the partial structure of a very large, sparse antenna aperture reflector. The aperture is designed to fit within existing launch vehicle payload fairings and be deployed on orbit, where its large diameter can reduce long range communications power requirements by an order of magnitude. The truss's deployment was simulated with multiple variations to show not only how the model reacted globally to varied design parameters, but to also demonstrate the capabilities of COMSOL's implicit solver. The pursuit of this simulation and the research involved was prompted by previous work done with the Large Deployable Spare Aperture Reflector project.

A methodology has been presented here that creates 3D deployment simulations from nominal 2D engineering designs. These designs are based on historical concepts and hardware with exceptional flight heritage. The first major milestone in this work was the choice of FEA solver software. It was determined that COMSOL was the best match for this work due to its under-the-hood transparency, plethora of adjustable components, and extensive knowledge base. From here, the methodology followed a typical engineering path from geometry creation to simulation results and analysis. This path is summarized as follows:

1. 3D geometry creation from 2D drawings
2. As-designed 3D geometry simplification to 3D simulation geometry
3. Creation of equivalent material properties for simplified geometry
4. Establishment of modeling shorthand nomenclature

5. Importation, conditioning, meshing, material application, and physics setup of geometry in COMSOL
6. Cable elements modeling
7. Probe declaration and solver configuration in COMSOL
8. Simulation results analysis and deployment envelope calculations

5.2 Analysis Conclusions

The uncontrolled simulation represents the most unconstrained model that deploys in a spontaneous manner. Analysis of this simulation revealed many emergent characteristics of the truss's deployment. First of all, a relationship between the geometry configuration of the entire truss and an individual cell's lockout prospects were established. Due to the longer lower longerons of the cells, an upward motion was experienced in the truss's deployment that forced awkward or incomplete truss deployments. Using a combination of COMSOL's built-in energy measurements and cable strain energies, it was shown that the kinetic energy of the truss was a major factor in cell deployments. Although the summed total energy momentarily increases in the simulation and is not realistic, the kinetic energy showed how cells closer to the root of the truss could be pulled radially to lockout via momentum. Before, during, and after the cells full deployment, the implicit solver utilized by COMSOL was able to adjust the number of time steps used. This allowed the displacements of the longerons during this critical period to be modeled precisely without burdening the rest of the simulation with excessive time steps. The stresses resulting from these displacements are only representative of a truss deployment, but showed that the declared hinges throughout the model were transmitting the stress waves throughout the model during the simulation. The second half of the simulation illustrated how the transient motions of the structure cause it to sway unpredictably. Although the added damping or the tension cables were necessary for successful deployments, it also proved to be a boon to the structure in this latter part of the simulation. Such a necessary addition to the simulation may point to possible design space additions for further iterations of this deployable structure.

The uncontrolled simulations placed into rotating frames hints at the added capabilities of COMSOL. Due to the nature of the changing moment of inertia of the structure, the rotation was only present in the first two cell deployments. Although the speed of rotation between the two simulations varies greatly, the differences in their analyses were very similar. They both showed the same longeron velocity and lockout times due to the small amount of damping present in the hinges, but the lockout stress was sometimes up to twice that of the original unconstrained deployment. The added stress is most likely a result of the higher axial load from the centripetal force present in the simulation. This stress also contributes to some observed harmonic displacement within the longerons that is noticeable for the simulations in the rotating frame. It was mentioned that the implicit solver may be able to even more accurately track these displacements through the structure if given tighter tolerance settings. The results from these simulations are far from conclusive, but also seem to suggest that adding centripetal force to the simulation would not be beneficial for a mechanism configured in this way.

Weakened hinges were placed throughout the structure to again challenge COMSOL's solver as well as study the effect of manufacturing errors on the truss deployments. Of the eight simulations run, only half of them completed successfully. The other half of the simulations' deployments failed as the global motion was altered by the weak hinge in such a way as to prevent the complete lockout of one or more hinges. In most cases, the lower longeron hinges proved critical to the lockout success of the truss cells. One case in particular, where one of the lower hinges was weakened in Cell 2, showed that the resulting truss deployment was displaced 32 meters vertically.

Such a large deployment envelope would most certainly compromise the deployment of the entire antenna array. The rest of the simulations' envelopes showed that typically the deployment of the truss arm does not exceed approximately 12 meters of vertical motion with the presence of the weak hinges.

The controlled deployment simulations of the truss arm did not function entirely as expected. Between concerns for computation time and geometry intersections, a compromised control solution was put forward. However, the lessons learned from the behavior exhibited without this solution were not expected, and are therefore of value to the design of the truss mechanism. For example, the contact made between the end fittings while the end trusses pushed off the root trusses is considerable, and if not constrained properly could cause damage. It should also be noted that the control scheme did reduce the total ratio of kinetic to strain energy present in the structure during the simulation, and proves why controlled deployments are necessary. In the future, an alternate control scheme should to be devised to more accurately model the deployment of the as-designed truss.

It can be concluded from these analyses that the simulations presented are representative of the deployment of the as-designed truss for the Large Deployable Sparse Aperture Reflector. The simulation modeled here lacks the component detail needed to establish definitive conclusions of the as-designed structure, but many key results are useful for further research. The overall behavior of the system in response to an uncontrolled deployment or parameter alterations hints at possible areas of concern as well as new design considerations when moving forward. Although the design seems simple, the kinetics of its deployment should not be understated.

5.3 Broader Impact

The methodology presented in this paper applies not only to the Large Deployable Sparse Aperture Reflector, but can also be extended to similar space structures. Such structures are not built for Earth's gravity and must be properly designed through use of computer simulations before they are built. This work shows that solid body simulations can be conducted in COMSOL and the results can make significant contributions to the structure's design. The resolution of the simulations performed are low due to time and resource constraints, yet can be improved in the future due to COMSOL's proven scalability. Therefore, it can be said that this work contributes to the study of large deployable space structures by providing a configurable deployment simulation methodology. Through these studies, larger and more dependable deployable space structures can be designed which will further humanity's space exploration efforts.

5.4 Future Work

The work presented here details a comprehensive method of modeling locking truss deployments in COMSOL. As such, there are many aspects of the model that need to be improved in order to continue contributing to the Large Deployable Sparse Aperture Reflector project. These improvements include:

1. Study of geometric simplification effects on simulation results
2. Investigation of energy parameters to determine source of increasing energy in the latter half of the simulation
3. Addition of truss cells to comprise the full eight cell truss arm
4. Optimization of design parameters using parametric sweeps in COMSOL
5. Inclusion of cable forces from center mast and adjacent arms

6. Structural analysis of deployed truss cells to slewing maneuvers

In addition to the work that can be done to the existing model, future work may also include the modeling of the complete reflector structure that may even include component-level details. Once a full model is constructed, structural and environmental analyses can be conducted to determine the performance of the reflector on orbit. Although a more powerful computing solution may be needed, a full simulation of the as-designed geometry would undoubtedly further this concept's future feasibility.

Bibliography

1. Mitsugi, J., Ando, K., Senbokuya, Y., and Meguro, A., "Deployment Analysis of Large Space Antenna Using Flexible Multibody Dynamics Simulation," *Acta Astronautica*, 2000.

2. Coyner, J. V., "Box Truss Development and Applications," *NASA Conference Publication 2269, Part 1*, 1982, pp. 527–543.

3. Jet Propulsion Laboratory, the California Institute of Technology, "Shuttle Radar Topography Mission," Webpage, 2005, http://www2.jpl.nasa.gov/srtm/mission.htm.

4. Jet Propulsion Laboratory and the California Institute of Technology, "NuSTAR Deployable Mast," Webpage, 2012, http://www.nustar.caltech.edu/page/mast.

5. Greschik, G., "Satellite Boom Study for Sparse Aperture Mesh Reflector with Four Arms of a Modified Box Truss Architecture," TentGuild Eng. Co., Boulder, CO, Dec 2013.

6. College of Engineering and Applied Science Advanced Finite Element Methods, *The Linear Tetrahedron, The Quadratic Tetrahedron, Hexahedron Elements*, chap. 9, 10, 11, University of Colorado Boulder, 2013.

7. Cook, R. D., *Concepts and Applications of Finite Element Analysis*.

8. Dyne, D. V., "MECH 644 Final Report," Tech. rep., Air Force Institute of Technology, 2014.

9. Roddy, D., *Satellite Communications*, McGraw-Hill, 4th ed., 2006.

10. Black, J., Cobb, R., and Swenson, E., "New Deployment Methods for Very Large Antennas," Air Force Institute of Technology, Wright-Patterson Air Force Base, OH, Dec 2012.

11. Greschik, G. and Belvin, W. K., "High-Fidelity Gravity Offloading System for Free-Free Vibration Testing," *Journal of Spacecraft and Rockets*, Vol. 44, No. 1, January 2007, pp. 132–142.

12. Heller, J. C., "Feasibility of Very Large Sparse Aperture Deployable Antennas," Air Force Institute of Technology, Wright-Patterson Air Force Base, OH, Mar 2014, MS Thesis.

13. Kane, T., Ryan, R., and Banerjee, A., "Dynamics of a Cantilever Beam Attached to a Moving Base," *AIAA*, 1987.

14. ATK Goleta, *Articulated Mast Systems*, ATK, 2012.

15. Wilson, J. M., “The Design and Analysis of Electrically Large Custom-Shaped Reflector Antennas,” Air Force Institute of Technology, Wright-Patterson Air Force Base, OH, Mar 2012, MS Thesis.

16. NASA Lyndon B. Johnson Space Center (JSC), “NASA Reduced Gravity Research Program,” Website, 2014.

17. COMSOL, “Meshing Considerations for Linear Static Problems,” Webpage, 2013, http://www.comsol.com/blogs/meshing-considerations-linear-static-problems/.

18. COMSOL, “COMSOL User Documentation v4.4,” Nov 2013.

19. Hindmarsh, A. C., Serban, R., and Collier, A., “User Documentation for IDA v2.7.0,” Mar 2012.

20. COMSOL, “What hardware do you recommend for COMSOL Multiphysics?” Webpage, 2012, http://www.comsol.com/support/knowledgebase/866/.

21. Rodgers, D. P., “Improvements in multiprocessor system design,” *ISCA ’85 Proceedings of the 12th annual international symposium on Computer architecture*, IEEE Computer Society, Los Alamitos, CA, Jun 1985, pp. 225–231.

22. Ross, B., “FunctionBay,” Website, 2014.

23. Modal Analysis and Controls Laboratory, “Natural Frequencies for Common Systems,” Handbook, 2000.

24. Ruina, A., “Beam Deflection Formulae,” Website, 2013.

25. Performance Composites Ltd., “Mechanical Properties of Carbon Fibre Composite Materials,” Reference Book, 2009.

26. Dassault Systemes, *Abaqus Analysis User’s Manual*, version 6.7 ed., Provided by Michigan State University.

VI. Appendix

6.1 Appendix A - MATLAB Code

Mesh Study Plots.

```
%% 141217 Mesh Study
% Dylan Van Dyne

clear all; close all; clc;

P = 100;
E = 34.892e9;
I = 5.2083e-7;
L = 9.5;
A = 0.05^2;
rho = 32.3543;
disp_exact = (P*(L^3))/(48*(E)*(I));
w1_exact = (1/(2*pi))*((pi/L)^2)*sqrt((E*I)/(rho*A))
w2_exact = (4/(2*pi))*((pi/L)^2)*sqrt((E*I)/(rho*A))
% w3_exact = (8/(2*pi))*((pi/L)^2)*sqrt((E*I)/(rho*A))
% w4_exact = (16/(2*pi))*((pi/L)^2)*sqrt((E*I)/(rho*A))
% w5_exact = (32/(2*pi))*((pi/L)^2)*sqrt((E*I)/(rho*A))
w3_exact = 74.177
w4_exact = 131.77
w5_exact = 205.67

tetmeshlin = [348 600 826 3595 4104;
            708 1212 1632 4242 4914;
            0.005564 0.011290 0.015557 0.045450 0.053525;
            35.076 24.275 20.658 12.14 11.076;
            143.53 96.033 80.248 48.478 43.377]';
for n = 1:length(tetmeshlin(:,3))
    tetmeshlin(n,3) = abs(tetmeshlin(n,3)-disp_exact)*100/abs(disp_exact);
end
for n = 1:length(tetmeshlin(:,4))
    tetmeshlin(n,4) = abs(tetmeshlin(n,4)-w1_exact)*100/abs(w1_exact);
end
for n = 1:length(tetmeshlin(:,5))
    tetmeshlin(n,5) = abs(tetmeshlin(n,5)-w2_exact)*100/abs(w2_exact);
end

tetmeshquad = [125 164 202 228 348;
            1014 1353 1683 2079 3159;
            0.097919 0.098088 0.098173 0.098236 0.098276;
            8.2621 8.2563 8.2534 8.2512 8.2498;
            33.174 33.084 33.047 33.017 32.997;
            75.247 74.766 74.529 74.351 74.240;
            135.01 133.43 132.77 132.28 131.96;
            214.01 210.23 208.39 207.01 206.15]';
```

```
for n = 1:length(tetmeshquad(:,3))
    tetmeshquad(n,3) = abs(tetmeshquad(n,3)-disp_exact)*100/abs(disp_exact);
end
for n = 1:length(tetmeshquad(:,4))
    tetmeshquad(n,4) = abs(tetmeshquad(n,4)-w1_exact)*100/abs(w1_exact);
end
for n = 1:length(tetmeshquad(:,5))
    tetmeshquad(n,5) = abs(tetmeshquad(n,5)-w2_exact)*100/abs(w2_exact);
end
for n = 1:length(tetmeshquad(:,6))
    tetmeshquad(n,6) = abs(tetmeshquad(n,6)-w3_exact)*100/abs(w3_exact);
end
for n = 1:length(tetmeshquad(:,7))
    tetmeshquad(n,7) = abs(tetmeshquad(n,7)-w4_exact)*100/abs(w4_exact);
end
for n = 1:length(tetmeshquad(:,8))
    tetmeshquad(n,8) = abs(tetmeshquad(n,8)-w5_exact)*100/abs(w5_exact);
end

tetmeshcub = [125 164 202 228 348;
            2754 3663 4551 5220 8400;
            0.098299 0.098299 0.098299 0.098298 0.098298;
            8.249 8.249 8.249 8.249 8.249;
            32.986 32.986 32.986 32.985 32.985;
            74.183 74.179 74.178 74.177 74.177;
            131.80 131.78 131.77 131.77 131.77;
            205.80 205.72 205.69 205.68 205.67]';
for n = 1:length(tetmeshcub(:,3))
    tetmeshcub(n,3) = abs(tetmeshcub(n,3)-disp_exact)*100/abs(disp_exact);
end
for n = 1:length(tetmeshcub(:,4))
    tetmeshcub(n,4) = abs(tetmeshcub(n,4)-w1_exact)*100/abs(w1_exact);
end
for n = 1:length(tetmeshcub(:,5))
    tetmeshcub(n,5) = abs(tetmeshcub(n,5)-w2_exact)*100/abs(w2_exact);
end
for n = 1:length(tetmeshcub(:,6))
    tetmeshcub(n,6) = abs(tetmeshcub(n,6)-w3_exact)*100/abs(w3_exact);
end
for n = 1:length(tetmeshcub(:,7))
    tetmeshcub(n,7) = abs(tetmeshcub(n,7)-w4_exact)*100/abs(w4_exact);
end
for n = 1:length(tetmeshcub(:,8))
    tetmeshcub(n,8) = abs(tetmeshcub(n,8)-w5_exact)*100/abs(w5_exact);
end

hexmeshlin = [10 14 20 30 50;
            132 180 252 372 612;
            0.0005416 0.0010559 0.0021311 0.0046685 0.011958;
            112.05 79.925 56.139 37.886 23.658;
            459.14 323.62 225.87 151.91 94.697]';
for n = 1:length(hexmeshlin(:,3))
```

```
    hexmeshlin(n,3) = abs(hexmeshlin(n,3)-disp_exact)*100/abs(disp_exact);
end
for n = 1:length(hexmeshlin(:,4))
    hexmeshlin(n,4) = abs(hexmeshlin(n,4)-w1_exact)*100/abs(w1_exact);
end
for n = 1:length(hexmeshlin(:,5))
    hexmeshlin(n,5) = abs(hexmeshlin(n,5)-w2_exact)*100/abs(w2_exact);
end

hexmeshquad = [2 4 6 8 10 14 20;
            135 243 351 459 567 783 1107;
            0.073735 0.092182 0.095594 0.096789 0.097341 0.097822 0.098076;
            9.1544 8.4639 8.3431 8.3014 8.2821 8.2655 8.2567;
            36.606 36.589 34.524 33.833 33.519 33.25 33.108
            200 92.264 82.221 78.55 76.912 75.522 74.8;
            300 146.17 157.61 145.91 140.54 136.05 133.74;
            1500 1099.5 260.38 240.69 227.44 216.2 210.5]';
for n = 1:length(hexmeshquad(:,3))
    hexmeshquad(n,3) = abs(hexmeshquad(n,3)-disp_exact)*100/abs(disp_exact);
end
for n = 1:length(hexmeshquad(:,4))
    hexmeshquad(n,4) = abs(hexmeshquad(n,4)-w1_exact)*100/abs(w1_exact);
end
for n = 1:length(hexmeshquad(:,5))
    hexmeshquad(n,5) = abs(hexmeshquad(n,5)-w2_exact)*100/abs(w2_exact);
end
for n = 1:length(hexmeshquad(:,6))
    hexmeshquad(n,6) = abs(hexmeshquad(n,6)-w3_exact)*100/abs(w3_exact);
end
for n = 1:length(hexmeshquad(:,7))
    hexmeshquad(n,7) = abs(hexmeshquad(n,7)-w4_exact)*100/abs(w4_exact);
end
for n = 1:length(hexmeshquad(:,8))
    hexmeshquad(n,8) = abs(hexmeshquad(n,8)-w5_exact)*100/abs(w5_exact);
end

hexmeshcub = [2 4 6 8 10;
            336 624 912 1200 1488;
            0.098299 0.098299 0.098299 0.098299 0.098299;
            8.82815 8.2511 8.2494 8.2491 8.2491;
            36.594 33.114 33.012 32.994 32.989;
            91.805 75.515 74.462 74.268 74.214;
            167.2 145.97 133.28 132.26 131.97;
            500 231.43 210.43 207.49 206.43]';
for n = 1:length(hexmeshcub(:,3))
    hexmeshcub(n,3) = abs(hexmeshcub(n,3)-disp_exact)*100/abs(disp_exact);
end
for n = 1:length(hexmeshcub(:,4))
    hexmeshcub(n,4) = abs(hexmeshcub(n,4)-w1_exact)*100/abs(w1_exact);
end
for n = 1:length(hexmeshcub(:,5))
    hexmeshcub(n,5) = abs(hexmeshcub(n,5)-w2_exact)*100/abs(w2_exact);
```

```
end
for n = 1:length(hexmeshcub(:,6))
    hexmeshcub(n,6) = abs(hexmeshcub(n,6)-w3_exact)*100/abs(w3_exact);
end
for n = 1:length(hexmeshcub(:,7))
    hexmeshcub(n,7) = abs(hexmeshcub(n,7)-w4_exact)*100/abs(w4_exact);
end
for n = 1:length(hexmeshcub(:,8))
    hexmeshcub(n,8) = abs(hexmeshcub(n,8)-w5_exact)*100/abs(w5_exact);
end

figure;
loglog( tetmeshcub(:,2),tetmeshcub(:,3),hexmeshcub(:,2),hexmeshcub(:,3),...
    tetmeshquad(:,2),tetmeshquad(:,3),hexmeshquad(:,2),hexmeshquad(:,3),...
    tetmeshlin(:,2),tetmeshlin(:,3),hexmeshlin(:,2),hexmeshlin(:,3))
xlabel('Number of Degrees of Freedom')
ylabel('Percent Error from Exact Answer')
legend('Cubic Tet Mesh','Cubic Hex Mesh','Quadratic Tet Mesh',...
    'Quadratic Hex Mesh','Linear Tet Mesh','Linear Hex Mesh')
title('Solution Efficiency: Beam Deflection (0.98 meters)')

figure;
loglog( tetmeshcub(:,2),tetmeshcub(:,4),hexmeshcub(:,2),hexmeshcub(:,4),...
    tetmeshquad(:,2),tetmeshquad(:,4),hexmeshquad(:,2),hexmeshquad(:,4),...
    tetmeshlin(:,2),tetmeshlin(:,4),hexmeshlin(:,2),hexmeshlin(:,4))
xlabel('Number of Degrees of Freedom')
ylabel('Percent Error from Exact Answer')
legend('Cubic Tet Mesh','Cubic Hex Mesh','Quadratic Tet Mesh',...
    'Quadratic Hex Mesh','Linear Tet Mesh','Linear Hex Mesh')
title('Solution Efficiency: Beam 1st Natural Frequency (8.25 Hz)')

figure;
loglog( tetmeshcub(:,2),tetmeshcub(:,5),hexmeshcub(:,2),hexmeshcub(:,5),...
    tetmeshquad(:,2),tetmeshquad(:,5),hexmeshquad(:,2),hexmeshquad(:,5),...
    tetmeshlin(:,2),tetmeshlin(:,5),hexmeshlin(:,2),hexmeshlin(:,5))
xlabel('Number of Degrees of Freedom')
ylabel('Percent Error from Exact Answer')
legend('Cubic Tet Mesh','Cubic Hex Mesh','Quadratic Tet Mesh',...
    'Quadratic Hex Mesh','Linear Tet Mesh','Linear Hex Mesh')
title('Solution Efficiency: Beam 2nd Natural Frequency (32.99 Hz)')

figure;
loglog(tetmeshcub(:,2),tetmeshcub(:,6),hexmeshcub(:,2),hexmeshcub(:,6),...
    tetmeshquad(:,2),tetmeshquad(:,6),hexmeshquad(:,2),hexmeshquad(:,6))
xlabel('Number of Degrees of Freedom')
ylabel('Percent Error from Exact Answer')
legend('Cubic Tet Mesh','Cubic Hex Mesh','Quadratic Tet Mesh',...
    'Quadratic Hex Mesh')
title('Solution Efficiency: Beam 3rd Natural Frequency (~74.18 Hz)')

figure;
loglog( tetmeshcub(:,2),tetmeshcub(:,7),hexmeshcub(:,2),hexmeshcub(:,7),...
    tetmeshquad(:,2),tetmeshquad(:,7),hexmeshquad(:,2),hexmeshquad(:,7))
xlabel('Number of Degrees of Freedom')
ylabel('Percent Error from Exact Answer')
legend('Cubic Tet Mesh','Cubic Hex Mesh','Quadratic Tet Mesh',...
    'Quadratic Hex Mesh')
title('Solution Efficiency: Beam 4th Natural Frequency (~131.77 Hz)')

figure;
loglog( tetmeshcub(:,2),tetmeshcub(:,8),hexmeshcub(:,2),hexmeshcub(:,8),...
    tetmeshquad(:,2),tetmeshquad(:,8),hexmeshquad(:,2),hexmeshquad(:,8))
xlabel('Number of Degrees of Freedom')
ylabel('Percent Error from Exact Answer')
legend('Cubic Tet Mesh','Cubic Hex Mesh','Quadratic Tet Mesh',...
    'Quadratic Hex Mesh')
title('Solution Efficiency: Beam 5th Natural Frequency (~205.67 Hz)')


% Upon viewing the graphs, goal will be to aim for a discretization in the
% final model similar to the Coarser Quadratic Hex Mesh, which is the 3rd
% row in the hexmeshquad matrix.
```

Deployment Envelope Calculations.

```
%% Displacement Envelope of Four Cell Truss Simulation
% Dylan Van Dyne 141219

clear all; clc; close all;

load('TrussC1C4_R3_disp.mat');
len = length(C1C4_R3_disp)/24;
h = 5.31;
w = 8.74;

% Cell 4 extrapolations
c4pxny = zeros(len,6);
c4nxpy = zeros(len,6);
c4pxny(:,1) = (w/2)+C1C4_R3_disp(1:24:end)';
c4pxny(:,2) = -(h/2)+C1C4_R3_disp(2:24:end)';
c4pxny(:,3) = C1C4_R3_disp(3:24:end)';
c4pxny(:,4) = C1C4_R3_disp(4:24:end)';
c4pxny(:,5) = C1C4_R3_disp(5:24:end)';
c4pxny(:,6) = C1C4_R3_disp(6:24:end)';
c4nxpy(:,1) = c4pxny(:,1)-w*cos(c4pxny(:,5));
c4nxpy(:,2) = c4pxny(:,2)+h*cos(c4pxny(:,4));
c4nxpy(:,3) = c4pxny(:,3)+h*sin(c4pxny(:,4));

% Cell 3 extrapolations
c3pxny = zeros(len,6);
c3nxpy = zeros(len,6);
c3pxny(:,1) = (w/2)+C1C4_R3_disp(7:24:end)';
c3pxny(:,2) = -(h/2)+C1C4_R3_disp(8:24:end)';
```

```
c3pxny(:,3) = C1C4_R3_disp(9:24:end)';
c3pxny(:,4) = C1C4_R3_disp(10:24:end)';
c3pxny(:,5) = C1C4_R3_disp(11:24:end)';
c3pxny(:,6) = C1C4_R3_disp(12:24:end)';
c3nxpy(:,1) = c3pxny(:,1)-w*cos(c3pxny(:,5));
c3nxpy(:,2) = c3pxny(:,2)+h*cos(c3pxny(:,4));
c3nxpy(:,3) = c3pxny(:,3)+h*sin(c3pxny(:,4));

% Cell 2 extrapolations
c2pxny = zeros(len,6);
c2nxpy = zeros(len,6);
c2pxny(:,1) = (w/2)+C1C4_R3_disp(13:24:end)';
c2pxny(:,2) = -(h/2)+C1C4_R3_disp(14:24:end)';
c2pxny(:,3) = C1C4_R3_disp(15:24:end)';
c2pxny(:,4) = C1C4_R3_disp(16:24:end)';
c2pxny(:,5) = C1C4_R3_disp(17:24:end)';
c2pxny(:,6) = C1C4_R3_disp(18:24:end)';
c2nxpy(:,1) = c2pxny(:,1)-w*cos(c2pxny(:,5));
c2nxpy(:,2) = c2pxny(:,2)+h*cos(c2pxny(:,4));
c2nxpy(:,3) = c2pxny(:,3)+h*sin(c2pxny(:,4));

% Cell 1 extrapolations
c1pxny = zeros(len,6);
c1nxpy = zeros(len,6);
c1pxny(:,1) = (w/2)+C1C4_R3_disp(19:24:end)';
c1pxny(:,2) = -(h/2)+C1C4_R3_disp(20:24:end)';
c1pxny(:,3) = C1C4_R3_disp(21:24:end)';
c1pxny(:,4) = C1C4_R3_disp(22:24:end)';
c1pxny(:,5) = C1C4_R3_disp(23:24:end)';
c1pxny(:,6) = C1C4_R3_disp(24:24:end)';
c1nxpy(:,1) = c1pxny(:,1)-w*cos(c1pxny(:,5));
c1nxpy(:,2) = c1pxny(:,2)+h*cos(c1pxny(:,4));
c1nxpy(:,3) = c1pxny(:,3)+h*sin(c1pxny(:,4));

% Maximum/Minimum solution for bounding box
xMax = [max(c1pxny(:,1)) max(c2pxny(:,1)) max(c3pxny(:,1)) max(c4pxny(:,1))];
xMin = [min(c1nxpy(:,1)) min(c2nxpy(:,1)) min(c3nxpy(:,1)) min(c4nxpy(:,1))];
xUpperBound = max(xMax)
xLowerBound = min(xMin)
yMax = [max(c1nxpy(:,2)) max(c2nxpy(:,2)) max(c3nxpy(:,2)) max(c4nxpy(:,2))];
yMin = [min(c1pxny(:,2)) min(c2pxny(:,2)) min(c3pxny(:,2)) min(c4pxny(:,2))];
yUpperBound = max(yMax)
yLowerBound = min(yMin)
zMax = [max(c1pxny(:,3)) max(c2pxny(:,3)) max(c3pxny(:,3)) max(c4pxny(:,3))...
    max(c1nxpy(:,3))  max(c2nxpy(:,3))  max(c3nxpy(:,3))  max(c4nxpy(:,3))];
zMin = [min(c1pxny(:,3)) min(c2pxny(:,3)) min(c3pxny(:,3)) min(c4pxny(:,3))...
    min(c1nxpy(:,3))  min(c2nxpy(:,3))  min(c3nxpy(:,3))  min(c4nxpy(:,3))];
zUpperBound = max(zMax)
zLowerBound = min(zMin)
```

Cable Length Calculations, Completed Deployment Envelope, and Weakened Hinge Visualization.

```
%% Cable Lengths Calculations
% Dylan Van Dyne 10 Dec 2014

clear all; clc; close all;

%% Calculating Cable Lengths
% Assuming the desired resting tension for these cables is 10N, with 25
% N/m spring constant, so the x0 is set to 0.2 meters.  Setting back
% corners of cells to 90 degrees with this method.

F = 10; % Desired force
k = 25; % Cable spring constant
str = F/k   % Desired stretch in cables

vb = 5.310-0.0255; % Vertical batten length (adjusted for corners)
hb = 8.74-.102;    % Horizontal batten length (adjusted for corners)
c1_top = 4.583*2;   % Cell 1 top length (adjusted for joints)
c1_bot = 4.7215*2;  % Cell 1 bottom length (adjusted for joints)
c1_nypy = sqrt(vb^2+c1_top^2)-str
c1_pyny = sqrt(vb^2+c1_bot^2)-str
c1_py = sqrt(hb^2+c1_top^2)-str
c1_ny = sqrt(hb^2+c1_bot^2)-str
c2_top = 4.598*2;
c2_bot = 4.7385*2;
c2_nypy = sqrt(vb^2+c2_top^2)-str
c2_pyny = sqrt(vb^2+c2_bot^2)-str
c2_py = sqrt(hb^2+c2_top^2)-str
c2_ny = sqrt(hb^2+c2_bot^2)-str
c3_top = 4.6285*2;
c3_bot = 4.7725*2;
c3_nypy = sqrt(vb^2+c3_top^2)-str
c3_pyny = sqrt(vb^2+c3_bot^2)-str
c3_py = sqrt(hb^2+c3_top^2)-str
c3_ny = sqrt(hb^2+c3_bot^2)-str
c4_top = 4.6735*2;
c4_bot = 4.823*2;
c4_nypy = sqrt(vb^2+c4_top^2)-str
c4_pyny = sqrt(vb^2+c4_bot^2)-str
c4_py = sqrt(hb^2+c4_top^2)-str
c4_ny = sqrt(hb^2+c4_bot^2)-str

%% Determining Completed Geometry Envelope
xmax = (8.74+.202)/2
lg_adj = 0.051;  % Longeron corner
theta_f1 = atand(vb/(c1_bot-c1_top));   % Forward angle of cell
theta_c1r = 90-theta_f1;    % Cell 1 raise angle
c2_zdist = (lg_adj+c2_bot)*cosd(theta_c1r);   % Adjusted y distance for Cell 2
theta_f2 = atand(vb/(c2_bot-c2_top));
theta_c2r = 90-theta_f2+theta_c1r;
c3_zdist = (lg_adj+c3_bot)*cosd(theta_c2r);
theta_f3 = atand(vb/(c3_bot-c3_top));
theta_c3r = 90-theta_f3+theta_c2r+theta_c1r;
```

```
c4_zdist = (lg_adj+c4_bot)*cosd(theta_c3r);
c2_ydist = c2_top*sind(theta_c1r);
c3_ydist = c3_top*sind(theta_c2r);
c4_ydist = c4_top*sind(theta_c3r);
ymax = vb/2+c2_ydist+c3_ydist+c4_ydist
zmax = c1_bot+c2_zdist+c3_zdist+c4_zdist

%% Draw Deployed Truss Arm
figure;
c1z = [0 0 c1_bot c1_top 0];
c1y = [vb/2 -vb/2 -vb/2 vb/2 vb/2];
c2_blx = c1_bot;
c2_bly = -vb/2;
c2_tlx = c1_top;
c2_tly = vb/2;
c2_trx = c1_top+c2_top*cosd(theta_c1r);
c2_try = vb/2+c2_top*sind(theta_c1r);
c2_brx = c1_bot+c2_bot*cosd(theta_c1r);
c2_bry = -vb/2+c2_bot*sind(theta_c1r);
c2z = [c2_blx c2_tlx c2_trx c2_brx c2_blx];
c2y = [c2_bly c2_tly c2_try c2_bry c2_bly];
c3_blx = c2_brx;
c3_bly = c2_bry;
c3_tlx = c2_trx;
c3_tly = c2_try;
c3_trx = c2_trx+c3_top*cosd(theta_c2r);
c3_try = c2_try+c3_top*sind(theta_c2r);
c3_brx = c2_brx+c3_bot*cosd(theta_c2r);
c3_bry = c2_bry+c3_bot*sind(theta_c2r);
c3z = [c3_blx c3_tlx c3_trx c3_brx c3_blx];
c3y = [c3_bly c3_tly c3_try c3_bry c3_bly];
c4_blx = c3_brx;
c4_bly = c3_bry;
c4_tlx = c3_trx;
c4_tly = c3_try;
c4_trx = c3_trx+c4_top*cosd(theta_c3r);
c4_try = c3_try+c4_top*sind(theta_c3r);
c4_brx = c3_brx+c4_bot*cosd(theta_c3r);
c4_bry = c3_bry+c4_bot*sind(theta_c3r);
c4z = [c4_blx c4_tlx c4_trx c4_brx c4_blx];
c4y = [c4_bly c4_tly c4_try c4_bry c4_bly];
% C1 Upper
subplot(4,2,1)
hold on
title('Weak Hinge in an Upper Longeron of Cell 1 (Success)')
plot(c1z(1:2),c1y(1:2),'k')
plot(c1z(4:5),c1y(4:5),':b')
plot(c1z(3:4),c1y(3:4),'k')
plot(c1z(2:3),c1y(2:3),'b')
plot(c2z(2:3),c2y(2:3),'b')
plot(c2z(3:4),c2y(3:4),'k')
plot(c2z(4:5),c2y(4:5),'b','LineWidth',2)
plot(c3z(2:3),c3y(2:3),'b')
plot(c3z(3:4),c3y(3:4),'k')
plot(c3z(4:5),c3y(4:5),'b','LineWidth',3)
plot(c4z(2:3),c4y(2:3),'b')
plot(c4z(3:4),c4y(3:4),'k')
plot(c4z(4:5),c4y(4:5),'b','LineWidth',6)
axis('equal')
axis([0 40 -5 10])
xlabel('Z Axis (m)')
ylabel('Y Axis (m)')
hold off
% C1 Lower
subplot(4,2,2)
hold on
title('Weak Hinge in a Lower Longeron of Cell 1 (Fail)')
plot(c1z(1:2),c1y(1:2),'k')
plot(c1z(4:5),c1y(4:5),'r')
plot(c1z(3:4),c1y(3:4),'k')
plot(c1z(2:3),c1y(2:3),':r')
plot(c2z(2:3),c2y(2:3),'r')
plot(c2z(3:4),c2y(3:4),'k')
plot(c2z(4:5),c2y(4:5),'r','LineWidth',2)
plot(c3z(2:3),c3y(2:3),'r')
plot(c3z(3:4),c3y(3:4),'k')
plot(c3z(4:5),c3y(4:5),'r','LineWidth',3)
plot(c4z(2:3),c4y(2:3),'r')
plot(c4z(3:4),c4y(3:4),'k')
plot(c4z(4:5),c4y(4:5),'w')
axis('equal')
axis([0 40 -5 10])
xlabel('Z Axis (m)')
ylabel('Y Axis (m)')
hold off
% C2 Upper
subplot(4,2,3)
hold on
title('Weak Hinge in an Upper Longeron of Cell 2 (Fail)')
plot(c1z(1:2),c1y(1:2),'k')
plot(c1z(4:5),c1y(4:5),'r')
plot(c1z(3:4),c1y(3:4),'k')
plot(c1z(2:3),c1y(2:3),'r')
plot(c2z(2:3),c2y(2:3),':r','LineWidth',2)
plot(c2z(3:4),c2y(3:4),'k')
plot(c2z(4:5),c2y(4:5),'r')
plot(c3z(2:3),c3y(2:3),'r')
plot(c3z(3:4),c3y(3:4),'k')
plot(c3z(4:5),c3y(4:5),'r','LineWidth',3)
plot(c4z(2:3),c4y(2:3),'r')
plot(c4z(3:4),c4y(3:4),'k')
plot(c4z(4:5),c4y(4:5),'w')
axis('equal')
axis([0 40 -5 10])
```

```
xlabel('Z Axis (m)')
ylabel('Y Axis (m)')
hold off
% C2 Lower
subplot(4,2,4)
hold on
title('Weak Hinge in a Lower Longeron of Cell 2 (Fail)')
plot(c1z(1:2),c1y(1:2),'k')
plot(c1z(4:5),c1y(4:5),'w')
plot(c1z(3:4),c1y(3:4),'k')
plot(c1z(2:3),c1y(2:3),'r')
plot(c2z(2:3),c2y(2:3),'r')
plot(c2z(3:4),c2y(3:4),'k')
plot(c2z(4:5),c2y(4:5),':r','LineWidth',2)
plot(c3z(2:3),c3y(2:3),'r','LineWidth',2)
plot(c3z(3:4),c3y(3:4),'k')
plot(c3z(4:5),c3y(4:5),'r','LineWidth',4)
plot(c4z(2:3),c4y(2:3),'r')
plot(c4z(3:4),c4y(3:4),'k')
plot(c4z(4:5),c4y(4:5),'w')
axis('equal')
axis([0 40 -5 10])
xlabel('Z Axis (m)')
ylabel('Y Axis (m)')
hold off
% C3 Upper
subplot(4,2,5)
hold on
title('Weak Hinge in an Upper Longeron of Cell 3 (Success)')
plot(c1z(1:2),c1y(1:2),'k')
plot(c1z(4:5),c1y(4:5),'b')
plot(c1z(3:4),c1y(3:4),'k')
plot(c1z(2:3),c1y(2:3),'b')
plot(c2z(2:3),c2y(2:3),'b')
plot(c2z(3:4),c2y(3:4),'k')
plot(c2z(4:5),c2y(4:5),'b','LineWidth',2)
plot(c3z(2:3),c3y(2:3),':b','LineWidth',2)
plot(c3z(3:4),c3y(3:4),'k')
plot(c3z(4:5),c3y(4:5),'b')
plot(c4z(2:3),c4y(2:3),'b')
plot(c4z(3:4),c4y(3:4),'k')
plot(c4z(4:5),c4y(4:5),'b','LineWidth',6)
axis('equal')
axis([0 40 -5 10])
xlabel('Z Axis (m)')
ylabel('Y Axis (m)')
hold off
% C3 Lower
subplot(4,2,6)
hold on
title('Weak Hinge in a Lower Longeron of Cell 3 (Success)')
plot(c1z(1:2),c1y(1:2),'k')
plot(c1z(4:5),c1y(4:5),'b')
plot(c1z(3:4),c1y(3:4),'k')
plot(c1z(2:3),c1y(2:3),'b')
plot(c2z(2:3),c2y(2:3),'b')
plot(c2z(3:4),c2y(3:4),'k')
plot(c2z(4:5),c2y(4:5),'b')
plot(c3z(2:3),c3y(2:3),'b')
plot(c3z(3:4),c3y(3:4),'k')
plot(c3z(4:5),c3y(4:5),':b','LineWidth',3)
plot(c4z(2:3),c4y(2:3),'b')
plot(c4z(3:4),c4y(3:4),'k')
plot(c4z(4:5),c4y(4:5),'b')
axis('equal')
axis([0 40 -5 10])
xlabel('Z Axis (m)')
ylabel('Y Axis (m)')
hold off
% C4 Upper
subplot(4,2,7)
hold on
title('Weak Hinge in an Upper Longeron of Cell 4 (Success)')
plot(c1z(1:2),c1y(1:2),'k')
plot(c1z(4:5),c1y(4:5),'b')
plot(c1z(3:4),c1y(3:4),'k')
plot(c1z(2:3),c1y(2:3),'b')
plot(c2z(2:3),c2y(2:3),'b')
plot(c2z(3:4),c2y(3:4),'k')
plot(c2z(4:5),c2y(4:5),'b','LineWidth',2)
plot(c3z(2:3),c3y(2:3),'b')
plot(c3z(3:4),c3y(3:4),'k')
plot(c3z(4:5),c3y(4:5),'b','LineWidth',4)
plot(c4z(2:3),c4y(2:3),':b','LineWidth',4)
plot(c4z(3:4),c4y(3:4),'k')
plot(c4z(4:5),c4y(4:5),'b')
axis('equal')
axis([0 40 -5 10])
xlabel('Z Axis (m)')
ylabel('Y Axis (m)')
hold off
% C4 Lower
subplot(4,2,8)
hold on
title('Weak Hinge in a Lower Longeron of Cell 4 (Fail)')
plot(c1z(1:2),c1y(1:2),'k')
plot(c1z(4:5),c1y(4:5),'r')
plot(c1z(3:4),c1y(3:4),'k')
plot(c1z(2:3),c1y(2:3),'r')
plot(c2z(2:3),c2y(2:3),'r')
plot(c2z(3:4),c2y(3:4),'k')
plot(c2z(4:5),c2y(4:5),'r','LineWidth',2)
plot(c3z(2:3),c3y(2:3),'r')
plot(c3z(3:4),c3y(3:4),'k')
plot(c3z(4:5),c3y(4:5),'r','LineWidth',3)
plot(c4z(2:3),c4y(2:3),'r')
plot(c4z(3:4),c4y(3:4),'k')
plot(c4z(4:5),c4y(4:5),'w')
axis('equal')
axis([0 40 -5 10])
xlabel('Z Axis (m)')
ylabel('Y Axis (m)')
hold off
```

6.2 Appendix B - Simulation Import Files Examples

Simulation Parameter Input File.

ks 5 Spring Constant
thl 3.14 Locking Angle
k 50 Cable Spring Constant
c 5 Cable Damping Constant
l.c1.nypy 10.3802
l.c1.pyny 10.6211
l.c1.py 12.3949
l.c1.ny 12.5979
l.c2.nypy 10.4062
l.c2.pyny 10.6508
l.c2.py 12.4167
l.c2.ny 12.6230
l.c3.nypy 10.4592
l.c3.pyny 10.7102
l.c3.py 12.4612
l.c3.ny 12.6733
l.c4.nypy 10.5374
l.c4.pyny 10.7987
l.c4.py 12.5272
l.c4.ny 12.7484

Truss Cell 1 Cable File.

mbd.dsj1.xsx mbd.att6.xcx
mbd.dsj1.xsy mbd.att6.xcy
mbd.dsj1.xsz mbd.att6.xcz
mbd.dsj1.xdx mbd.att7.xcx
mbd.dsj1.xdy mbd.att7.xcy
mbd.dsj1.xdz mbd.att7.xcz
mbd.dsj1.uc.src mbd.att6.u
mbd.dsj1.vc.src mbd.att6.v

```
mbd.dsj1.wc.src mbd.att6.w
mbd.dsj1.uc.dest mbd.att7.u
mbd.dsj1.vc.dest mbd.att7.v
mbd.dsj1.wc.dest mbd.att7.w
c1.NXnypy.dist sqrt((mbd.dsj1.xsx+mbd.dsj1.uc.src-mbd.dsj1.xdx-mbd.dsj1.uc.dest)ˆ2
+(mbd.dsj1.xsy+mbd.dsj1.vc.src-mbd.dsj1.xdy-mbd.dsj1.vc.dest)ˆ2
+(mbd.dsj1.xsz+mbd.dsj1.wc.src-mbd.dsj1.xdz-mbd.dsj1.wc.dest)ˆ2+eps)
c1.NXnypy.distx (mbd.dsj1.xsx+mbd.dsj1.uc.src-mbd.dsj1.xdx-mbd.dsj1.uc.dest)
/c1.NXnypy.dist
c1.NXnypy.disty (mbd.dsj1.xsy+mbd.dsj1.vc.src-mbd.dsj1.xdy-mbd.dsj1.vc.dest)
/c1.NXnypy.dist
c1.NXnypy.distz (mbd.dsj1.xsz+mbd.dsj1.wc.src-mbd.dsj1.xdz-mbd.dsj1.wc.dest)
/c1.NXnypy.dist
c1.NXnypy.damp d(c1.NXnypy.dist,TIME)
c1.NXnypy.sw c1.NXnypy.dist¿l.c1.nypy
c1.NXnypy.f (k*(l.c1.nypy-c1.NXnypy.dist)
-c*(c1.NXnypy.damp¿0)*c1.NXnypy.damp)*c1.NXnypy.sw
c1.NXnypy.Ws c1.NXnypy.sw*.5*k*(l.c1.nypy-c1.NXnypy.dist)ˆ2
c1.NXnypy.fx c1.NXnypy.f*c1.NXnypy.distx
c1.NXnypy.fy c1.NXnypy.f*c1.NXnypy.disty
c1.NXnypy.fz c1.NXnypy.f*c1.NXnypy.distz
mbd.dsj2.xsx mbd.att12.xcx
mbd.dsj2.xsy mbd.att12.xcy
mbd.dsj2.xsz mbd.att12.xcz
mbd.dsj2.xdx mbd.att1.xcx
mbd.dsj2.xdy mbd.att1.xcy
mbd.dsj2.xdz mbd.att1.xcz
mbd.dsj2.uc.src mbd.att12.u
mbd.dsj2.vc.src mbd.att12.v
mbd.dsj2.wc.src mbd.att12.w
mbd.dsj2.uc.dest mbd.att1.u
mbd.dsj2.vc.dest mbd.att1.v
mbd.dsj2.wc.dest mbd.att1.w
c1.NXpyny.dist sqrt((mbd.dsj2.xsx+mbd.dsj2.uc.src-mbd.dsj2.xdx-mbd.dsj2.uc.dest)ˆ2
+(mbd.dsj2.xsy+mbd.dsj2.vc.src-mbd.dsj2.xdy-mbd.dsj2.vc.dest)ˆ2
+(mbd.dsj2.xsz+mbd.dsj2.wc.src-mbd.dsj2.xdz-mbd.dsj2.wc.dest)ˆ2+eps)
c1.NXpyny.distx (mbd.dsj2.xsx+mbd.dsj2.uc.src-mbd.dsj2.xdx-mbd.dsj2.uc.dest)
/c1.NXpyny.dist
c1.NXpyny.disty (mbd.dsj2.xsy+mbd.dsj2.vc.src-mbd.dsj2.xdy-mbd.dsj2.vc.dest)
/c1.NXpyny.dist
c1.NXpyny.distz (mbd.dsj2.xsz+mbd.dsj2.wc.src-mbd.dsj2.xdz-mbd.dsj2.wc.dest)
/c1.NXpyny.dist
c1.NXpyny.damp d(c1.NXpyny.dist,TIME)
```

```
c1.NXpyny.sw c1.NXpyny.dist¿l.c1.pyny
c1.NXpyny.f (k*(l.c1.pyny-c1.NXpyny.dist)
-c*(c1.NXpyny.damp¿0)*c1.NXpyny.damp)*c1.NXpyny.sw
c1.NXpyny.Ws c1.NXpyny.sw*.5*k*(l.c1.pyny-c1.NXpyny.dist)ˆ2
c1.NXpyny.fx c1.NXpyny.f*c1.NXpyny.distx
c1.NXpyny.fy c1.NXpyny.f*c1.NXpyny.disty
c1.NXpyny.fz c1.NXpyny.f*c1.NXpyny.distz
mbd.dsj3.xsx mbd.att18.xcx
mbd.dsj3.xsy mbd.att18.xcy
mbd.dsj3.xsz mbd.att18.xcz
mbd.dsj3.xdx mbd.att19.xcx
mbd.dsj3.xdy mbd.att19.xcy
mbd.dsj3.xdz mbd.att19.xcz
mbd.dsj3.uc.src mbd.att18.u
mbd.dsj3.vc.src mbd.att18.v
mbd.dsj3.wc.src mbd.att18.w
mbd.dsj3.uc.dest mbd.att19.u
mbd.dsj3.vc.dest mbd.att19.v
mbd.dsj3.wc.dest mbd.att19.w
c1.PXnypy.dist sqrt((mbd.dsj3.xsx+mbd.dsj3.uc.src-mbd.dsj3.xdx-mbd.dsj3.uc.dest)ˆ2
+(mbd.dsj3.xsy+mbd.dsj3.vc.src-mbd.dsj3.xdy-mbd.dsj3.vc.dest)ˆ2
+(mbd.dsj3.xsz+mbd.dsj3.wc.src-mbd.dsj3.xdz-mbd.dsj3.wc.dest)ˆ2+eps)
c1.PXnypy.distx (mbd.dsj3.xsx+mbd.dsj3.uc.src-mbd.dsj3.xdx-mbd.dsj3.uc.dest)
/c1.PXnypy.dist
c1.PXnypy.disty (mbd.dsj3.xsy+mbd.dsj3.vc.src-mbd.dsj3.xdy-mbd.dsj3.vc.dest)
/c1.PXnypy.dist
c1.PXnypy.distz (mbd.dsj3.xsz+mbd.dsj3.wc.src-mbd.dsj3.xdz-mbd.dsj3.wc.dest)
/c1.PXnypy.dist
c1.PXnypy.damp d(c1.PXnypy.dist,TIME)
c1.PXnypy.sw c1.PXnypy.dist¿l.c1.nypy
c1.PXnypy.f (k*(l.c1.nypy-c1.PXnypy.dist)
-c*(c1.PXnypy.damp¿0)*c1.PXnypy.damp)*c1.PXnypy.sw
c1.PXnypy.Ws c1.PXnypy.sw*.5*k*(l.c1.nypy-c1.PXnypy.dist)ˆ2
c1.PXnypy.fx c1.PXnypy.f*c1.PXnypy.distx
c1.PXnypy.fy c1.PXnypy.f*c1.PXnypy.disty
c1.PXnypy.fz c1.PXnypy.f*c1.PXnypy.distz
mbd.dsj4.xsx mbd.att24.xcx
mbd.dsj4.xsy mbd.att24.xcy
mbd.dsj4.xsz mbd.att24.xcz
mbd.dsj4.xdx mbd.att13.xcx
mbd.dsj4.xdy mbd.att13.xcy
mbd.dsj4.xdz mbd.att13.xcz
mbd.dsj4.uc.src mbd.att24.u
mbd.dsj4.vc.src mbd.att24.v
mbd.dsj4.wc.src mbd.att24.w
mbd.dsj4.uc.dest mbd.att13.u
mbd.dsj4.vc.dest mbd.att13.v
mbd.dsj4.wc.dest mbd.att13.w
c1.PXpyny.dist sqrt((mbd.dsj4.xsx+mbd.dsj4.uc.src-mbd.dsj4.xdx-mbd.dsj4.uc.dest)ˆ2
+(mbd.dsj4.xsy+mbd.dsj4.vc.src-mbd.dsj4.xdy-mbd.dsj4.vc.dest)ˆ2
+(mbd.dsj4.xsz+mbd.dsj4.wc.src-mbd.dsj4.xdz-mbd.dsj4.wc.dest)ˆ2+eps)
c1.PXpyny.distx (mbd.dsj4.xsx+mbd.dsj4.uc.src-mbd.dsj4.xdx-mbd.dsj4.uc.dest)
/c1.PXpyny.dist
c1.PXpyny.disty (mbd.dsj4.xsy+mbd.dsj4.vc.src-mbd.dsj4.xdy-mbd.dsj4.vc.dest)
/c1.PXpyny.dist
c1.PXpyny.distz (mbd.dsj4.xsz+mbd.dsj4.wc.src-mbd.dsj4.xdz-mbd.dsj4.wc.dest)
/c1.PXpyny.dist
c1.PXpyny.damp d(c1.PXpyny.dist,TIME)
c1.PXpyny.sw c1.PXpyny.dist¿l.c1.pyny
c1.PXpyny.f (k*(l.c1.pyny-c1.PXpyny.dist)
-c*(c1.PXpyny.damp¿0)*c1.PXpyny.damp)*c1.PXpyny.sw
c1.PXpyny.Ws c1.PXpyny.sw*.5*k*(l.c1.pyny-c1.PXpyny.dist)ˆ2
c1.PXpyny.fx c1.PXpyny.f*c1.PXpyny.distx
c1.PXpyny.fy c1.PXpyny.f*c1.PXpyny.disty
c1.PXpyny.fz c1.PXpyny.f*c1.PXpyny.distz
mbd.dsj5.xsx mbd.att18.xcx
mbd.dsj5.xsy mbd.att18.xcy
mbd.dsj5.xsz mbd.att18.xcz
mbd.dsj5.xdx mbd.att1.xcx
mbd.dsj5.xdy mbd.att1.xcy
mbd.dsj5.xdz mbd.att1.xcz
mbd.dsj5.uc.src mbd.att18.u
mbd.dsj5.vc.src mbd.att18.v
mbd.dsj5.wc.src mbd.att18.w
mbd.dsj5.uc.dest mbd.att1.u
mbd.dsj5.vc.dest mbd.att1.v
mbd.dsj5.wc.dest mbd.att1.w
c1.nxpxPY.dist sqrt((mbd.dsj5.xsx+mbd.dsj5.uc.src-mbd.dsj5.xdx-mbd.dsj5.uc.dest)ˆ2
+(mbd.dsj5.xsy+mbd.dsj5.vc.src-mbd.dsj5.xdy-mbd.dsj5.vc.dest)ˆ2
+(mbd.dsj5.xsz+mbd.dsj5.wc.src-mbd.dsj5.xdz-mbd.dsj5.wc.dest)ˆ2+eps)
c1.nxpxPY.distx (mbd.dsj5.xsx+mbd.dsj5.uc.src-mbd.dsj5.xdx-mbd.dsj5.uc.dest)
/c1.nxpxPY.dist
c1.nxpxPY.disty (mbd.dsj5.xsy+mbd.dsj5.vc.src-mbd.dsj5.xdy-mbd.dsj5.vc.dest)
/c1.nxpxPY.dist
c1.nxpxPY.distz (mbd.dsj5.xsz+mbd.dsj5.wc.src-mbd.dsj5.xdz-mbd.dsj5.wc.dest)
/c1.nxpxPY.dist
```

```
c1.nxpxPY.damp d(c1.nxpxPY.dist,TIME)
c1.nxpxPY.sw c1.nxpxPY.dist¿l.c1.py
c1.nxpxPY.f (k*(l.c1.py-c1.nxpxPY.dist)
-c*(c1.nxpxPY.damp¿0)*c1.nxpxPY.damp)*c1.nxpxPY.sw
c1.nxpxPY.Ws c1.nxpxPY.sw*.5*k*(l.c1.py-c1.nxpxPY.dist)ˆ2
c1.nxpxPY.fx c1.nxpxPY.f*c1.nxpxPY.distx
c1.nxpxPY.fy c1.nxpxPY.f*c1.nxpxPY.disty
c1.nxpxPY.fz c1.nxpxPY.f*c1.nxpxPY.distz
mbd.dsj6.xsx mbd.att6.xcx
mbd.dsj6.xsy mbd.att6.xcy
mbd.dsj6.xsz mbd.att6.xcz
mbd.dsj6.xdx mbd.att13.xcx
mbd.dsj6.xdy mbd.att13.xcy
mbd.dsj6.xdz mbd.att13.xcz
mbd.dsj6.uc.src mbd.att6.u
mbd.dsj6.vc.src mbd.att6.v
mbd.dsj6.wc.src mbd.att6.w
mbd.dsj6.uc.dest mbd.att13.u
mbd.dsj6.vc.dest mbd.att13.v
mbd.dsj6.wc.dest mbd.att13.w
c1.pxnxPY.dist sqrt((mbd.dsj6.xsx+mbd.dsj6.uc.src-mbd.dsj6.xdx-mbd.dsj6.uc.dest)ˆ2
+(mbd.dsj6.xsy+mbd.dsj6.vc.src-mbd.dsj6.xdy-mbd.dsj6.vc.dest)ˆ2
+(mbd.dsj6.xsz+mbd.dsj6.wc.src-mbd.dsj6.xdz-mbd.dsj6.wc.dest)ˆ2+eps)
c1.pxnxPY.distx (mbd.dsj6.xsx+mbd.dsj6.uc.src-mbd.dsj6.xdx-mbd.dsj6.uc.dest)
/c1.pxnxPY.dist
c1.pxnxPY.disty (mbd.dsj6.xsy+mbd.dsj6.vc.src-mbd.dsj6.xdy-mbd.dsj6.vc.dest)
/c1.pxnxPY.dist
c1.pxnxPY.distz (mbd.dsj6.xsz+mbd.dsj6.wc.src-mbd.dsj6.xdz-mbd.dsj6.wc.dest)
/c1.pxnxPY.dist
c1.pxnxPY.damp d(c1.pxnxPY.dist,TIME)
c1.pxnxPY.sw c1.pxnxPY.dist¿l.c1.py
c1.pxnxPY.f (k*(l.c1.py-c1.pxnxPY.dist)
-c*(c1.pxnxPY.damp¿0)*c1.pxnxPY.damp)*c1.pxnxPY.sw
c1.pxnxPY.Ws c1.pxnxPY.sw*.5*k*(l.c1.py-c1.pxnxPY.dist)ˆ2
c1.pxnxPY.fx c1.pxnxPY.f*c1.pxnxPY.distx
c1.pxnxPY.fy c1.pxnxPY.f*c1.pxnxPY.disty
c1.pxnxPY.fz c1.pxnxPY.f*c1.pxnxPY.distz
mbd.dsj7.xsx mbd.att24.xcx
mbd.dsj7.xsy mbd.att24.xcy
mbd.dsj7.xsz mbd.att24.xcz
mbd.dsj7.xdx mbd.att7.xcx
mbd.dsj7.xdy mbd.att7.xcy
mbd.dsj7.xdz mbd.att7.xcz
mbd.dsj7.uc.src mbd.att24.u
mbd.dsj7.vc.src mbd.att24.v
mbd.dsj7.wc.src mbd.att24.w
mbd.dsj7.uc.dest mbd.att7.u
mbd.dsj7.vc.dest mbd.att7.v
mbd.dsj7.wc.dest mbd.att7.w
c1.nxpxNY.dist sqrt((mbd.dsj7.xsx+mbd.dsj7.uc.src-mbd.dsj7.xdx-mbd.dsj7.uc.dest)^2
+(mbd.dsj7.xsy+mbd.dsj7.vc.src-mbd.dsj7.xdy-mbd.dsj7.vc.dest)^2
+(mbd.dsj7.xsz+mbd.dsj7.wc.src-mbd.dsj7.xdz-mbd.dsj7.wc.dest)^2+eps)
c1.nxpxNY.distx (mbd.dsj7.xsx+mbd.dsj7.uc.src-mbd.dsj7.xdx-mbd.dsj7.uc.dest)
/c1.nxpxNY.dist
c1.nxpxNY.disty (mbd.dsj7.xsy+mbd.dsj7.vc.src-mbd.dsj7.xdy-mbd.dsj7.vc.dest)
/c1.nxpxNY.dist
c1.nxpxNY.distz (mbd.dsj7.xsz+mbd.dsj7.wc.src-mbd.dsj7.xdz-mbd.dsj7.wc.dest)
/c1.nxpxNY.dist
c1.nxpxNY.damp d(c1.nxpxNY.dist,TIME)
c1.nxpxNY.sw c1.nxpxNY.dist¿l.c1.ny
c1.nxpxNY.f (k*(l.c1.ny-c1.nxpxNY.dist)
-c*(c1.nxpxNY.damp¿0)*c1.nxpxNY.damp)*c1.nxpxNY.sw
c1.nxpxNY.Ws c1.nxpxNY.sw*.5*k*(l.c1.ny-c1.nxpxNY.dist)^2
c1.nxpxNY.fx c1.nxpxNY.f*c1.nxpxNY.distx
c1.nxpxNY.fy c1.nxpxNY.f*c1.nxpxNY.disty
c1.nxpxNY.fz c1.nxpxNY.f*c1.nxpxNY.distz
mbd.dsj8.xsx mbd.att12.xcx
mbd.dsj8.xsy mbd.att12.xcy
mbd.dsj8.xsz mbd.att12.xcz
mbd.dsj8.xdx mbd.att19.xcx
mbd.dsj8.xdy mbd.att19.xcy
mbd.dsj8.xdz mbd.att19.xcz
mbd.dsj8.uc.src mbd.att12.u
mbd.dsj8.vc.src mbd.att12.v
mbd.dsj8.wc.src mbd.att12.w
mbd.dsj8.uc.dest mbd.att19.u
mbd.dsj8.vc.dest mbd.att19.v
mbd.dsj8.wc.dest mbd.att19.w
c1.pxnxNY.dist sqrt((mbd.dsj8.xsx+mbd.dsj8.uc.src-mbd.dsj8.xdx-mbd.dsj8.uc.dest)^2
+(mbd.dsj8.xsy+mbd.dsj8.vc.src-mbd.dsj8.xdy-mbd.dsj8.vc.dest)^2
+(mbd.dsj8.xsz+mbd.dsj8.wc.src-mbd.dsj8.xdz-mbd.dsj8.wc.dest)^2+eps)
c1.pxnxNY.distx (mbd.dsj8.xsx+mbd.dsj8.uc.src-mbd.dsj8.xdx-mbd.dsj8.uc.dest)
/c1.pxnxNY.dist
c1.pxnxNY.disty (mbd.dsj8.xsy+mbd.dsj8.vc.src-mbd.dsj8.xdy-mbd.dsj8.vc.dest)
/c1.pxnxNY.dist
c1.pxnxNY.distz (mbd.dsj8.xsz+mbd.dsj8.wc.src-mbd.dsj8.xdz-mbd.dsj8.wc.dest)
```

```
/c1.pxnxNY.dist
c1.pxnxNY.damp d(c1.pxnxNY.dist,TIME)
c1.pxnxNY.sw c1.pxnxNY.dist¿l.c1.ny
c1.pxnxNY.f (k*(l.c1.ny-c1.pxnxNY.dist)
-c*(c1.pxnxNY.damp¿0)*c1.pxnxNY.damp)*c1.pxnxNY.sw
c1.pxnxNY.Ws c1.pxnxNY.sw*.5*k*(l.c1.ny-c1.pxnxNY.dist)ˆ2
c1.pxnxNY.fx c1.pxnxNY.f*c1.pxnxNY.distx
c1.pxnxNY.fy c1.pxnxNY.f*c1.pxnxNY.disty
c1.pxnxNY.fz c1.pxnxNY.f*c1.pxnxNY.distz
c1.tot.Ws c1.NXnypy.Ws+c1.NXpyny.Ws+c1.PXnypy.Ws+c1.PXpyny.Ws
+c1.nxpxPY.Ws+c1.pxnxPY.Ws+c1.nxpxNY.Ws+c1.pxnxNY.Ws
```

REPORT DOCUMENTATION PAGE	*Form Approved OMB No. 0704–0188*

1. REPORT DATE *(DD–MM–YYYY)* 26–03–2015	**2. REPORT TYPE** Master's Thesis	**3. DATES COVERED** *(From — To)* Oct 2013 — Mar 2015

4. TITLE AND SUBTITLE Simulation of Locking Space Truss Deployments for a Large Deployable Sparse Aperture Reflector	**5a. CONTRACT NUMBER**
	5b. GRANT NUMBER
	5c. PROGRAM ELEMENT NUMBER
6. AUTHOR(S) Van Dyne, Dylan M.	**5d. PROJECT NUMBER** JON157454B
	5e. TASK NUMBER
	5f. WORK UNIT NUMBER

7. PERFORMING ORGANIZATION NAME(S) AND ADDRESS(ES) Air Force Institute of Technology Graduate School of Engineering and Management 2950 Hobson Way WPAFB OH 45433-7765	**8. PERFORMING ORGANIZATION REPORT NUMBER** AFIT-ENY-MS-15-M-250
9. SPONSORING / MONITORING AGENCY NAME(S) AND ADDRESS(ES) Dr. David S. Stargel Chief, Dynamics Systems and Control Air Force Office of Scientific Research 875 N. Randolph St., Suite 325, Room 3112 Arlington, VA 22203-1768 Email: david.stargel@us.af.mil	**10. SPONSOR/MONITOR'S ACRONYM(S)** AFOSR/RTA **11. SPONSOR/MONITOR'S REPORT NUMBER(S)**

12. DISTRIBUTION / AVAILABILITY STATEMENT

Distribution Statement A:
Approved for Public Release; Distribution Unlimited.

13. SUPPLEMENTARY NOTES

This work is declared a work of the U.S. Government and is not subject to copyright protection in the United States.

14. ABSTRACT

Large deployable space structures require an inordinate amount of effort to fully design and test on Earth. To aid in the determination of the feasibility of the reflector, a method to simulate the structure's deployment was developed using COMSOL. The simulation model is comprised of a locking hinge truss that constitutes the partial reflector structure. To meet computational and temporal restrictions, the structure is simplified to use simple beams with square cross sections and is meshed to a sufficient accuracy with second order elements. The geometry is modeled in the truss's stowed configuration, with the connecting hinges and applied forces created via constraint equations in COMSOL. Many different simulations were run with varied design parameters in order to demonstrate the global motion of the deploying truss under differing conditions and to also showcase the capabilities of COMSOL's implicit solver. It was found through all of the simulation variations that the success of the truss's deployment is largely dependent on the condition of the lower truss members as well as the interaction between the spring-loaded hinges and tension cables. The results demonstrate how COMSOL can be used to aid in the advancement of the Large Deployable Space Aperture Reflector design.

15. SUBJECT TERMS

Space Structure, COMSOL, Multi-body-dynamics, Finite element analysis, Structure deployment

16. SECURITY CLASSIFICATION OF:			**17. LIMITATION OF ABSTRACT**	**18. NUMBER OF PAGES**	**19a. NAME OF RESPONSIBLE PERSON**
a. REPORT	**b. ABSTRACT**	**c. THIS PAGE**			Dr. Alan Jennings, AFIT/ENY
U	U	U	UU	185	**19b. TELEPHONE NUMBER** *(include area code)* (937) 255-3636, x7495; alan.jennings@afit.edu